UNIVERSITY OF CALIFORNIA,
IRVINE

Characterizing the Search for Ultra-High Energy Neutrinos with the ARIANNA Detector

DISSERTATION

submitted in partial satisfaction of the requirements
for the degree of

DOCTOR OF PHILOSOPHY

in Physics

by

Kamlesh Dookayka

Dissertation Committee:
Professor Steven Barwick, Chair
Professor Gaurang Yodh
Professor Manoj Kaplinghat

2011

DEDICATION

To my parents and my sisters for their support

TABLE OF CONTENTS

LIST OF FIGURES

LIST OF TABLES

ACKNOWLEDGMENTS

I would like to express my gratitude to all those who made this dissertation possible.

First, I would like to thank my advisor, Professor Steven Barwick, for his time and effort in guiding me through my doctoral studies.

Professor Gaurang Yodh and Manoj Kaplinghat have gratefully agreed to be part of my committee of my advancement to candidacy and dissertation defense. Arnold Guerra was a great mentor and positive presence. I would also like to thank the Physics department and their staff for all the logistic and administrative help.

I am indebted to Fenfang Wu. I inherited the simulation software that was initially put together by her. Sections of this thesis are also based on her work and provided me ideas for my content.

As part of the ARIANNA team, Jordan Hanson and Joulien Tatar have been supportive and productive colleagues in and outside the office.

I would like to thank late Dr. Andrea Silvestri for help with computing, as well as previous members of the group: Dr. David Goldstein and Dr. Jiwoo Nam for being part of the team of people that I worked with.

I would like to thank my parents and my siblings and their family for their support and patience during my studies. I thank the family relatives who helped me during my time living far away from my native Mauritius.

I also owe special thanks to many friends and colleagues whom I cannot list one by one for fear of missing some of them out. They were fellow graduate students and post-docs from the Physics department and friends I made within and without campus. Were it not for them, it would have been ever so harder to navigate those trying moments and challenges: academic and personal. They were here to lend me a listening ear, to share the fun and tough times, to provide me with the rides and meals.

Antarctic Ross Ice-shelf ANtenna Network Array (ARIANNA) project was supported by the U.S. NSF Office of Polar Programs and U.S. NSF Physics Divison, award numbers 0839133 and 0970175, and by the Department of Energy under contract DE-AC-76SF-00098.

CURRICULUM VITAE

Kamlesh Dookayka

Dept. of Physics & Astronomy
4129 F. Reines Hall
University of California
Irvine, CA 92697
dookayka@uci.edu

EDUCATION

Doctor of Philosophy in Physics **2011**
University of California, Irvine *Irvine, California*
"Characterizing the Search for Ultra-High Energy Neutrinos with the ARIANNA detector" (Doctoral Thesis title)

Masters in Physics **2004**
University of Oxford, England *Oxford, United Kingdom*
"The Universe at Low Frequencies"(Master's Thesis title)

RESEARCH EXPERIENCE

Graduate Research Assistant **2007–2011**
University of California, Irvine *Irvine, California*

Research Assistant **2003**
Rutherford Appleton Laboratory, Didcot *Oxfordshire, United Kingdom*

Student Researcher **2002**
University of Oxford *Oxford, United Kingdom*

Research Experience for Undergraduates **2001**
University of Minnesota, Twin Cities *Minneapolis, Minnesota*

TEACHING EXPERIENCE

California Community College Internship **2010–2011**
Orange Coast College & UC Irvine *Costa Mesa, California*

Teaching Assistant **2005-2009**
University of California, Irvine *Irvine, California*

PUBLICATIONS

Characterizing the search for UHE neutrinos with the ARIANNA detector, (Dookayka K. for the ARIANNA Collaboration) in International Cosmic Ray Conference Proceedings, 32nd ICRC, 2011.

A prototype station for ARIANNA: A detector for cosmic neutrinos, (Gerhardt, L. and Klein, S. and Stezelberger, T. and Barwick, S. and Dookayka, K. and Hanson, J. and Nichol, R.), 2010 Nuclear Instruments and Methods in Physics Research A, 624, 85.

ANITA status, (Connolly, A. for the Anita Collaboration), 2009 Nuclear Instruments and Methods in Physics Research A, 604, 98.

CONFERENCES

Characterizing the search for UHE neutrinos with the ARIANNA detector
International Cosmic Ray Conference, 32nd ICRC August 2011, Beijing, China.

Characterizing the search for UHE neutrinos with the ARIANNA detector
American Physical Society, APS April Meeting 2011, Anaheim.

Antarctic surface roughness effects on radio pulse propagation
American Physical Society, 2009 APS April Meeting, Denver.

Simulating Surface Roughness and its effects on EM wave scattering for ANITA
International School of Cosmic Ray Astrophysics, 2008 Erice, Italy.

Simulating surface roughness and its effects on electromagnetic waves scattering
American Physical Society, 2008 APS April Meeting, St. Louis.

AWARDS

GAANN Fellowship, University of California Irvine (2004-2007)
Waverley Scholarshi, University of Oxford, UK (2000-2004)

PROFESSIONAL MEMBERSHIPS

American Physical Society (2008-present)
Institute of Physics, UK (2000-present)
African Astronomer Society (2011-present)

ABSTRACT OF THE DISSERTATION

Characterizing the Search for Ultra-High Energy Neutrinos with the ARIANNA Detector

By

Kamlesh Dookayka

Doctor of Philosophy in Physics

University of California, Irvine, 2011

Professor Steven Barwick, Chair

The **A**ntarctic **R**oss **I**ce-shelf **AN**tenna **N**eutrino **A**rray (ARIANNA) experiment exploits unique properties of the Ross Ice Shelf, namely its radio transparency and reflectivity at the ice-water boundary beneath the shelf, to search for ultra-high energy neutrinos. It consists of an array of detectors embedded just beneath the surface with antennas facing down to listen to characteristic radio Cherenkov pulses generated by neutrino interactions in the ice.

A simulation tool has been developed and used for optimization studies and to evaluate ARIANNA's energy-dependent aperture (effective volume $\times$ steradians). This metric can be used to estimate the expected number of neutrinos detected from a given model prediction. The software and its physics, as well as the enhancements and additions to the original version, are described. We have included an improved treatment of the firn layer with an updated parametrization (based on latest measurements) of its graded index which impact signal path and polarization. Tau-neutrino interactions now take into account regeneration from their passage through Earth, and an approximation of the 'double-bang' effect. The antenna response is more accurately represented by averaging the relative gain in both E and H-planes.

Studies show that ARIANNA can detect ~ 35 events/year from the GZK mechanism using the ESS model prediction. The high sensitivity results from nearly six months or more

of continuous yearly operation, low energy threshold ($> 3 \times 10^{17}$ eV), large volume (513 km^3), and a view of slightly more than half the sky (declination +30° to -90°). The rates of background events are consistent with thermal noise fluctuations.

A new reconstruction framework has been devised for the energy and direction of a detected neutrino using measured parameters from a single station, such as relative time differences between antenna and signal amplitudes. Using simulated data, the energy and angular resolutions with a single station is calculated as

$$\delta E/E \approx 2.2 \qquad\qquad \sigma_\theta \approx 2.9^\circ,\ \sigma_\phi \approx 2.5^\circ$$

respectively. In addition to ARIANNA's potential for diffuse flux studies, these capabilities bode well for future UHE neutrino point source studies.

Chapter 1

Neutrino Astrophysics

Introduction

The field of astroparticle physics is currently undergoing rapid development. The traditional 'eye' on the sky, the photon, has been complemented by charged cosmic rays observations, starting early last century and in its latter part, with searches for sources emitting neutrinos They are all rich messengers allowing us to probe the properties of astrophysics sources. Optical astronomy, in one form or the other, has been around since the dawn of civilization while many properties of charged particle cosmic radiation are known. For example, the energy spectrum of cosmic rays is measured over an astonishing fourteen orders of magnitude in energy. Neutrinos, which interact solely by the weak force, are much more elusive. Though difficult to observe, it is not impossible and particle astrophysicists are stepping up to the challenge. The era of dedicated high-energy neutrino telescopes, began in earnest a couple of decades ago, promises to open a new and exciting window on the Universe. There are several extensive reviews [1, 2] highlighting the potential physics and astrophysics objectives utilizing the neutrino messenger. In this thesis, we focus on the energy interval between

10^{15}eV to 10^{20}eV, which is sometimes called the Ultra High Energy (UHE) regime.

1.1 Why UHE Neutrinos?

In the 1960s, Greisen, Zatsepin and Kuzmin (GZK) [3, 4] first proposed that ultra high energy cosmic rays (UHECR) ($\geq 5 \times 10^{19}$ eV) would rapidly lose energy through interactions with ambient cosmic microwave background (CMB) via

$$p + \gamma_{CMB} \rightarrow \Delta^{+} \rightarrow n + \pi^{+} \tag{1.1}$$

thereby slowing cosmic rays (proton or heavy nuclei) above that threshold to propagation distances of $\sim$ 50 Mpc from their source [5]. Since UHECR are almost certain to be extra-galactic, the GZK mechanism limits the maximum energy that can be observed on the Earth and predicts the cosmic ray spectrum to be suppressed above 50 EeV.

Cosmic ray experiments HiRes[6] and AGASA[7] early on reported conflicting results regarding the flux of particles above $10^{19.5}$eV. The Pierre Auger Observatory borrows the detection techniques from these two experiments and measurements reported from higher statistics due to larger exposure confirmed the expected break in the spectrum, as shown in Figure 1.1. as originally claimed by HiRes. The break energy of $10^{19.6}$ eV is consistent with the expectation from the GZK cutoff.

However, ultra-high energy cosmic rays do not offer a complete picture for investigation of astrophysical sources. Those few that reaches us may not even point back to their origin because their trajectories can be bent by the galactic and possibly intergalactic magnetic fields. Photons above $\sim$ 10^{15}eV of extragalactic nature, on the other hand, never reach our local neighborhood due to electron pair production when they collide with the infrared background radiation [9, 10]. This leaves the third type of messenger - the neutrino- as an

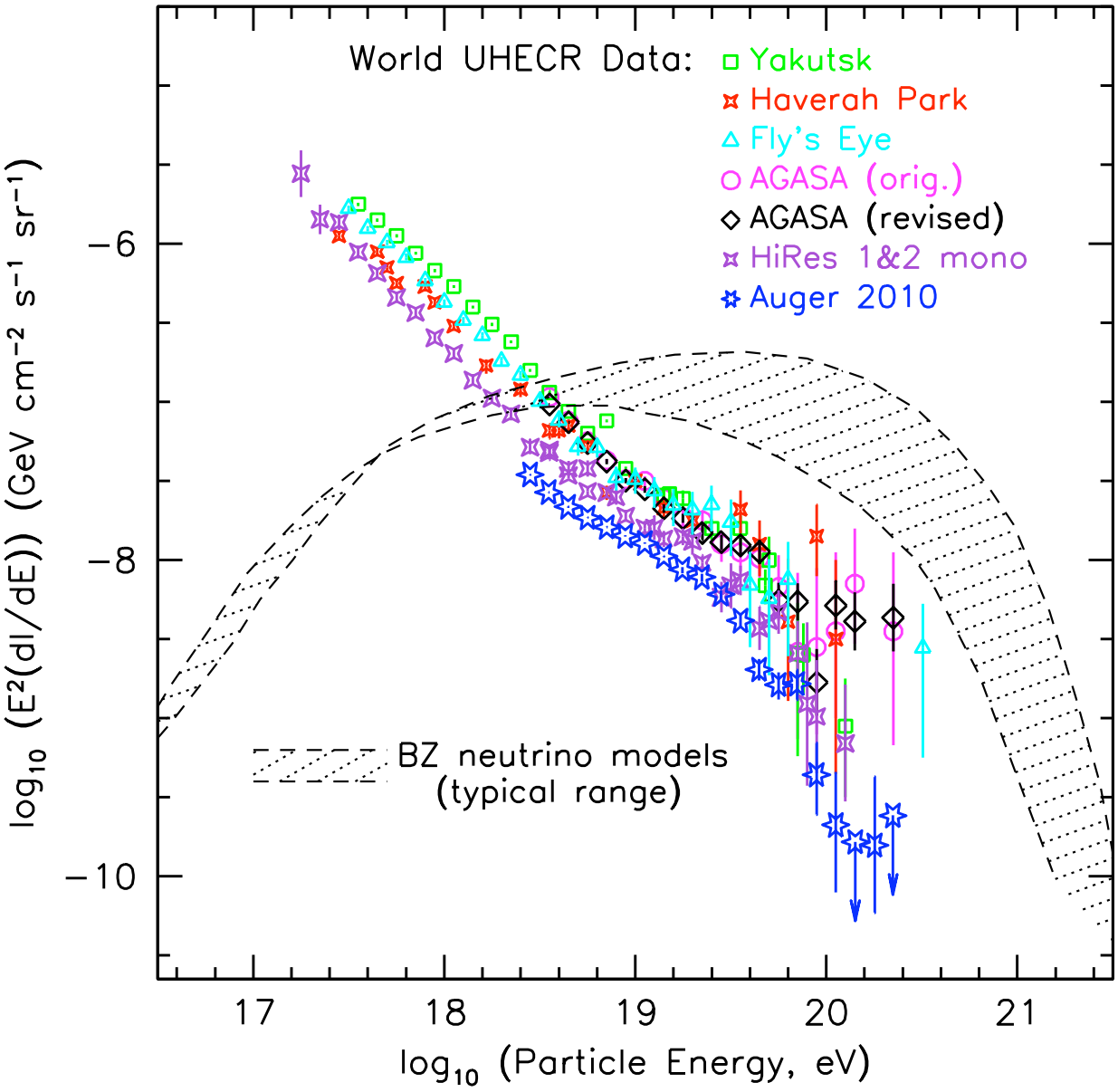

Figure 1.1: Ultra high energy cosmic-ray spectrum as measured by several experiments above 100 PeV. Recent results from Auger indicate the break in the spectrum at $10^{19.5}$ eV. The HiRes, AGASA and Auger experiments are briefly described in §1.4. The shaded region contains the range of neutrino flux predictions from the GZK mechanism (labeled here as BZ) as referred to in §1.2.1. Figure is from Ref. [8].

option for investigation at the highest reaches of astrophysics.

Indeed, soon after the GZK theory was proposed, it was realized that high energy neutrinos, which we call cosmological or GZK neutrinos, were a natural by-product of that process through its consequent pion decay [11, 12]

$$\pi^+ \rightarrow \mu^+ + \nu_\mu \tag{1.2}$$

followed by

$$\mu^+ \rightarrow e^+ + \nu_e + \bar{\nu}_\mu. \tag{1.3}$$

Neutrinos do not suffer from any of the aforementioned disadvantages. Interacting only through the weak interaction with a very small cross section [13], they can penetrate cosmological distances (hundreds of Mpc), escaping directly from close to event horizons of massive black holes or from the early moments of gamma-ray burst events. Being electrically neutral, they will not be bent by the magnetic fields of the universe and point back to their origin. Therefore, neutrinos are the unique messengers with which we can probe the possible sources of cosmic rays and study the mechanism of UHECR during their propagation in the Universe. Furthermore, with energies above 10^{17} eV, they would produce interactions with nucleons at center-of-mass energies near 100 TeV, exceeding those achieved at terrestrial accelerators. This provide a laboratory to search for new physics beyond the scope of the Standard Model of particle physics.

In the following sections of this chapter, we will present a discussion of astrophysical neutrino sources and fluxes, namely from the GZK mechanism, Active Galactic Nuclei (AGNs) and Gamma Ray Bursts (GRBs). We also briefly survey past, current and future experimental endeavors in the field. These will lead us to recognize the motivation for a next-generation

neutrino detector that can achieve the large aperture required in this specific field of astronomy.

1.2 Potential Sources of Diffuse Neutrino Flux

Various models in the literature predict the sources of UHE neutrinos and estimate their corresponding fluxes. As mentioned, the positive observations of UHECRs and the GZK cutoff imply the almost certain existence of cosmological neutrinos. Generation of neutrinos occur during propagation through the Universe or the progenitors of UHECR could themselves be the sources of neutrinos. It is theorized that they could also potentially be produced by the acceleration of hadrons of active galactic nuclei(AGN) [14], or by photopion production in cosmological gamma ray burst (GRB) [15]. Detectors such as AMANDA, or IceCube, its successor, are well-suited to search sources with strong power law ($\sim E^{-2}$) energy spectra that extends from TeV to PeV scales. Sources that emit neutrino with energy spectra that peak at energies above 10 PeV require new detectors with large apertures and exposures. The ARIANNA detector was designed to search for peaked spectra sources (such as expected for cosmogenic neutrinos) with much greater sensitivity.

It has been previously speculated that UHE neutrinos could also possibly be associated with the decays of extremely massive exotic particles such as topological defects [16], or the interaction of energetic neutrinos with big-bang relic cosmic background neutrinos via the Z-burst [17]. These ideas, primarily motivated to explain the highest energies cosmic rays, have now been severely constrained by recent experiments. A review can be be found in Ref [18] and [19]; we summarize the main ideas here.

1.2.1 GZK Neutrinos

GZK theory proposed that as cosmic rays with energies greater than 5×10^{19} eV propagate in the universe, they interact with the cosmic microwave background and generate neutrinos via pion decay through the sequence seen earlier:

$$p + \gamma \rightarrow \Delta^{+} \rightarrow \pi^{+} \rightarrow \mu^{+} + \nu_{\mu} \rightarrow e^{+} + \nu_{e} + \overline{\nu}_{\mu} + \nu_{\mu}. \tag{1.4}$$

The presence of the GZK cut-off and the indication by Auger of anisotropies in the distributions of UHECR hint that they are likely to be extragalactic. These observations of UHECR imply that GZK neutrinos are the most secure predictions for neutrino fluxes in the energy interval between 10^{16} eV and 10^{21} eV [3, 4]. Nevertheless there are significant theoretical uncertainties in the calculations as we see next.

Estimates of the flux and shape of the GZK neutrino flux depend on the following factors [17], [20], [21], [22], [23], [24]:

1. the composition of UHECRs,
2. UHECR energy spectrum - spectral shape, normalization and energy cutoff,
3. cosmological model,
4. the distribution of UHECR sources,
5. the cosmological evolution of the sources with redshift,
6. the proton-photon cross section, and
7. neutrino oscillations.

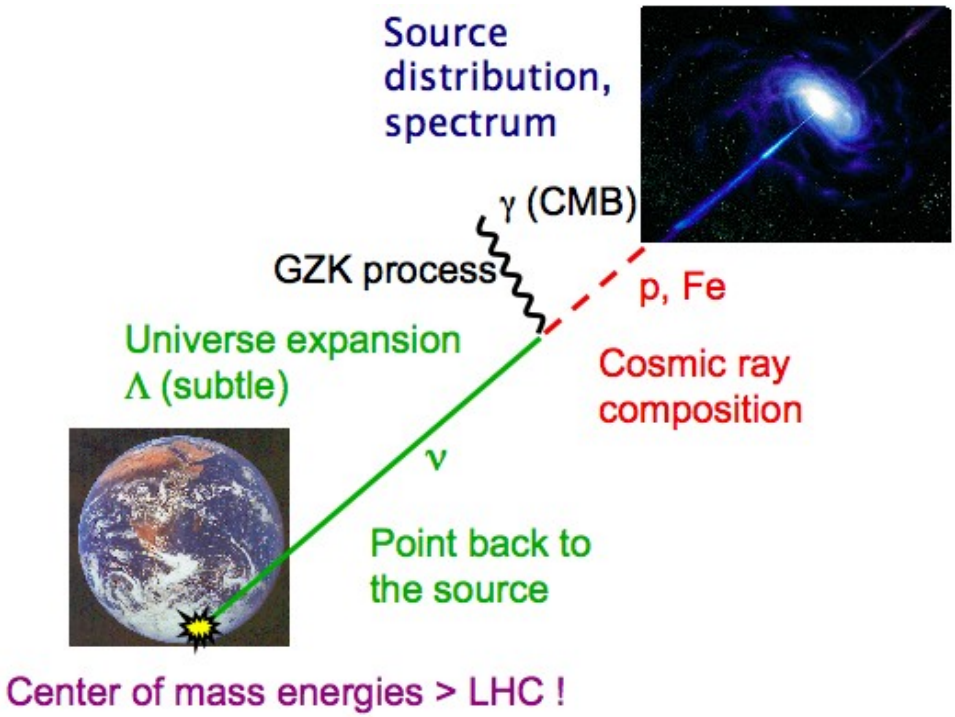

Figure 1.2: A sketch, adopted from [25], identifying the main Physics affecting neutrino fluxes predictions. Uncertainties prevail at the both the source and propagation levels due to variations in injected spectral index, chemical composition, maximum acceleration energy and source evolution history.

1. Composition of UHECR Most early predictions of the cosmological neutrino flux assume that the UHECR primaries are pure protons. A few more recent cosmological neutrino fluxes calculations [21][26] take pure ^{56}Fe, ^{4}He, or ^{16}O as the primaries. The heavier nuclei lose energy via photo-disintegration, in which secondary nucleons are produced. The photopion production of these secondary nucleons create UHE neutrinos. In addition, a small flux of anti-electron neutrinos are produced via neutron decays [27] but the energies are too small to be of interest to ARIANNA. For non-pure proton composition, the neutrino flux is small compared with pure proton component as pointed out in Ref. [26]. Since the energy per nucleon after photo-disintegration is much smaller than the primary energy (in the case of Fe, $E/nucl \sim E_p/56$) and may be to low to interact by the GZK process. Some neutrino flux estimations assume the sources inject a mixture of primaries with the same initial abundances as the observed Galactic cosmic rays [23]. Various primary component models create uncertainty in the prediction of neutrino flux by more than an order of magnitude.

Recent experimental results by Auger [28] , though highly debated, indicate that UHECRs may be dominated by heavier nuclei. This contradicts the results from HiRes, and more recently, Telescope Array (TA)[29]. Conversely, if neutrino fluxes are observed above the diminished predictions of heavy Z cosmic ray composition, then they will shed light on the elemental composition of extragalactic cosmic ray sources or rule out heavy composition.

2. Energy profile The injection spectrum of UHECR can be inferred from experimental results of cosmic ray detectors on Earth. Typically it is assumed that the UHECR spectrum at injection is a power law in the form of

$$\frac{\mathrm{d}N}{\mathrm{d}E} = P_0 \cdot E^{-\alpha} \cdot \exp(-\frac{E}{E_c}) \tag{1.5}$$

where P_0 is a normalization constant for the flux. The spectral index α lies between 1.8 and 2.7, favored to be close to $\alpha \approx 2.3$. The cutoff energy at injection, E_c, is assumed to

be between 10^{20} eV and 10^{23} eV. The values of α and E_c are both dependent on the source type assumption, the corresponding source characteristics and the acceleration mechanism of cosmic rays at the source. The measurements at the Earth and the mechanism during propagation of cosmic rays in the inter-galactic space also affect the predictions of UHECR initial spectrum. A steeper injection spectra and smaller cutoff energy generate smaller neutrino fluxes at high energy due to the decreased number of protons at high energies that would be responsible for such neutrinos.

3. Cosmological model The cosmology of the Universe is another factor that drives the uncertainty of GZK neutrino flux. Astrophysical observations now point to models with a cosmological constant Λ [30], compared with the flat, mass dominated Einstein-de Sitter Universe ($\Omega_M = 1$) typically assumed by calculations prior to mid-90's. The currently favored "concordance" model is one with $\Omega_\Lambda = 0.7$ and $\Omega_M = 0.3$ [31], which means that dark energy accounts for 70% of the total mass-energy of the Universe. Consequently, the Universe is expanding more quickly during the epoch that generate cosmological ν's leading to a proportionally larger contribution to the neutrino yield from higher redshifts. Engel et al. [20] compared the neutrino fluxes derived from the two cosmologies and found that the $\Omega_\Lambda = 0.7$ model increases neutrino flux by 60% for a moderate redshift evolution.

4. Distribution of sources Most calculations of cosmological neutrino fluxes assume uniformly distributed homogeneous sources with identical injection spectra. However, it is also possible that contributions to the cosmic rays come from a relatively nearby extragalactic point source (so-called "local"). If the local source is injecting heavy primaries then they would appear isotropic due to scattering and diffusion by the galactic magnetic field. Engel et al. [20] studied the case where the injection power of homogeneously distributed sources contribute half and the other half of the local UHECR are generated by a single source at a distance of 20 Mpc.

5. Cosmological evolution Prediction of neutrino flux is strongly dependent on the cosmological evolution of the potential cosmic ray sources. There are at least four evolution models that have been most commonly discussed in the literature, namely (i) no evolution and a set of relatively moderate evolution like (ii) Star Formation Rate (SFR), (iii) Active Galactic Nuclei (AGN), and (iv) strong Gamma Ray Burst (GRB) evolutions.

To describe the cosmological evolution of sources, a source evolution term $\mathcal{H}(z)$ is used to specify evolution of mass (or rate) density of sources with redshift z within a comoving volume. It represents the ratio of the mass (or rate) density of sources between redshift z and now. The mass density of sources at redshift of z would be $\rho(z) = \mathcal{H}(z) \times \rho(0)$.

(i) The simplest model assumes that there is no evolution with redshift (i.e. $\mathcal{H}(z) = 1$) and it yields the most conservative neutrino flux.

(ii) In the SFR evolution first introduced in Ref. [32], we have

$$\mathcal{H}(z) = \begin{cases} (1+z)^3, & z < 1.3, \\ (1+1.3)^3, & 1.3 < z < 6, \end{cases} \tag{1.6}$$

followed by a sharp-cutoff.

(iii) The QSO (Quasi Stellar Objects) evolution model, that fits the AGN classification scheme, used in Ref. [20] and [33] has the following form for the source evolution term,

$$\mathcal{H}(z) = \begin{cases} (1+z)^n, & z < 1.9, \\ (1+1.9)^n, & 1.9 < z < 2.7, \\ (1+1.9)^n \exp[(2.7-z)/2.7], & z > 2.7, \end{cases} \tag{1.7}$$

where $n = 3$ describes the source evolution up to moderate redshifts. A stronger AGN evolution model sets $n = 4$ up to $z = 1.9$ and flat at higher redshifts.

(iv) H. Yuksel et al. proposed the source evolution term, $\mathcal{H}(z)$ as

$$\mathcal{H}(z) = \begin{cases} (1+z)^{4.8}, & z < 1, \\ (1+z)^{1.4}, & 1 < z < 4.5, \\ (1+z)^{-5.6}, & 4.5 < z. \end{cases} \tag{1.8}$$

It is a stronger redshift evolution in the "local" universe generally called as GRB evolution, which could lead to an enhancement in the flux of cosmological neutrinos [24].

6. Proton-photon cross-section The neutrino yield from the interaction

$$p\gamma \rightarrow \Delta^{+} \rightarrow n\pi^{+} \rightarrow n\nu_{\mu}e^{+}\nu_{e}\bar{\nu}_{\mu} \tag{1.9}$$

is determined by the proton-photon cross-section, $\sigma_{p\gamma}$. Cross-section measurements from accelerator data are used to estimate the fraction of energy going into neutrinos and the number of neutrinos produced in one interaction. Generally, it is assumed that the fraction of energy going into the charge pion from the proton is $x_{p\rightarrow\pi} \approx 0.2$ and the four leptons carry an equal amount of energy, so on average each neutrino carries about 1/20 of the proton energy.

7. Neutrino oscillations The GZK neutrino production (Eq. 1.4) shows that the resultant ratio of muon neutrinos to electron neutrinos is about 2, with the tau neutrinos being heavily suppressed. In the dissertation, unless stated otherwise, muon neutrinos (ν_{μ}) refer to $\nu_{\mu} + \bar{\nu}_{\mu}$, and the same applies for electron neutrinos (ν_{e}) and tau neutrinos (ν_{τ}). Due to the long distance that neutrinos travel before reaching the Earth, original cosmic neutrino fluxes with a $\nu_{e} : \nu_{\mu} : \nu_{\tau}$ ratio at the source of 1:2:0 inevitably oscillate to a ratio of 1:1:1([1]).

The overall picture Though the existence of cosmological neutrino fluxes is one of the most secure in particle astrophysics, flux predictions span four orders of magnitude. Some of these predictions are shown in Fig. 1.3 for the total neutrino flux summed over all three flavors. The sum of all ν flavors is a useful variable for ARIANNA because it is sensitive to all flavors (ν_μ slightly less than ν_e, ν_τ) but flavor identification is not straightforward.

ESS GZK Neutrino Flux

In the preceding discussion, we have referred to models by Engel, Seckel and Stanev (ESS) in Ref. [20]. In our work, we adopt a version of their cosmological neutrino flux predictions a baseline for our studies. Their flux was calculated using the event generator SOPHIA [34] to simulate the photopion production interactions, under the assumption of uniformly distributed sources with identical pure proton injection spectra. The spectrum is a power law with an exponential high-energy cutoff as in Eqn. 1.5 where P_0 is derived by Waxman with the value of $(4.5 \pm 1.5) \times 10^{44}$ ergMpc^{-3}yr^{-1} between 10^{19} and 10^{22} eV [33], $\alpha = 2$ and $E_c = 10^{21.5}$ eV. For the cosmological evolution of the cosmic ray sources, $\mathcal{H}(z)$, they use the aforementioned QSO model with the parameterization of Ref. [33], as given in Eqn.1.7. The default cosmological assumption used is the model with $\Omega_M = 0.3$ and $\Omega_\Lambda = 0.7$.

With all the choices of cosmological parameters listed above and by carrying out an integration to a redshift of $z_{\max}$ to 8, electron and muon neutrino fluxes were obtained and the total neutrino flux is displayed in Fig.1.3.

Using a stronger cosmological evolution of $(1+z)^4$ up to redshifts of 1.9 and flat at higher redshifts, the neutrino flux from homogeneous source distribution increases by about factor of 3, as shown in the same figure. In this dissertation we use this more optimistic ESS differential flux, Φ_{ESS} with stronger evolution ($n = 4$), hereafter called as ESS flux or ESS_{Fig9}, for our simulations and calculations. We note that neither predictions has been

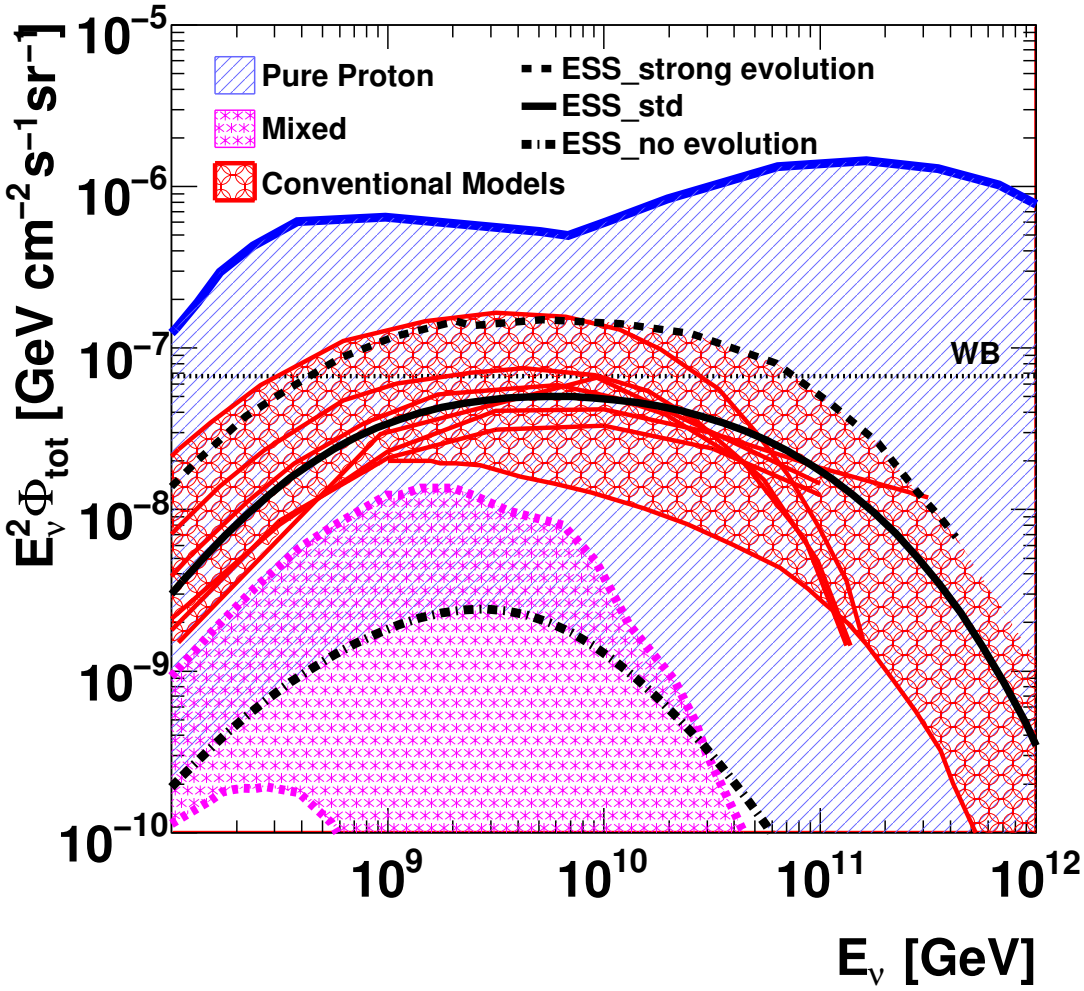

Figure 1.3: Total GZK neutrino fluxes summed over all flavors. The blue lined band includes most of the GZK neutrino flux models under the assumption that UHECR are primarily pure protons [17]. The upper thick curve represents an envelope of models with extreme parameters such as strong cosmic evolution, hard cosmic ray injection spectrum etc. The red circled band lies within the blue band, and it represents GZK neutrino flux models with parameters which are more conservative and consistent with current observation results in the literature. The pink starred band describes neutrino fluxes generated by mixed components [20], [21], [22] [23] [24]. The black curves are the different predictions from ESS [20]. Black dashed line: using a cosmological evolution of $(1+z)^4$ up to redshift of 1.9 and flat at higher redshifts, generally referred to as ESS_{Fig9}. Black solid curve: QSO cosmological evolution model with n=3, called as ESS_{std}. Black dash-dotted curve: no evolution.

ruled out by current experiments. In fact, model rejection factors allow $\sim 3\Phi_{ESS}$.

1.2.2 Active Galactic Nuclei

Active Galactic Nuclei (AGN) are the most persistent objects isotropically distributed in the sky and one of the most powerful source classes with luminosities on the order of $10^{45\pm3}$ erg/s [2]. Therefore they are considered as one of the best candidate sources for UHE cosmic ray production and many authors predict measurable fluxes of neutrinos if the acceleration site is surrounded by a sufficiently thick cocoon of material.

The enormous radiation from AGNs are proposed to be fueled by gravitational energy released as matter infalls to a supermassive black hole at its center. During this process, angular momentum causes the material to flatten into an accretion disk. By some poorly defined mechanism, infalling matter is diverted into a perpendicular oriented jet, with turbulent shocks accelerating particles to high energies. Thereby, a significant fraction of total gravitational energy is converted into highly relativistic particles via first-order Fermi acceleration [35] of charged particles. Frictional heating turns the infalling matter into plasma, which thereby produces a strong magnetic field. The collisions of ultra-relativistic protons with the intense photon fields of AGN yield high energy neutrinos under photopion production via $p\gamma \rightarrow \pi^+ n$ or $p\gamma \rightarrow \pi^0 p$ and subsequent decay of $\pi^+ \rightarrow \mu^+ \nu_\mu$ followed by $\mu^+ \rightarrow e^+ \nu_e \bar{\nu}_\mu$. Other models imagine protons collide with gas and dust, so the mechanism is $pp \rightarrow \pi + X$. The neutrinos initially only include ν_μ and ν_e, but oscillation turns them into equal flavor ratio on their way to Earth [36].

Depending on where neutrino production takes place, there are two classifications: AGN core model or AGN jet model. In this first one, initially proposed in by Stecker et al [14] protons are accelerated and interact with the photon field inside the cores of AGNs. In the second model, there are two relativistic jets that are emitted perpendicular to the accretion

disk, which transport matter in form of lobes. Protons are accelerated at shock wave in the jets and then, upon interacting with photons radiated from the accretion disk, produce neutrinos. Neutrino flux can be estimated using measured luminosity function for AGNs and by integrating over redshift and luminosity [37]. Mannheim et al.[38] calculated the maximum possible neutrino flux originating from AGNs using source evolution functions for blazars and varying the energy where the cosmic ray spectrum changes its slope.

1.2.3 Gamma Ray Bursts

Gamma Ray Bursts (GRBs) are brief flashes of γ-ray light emitted by sources at cosmological distances. They are the most energetic explosions in the Universe and are thought to be possible sources of high energy neutrinos. Their neutrino emissions have been calculated under various scenarios.

In the currently favored GRB fireball shock model [39] [40], the prompt γ rays are produced by collisions of plasma material moving relativistically along a jet (internal shocks), i.e. a fireball. Late time collisions of jetted material with an external medium like interstellar medium (external shocks) produce a broad band radiation like X-ray, UV and optical radiation, collectively known as the GRB afterglow. In the jet, electrons and protons are accelerated by relativistic shocks via Fermi mechanism. The synchrotron radiation and inverse Compton scattering by the high energy electrons lead to the observed photons. The accelerated protons on the other hand interact with observed prompt γ-rays or afterglow photons via photopion production interaction, and produce a burst of high energy neutrinos accompanying the GRB. The neutrinos generated in the original fireball with internal shock are called burst neutrinos, and those from GRB external shock are called afterglow neutrinos.

Another popular GRB model is the supernova model [41] in which a supernova remnant shell from the progenitor star is ejected prior to the GRB burst. Protons in the supernova

remnant shell and photons entrapped from a supernova explosion or a pulsar wind from a fast-rotating neutron star remnant provide ample targets for protons escaping the internal shocks of the gamma-ray burst to interact and produce high energy neutrinos.

1.2.4 Unconventional Neutrino Sources

We briefly mention some of the more exotic sources of ultra-high energy neutrinos, even though their predictions are ruled out by recent stringent experimental results from ANITA (see Ref.[42] and §1.4). We note that these various models were proposed were to explain the apparent lack of a GZK cutoff in the high energy cosmic ray spectrum in early observations.

Top-down (TD) models are based on the assumption that both UHECR and neutrinos are the decay products of some super-massive exotic particles (X) with mass of $m_X \gg 10^{20}$ eV and energies all the way up to the grand unified theory scale ($\sim 10^{16}$ GeV $= 10^{25}$ eV). The X particles first decay into quarks and leptons. As the quarks hadronize, jets of hadrons are produced. The decay products of the unstable leptons, together with the jets of hadrons, result in a cascade of energetic photons, neutrinos and light leptons with a small fraction of neutrons and protons, some of which contribute to the observed UHECR. S. Yoshida et al. proposed that the X particles could be released from topological defects, such as monopoles and cosmic strings, which were formed in the early universe; and that the UHECR well above 10^{20} eV and UHE neutrinos are the result of the annihilation or collapse of topological defects [16].

The Z-Burst model proposed that neutrinos may not only be cosmological by-products but could also be closely associated with sources of UHECR. If there are large fluxes of neutrinos at energies of order 10^{22-23} eV, they can annihilate with big-bang relic cosmic background neutrinos ($T_\nu \sim 1.9$ K) in our own Galactic halo via the interaction as [17], $\nu + \nu \rightarrow Z^0$. The decays of the neutral weak vector boson Z^0 yield UHECR while those high energy neutrinos

that do not interact could be detected at the Earth.

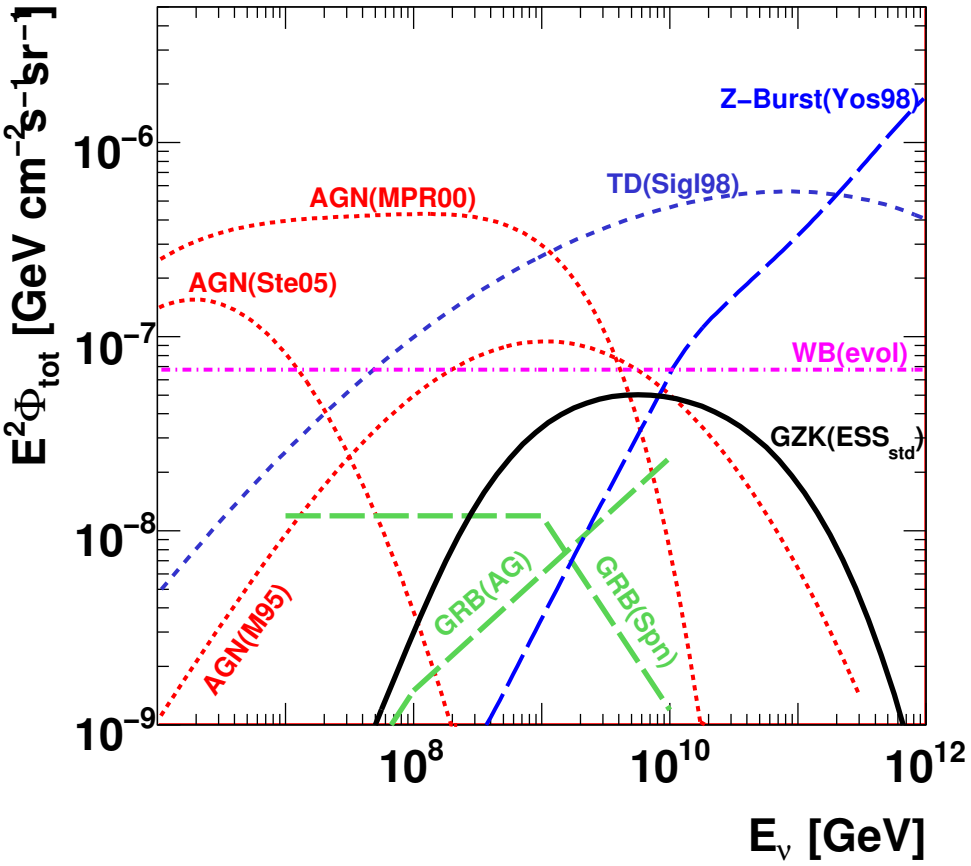

Figure 1.4: Representative models of all flavor neutrino fluxes including GZK, AGN, GRB, TD and Z-Burst models. Theoretical WB bounds are also shown [43]. The key is as follows: GZK(ESS_{std}) from [20],AGN(Ste05) from [36], AGN(MPR00) from [38], AGN(M95) from [44], GRB(Spn) from [41], GRB(AG) from [40], TD(Sigl98) from [45] and Z-Burst(Yos98) from [17].

1.3 Limits on Neutrino Flux

The Waxman-Bahcall Bound on Neutrino Flux

E. Waxman and J. Bahcall in Ref [43] established theoretical bounds on the flux of neutrinos produced by photopion interactions of protons. Based on the observed cosmic ray spectrum, the rate at which high energy protons are produced at sources can be determined [33]. Assuming that all the energy injected as high-energy protons is converted to pions via photopion or p-p collision, the energy generation rate of neutrinos cannot exceed the energy generation rate of protons at sources. The authors argued that the material surrounding the source cannot be too thick, or else, there would be an insufficient number of protons escaping to become the cosmic rays, and then cosmic rays lose the connection to neutrinos. On average, all sources are tuned to be surrounded by one interaction length of material to produce a maximum neutrino flux yet still capable of generating the cosmic ray flux.

Using the energy-dependent generation rate of cosmic-rays of

$$E_{CR}^2 \frac{\mathrm{d}N_{CR}}{\mathrm{d}E_{CR}} \simeq 10^{44} \text{ erg Mpc}^{-3} \text{ yr}^{-1}, \tag{1.10}$$

Waxman derived a characteristic E^{-2} spectrum bound on the muon neutrino flux (ν_μ and $\bar{\nu}_\mu$ combined) as

$$E^2 \Phi_\nu < 9 \times 10^{-9} \text{ GeV cm}^{-2} \text{ s}^{-1} \text{ sr}^{-1} \tag{1.11}$$

for the cosmological model of no redshift evolution,and

$$E^2 \Phi_\nu < 4.5 \times 10^{-8} \text{ GeV cm}^{-2} \text{ s}^{-1} \text{ sr}^{-1} \tag{1.12}$$

for the QSO cosmological model (see §1.2.1 above for description). To get an upper bound

on the total neutrino flux, the muon neutrino intensities are multiplied by 1.5 due to the ratio of $\nu_e : \nu_\mu : \nu_\tau = 1 : 2 : 0$ at the origin. This bound is illustrated in Fig. 1.4 and 1.5.

Eqn. 1.10 was derived by assuming the extragalactic flux of cosmic rays only begin to dominate galactic cosmic rays above the 'ankle' at $E_{CR} \sim 10^{19}$eV, to set the normalization, and follow an energy spectrum proportional to E^{-2}. Since it is not clear when extragalactic cosmic rays dominate, others have relaxed the WB bound by assuming that extra-galactic cosmic rays begin just above the know. It is important to emphasize that the calculations produce an upper bound: much lower and even no flux of high energy neutrinos are compatible with this idea.

Limits on Neutrino Flux from Experiments

Over the past decade, various results have been improving the experiment bounds by orders of magnitude. The searches and detection techniques are outlined in the next section. Here, in Figure 1.5, we summarize the flux limits imposed in the 10^{17}-10^{21} eV energy range. Recent results from IceCube have now constrained the flux below the W-B bound [46].

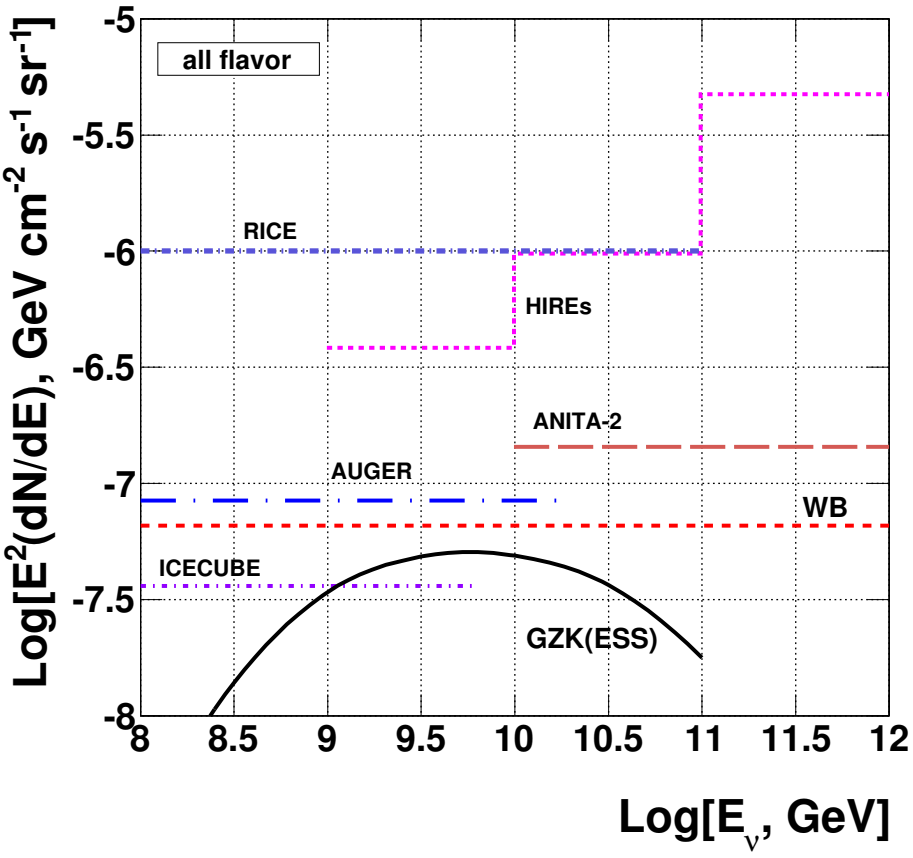

Figure 1.5: Limits for a diffuse neutrino flux of all flavors from the Pierre Auger Observatory [47], RICE [48] (scaled to 90% C.L.), ICECUBE (IC-40) [46], ANITA-2 [49] and HiRes [50]). The black solid curve shows the expected flux of GZK neutrinos from Ref. [20], generally called ESS_{std}.

1.4 Experimental searches

We review[1] some current and upcoming experiments that are involved in searches for UHE neutrinos of cosmic origin. The detection techniques rely on Cherenkov radiation (described later in §2.1), either in optical or radio for the very highest energies. Acoustic detectors sensitive to the sudden local expansion that occurs when a high-energy neutrino interaction deposits energy in water or ice are also methods being considered.

1.4.1 Optical Methods

Particle tracks from products on neutrino interaction a dense medium can create visible Cherenkov radiation than can be picked up by photomultiplier tubes. The largest of such experimental searches is IceCube, the successor to AMANDA (Antarctic Muon And Neutrino Detector Array). It consists of thousands of spherical optical sensors between 1450 m and 2450 m deep within a km^3 of the South Pole ice. The goal is to detect neutrinos of energies spanning from 10^{11} eV to about 10^{21} eV through Cherenkov light given off by the muons produced through a charged-current interaction of a muon-neutrino with nucleons in the ice. Construction was completed in early 2011 and recent data are helping further constrain the astrophysical neutrino flux over different energy regimes.

The latest published results on extremely-high energy diffuse neutrino searches with data collected between April 2008 and May 2009 (333.5 days of livetime) from the half-completed array places a limit of

$$E^2 \frac{\mathrm{d}N}{\mathrm{d}E_\nu} < 3.6 \times 10^{-8}\ \mathrm{GeV\ cm^{-2}\ s^{-1}\ sr^{-1}} \tag{1.13}$$

[1]Many extensive reviews and status reports appear in the literature. Ref [51] and [25] provide concise summary of astrophysical neutrino searches.

over the energies of 2×10^6 GeV to 6.3×10^9 GeV. In this energy region, this result is the first constraint of neutrino fluxes below the Waxman-Bahcall flux bound [46].

The Mediterranean Sea is the location site of the ANTARES [52] (off the coast of Southern France), NEMO [53] (near Sicily) and NESTOR (15 km from the Greek coast) [54] efforts. KM3NeT [55] is a future experiment that will complement IceCube and contribute in viewing the full sky. Lake Baikal in Siberia is host to NT-200 [56] of the pioneering experiments searching for neutrino detection using phototubes. Optical searches have improved neutrino flux limits by several orders of magnitude in the TeV-PeV energy interval.

1.4.2 Radio Cherenkov

At EeV (10^{18} eV) energies and above, the expected neutrino flux is too small to be detectable in km^3 telescopes. Radio detection presents a viable way to probe the ultra-high energy range and have been proposed as an avenue for neutrino detection by Gurgen Askaryan in the early 1960's [57]. He realized that the coherence of the Cherenkov radiation in the radio regime results in the power of the pulse being proportional to the square of the primary of energy of the initial particle (this is elaborated upon in the §2.1 of the next chapter). Coupled with the fact that the attenuation lengths in naturally occurring media like ice, salt and sand is very long at such frequencies ($\lesssim 1$ GHz), it is promising to instrument large volume of such media to listen to RF pulses. All the past, present and proposed radio Cherenkov experiments use one of these three media.

RICE (the Radio Ice Cherenkov Experiment) searches for radio emission from electromagnetic and hadronic cascades induced by UHE neutrinos colliding with nuclei in the Antarctic ice. It is an array of 16 antennas of bandwidth 200-1000 MHz contained within a cube of ice 200 m on a side, with a center about 150 m deep, near the South Pole. Based on data collected from 1999 to 2005, with a livetime of 74.1×10^6 s, RICE placed a 95% confidence-level

model-dependent limits on the neutrino flux of all three flavors of

$$E_\nu^2 \frac{\mathrm{d}N}{\mathrm{d}E_\nu} < 10^{-6} \text{ GeV cm}^{-2} \text{ s}^{-1} \text{ sr}^{-1} \tag{1.14}$$

over the energy regime of 10^8 GeV to 10^{11} GeV [48], after no neutrino candidate events were found. For similar comparison with other flux limits, we scale the limit to 90% C.L. in Fig. 1.5.

FORTE (Fast On-orbit Recording of Transient Event) has monitored the Greenland ice from a satellite and recorded electromagnetic waves arising from near the Earth's surface in the radio frequency range 30-300 MHz using a dual polarization antenna. Based on the data from 1997 to 1999, a single neutrino candidate out of several thousand raw triggers survives all cuts and limits on the corresponding particle fluxes assuming this event represents the background level. The details about how FORTE concluded that this candidate can only be due to a neutrino are presented in Ref. [58].

ANITA (ANtarctic Impulsive Transient Array) is an Antarctic balloon-borne experiment that is launched under NASA's long duration balloon program from McMurdo station. It consists of an array of broadband (200-1200 MHz) dual-polarization quad-ridged horn antennas that view the Antarctic ice sheet from its in-flight altitude of 37 km where it is in view of of ice surface. The first full ANITA flight, following the ANITA-LITE prototype test flight in early 2004, was launched on December 2006 and remained aloft above the Southern continent for 35 days [42].

The second flight, with a payload enhanced from 32 to 40 antennas and other hardware improvement, was in December 2008. From 28.5 days livetime and using one observed candidates, ANITA-II set a 90% CL integral flux limit on all neutrino flavors of

$$E_\nu^2 \frac{\mathrm{d}N}{\mathrm{d}E_\nu} < 1.3 \times 10^{-7} \text{GeV cm}^{-2} \text{ s}^{-1} \text{ sr}^{-1}, \tag{1.15}$$

the strongest constraint to date over the energy range 10^{18} eV to $10^{23.5}$ eV [59].

FORTE and ANITA remotely monitor their target medium. The same concept is extended to radio telescopes observing the moon for neutrino signals. **GLUE** (Goldstone Lunar Ultrahigh Energy) searched for ∼10 ns microwave pulses from the lunar soil, appearing in coincidence at two large radio telescopes separated by about 20 km and linked by optical fiber. The pulses can arise from subsurface electromagnetic cascades induced by interactions of upcoming UHE neutrinos in the lunar regolith. Using data of about 30 hours of livetime which yielded zero event, GLUE sets upper limits on the diffuse cosmic neutrino fluxes over the energy range from 10^{19} eV to $10^{22.5}$ eV [60]. Kalyazin [61] and Parkes [62] experiments have also previously monitored the moon for signals, There are ongoing efforts to exploit either existing radio telescopes like Westerbork Synthesis Radio Telescope through the NuMoon [63], and future giant arrays like the planned Square Kilometer Array (SKA), that is to be located in South Africa or Australia [64]. LUNASKA(Lunar UHE Neutrino Astrophysics using the Square Kilometer Array) is one such proposal [65].

ARA (Askaryan Radio Array) is an initiative to develop a multi-phased teraton-scale ultra-high energy neutrino detector in deep, radio-transparent ice near the South Pole [66]. A station design consists of a cluster of 16 embedded antennas deployed up to 200 m deep in several vertical boreholes placed with tens-of-meter horizontal spacing to form a small sub-array. An initial prototype detector system was installed in January 2011 to perform studies relating to the radio environment of the site: background noise levels and radio clarity of the ice. There are plans to build a 200 km^2 array, known as ARA-37.

SalSA (Salt Sensor Array) is a detector concept to deploy radio detectors in one of the large salt formations (a few km × a few km × 10 km are not atypical) that exist in many locations around the world [67]. One would find 2.5 times as many neutrino interactions per unit volume in salt compared to ice due to its higher density. Although the peak power of the emitted radio Cherenkov signal is lower than in ice, the width of the Cherenkov cone is

broader [68]. Additionally, an experiment in the Northern Hemisphere would view a region of the sky not in view of an experiment in the South. Ground Penetrating Radar (GPR) experts have reported low radio loss in salt mines in the US, but it is difficult to deduce attenuation length measurements from their findings [69]. Before a SalSA experiment can move forward, long attenuation lengths ($\gtrsim$ 250 m) must be measured definitively at radio frequencies [25].

1.4.3 Cosmic Ray Detectors

We earlier introduced three cosmic ray experiments that were involved in the determination of the GZK cut-off. Though designed for UHECR studies, they can be employed to observe neutrinos as by-products.

AGASA (Akeno Giant Air Shower Array) used a widely spread ground array, consisting of 111 plastic scintillation detectors of 2.2 m^2 over an area of 100 km^2 with a separation of 1 km, to detect UHECR by measuring the secondary particles produced in a cosmic ray shower [7].

The **HiRes** (High Resolution Fly's Eye) experiment consists of two detector stations located 12.6 km apart. Each station monitors its surrounding sky for observing fluorescent emission from cosmic ray air showers in atmosphere [6]. The GZK feature in their measurements have been corroborated by Auger, as seen earlier in Figure 1.1. However, they diverge on other CR observations: no anisotropy in their smaller data sample and light primaries composition persistent up to the higher energies. With regards to neutrino detection, they have reported 90% C.L integrated flux limits ($E_\nu^2 \mathrm{d}N_\nu/\mathrm{d}E_\nu$) of 3.81×10^{-7}, 9.73×10^{-7} and 4.71×10^{-6} GeV cm^{-2} sr^{-1} s^{-1} over three decades energy centered around $10^{18.5}$, $10^{19.5}$ and $10^{20.5}$ respectively. This calculation was based on a livetime of 3638 hours, with no neutrino events, and combining results from ν_τ and ν_e studies [50]. They were sensitive to

decays of the outgoing tau's following ν_τ interactions in the Earth's crust, and to ν_e induced electromagnetic showers in the earth and in the atmosphere [70].

Auger (Pierre Auger Observatory) hybrids both techniques of surface and fluorescence detectors to observe showers simultaneously [71]. It can detect UHE neutrinos by searching for an extended air shower from down-going neutrinos of any flavor or up-going tau neutrinos through a distinctive broad signal in time as their signature. In the first case, the neutrino can interact at any atmospheric depth to produce an extensive air shower. Earth skimming τ neutrinos with UHE may undergo a charged-current interaction to produce τ, and those τ being close to the surface can exit the Earth and decay in the atmosphere to produce a nearly horizontal electromagnetic shower [47]. Based on the published data taken from January 2004 until 30 April 2008, an upper limit on the diffuse flux of UHE ν_τ is set at 90% C.L. of

$$E_{\nu_\tau}^2 \frac{\mathrm{d}N_{\nu_\tau}}{\mathrm{d}E_{\nu_\tau}} < 9 \times 10^{-8}\ \mathrm{GeV\ cm^{-2}\ s^{-1}\ sr^{-1}} \tag{1.16}$$

in the energy range 2×10^{17} eV $< E_\nu < 2 \times 10^{19}$ eV [72]. For better comparison with other flux limits, we convert the limits on ν_τ to limits on all flavors by multiplying 3. More recently, Auger collaboration has updated [47] their diffuse neutrino limits as:

$$E_{\nu_\tau}^2 \frac{\mathrm{d}N_{\nu_\tau}}{\mathrm{d}E_{\nu_\tau}} < 2.8 \times 10^{-8}\ \mathrm{GeV\ cm^{-2}\ s^{-1}\ sr^{-1}} \tag{1.17}$$

in the energy range 1.6×10^{17} eV $< E_\nu < 2 \times 10^{19}$ eV for Earth skimming ν_τs over 3.5 years of livetime, and

$$E_{\nu}^2 \frac{\mathrm{d}N_{\nu_\tau}}{\mathrm{d}E_{\nu}} < 1.7 \times 10^{-7}\ \mathrm{GeV\ cm^{-2}\ s^{-1}\ sr^{-1}} \tag{1.18}$$

in the energy range 1×10^{17} eV $< E_\nu < 1 \times 10^{19}$ eV for 2 years of data .

1.5 A Next Generation Detector

UHE neutrino detection using the radio Cherenkov technique has become a mature field, with existing experiments beginning to probe the expected neutrino flux from the GZK process. There is no neutrino observation claimed to date, but limits on the neutrino diffuse flux have been improved by several orders of magnitude at EeV regime and above. Still, with its relatively easy scalability, the technique is tantalizingly close to detection. Further, it is capable of moving beyond the discovery stage and into an era of making particle- and astrophysics measurements with 10-100 UHE neutrinos per year.

Reaching such numbers in the vicinity of EeV energies is possible by a lowering of the energy threshold. An experiment embedded in its detection medium can, with adequate volume, be sensitive to a lower energy regime than experiments where the medium and instrumentation are well separated. Since the expected neutrino spectrum, like the measured cosmic ray spectrum, is steeply falling, a lower threshold is a great advantage in terms of predicted neutrino rates. The idea of using a surface array of radio receivers to search for astrophysical sources has a long history [73].

Antarctic Ross Ice-shelf ANtenna Neutrino Array (ARIANNA), first proposed in the middle of the last decade [74], aims to achieve this leap of an order of magnitude in sensitivity. Utilizing the enormous Ross Ice Shelf near the coast of Antarctica, it is designed to detect UHE neutrinos with energy greater than $10^{17.5}$ eV and hence reach the heart of the GZK predictions.

The concept emerged following recent studies [75] at the Ross Ice Shelf that confirmed earlier glaciological surveys that found high fidelity radio reflectivity of the ice-water bottom. This would allow for detection of the reflected conical Cherenkov pulses generated by 'downward' traveling neutrinos arriving from the whole southern celestial hemisphere . With low levels of anthropogenic radio noise in Antarctica, coupled with possibility of long livetime and the

scalability to large volumes attainable by covering vast expanses of the area with autonomous radio antenna stations, the scope of neutrino astronomy with the detector quickly becomes clear. Simulation studies are the basis of assessing the sensitivity of the experiment and is the main aim of this dissertation.

Thesis Outline Chapter 2 that follows describes the ARIANNA detector as a neutrino telescope exploiting the Askaryan effect. Details of the prototype station installed at the Rosse Ice Shelf are also provided. The development of the simulation package and the physics involved is given in Chapter 3 with the findings and results derived from it presented in Chapter 4. They allow for an assessment of the competitive reach of the instrument as an ultra-high energy neutrino detector. In Chapter 5, we detail the angular and energy reconstruction techniques based on simulation data, and derive the angular and energy resolution of the radiodetector. Some systematics effects are considered in Chapter 6, before a summary and a future plans are laid out in the concluding Chapter 7.

Chapter 2

The ARIANNA Detector

Antarctic **R**oss **I**ce-shelf **AN**tenna **N**eutrino **A**rray (ARIANNA) is a next generation experiment being developed to measure or provide the best constraint on the neutrino flux in the ultra-high energy(UHE) range ($10^{16} - 10^{20}$ eV). The goal is the detection of sub-nanosecond radio pulses initiated through the Askaryan effect [57][76] produced via neutrino-nucleon interaction in the ice of the Ross Ice Shelf. This chapter describes the instrument and the site properties that it exploits, namely the radio transparency of the cold ice and high fidelity reflection at the bottom ice-water boundary. The Askaryan effect, with its radiated power scaling quadratically with shower energy, as the source of neutrino signal is discussed. A detailed experimental set-up of the first prototype detector is given and design options for future array are briefly considered.

2.1 The Principle of Neutrino Detection by ARIANNA

2.1.1 Need for Large Volume Detector

The estimated flux of neutrino from the GZK effect is extremely low [20], (typically of order 1 neutrino per km^2 per week arriving over 2π sr at $\sim$EeV), and the Standard Model predicts small neutrino interaction cross section ($\sim 10^{-32}$ cm^{-2} at EeV)[77]. Therefore, neutrino detection in the UHE regime is extremely challenging. It is necessary to have a very large target volume with low loss medium for converting incoming neutrinos to RF signals. Given its radio transparency and low anthropogenic noise levels, Antarctic ice acts as the ideal target and has already played host to several high energy neutrino detectors as mentioned in §1.4.

2.1.2 ARIANNA as a Half-Teraton Scale Detector

As an UHE neutrino travels through the Antarctic ice, it interacts with nucleons in ice and creates a shower of particles which generates coherent Cherenkov radio pulses, the so-called Askaryan effect (see Sections 2.2 below and 3.4 for more details). The aim of ARIANNA neutrino telescope is to detect these characteristic signals through sets of radio antennas embedded at the surface and hosted within independent stations installed in a grid like structure. The experiment achieves a large aperture (effective volume $\times$ solid angle) by covering a vast area (900 km^2 over 0.57 km thick) combined with a larger than 2π steradian view of the sky. The exposure, defined as aperture $\times$ time, represents a figure of merit for neutrino detectors and is further enhanced by year round autonomous operations.

The first feature, that of large area, is accomplished by placing the stations 1 km apart and scaling the grid up to a 31 $\times$ 31 station array to cover the required extent. Fig 2.1 shows

the proposed scheme. In fact, one of the crucial assets of ARIANNA is its ability to easily scale up and the stations can be re-arranged to follow the science goals of UHE neutrino astronomy (see also §4.6).

The second feature, that of a large solid angle coverage, is achieved by taking advantage of a unique characteristic of ice-shelves in that radio pulses generated within the ice are reflected with high-fidelity at the ice-water bottom. The Askaryan effect produces a radio Cherenkov cone originating in the close vicinity of the neutrino-nucleon interaction vertex. Depending of the direction of the incoming neutrino, the signal can either travel through a direct or a reflected path (or a combination of both) to surface detectors, as illustrated in Fig 2.2. The reflected signals of downgoing neutrinos will generally trigger the detector while neutrinos coming from about the horizon will trigger mainly through direct rays. Hence, ARIANNA is sensitive to downward neutrinos to ones originating from just below the horizon, resulting in a large sky view. The nearly uniform angular coverage will be examined in §4.3.2.

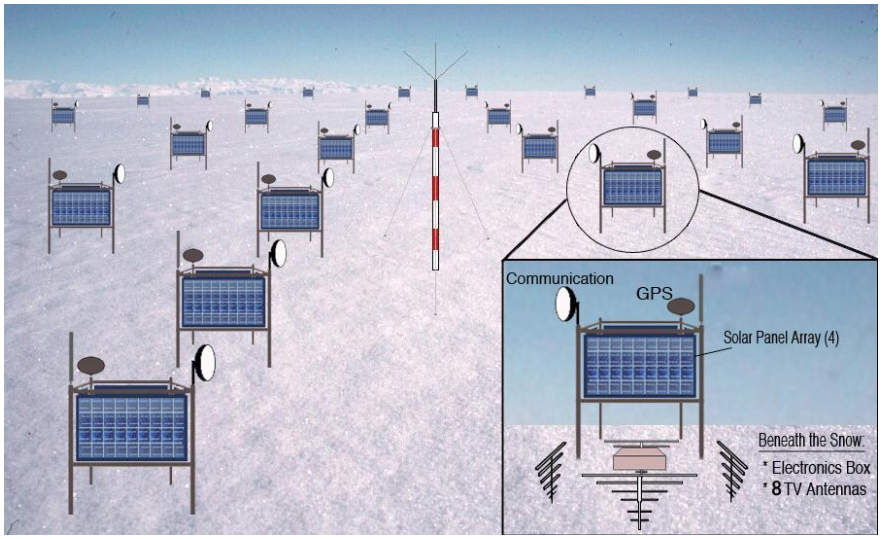

Figure 2.1: Diagram showing the scheme for an array of stations deployed in grid along Ross Ice Shelf.

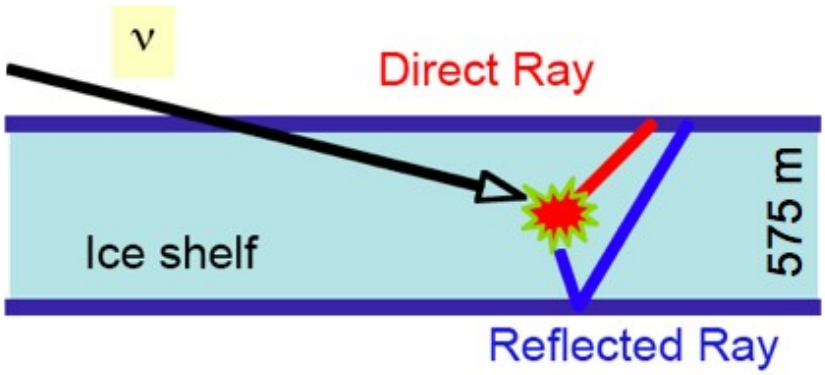

Figure 2.2: ARIANNA achieves a large aperture by detecting direct and reflected radio signals, a unique feature of current UHE neutrino experiments deployed. It can therefore view more than half of the sky.

2.2 The Askaryan Effect

The neutrino detection of ARIANNA relies on the phenomenon that is generally referred to as the Askaryan effect [76]: coherent impulsive radio Cherenkov radiation from the charge asymmetry in a charged particle shower. In other words, an Askaryan radio pulse is the collective result of Cherenkov radiations generated by individual charged particles.

As a charged particle travels (with a speed of v), it disrupts the local electromagnetic field in its medium. Electrons in the atoms of a medium will be displaced and polarized by the passing EM field of a charged particle. Photons are emitted as an insulator's electrons restore themselves to equilibrium after the disruption has passed, which is different from a conductor in which the EM disruption can be restored without emitting a photon. In normal circumstances, these photons destructively interfere with each other and no radiation comes out. When a disruption propagating through the medium with a speed faster than the local speed of light (c_n), the photons constructively interfere and intensify the observed radiation. Fig. 2.3 displays how the Cherenkov condition ($v > c_n$) is satisfied to create radiation. The left panel shows the field of a charged particle traveling with $v < c_n$. The right one is the field of a charge with a speed larger than c_n, which emits radiation with a strong peak at

an angle θ_c from the moving axis. This angle is called the Cherenkov angle, given by the expression of $\theta_c = \cos^{-1}(c_n/v)$.

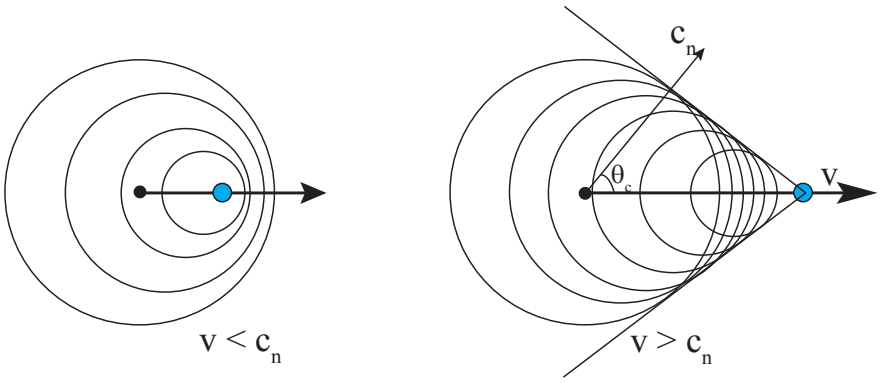

Figure 2.3: Cherenkov effect. v is the speed of a charged particle, c_n is the speed of light in a medium with a refraction index n and θ_c is the Cherenkov angle.

The Askaryan effect states that a charged particle traveling faster than the phase speed of light in dielectric media (like water, ice, salt or lunar soil) creates a shower of secondary charged particles, which contains charge anisotropy and thus emits a cone of coherent radiation in the radio part of the electromagnetic spectrum [76]. The particle shower mainly consists of electron-positron pairs and photons and each particle fulfills the Cherenkov condition, so the Cherenkov radiation from each particle has to be summed up. At the beginning the shower of charges has equal positrons and electrons, so there is no net charge and thus no Cherenkov radiation. During the development of the EM shower, the annihilation of e^+ with the e^- in the medium, combined with the available of atomic electrons which can be up-scattered into the shower by the Compton scattering, leads to a 20% excess of negative charges. During the propagation of the extra charges, there will be a small transverse deviation for each individual particle, which causes the shower to have a transverse width of order a few cm in dense media. At less than GHz frequencies the wavelength of the Cherenkov radiation of each negative charge exceeds the dimension of the compact charged-particle and photon bunch, and therefore the overall radiation of the particle shower is coherent in the form of impulses. Askaryan recognized that the phases of all emitted photons are not

random. This means the power of the coherent radio pulse is proportional to the square of the net charge in the shower. With the net charge being proportional to the primary energy of the initial particle, the radiated power of the signal scales quadratically with the shower energy.

Various experiments have confirmed the Askaryan effect under different conditions in the last decade. The first laboratory tests took place in 1999-2000 using silica sand followed by subsequent measurements in rock salt [78] [79] [80] [81]. The SLAC test beam experiment T486, performed in the summer of 2006 as part of the ANITA-I pre-flight calibration, established the behavior of the Askaryan effect in ice [82]. It confirmed the theoretical estimates for field strength and that the pulse power is proportional to the square of the shower energy. The measurements also showed the narrowing of the Cherenkov width at higher frequencies. The parametrization of the electric field and its characteristics are described in §3.4.

2.3 Site Properties

Prior studies at the South Pole had already established large attenuation lengths ($\approx$ 1km) at radio frequencies (200-800 MHz) in the cold ice [83]. In addition, initial surveys in the 70's by Neal [84] indicated the low reflectivity loss at the bottom of the Ross Ice Shelf. Subsequent measurements by ARIANNA team members at Moores' Bay in 2006, 2009 and 2010 confirmed the high fidelity of pulse reflection and radio clarity of the shelf ice, indicating that the site is an excellent candidate for radio signal detection.

The ARIANNA experiment is being deployed on the surface of the Ross Ice Shelf near the Minna Bluff mountains as indicated in Fig. 2.4 below. The first prototype station was deployed at GPS coordinates 78°44'523"S, 165°02'414"E, about 110 km south of McMurdo station. Being geographically close to the largest US base in Antarctica provides affordable logistical support.

The site provides the advantage of being isolated from man-made noise sources by the mountains and initial survey of the anthropogenic noise sources showed low levels of background noise [85], in stark contrast to other Antarctic sites, e.g. the South Pole, being considered for radio detectors.

Findings from the field works are addressed in this section, as are the detailed properties of the ice (thickness, reflectivity, radio transparency, index of refraction). These parameters are critical in correctly assessing the capabilities of the detector, which will be described in Chapter 4.

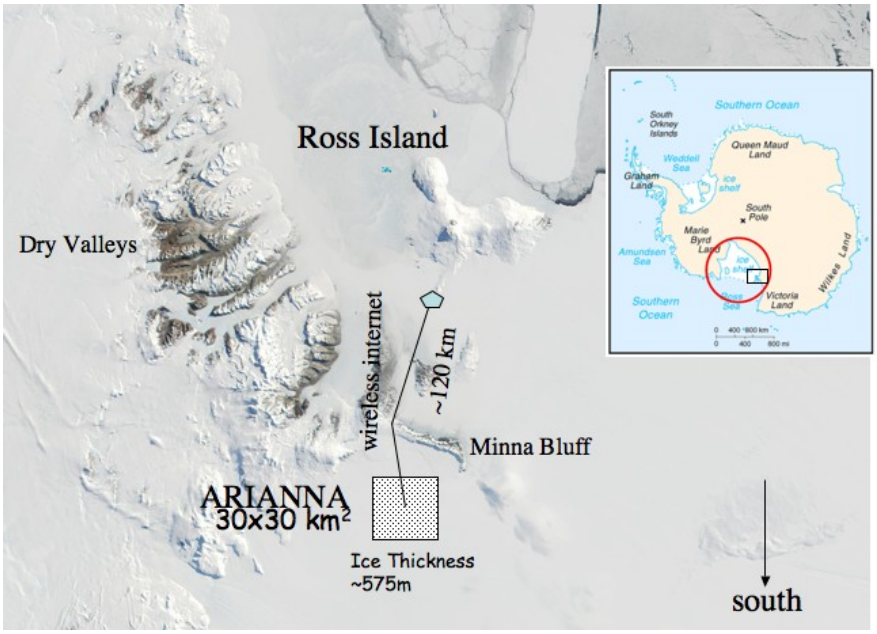

Figure 2.4: Satellite Image of Victoria Land and Ross Ice Shelf showing location of ARIANNA array of stations. The Minna Bluff mountains shield the experiment from anthropogenic noise from manned stations at the nearby Ross Island.

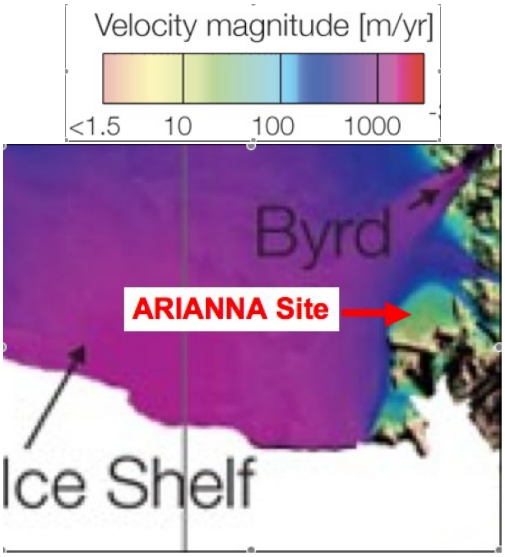

Figure 2.5: Ice velocity in the Ross Ice Shelf area from satellite measurements. Ice velocity is $\sim$50 ms^{-1} at the ARIANNA site. From Ref.[86]

2.3.1 Ross Ice Shelf

Ice-shelves are the floating extensions of ice-sheets that move seaward but are confined horizontally by the rocky coast. They form at the margins where the ice sheet becomes thin enough to float free of a bed that lies below sea level, allowing seawater to circulate beneath the ice [87].

The Ross Ice Shelf is considered part of the West Antarctic Ice Sheet (WAIS) where about half of the grounded ice flows into it. It undergoes various processes of ice gain and loss: it gains mass through atmospheric precipitation and by freezing of ice on the underside of the ice shelves. It loses mass through evaporation, by melting and runoff at its surfaces and by calving of icebergs at the front of ice shelves.

Stability of the shelf

Anticipated construction phase of approximately half a decade and the planned operation for a decade begs the question of the stability of the research environment. Various effects are at play on the dynamics of the ice-sheets and ice-shelves and several studies have examined the long-term stability of the Antarctic ice (see for example [88] and references therein).

The ice-shelf motion is restricted by contact with rises on the ocean floor and by friction with the perimeter walls of the embayments. Latest results from satellite data indicate ice velocity under 50 m yr^{-1} in the vicinity of the ARIANNA location (see Figure 3 in Ref [86]). This indicates that the whole area is relatively stable for the decade-long instrumentation of stations on the surface. In fact, the GPS receivers will allow monitoring of station movements over short to medium terms, further refining data on ice-shelf movement in that region. Moreover, the modular construction of stations at the surface means that they will be easily relocated if required.

2.3.2 Ice Field Attenuation

The electric field attenuation length, L_α, is defined as the length over which the signal amplitude diminished by a factor of $1/e$. The attenuation length for radio propagation depends on frequency and on initial depth of interaction due to the strong temperature dependence of the radio attenuation.

As part of *in situ* study of the ARIANNA site, Barwick et al. carried out assessments of the RF attenuation length at the Moores' Bay area in November 2006 [75]. The team measured the one way attenuation length of the ice of the Ross Ice Shelf between 75 and 1250 MHz, the frequencies relevant to ARIANNA; radio attenuation of ice is believed to increase rapidly above 1 GHz. The calculation assumed no loss of reflected power ($R = 1$) at the bottom of the ice-shelf, which results in the most conservative value of field attenuation of radio signals in the ice. More recent field studies [89] have been carried out with the aim to further constrain the reflectivity and attenuation lengths; this is discussed in §2.3.3 next and their results summarized in Figure 2.6. We also note that studies of ARIANNA sensitivity (see §6.2) with reflective losses and attenuation length adjusted accordingly do not find significant impact over $0.5 \lesssim R \lesssim 0.82$, the range of interest from Figure 2.6. Modeling of attenuation losses for simulation purposes is described in further details in the next chapter, see §3.5.3.

The average attenuation lengths over a range of VHF and UHF frequencies (75 to 1250 MHz) were found to range from 500 m to 300 m with an uncertainty of order the RMS of the variation, or 55 m to 15 m over this range. Since the variations are small and likely an artifact as argued by the authors, the E-field attenuation length (in m) can be summarized with a parameterization over the range 75 to 1250 MHz as

$$\langle L_\alpha \rangle = 469 - 0.205\nu + 4.87 \times 10^{-5}\nu^2 \tag{2.1}$$

where ν is in MHz.

This data is consistent with previous studies of Neal of the Ross Ice Shelf [84] and Nicholls of the Fimbul Ice Shelf [90] at lower frequencies. By assuming that the bottom has a -3 dB power reflection loss, the one-way field attenuation length of ice is about 400 m. Fig. 2.8 gives measured attenuation length data. It shows that radio frequency signals has very little loss during the propagation through the ice of Antarctica, and thus confirms the feasibility of the radio technology for detecting UHE neutrino in the Ross Ice Shelf.

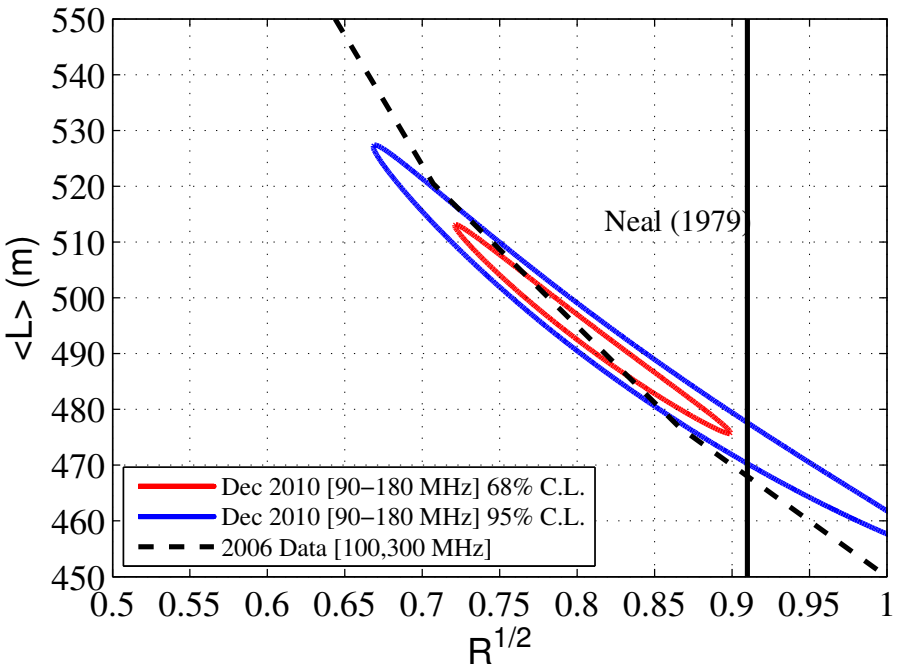

Figure 2.6: Depth-averaged electrical field attenuation lengths versus electric field reflection coefficient. Note that the x-axis is $\sqrt{R}$ while through the text, we refer to reflectivity, R, for power. This plot shows that assuming no loss of reflected power results in the most conservative value of field attenuation of radio signals in ice. From Ref.[89].

2.3.3 Ice Bottom Reflection Property

Detection of reflected radio pulses requires good specular reflection from the ice-water boundary beneath the Ross Ice Shelf. This is critical given that, to achieve large angular coverage, ARIANNA capitalizes on high-fidelity reflections. These were first observed during the

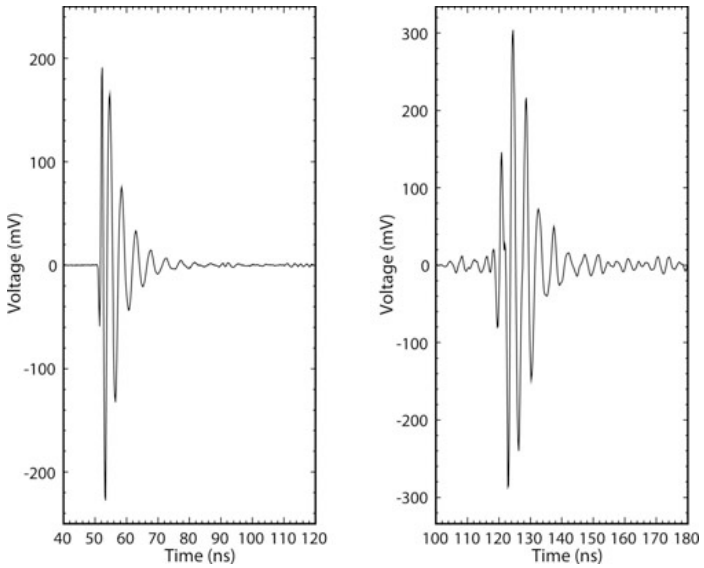

Figure 2.7: Typical waveforms of pulses reflected back from the ice-saltwater of Ross Ice Shelf (through 1155 m of ice, right) compared with the direct pulse (through 9 m of air, left) . The amplitude of the reflected signal is arbitrarily scaled. From Ref.[75].

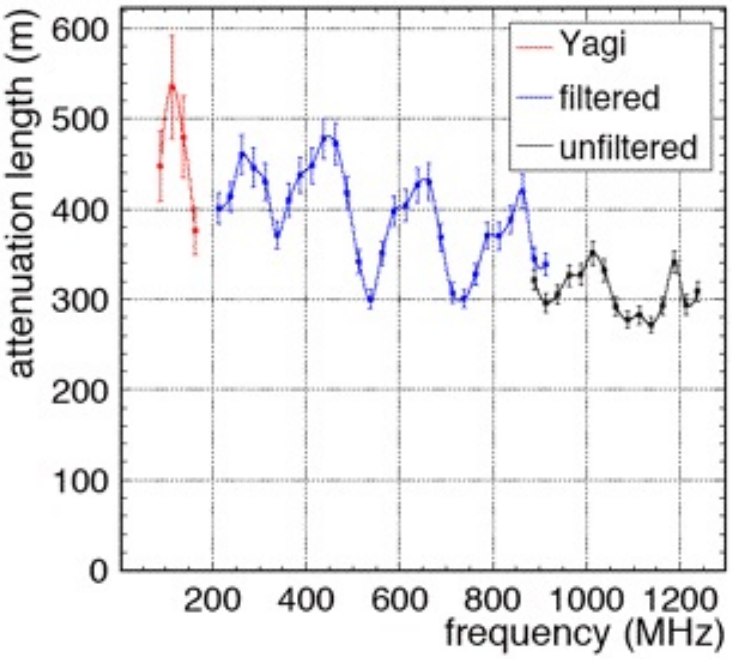

Figure 2.8: Calculated average attenuation length, $\langle L_\alpha \rangle$, as a function of frequency. The red line corresponds to data taken with the Yagi antennas, and the blue and black lines correspond to quad-ridged horn data taken with and without a low-pass 900 MHz. The modulation versus frequency is probably an artifact, as argued by the authors of Ref.[75].

1974-75 austral summer when scientists in the Scott Polar Research Institute used radio-echo techniques to investigate the physical nature of the Ross Ice Shelf in Antarctica. Based on the data collected by the radar system mounted on board of an aircraft, which had a series of flight lines about 1 km above the Ross Ice Shelf, they derived the reflection coefficient of the ice-saltwater interface. Their results showed that the reflection loss is typically less than the loss of -3 dB over a majority of the Ross Ice Shelf. This is because bottom melting generally produces a smooth ice-water interface and the rms variation in depth from a smooth surface is 0.03 m in the region of the Ross Ice Shelf that exhibits low reflection losses [84]. Their data also indicates that narrow regions of the Ross Ice Shelf exhibit losses due to flow traces (strong currents induced by tides) under the saltwater-ice interface. However, these regions are not close to the ARIANNA location.

The smoothness of the ice-water interface at the bottom of Antarctic ice-shelves has also been confirmed by acoustic measurements. In their underwater mission in 2005 beneath the Fimbul Ice Shelf, Nicholls et al [90] saw that most of the ice shelf base along a 26 km track is flat (except for small regions of flow traces) and responsible for almost specular reflection at their echosounder wavelength of 7.5mm.

The 2006 attenuation length studies at Moore's Bay referred to in the preceding subsection, confirmed that the ice-saltwater interface underneath the ice shelf acts like a smooth mirror [75]. Impulse waveforms were transmitted through the air over short distances and compared to the radio pulses that were reflected from the bottom of the Ross Ice Shelf. Fig. 2.7 shows the reflected pulse compared with the corresponding direct pulse. The excellent fidelity of the reflected pulse and the absence of significant scattered power inferred by lack of delayed power in Fig. 2.7 are compatible with a very good reflective surface.

On-site measurements in December 2009, carried out by Klein and Stezelberger, confirmed such findings as described in the "Ice Soundings" section of the ARIANNA prototype station instrumentation paper [85]. A pulser was used to transmit signals from one buried antenna

to another, bouncing them off of the ice-water interface. Data were taken with both parallel antennas orientations and perpendicular. Figure 2.10 shows an example of a reflected trace, using signal averaging; the pulse-to-pulse jitter was small and the reflected pulse is about 20 ns long. This is consistent with what is expected from a smooth ice-water interface. For comparison, Figure 2.9 shows a similar signal, taken when two antennas were placed facing each other (nose-to-nose) with a 2.7 m spacing, in air. The signal is somewhat longer for the air-to-air transmission, likely because there was less attenuation of low-frequency components. However, the two signals are quite compatible, indicating that the ice-water interface provides smooth reflection.

A recent study by Hanson and Barwick [89] examined reflected radio pulses at several horizontal baselines, which allowed them to disentangle losses due to attenuation from reflective losses. The best fit reflection loss in these studies indicate $R = 0.5$, but errors are sufficiently large so that $R = 0.83$, which corresponds to a theoretical expectation from a perfectly flat surface, is also accommodated. A discussion of the impact of reflectivity on ARIANNA's sensitivity is given in §6.2.

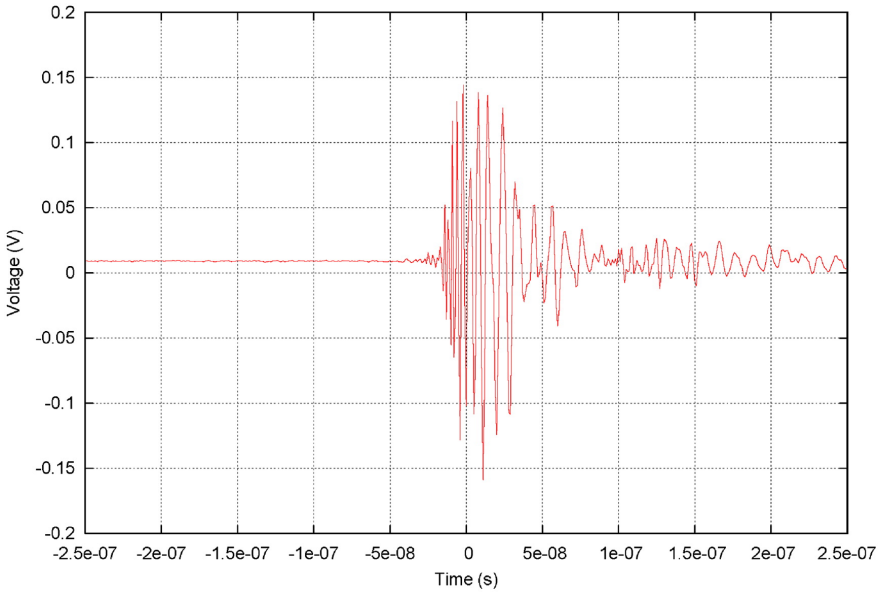

Figure 2.9: The transmitted signal from an Avtech pulser sent between two CLP5130-2 LPDA antennas sitting head-to-head, in air, separated by 2.7 m. No low-pass filter was used. From Ref.[85].

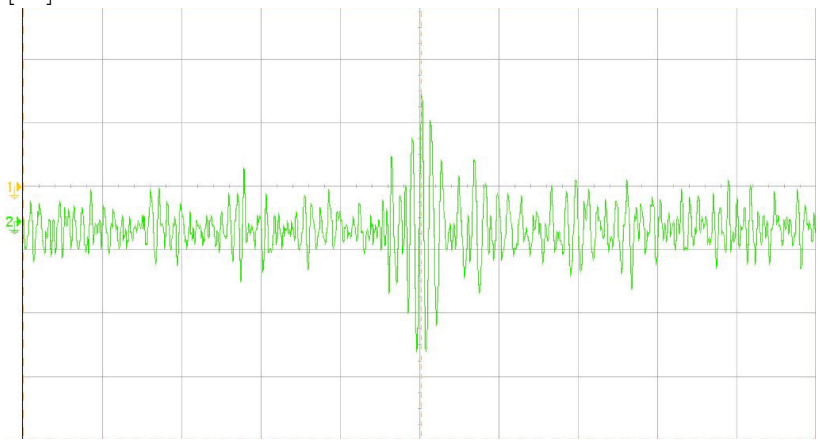

Figure 2.10: Oscilloscope trace of the signal reflected from the ice-water interface. Signal averaging (65536 averages) was used. The main reflected pulse train is about 15 ns long. From Ref.[85]

2.3.4 Ice Thickness

The thickness of the ice at the ARIANNA site can be determined by the round-trip travel time and knowledge of the index of refraction. This is described, for instance in Ref. [85], and is reproduced in the next paragraph. The shelf ice in not homogeneous: it is solid ice at depths greater than about 75-100 m, but above this it is firn; the gradual transition from packed snow (at the surface) to ice. A plot of the measured density vs. depth for the Ross Ice Shelf is given in Figure 2.11. The transition to solid ice occurs at a shallower depth than in central Antarctica but as discussed in §6.3.1, the size of the firn layer does not have a significant impact on the ARIANNA's aperture.

Depth determination During the deployment of the first prototype station in December 2009, the bounce tests at the ice-water interface, as described in the preceding subsection(§2.3.3), are used to determine the ice thickness. A return signal was observed at time t=6.745 μs after the original downgoing pulse. A $\pm$15 ns uncertainty is attributed to the round-trip travel time, to account for uncertainties in the cable lengths, geometry, and arrival times (due to the pulse width).

The relationship between the round-trip travel time and the ice thickness depends on the index of refraction in the ice, which itself depends on the density, and, to a much lesser extent, on the possible presence of impurities [91] [92]. The ice in Moore's Bay is glacial ice, and assumed free of impurities; there was no evidence of infiltrating brine layers in the radio reflections.

The calculation, reproduced here from Ref.[85], follows Ref. [91]. The index of refraction, n, is the square root of the real part of the dielectric constant ϵ. The index of refraction of pure, solid ice has a very slight temperature dependence, $\epsilon = (3.18 \pm 0.01) + (8 \times 10^{-4} T)$, where T is in centigrade. The ice temperature varies with depth, from near 0° C at the ice-water

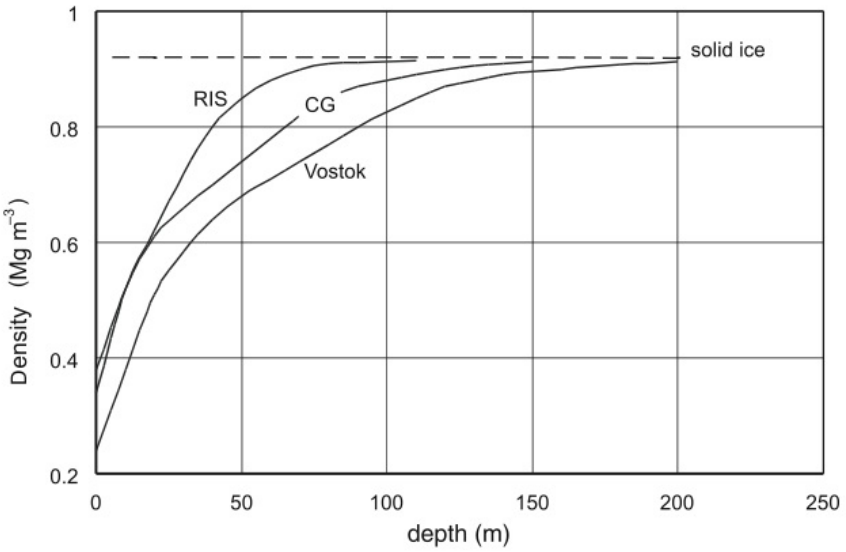

Figure 2.11: Firn density versus depth at three polar locations: the Ross Ice Shelf (RIS) and Vostok Station in Antarctica and Central Greenland(CG). The density profile indicates that the firn extends to about 75-100m m deep in RIS. From Ref.[91].

interface, to about -20° C just below the firn surface [93], implying a mean temperature (averaged over the radio path) of -10±5° C, and giving an average index of refraction of n=1.78 for solid ice. The upper 75 m of ice is firn, which has a lower density, where the radio signal will travel faster; $(n-1)$ scales linearly with the density. Dowdeswell and Evans [91] treat this region by including a correction in the calculated ice thickness, z_{max}:

$$z_{max} = \frac{1}{2}\left(\frac{ct}{n} + z_f\right) \tag{2.2}$$

where c is the speed of light. For the Ross Ice Shelf, the correction z_f is +7±2 m where the error is due to possible variation in density profile. From this, a thickness of 572 m is determined, with uncertainties due to the travel time (5 m), temperature (1 m), index of refraction (1 m), and firn correction (2 m), and treating all errors as statistically independent, gives a total uncertainty of ±6 m. A similar strategy has been employed for the 2006 and 2010 field studies. Table 2.1 summarizes these results that are seen to be consistent.

Year	Delay (ns)	Depth (m)
2006	6783 ± 10	577.5 ± 10
2009	6745 ± 15	572 ± 6
2010	6772 ± 15	576 ± 10

Table 2.1: Various depths measurements of the ice-shelf at the ARIANNA site. 2009[85] and 2010[89] measurements were performed at the same geographical location, whereas the 2006[75] one was carried out at a location about 1 km away.

2.3.5 Index of Refraction

The change in density of the firn is due to the inclusion of air pockets (or bubbles) which are small compared to the wavelength of interest, and sufficiently dense to approximate a continuous medium. Under these conditions, the index of refraction, n, depends linearly on snow density, and remain independent of frequency[94]. Given that the density changes with depth, n is depth-dependent and needs to be properly accounted for in simulation studies and other calculations. In their RF attenuation assessment, Barella, Barwick and Saltzberg [75] followed Dowdeswell and Evans[91] modeling of the ice as two regions: a slab of bulk ice with constant n surmounted by a firn layer with varying $n(z)$. The bulk is taken as $n = 1.78$ as described in the preceding subsection. As for the firn layer, Schytt models [95] the index of refraction versus density, ρ as

$$n(z) = 1.0 + 0.86\rho(z) \tag{2.3}$$

where $\rho(z)$ is the specific gravity, at depth z in meters, measured using core samples on the Ross Ice Shelf (Williams Field):

$$\rho(z) = 1.0 - 0.638e^{(-z/34.7)} \tag{2.4}$$

In this model, the index of refraction in the firn matches the deep ice at a depth of 67 m, consistent with the results in Figure 2.11.

2.4 The Prototype Detector

To test the ARIANNA concept, and also to learn more about the site and the technology, a prototype detector was deployed at the ARIANNA site from 11-21 December 2009, where it collected data for approximately one year. The work, as reported in Ref. [85], is reproduced in detail here because the description contains some of the essential features of future stations. The main goals of that expedition were to study:

- radio signal attenuation in the ice and reflection at the ice-seawater interface, as already reported in the preceding section (§2.3),
- radio backgrounds, especially anthropogenic noise, over time periods of a fraction of a year,
- wind speed, to help investigate the reliability of using a wind generator to power the station,
- air and subsurface temperature profiles over the year, and
- performance of the prototype hardware in the polar environment.

A subsequent expedition was carried out in December 2010 when an assessment of the station after one year of operation was made. The modifications implemented during that second trip will be discussed in the next section (§2.5).

2.4.1 Detector overview

Figure 2.12 shows a block diagram of the prototype detector. Four log-periodic dipole antennas are buried in the snow, pointing down. Each antenna feeds a low-noise amplifier, which itself feeds a switched capacitor array (SCA) analog-to-digital converter (ADC) and

programmable trigger circuit. The SCAs are digitized and read out whenever the trigger fires. The standard trigger requires signals in at least two of the four antennas. Simulation studies described later in this dissertation investigates other trigger conditions for the concept ARIANNA station.

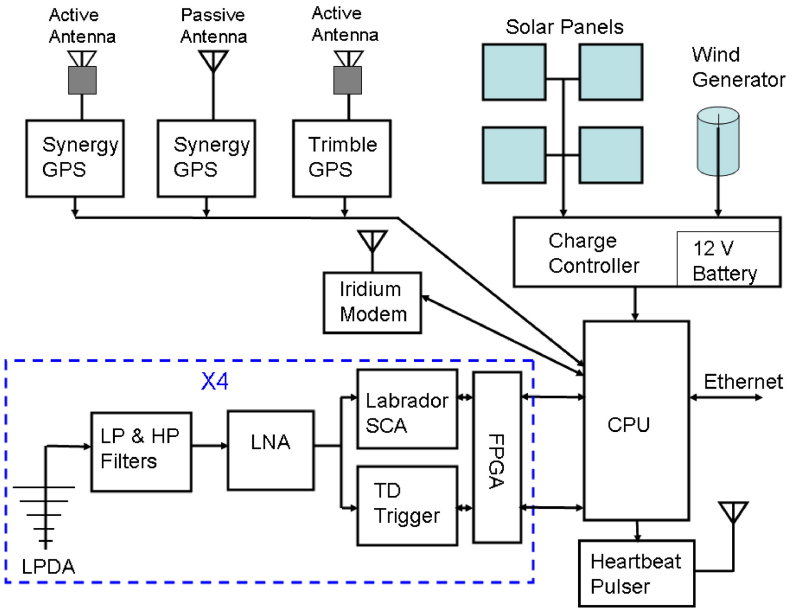

Figure 2.12: Block diagram of the ARIANNA prototype electronics deployed in December 2009. Each log-periodic dipole antenna (LPDA) feeds low-pass (LP) and high-pass (HP) filters (in series), a low-noise amplifier (LNA) which go to a tunnel diode (TD) trigger and the Labrador switched capacitor array (SCA) digitizer. The trigger and SCA are controlled by a field-programmable gate array (FPGA). The 3 GPS receivers were for comparison purposes. The "heartbeat" pulser transmits test pulses. From Ref. [85].

The system is controlled by a PC104plus linux-based computer with a flash disk for storage. GPS receivers are used for accurate time-keeping. The station has GPS receivers; in the prototype station, three were installed for comparison purposes. The station communicates via an Iridium satellite modem. During the summer, it also had a wired Ethernet connection, which was connected to a wireless Bridge station. This station communicated with a repeater, which was installed on Mt. Discovery, about 40 km away, which in turn connected to McMurdo Station. When fully operational, the prototype station consumed about 25 W. Power is provided by four 30-Watt solar panels during the day, and in the austral winter, a Forgen 1000LT wind generator provided some power. The power controller includes a gel

battery to buffer the generators through periods of darkness (during the spring/fall) and/or low winds. The computer can turn off various pieces of the station (including data collection) to reduce the power consumption.

Most of the electronics are in a steel box, which is buried with its top flush with the snow level. The power controller and battery are in a separate box, which was buried about a foot away. The antennas, four solar panels, a wind generator and an anemometer are mounted on a square tower structure shown in Figure 2.13. The tower is constructed of aluminum pipe held together with cast aluminum fittings, supported (on the ground) by plywood 'feet'.

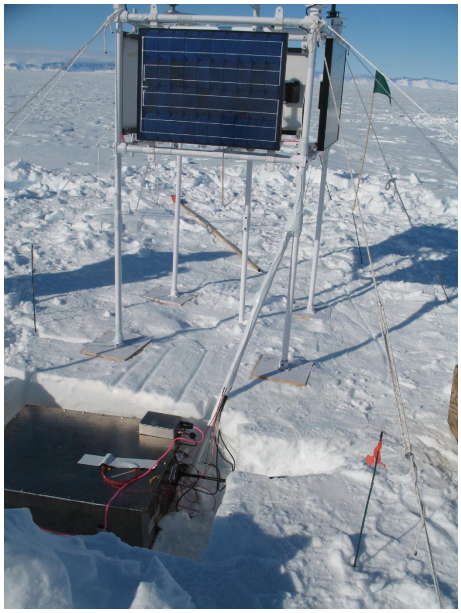

Figure 2.13: A photo of the ARIANNA station during installation, showing the tower structure and solar panels. The main electronics box is visible in the foreground, before being covered in snow. The small box with the pink cable is an Ethernet converter module. The plywood supports were later buried in snow. For scale, the four tower support legs form a square with sides about 96 cm long. Photograph by S.Klein and T.Stezelberger from Ref.[85].

2.4.2 Antennas

The ARIANNA prototype uses four Creative Design Corp. CLP5130-2 [96], 17-element log-periodic dipole antennas, much like VHF/UHF TV antennas. Ideally, the antennas would

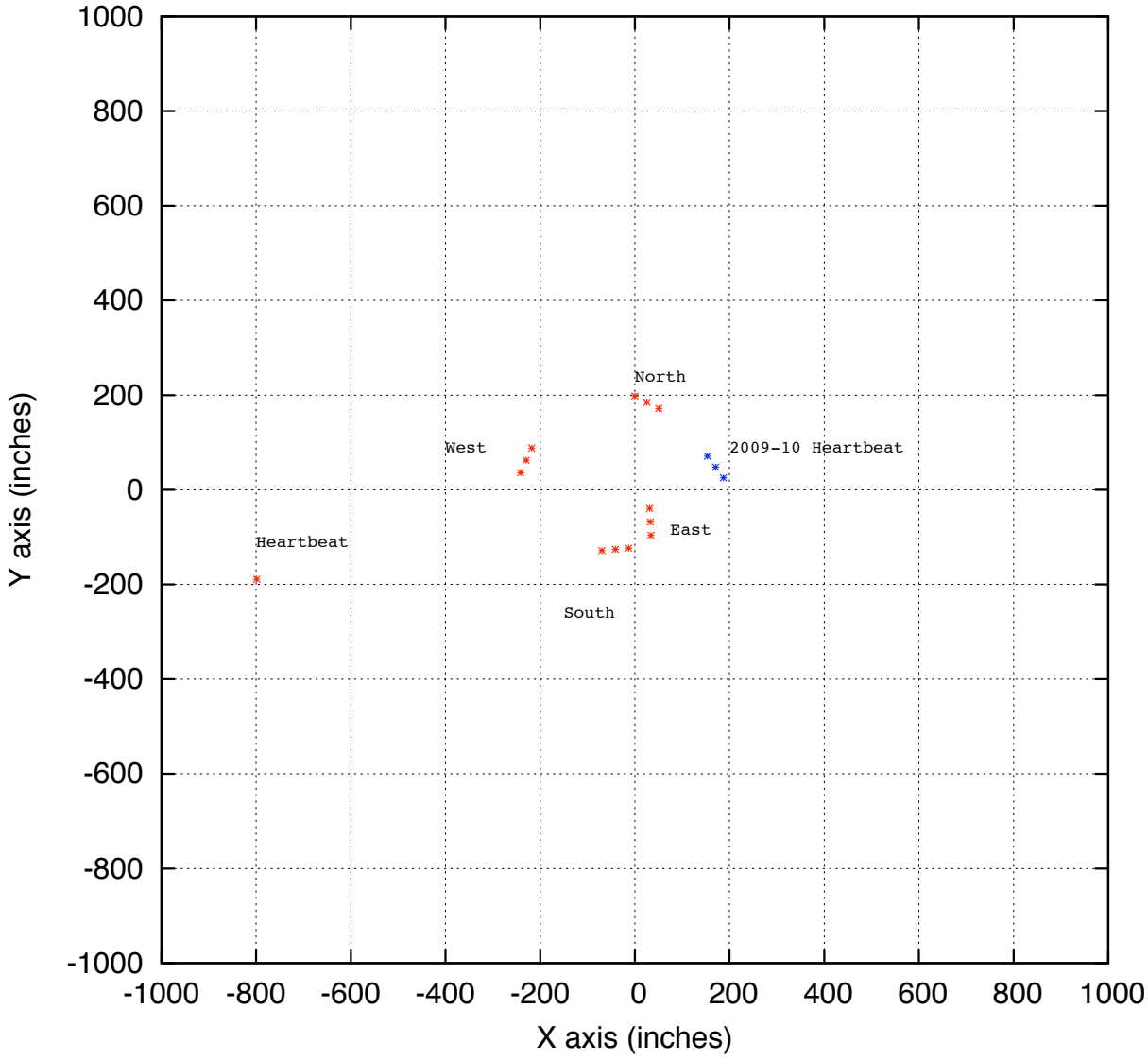

Figure 2.14: Site map showing relative locations of antennas in the prototype station

be oriented pointing down, forming a square, so that two antennas are sensitive to each polarization. Due to the need to avoid the 'deadman' anchors for the guy wires (that serve to stabilize the tower), the antenna pairs (North and South, East, and West) were deployed parallel to each other, but not in a square (see Figure 2.14); this departure from the ideal is only relevant in considering relative arrival times for perpendicular antennas (i.e. East and North). The antennas are connected to the prototype box by 6 m of LMR-600 cable.

The antennas are designed for frequencies (in air) of 105-1300 MHz. They are specified to have an 7-8 dBi forward gain in free space, and half power angles of 60-70° in the E plane, and 110-130° in the H plane (see Fig.3.9); this provides a good 'field of view' for neutrino hunting, as will discussed in §4.1 later. They have 50Ω impedance and a quoted voltage standing wave ratio (VSWR) of 2:1 or better across the frequency range of interest. The VSWR is an efficiency measure of the transmission between antennas and their receivers, with an ideal transmission line having a VSWR of 1:1.

The antennas, which have a 1.4 m boom length, were buried by digging pits about 1.8 m deep, 1.8 m long, and 30 cm wide. The antennas were buried pointing down, with their topmost element between 15 and 25 cm below the surface.

Snow has an index of refraction different from air, so the antenna environment may potentially alter both the antenna frequency response and impedance of the antenna spine (thereby reducing the impedance matching with the preamplifier). This was studied by comparing the VSWR in four scenarios: with the antenna in air (about one and one half meters above the snow surface), lying flat on the snow, buried in an air-filled pit, and buried in snow. The antennas burials were shallow enough that there may be effects from the snow-air interface, as mentioned before.

The VSWR was measured with an Agilent 'FieldFox' N9912A network analyzer. Figure 2.15 shows the VSWR for one antenna at the different stages of deployment. It was observed

that there are clear changes in the VSWR, with the positions of various small resonances changing with the conditions. However, in the region from 200 to 1200 MHz, the VSWR is always less than 2.5. At higher frequencies, the VSWR rises, except for the study with the buried antenna; it may be that the increased dielectric constant shifted this increase to higher frequencies.

At low frequencies, the VSWR for the first three conditions increases dramatically below 100 MHz; for the buried antenna, the increase is at a lower frequency, 80 MHz. This could be explained by the fact that for a given frequency, the wavelength in ice is reduced by a factor $1/n$, so one might expect the response of a fixed-size antenna to be shifted to somewhat lower frequencies. Also, the snow moderates the increase in VSWR seen at low frequencies. The antennas in the air filled holes exhibits significant variation with frequencies; this may be due to some sort of a resonant effect from the width of the hole. Since the response of the antenna is noticeably altered only below $\sim$100MHz, the calibrations and simulations of the antenna response based on vacuum/air media remain valid for the case when the antenna is buried at the site. Nevertheless, the amplifiers and high-pass filters must capably capture signal from 80-100 MHz. One significant consequence of the altered response at low frequencies occurs during the direct and bounce tests off the bottom surface (see §2.3.3) since these tests are normalized to short distance transmission through the air. The antenna simulation is discussed in §3.6.

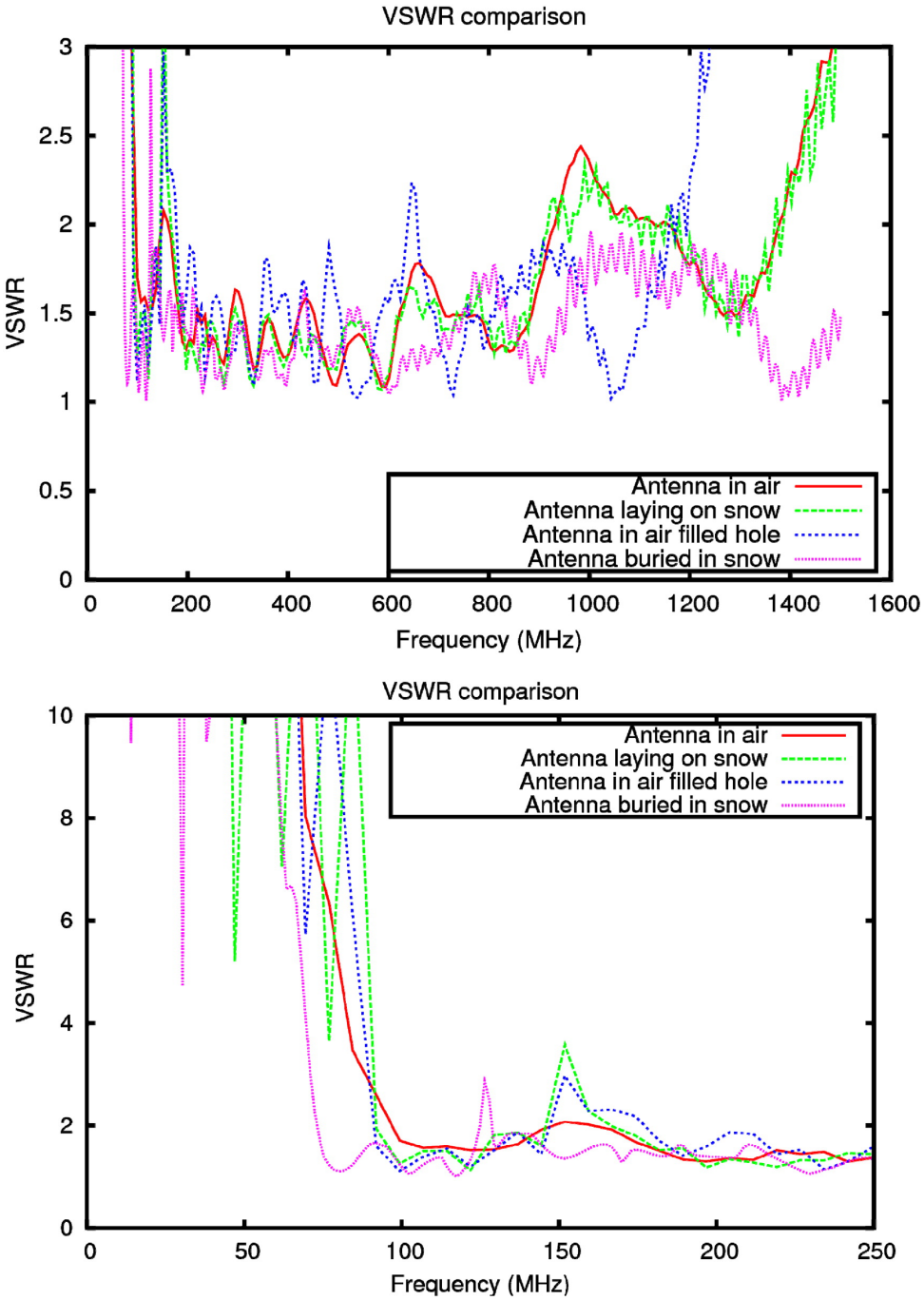

Figure 2.15: Voltage standing wave ratios (VSWR) for one of the log periodic dipole antennas under different conditions, (top) from 50 to 1500 MHz and (bottom) up to 250 MHz. Although the visible peaks and valleys move around depending on the antenna's environment, the VSWR remains below 2.5 in the range 200-1200 MHz, and is generally below 2, implying low transmission losses. It is likely that some of the larger peaks seen in the air filled holes are due to resonances. The VSWR increases dramatically below 100 MHz for the first three cases, and above 80 MHz for the antenna buried in snow. From Ref.[85].

2.4.3 System Electronics

Low-noise amplifiers

The low-noise amplifiers (LNAs), one for each antenna, amplify the received antennas signals before they are fed into the trigger and the digitizer. In the prototype, an 800 MHz low-pass filter and a 50 MHz high-pass filter at the input of the LNA block out-of-band frequencies. This is to remove local generated signals, for example from the 802.11 WiFi link and the Iridium modem and external signals like short wave radio stations. In addition the 50 MHz high pass reduces low frequency reflections, which could form standing waves in the antenna cable.

Each LNA has 4 stages, each consisting of an Avago MGA-68563 GaAs MMIC amplifier. They are broadband, with a gain of $\sim 68 \pm 2$ dB from 50 MHz to 1 GHz, and a quoted noise figure of 1.1 dB. The chips are run off of +5 V and the power consumption is 250 mW/channel. To reduce power by 30% in future designs, the amplifiers will be powered by a 3.3V source.

To prevent coupling and feedback, each amplifier is individually shielded. In addition, the 4 LNAs are mounted in a shielded box with filtered power feed through to prevent possible coupling from other system components like the CPU. The next generation of data acquisition will likely combine amplifiers, filters, limiters on the same electronics board as the digitizer.

Data acquisition and trigger circuitry

The data acquisition system in the prototype station is a modified version of the system used on the ANITA balloon flight [49]. Data are recorded with a LABRADOR (Large Analog

Bandwidth Recoder And Digitizer with Ordered Readout) [97] ASIC, which is a switched capacitor array (SCA) waveform sampler. Each channel of the trigger uses a tunnel-diode detector and field-programmable gate array based discriminator [98].

The LABRADOR SCA is a single chip with 8 channels: four were used for each antenna and a 5th channel is connected to a 40 MHz clock (this is used to calibrate the sampling rate). The chip has and an analog bandwidth of approximately 1 GHz, and, in ARIANNA, samples at 2.5 Giga-samples/second (GSPS).

The trigger circuit divides the input signal into two frequency bands: 130-460 MHz and 650-990 MHz. The low-band frequencies are defined by a Mini-Circuits LFCN-320 low-pass filter and a discrete LC circuit, while the high-band is defined by a Mini-Circuits HFCN-650 high-pass filter and a LFCN-800 low-pass filter. The filters have a fairly gradual roll-off; the low-band had a -3 dB roll off of 460 MHz, so the intermediate 'gap' was not so important. The two bands were used to allow for improved background rejection of low or high frequency noise. For instance, many man-made sources of RFI are narrowband and would not cause a trigger in a scheme that requires a coincidence of high and low bands. Fortunately, such backgrounds are not observed in the ARIANNA data. Since the RFI noise at the experiment site does not contain powerful narrowband emission, future data acquisition systems will not require a frequency band trigger.

Each band feeds a tunnel diode based trigger, which acts as a square-law detector. After amplification the tunnel diode feeds an FPGA-based discriminator with a programmable threshold [99]. The circuit threshold is electrically adjustable. Each of the 8 trigger bits (two frequency bands for four channels), are connected to the FPGA, which forms a logical trigger. For most of the prototype running, the trigger was one that ORed the outputs of the two frequency bands from a single antenna, and required at least two of the antennas to trigger.

The prototype station detected significant noise at 300 and 600 MHz, due to the subharmonics of the 2.4 GHz wireless carrier used to communicate with McMurdo station. So, in 2009-2010 seasons, the thresholds for the lower frequency tunnel diodes were set quite high; most of the triggers were formed using the higher frequency bands. In 2010-11, the transmitter power components (particularly the charge controller) were installed in a metal enclosure that prevented RFI from escaping.

When the system triggers, the FPGA initiates a LABRADOR digitization cycle and reads out the chip. Data are stored uncompressed, and can be transmitted North over the wireless link to McMurdo or Iridium modem. When the wireless is operational during the summer months, it is the primary data path.

Control, communication, and housekeeping

The entire system is controlled by a PC104plus based computer[1]. The interface to the data acquisition and trigger circuitry is done via USB2.0. In addition to the USB interface the CPU uses several serial ports to talk to peripherals and a Analog/Digital I/O card.

The serial ports are assigned to a serial console for debugging work, to an Iridium data modem, and to the GPS receivers. The Analog/Digital I/O card monitors the battery and power supply voltages, measure current draw, and monitors 3 temperature sensors and an anemometer that measures the wind speed. The digital outputs control solid-state power switches, which can shut down parts of the station to reduce power consumption. The switches control the RF amplifier, SCA and readout, GPS units, Iridium modem, Trimble GPS, anemometer, heartbeat pulser, and the Ethernet media converters.

Until early February, the system communicated primarily via a wired Ethernet connection to a wireless relay station (erected by the McMurdo Station IT Communications Department)

[1]The computer is a Parvus-CPU-1421.

about 15 m away; the electronics for this relay were removed in early February, before the austral winter began. After the wireless link was removed, the station communicated via an Iridium satellite modem. It was configured to communicate North once every 15 minutes during the summer and every 3 hours during the winter, giving housekeeping data and a few sample waveforms. During this period, most of the data were stored on the flash drive and was available for retrieval in the following austral summer.

Power system

Power is a problem for any Antarctic experiment, especially one that will work through the sunless winter. When fully operational, the deployed ARIANNA prototype draws about 25 W; much of this goes to the computer ($\sim$7 W), the data acquisition and trigger circuitry ($\sim$5.5 W) and the Ethernet media converters (8 W). Ongoing tests and designs with new electronics and system configurations are being carried to significantly reduce power consumption.

The prototype system has two power sources: four 30-Watt solar panels and a Forgen 1000LT wind driven generator. The power generated is buffered by a 100 Ah gel sealed lead-acid battery to bridge windless periods during the Antarctic night. The battery is about 30% efficient at Antarctic temperatures, The average battery temperature is around -28° C and at the depth of the battery enclosure, the temperatures varied from $-5°$ C in the summer to $-38°$ C in the middle of the winter.

The four solar panels provide ample energy to power the system during the summer, and even during 'shoulder periods' when the sun sets for part of the day. This was the primary data collection period for the prototype.

The Forgen wind generator produces about 10 W in a 15 ms^{-1} ($\sim$30 knots) wind. This did not provide enough power to provide operation during the winter. In 2010-22, a much more powerful wind generator (Aerogen 6) was installed at a height of 12 feet above the snow

surface. A major goal is to gather environmental data throughout winter months.

Calibrations and the "Heartbeat" system

To verify system performance and overall functionality during the winter, the prototype includes a "Heartbeat" pulser, an Avtech: AVP-AV-1S-P-UCIA, connected through about 10 m of cable to another CLP5130-2 LPDA antennas, also buried pointing downward, at about a 45 degree angle to the other antennas. It was relocated during the 2009-10 season, as indicated in Fig.2.14. The pulser[1] produces a single pulse with a width of about 1.5 ns FWHM and amplitude 6 V (into 50 Ω). It is programmed to pulse at the beginning of each run, and provides a quick "liveness" test and also a continuing calibration signal for timing offsets and trigger efficiency studies.

[1]Due to high cost, it is expected that this unit will be replaced by a dedicated pulse circuit in future station designs.

2.5 Prototype Performance and Future Instrumentation

In this section, we briefly present the findings from running the prototype station in 2009-2010 and outline a few of the planned improvements. More details about the next generation station appears in the "Future Outlook" of the Conclusion chapter (§7.2). A more comprehensive hardware description and discussion of the next generation station will be given in future publications on ARIANNA, eg. Ref. [100].

2.5.1 Initial Assessment

The prototype station, operational more than one year after its initial deployment, provides a wealth of information on technical issues associated with the ARIANNA concept. The station computer controlled a set of relays to turn on the various systems in the station. When fully operational, the station consumes 25W of power, but near sunset, it was running on half that. The station tower, solar panels, and Forgen wind generator survived the 2010 winter upright, and became operational when the sun re-appeared in the austral spring.

The key findings from one year of the prototype operation are summarized here.

1. The ambient RF noise conditions are excellent. In over one month of data collected between Jan. 5, 2010 and Feb. 16, 2010 there are no events that were confused with neutrino signal (Figure 2.16). After minor cleaning, the triggered events are distributed randomly in time and completely consistent with thermal noise in the ice. The average rates for the trigger condition of 2 of 3 antennas with amplitudes greater than a factor 5 above the rms noise fluctuations were measured to be 1 per 100 seconds.

2. In Figure 2.16, the planarity variable P sums the time differences for the four baselines

between neighboring antennas (the diagonal baselines were not used in this analysis). The nearly plane waves expected from neutrino signals would sum to approximately zero in this variable as shown by the solid blue histogram. The P values for thermal noise induced triggers are more diffusely distributed. The event cleaning removes a small sample of events with periodic time structure associated with Iridium communication and writing events to flash drive memory. Selection criteria based on straightforward timing causality and amplitude minimums remove all but 2 events and none in the signal region. The analysis of the triggered events indicate that the ARIANNA site has low anthropogenic sources of RF noise since it is shielded from narrow band transmitters at McMurdo by the high ridge known of Minna Bluff.

This observation partially justifies why we concentrate on the sensitivity to signal in the simulation programs. There is very little physics-related background to simulate. For now, potential background errors are ignored.

3. A heartbeat and calibration transmitter demonstrated timing resolutions of 0.1 ns per receiver channel and monitored slow drifts of absolute time delays. In some studies, we use this value of 100 ps as the timing resolution per channel as is seen in §5.1.

4. The average wind speed was typically 2.5-5 ms^{-1}(5-10 knots) between January and March, with only sporadic periods of winds over 10 ms^{-1}(20 knots). A new wind generator (Aerogen 6) was installed in December 2010 that should provide sufficient power during the winter if winds remain comparable or larger to the values measured during the summer months. This will pave the way for longer livetimes in ARIANNA.

2.5.2 Planned Improvements

As mentioned in the preceding section (§2.4.3), ANITA-based electronics was installed in the prototype station. While adequate for many of the preliminary studies performed by

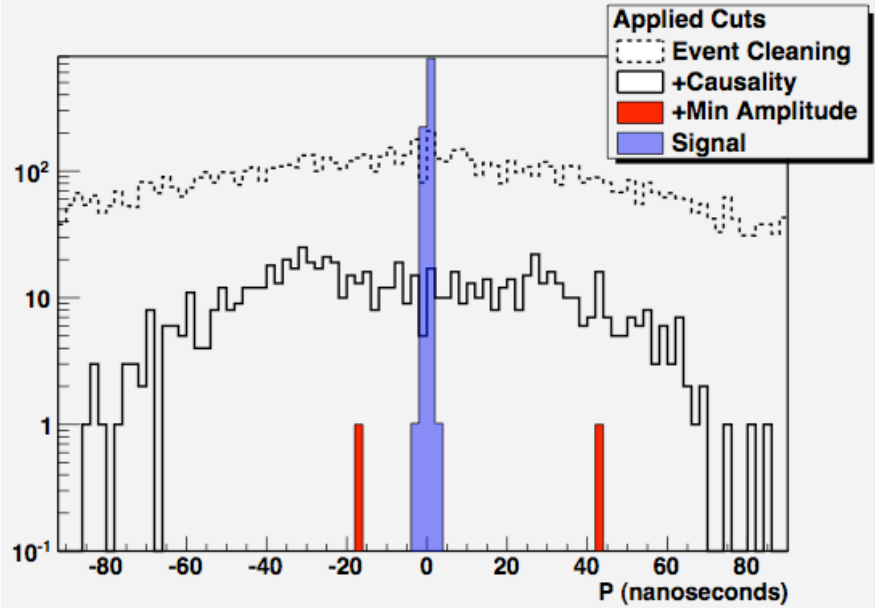

Figure 2.16: Data collected from ARIANNA prototype station between Jan-Feb 2010. Planarity for simulated signal (blue filled histogram) and data events as a function of selection criteria. Data cleaning includes minimum application selections. At the final cut level (red filled), no events remain [100].

the prototype station, it is clear that the ANITA-based electronics is not well suited to the demands of ARIANNA.

In late summer 2010, UC Irvine's Professor Stuart Kleinfelder and group members in the Engineering department began to design a single channel prototype of a data acquisition system that incorporated a custom 2 GHz waveform digitization integrated circuit known as the advanced ATWD (see Figure 2.17 and Ref. [101]). The advanced ATWD combines trigger decisions in the time domain with high speed digitization that requires relatively low power and provides good dynamic range and linearity.

Evaluation tests of the full waveform capture and data archiving procedures were carried out. The single-channel waveform capture board was installed within an RF-tight metal box, tested at -28°C in a refrigerator, and then transported for *in-situ* field performance evaluation to the ARIANNA site in December 2010 by S. Barwick and J. Hanson.

To illustrate the performance of these new precision electronics, the acquired waveforms were compared to those produced by a Tektronics digital oscilloscope running at 2 Gigasamples/second (Figure 2.18). In these studies, a short radio pulse from a Pockel Cell Driver was transmitted from an LPDA antenna buried in the surface snow, pointed vertically downward. A second LPDA separated horizontally from the first by about 20m, recorded the reflected radio pulse from the water-ice surface at the bottom of the Ross Ice Shelf. As shown, the fidelity and functionality of the prototype DAQ electronics is equivalent to the commercial digital oscilloscope, which is far more costly and power consumptive.

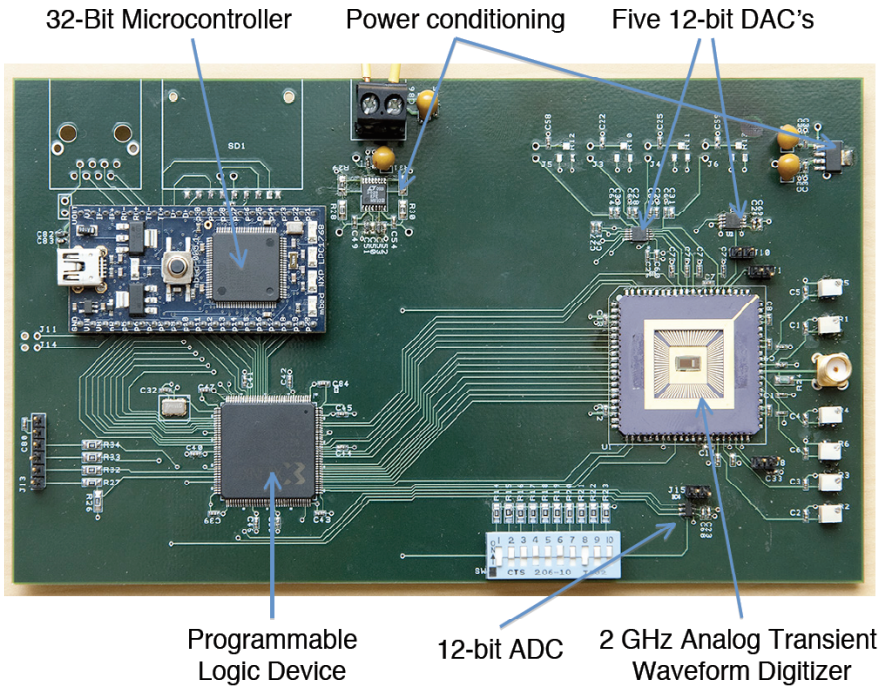

Figure 2.17: Prototype of high speed, low power waveform capture and control electronics, including the custom 2 GHz waveform digitizer integrated circuit for ARIANNA[101]. Photo credit: S. Kleinfelder.

The plan is for this existing single-channel data acquisition system to evolve into an 8-channel data acquisition electronics, and communication and calibration subsystems. This will be achieved by modularizing the existing single-channel system into a card format, such that each card (based on the existing, proven design) supports one channel. Only few modifications to the existing proven design is anticipated. A modularized system also limits

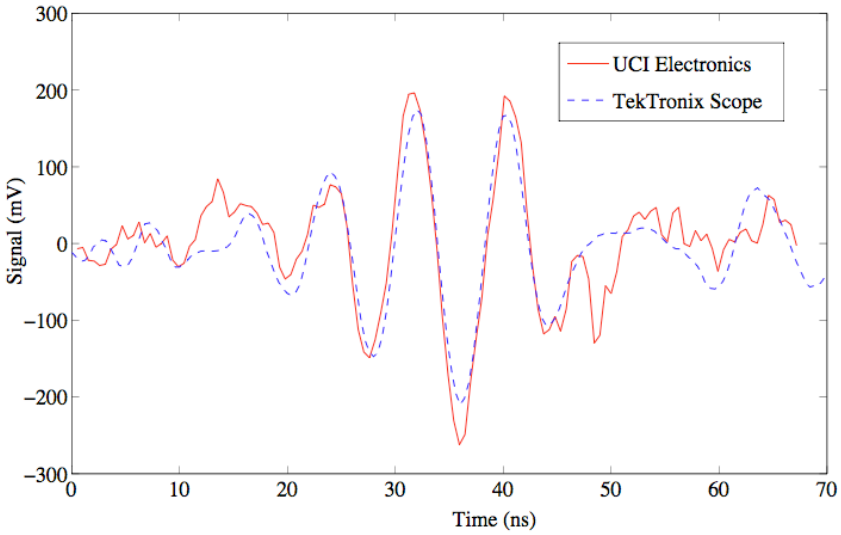

Figure 2.18: Comparison of waveform data collected by prototype data acquisition electronics to the data collected by Tektronix oscilloscope.

risk since channel cards can be swapped easily in the laboratory or in the field. A backplane supporting 8 cards will be desinged that performs the limited function of consolidating control and data from the single-channel modules. This has limited risk since its primary function is mechanical support and simple power and data distribution. Data will be transmitted to a commercial single-board computer running a commercial real-time Linux system.

2.5.3 Hexagonal Radio Array

Due to theoretical imprecision in the expected GZK flux, as discussed in the §1.2.1, we must allow for substantial flexibility in detector sensitivity. Initially, ARIANNA stations can be readily deployed on a sparse grid with 1 km spacing to maximize collecting power, and since they are located on the surface, can be redeployed at 300 m horizontal spacing to maximize angular and energy resolution once the flux is known. The surface area of the array can grow to follow science.

As a first phase, NSF will be funding and providing logistical support to deploy a Hexagonal

Radio Array (HRA) of ARIANNA stations at Moores Bay over the next four years (2010-2014). This will consist of six at the edges of a hexagon and one in the center at a nominal separation of 1 km from one another (see Figure 4.21). Preliminary simulation studies with the HRA will also be addressed in §4.6.

Experience gained in operating the HRA with precision electronics would frame the performance requirements needed to expand the array in the future to the size required to address the complete scope of scientific goals.

Summary

We have described the site properties and technique that ARIANNA exploits for neutrino hunting: radio transparency of the Ross Ice Shelf, excellent reflectivity at the ice-water bottom and access to a large volume of target medium. There was an explanation of the Askaryan effect: neutrino induced showers that result in radio waves. These pulses can travel directly or through reflection to the radio detectors embedded at the surface.

The ARIANNA prototype station, deployed in 2009-10 season has been described, together with the improvements and tests performed during the 2010-11 season. The electronics and antenna system has been described, as well as plans for future improvements.

From the *in situ* studies discussed in this chapter, there were several key results that feeds into the simulation software. The ice thickness is determined to be about 575 m at the prototype site, and measurements have helped refine the model for the firn depth and its graded index of refraction. Attenuation length parametrization has been briefly presented and will be discussed further in §3.5.3 of the next chapter.

Chapter 3

Numerical Simulations

Monte Carlo simulations are used to study the sensitivity, characteristics and optimization of the ARIANNA detector. In this chapter, we describe the features and ingredients of our simulation and Chapter 4 discusses the critical Physics results derived from the simulation studies. The first section in this Chapter (§3.1) summarizes the main ingredients of the code while the subsequent ones describe the salient features in more details.

The program, coined *shelfmc*, was initially developed by F.Wu, a previous member of the UCI group. It is based on a mature simulation code, *icemc*, that was created for the ANITA-I balloon-borne neutrino detector by UCLA collaborators. Therefore, some of the ideas presented in this dissertation parallel descriptions given in Ref.[19]. The original version of the code,*v0.0*, as inherited by the author, has been significantly upgraded through additions and changes as documented in this work; and has evolved to *shelfmc v1.0*.

While the focus of the simulation work here has been on a single station, we have also developed the code to study the Hexagonal Radio Array(HRA) set-up. The program also provide analysis tools to reconstruct the neutrino parameters such as direction and energy from measured quantities, as will be discussed in Chapter 5.

We note that throughout this and other chapters, most of the variables introduced in *italic* in the text are cataloged in Appendix **??** if featured in the simulation code. Those appearing in the equations here are also listed there if they are parameters of interest in the simulation. This should provide an easy cross-reference for future users of the software.

3.1 Overall Strategy

The *shelfmc* code models the detection of isotropic neutrinos of ultra high energies that interact in the ice and generate signals that propagate to ARIANNA the station. The flowchart in fig 3.1 gives a general overview of the simulation sequence implemented in the software and the following set of paragraphs in this section addresses the main components of the code.

Fiducial Volume First, a shelf volume is defined around a station location and a neutrino-nucleon interaction is then required to occur within that volume. For a single station, it is calculated as a square area centered around it multiplied by an ice thickness taken as 575 m, as average of measurements discussed in §2.3.4 . This depth is taken to be uniform over the entire fiducial volume at the ARIANNA site; a fair assumption given that ice thickness measurements at locations 1 km apart yield consistent values (see §2.3.4 and Table 2.1).

Ice Model There are three options for characterizing the shelf ice.

(Option 1) uniform ice + no firn The whole ice thickness is modeled with a uniform index, nominally set to $n_{ice} = 1.78$. No firn is included.

(Option 2) uniform ice + uniform firn The top layer is modeled as a uniform firn with a lower index, nominally set at $n_{firn} = 1.325$, and a specified firn depth, currently set

at 75 m. The lower 500 m layer of ice is uniform with $n_{ice} = 1.78$.

(Option 3) uniform ice + graded firn The top firn layer is graded with a depth-dependent index of refraction modeled by the combined Equations 2.3 and 2.4 as:

$$n(z) = 1.0 + 0.86(1.0 - 0.638e^{-z/34.7}) \tag{3.1}$$

where z is depth in meters.

Option 1, the simplest case, is usually employed as a first-step diagnostic tool or when we are introducing major new changes to the code. It is to be noted that this set-up greatly skews the rate and profile of direct events due to the fact that signals do not suffer total internal reflection or 'shadowing effects' and that there is an enhanced rate of events originating in the upper part of the ice due to the higher density. Option 2 introduces a simple firn layer and provides a first-order assessment of any new modification implemented.

Option 3 is more realistic picture of the ice, as has been presented in Ref.[91] and used in ice thickness determination and attenuation length studies in Ref.[75]. Unless otherwise specified, all results presented in this dissertation are with the ice layer modeled as in this third case with the firn depth at 75m and ice thickness at 575m.

Isotropic ν Source The vertices are randomly distributed in the fiducial volume. Based on the interaction and station position and using the Snell's law to trace the signal through ice layers, we find the unique path along which a radio frequency (RF) signal would travel from the vertex to the detector either directly and/or through reflection at the bottom boundary. Next, we pick a neutrino direction at random and keep it only if the direction satisfies the requirement that the corresponding Cherenkov cone is close enough to the ray path from interaction to station so that the signal is still detectable under a best-case scenario.

Weighting the Events The absorption of the neutrinos while they propagate through the standard atmosphere and the Earth Crust is taken into account by adding a weight factor to each event. This is elaborated in §3.10.2. For ν_τ's, regeneration effects are included through weight modifications as described in §3.9.1. In the presence of firn, a weight correction factor is also applied to all events generated in firn to account for the smaller density of nucleons present there.

Neutrino Energy The neutrino energy is either selected from a chosen spectrum model or set at a specified value depending on the choice of study. The spectra options currently available in the code are given in Table 3.1. Other spectra can be easily implemented by entering the flux of neutrinos at half decade energies within the appropriate ranges. These differential fluxes values have to be obtained for all flavors in GeV cm^{-2} s^{-1} sr^{-1} and multiplied by E^2.

Type	$\mathrm{ESS}_{baseline}$	E^{-2}
standard	$10^{17}\mathrm{eV} < E_\nu < 10^{20}\mathrm{eV}$	$10^{17}\mathrm{eV} < E_\nu < 10^{20}\mathrm{eV}$
wide	$10^{16}\mathrm{eV} < E_\nu < 10^{21.5}\mathrm{eV}$	$10^{16}\mathrm{eV} < E_\nu < 10^{21.5}\mathrm{eV}$

Table 3.1: Energy spectra and range currently implemented in *shelfmc*

Neutrino and Interaction Type The code assumes that the flavors of neutrinos reaching the Earth are fully mixed through oscillations into a 1:1:1 ratio given the long pathlengths, which is appropriate for models which involve pion production since the flavor ratio at the source is 2:1:0. Therefore *shelfmc* assigns an equal probability to each flavor when generating each neutrino. We point out that different flavor ratios can be studied by running the code for each flavor separately and averaging the detection rates of each flavor. §3.10.1 provides another way a user can alter the neutrino flavor ratio. As regards to interaction type, about two-thirds of the interactions are assigned as charged-current (CC). This consideration follows from the relative cross-sections between charged current (CC) and neutral current (NC) interactions over the relevant energy interval as given in Ref.[13] . Based on neutrino

flavor and interaction type, an inelasticity y is assigned for computation of the shower energy. This is detailed in §3.4.1 and the distribution summarized in Table 3.3.

Now that a neutrino interaction has been generated from the above set of processes, the simulation moves on to calculate the radio power received at antenna by the following steps.

Geometry Quantities between vertex and station antenna such as distance and angle deviation from Cherenkov cone are evaluated. Geometric calculations include refraction if the direct or reflected event vertex if crossing of the firn-ice boundary is involved. In the presence of a graded firn, a 'shadow zone' is included, as will be explained in §3.2.4.

Signal at Vertex The radio emission from the interaction is calculated using the parametrization of Alvarez-Muñiz et al.[102] , modified by a $\frac{1}{\sqrt{2}}$ factor, which has been validated following ANITA's pre-flight calibration test at SLAC [82]. The power is obtained at a reference point of 1 m from a combination of hadronic and/or electromagnetic components and corrected for deviation from Cherenkov angle. Section 3.4 is devoted to that discussion. For ν_e electromagnetic showers, the Landau-Pomeranchuk-Migdal (LPM) effect in approximately modeled through a narrowing of the emission cone, but no modification is made to the frequency dependent power spectrum. §3.4.2 describes how this is implemented.

Propagation Effects There are losses associated with the propagation of the signal through the ice. The code accounts for these in the following manner.

(1) Ice attenuation Propagation through ice attenuates the signal through an exponential

factor $\exp(r/L_\alpha(z))$ which is both frequency and depth dependent. §3.5.3 will detail the treatment of attenuation losses. The frequency dependence is not modeled yet. Rather *shelfmc* uses a weighted (by antenna aperture) average between 100 MHz and 1 GHz. The attenuation length is depth dependent due to the temperature variation across the shelf. An empirical model of the temperature gradient is used to compute a depth-dependent average attenuation length that integrates over the direct or reflected path between the interaction point and the station. There is also option to run the code with constant attenuation lengths.

(2) Propagation losses We include the $1/r^2$ loss in power resulting from propagation over a distance r.

(3) Reflective losses For reflected rays, the simulation nominally sets the loss in power at the ice-seawater boundary at 0.5 (-3 dB) which is consistent with recent measurements [89]. However, measurements are compatible with reflectivity, R=0.91, which is theoretical maximum for flat surface between ice and salt water.

Antenna Response The signal reaching the surface is convolved with the antenna response to obtain a voltage as a function of frequency. The antenna response also depends on the orientation of the incoming signal with respect the E- and H-planes of the antenna, with the default setup being down-facing log periodic dipole array (LPDA) antennas. The voltages are summed over the whole frequency range and is compared to a threshold for a trigger decision. Section 3.6 describes the characterization of the antenna response.

Noise and Backgrounds Signal fluctuations due to thermal noise is incorporated by modifying the summed voltage with a value selected from a Gaussian distribution (see §3.8.1). At this point, there is no simulation of background from cosmic rays or thermal triggers, which are events created by thermal fluctuations in the ice which in turn create fluctuations

in the radio power observed by the antenna.

Physics Calculations The triggered events are stored and their corresponding weights tallied. As shown in §3.10.1, effective volumes (V_{eff}) and apertures ($V_{eff}\Omega$) are then computed. Using the effective apertures, together with the system livetime, neutrino-nucleon cross section and a given neutrino flux model, we can estimate the expected number of events that the experiment detects. Based on the expected number of events and data analysis results, we can then make estimation or set upper limits on the UHE neutrino flux. The Physics capabilities of single or multi-station ARIANNA can thus be assessed.

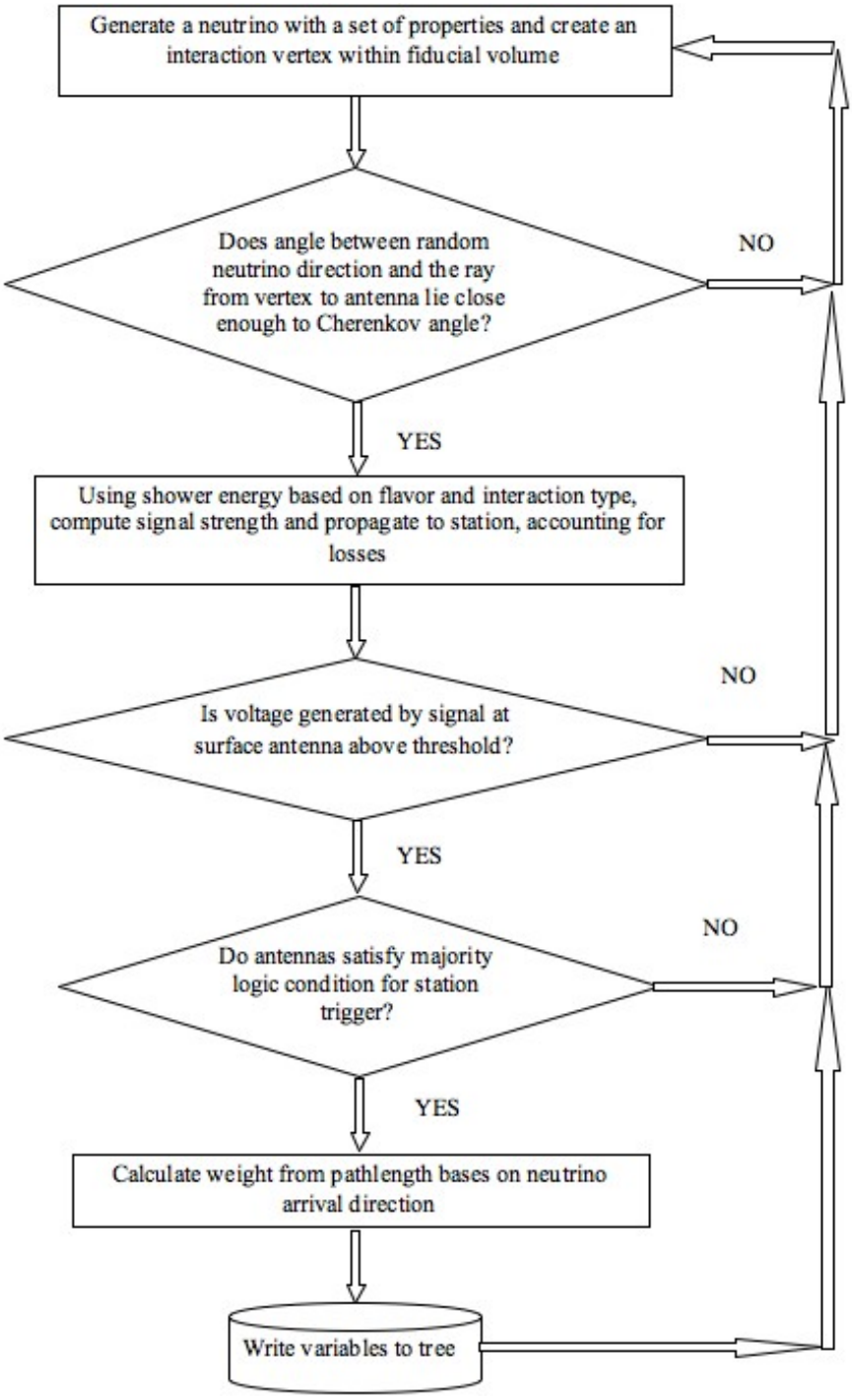

Figure 3.1: Flowchart showing main components of simulation sequence in *shelfmc*. The variables are output to a ROOT tree.

3.2 Event Geometry

The coordinate system used is either cartesian (usually for positions) or spherical (for directional vectors). When the former is referred to, we define x and y to zero at the center of the single/central station, with $z = 0$ at the ice-water surface and running positive to the surface. Hence, z at the station is a positive number given by the ice thickness, z_{max}. As explained later, modeling of reflected rays involve mirroring stations about the z-axis, implying negative z coordinates.

The ϕ coordinate is defined as usual, zero along the $+x$-axis, and increasing to 2π moving counter-clockwise when looking down the $+z$-axis. The θ coordinate is measured relative to the $+z$-axis, and ranges from 0 for upward pointing directions to π for downward pointing.

3.2.1 Random Selection of Interaction Position

As the first step outlined in the previous "Overall Strategy" section, a neutrino interaction is required to occur within a fiducial volume defined around a station:

$$\mathcal{V} = z_{max} \times \mathcal{L}_{max}^2 \tag{3.2}$$

where $\mathcal{L}_{max}$ is a maximum horizontal extent set in the code. This distance is determined by carrying out a study of horizontal distributions of event vertices for various values of $\mathcal{L}_{max}$. This helps establish a sufficiently large distance to encompass virtually all detectable vertices by an ARIANNA station, yet small enough to minimize the computing time spent on analyzing events too distant to trigger the station. The value chosen is 2 km from the station in one direction, implying that the current $\mathcal{L}_{max} = 2 \times 2\text{km} = 4\text{km}$. A discussion on horizontal distributions of event vertices is given in §4.3.1 in the next chapter, and §4.6 shows how the fiducial volume is evaluated for a square and a hexagonal array of stations.

The interaction position is assigned a coordinate $(x_{int}, y_{int}, z_{int})$ with reference to the central station located at $(0, 0, z_{max})$. The code also runs a quick check to determine if the distance of a direct and reflected path to a station exceeds $\mathcal{L}_{max}$; if true, a new interaction position is generated. In §3.2.5 later, we also discuss the assumption of point-like nature of the interaction position.

Once an interaction position is known, the code obtains the corresponding index of refraction that determines the Cherenkov angle, θ_c. The z coordinate also dictates the attenuation length values as elaborated in §3.5.3.

3.2.2 Finding Ray Path(s)

After picking an interaction position, a geometric path between the vertex and station is found for an electromagnetic ray. There are two options to explore: one is for the signal propagating directly upward to surface station ('direct' signals), and the other is for the signal that travels downwards and bounces back to travel upwards through the ice and firn to the station ('reflected' signals). To find the ray path for reflected signals, a new station (and by extension, antenna) position is obtained by reflecting the station about the ice bottom. This 'mirror-station' is then treated as a real station, so that we can repeat the tracing process as for direct signals.Ref[103]also provides details on that procedure.

Depending on the ice model option, the calculations may have to be modified. For the **uniform ice** model, the ray tracing are simply 'line-of-sight'/straight lines paths to the station. In the presence of a firn layer, Snell's law has to applied at the ice-firn interface. This 're-pathing' between a fixed source and destination with an intermediate change in medium index requires a solution to a transcendental equation that is done the simulation. The code loops through an iteration to find the path solution that satisfies the Snell's equation.

Fig. 3.2 summarizes the geometry of the two types of path in the presence of a firn layer. The method of mirror stations naturally applies the refraction twice, at each crossing of the ice-firn boundary, for reflected events originating in the firn. All associated parameters with the ray tracing process, name travel path distance r and zenith and azimuth angles for the rays in ice and /or firn, can be evaluated at this point.

It is to be noted that a given event can trigger a station (or different stations) through a combination of direct and reflected rays and the code does account for that. However, the fraction of such events are small ($\sim 2\%$) as seen in §4.3, where the relative distribution of direct and reflected events is discussed.

3.2.3 Polarization

The polarization, given by the electric field vector $\vec{\mathcal{E}}$, along the Cherenkov cone points away from the shower axis and is perpendicular to propagation vector, $\vec{P}$ (Poynting vector). In the code, it is obtained by the following pair of equations:

$$\vec{B}_i = \vec{D} \times \vec{P}_i \qquad\qquad \vec{\mathcal{E}}_i = \vec{B}_i \times \vec{P}_i \tag{3.3}$$

where $\vec{D}$ and $\vec{B}$ are the neutrino direction and magnetic field vectors respectively. The subscript i denotes the layer being considered: *firn* or *ice*.

The three different shelf models considered transforms the polarization vector in different ways depending on the refractive changes as the ray propagates. For the simple case of **uniform ice + no firn**, the polarization vector as defined by the ray direction and Cherenkov cone is clearly preserved all the way to the antennas.

In the **uniform firn + uniform ice** scenario, there are two cases. For vertices occuring in the upper firn layer, the polarization vector at the source gets preserved to the station

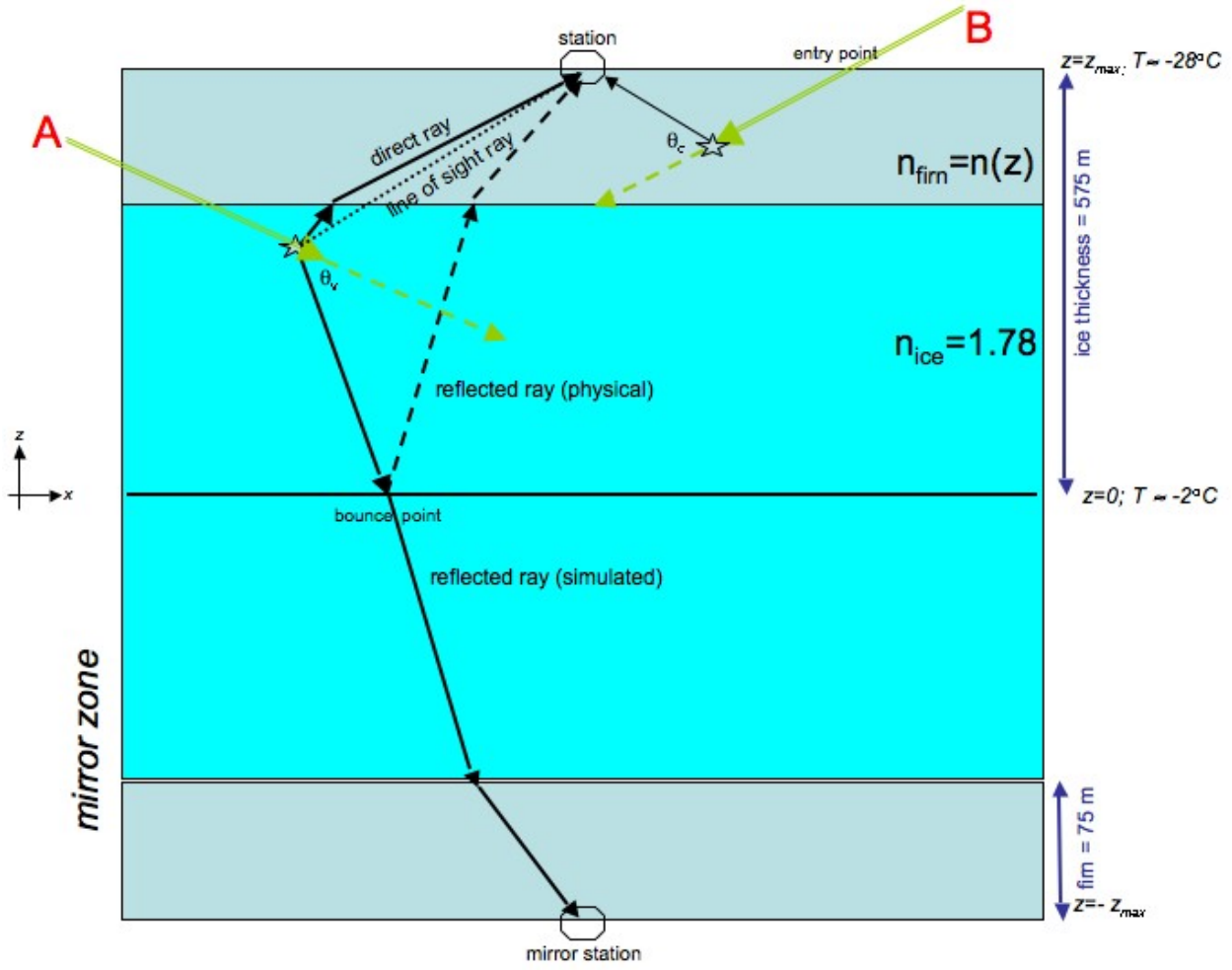

Figure 3.2: Schematic representation (not to scale) of event geometry for 'direct' and 'reflected' events. Event A interacts in the ice layer: a direct ray from the top part of the cone refracts at the firn to the station. A reflected ray from the bottom part of the cone bounces off the ice-water boundary and travels to the station. In the simulation, reflected rays are treated as traveling to a 'mirror' station that is replicated in the negative z direction, as illustrated. This simplifies the algorithm. The reflected ray of Event A is observed at a 'viewangle' θ_v that can be offset from the Cherenkov angle.
Event B is an interaction vertex in the firn and the top part of the cone propagates directly to the station. In our situation here, that ray is made to lie on the Cherenkov angle θ_c. The firn layer is less dense than the uniform ice, and in the simulation, can be represented with a uniform lower index or with a graded index $n(z)$, to match the natural conditions. Under a graded index, the ray path actually undergoes gradual refraction and follows a curved path, as discussed in §3.2.4. We note that in this example, we have shown Event A as triggering the station though both a direct and reflected ray (a 'combined' event type); this is actually a rare occurence.

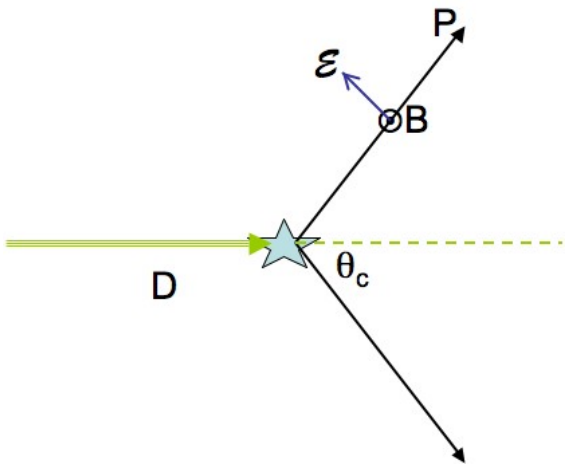

Figure 3.3: Diagram showing derivation of polarization $\vec{\mathcal{E}}$ of the signal from neutrino direction $\vec{D}$ and signal direction $\vec{P}$. The observed signal direction is not required to lie along the Cherenkov angle θ_c, but can be an observation angle θ_v. The shower axis (dotted line) is taken to be co-aligned with the incoming neutrino direction.

since there is no medium change. For interaction positions in the ice, the electric field undergoes loss through the Fresnel effect as the incident ray gets refracted at the discontinuous boundary. The details of the Fresnel calculations are given in Appendix B.2.

The more realistic realization of the **uniform ice + uniform firn** gives rise to an interesting effect due to the 'index matching' along the vertical path. This results in no loss in transmission of the electric field but but only a change in direction due to the continuous refraction of the incident ray through the firn on its way to the antennas.

In *shelfmc*, we simulate this by applying a 3-D rotation to polarization vector $\vec{\mathcal{E}}$ with an angle of rotation Ω that is given by difference between the incident and refracted angles. Note that we consider that the refracted angle near the surface as the physics of refraction shows that the angle difference depends on the initial and final indices only.

The rotation is carried out about a unit axis $\vec{u}$ that is perpendicular to both the incident and refracted ray and lies along the horizontal plane of the ice-firn boundary. The rotation

matrix by the angle Ω about an axis in the direction of $\vec{u}$ then becomes

$$\mathbb{R}_\Omega = \begin{pmatrix} \cos\Omega + u_x^2(1-\cos\Omega) & u_x u_y(1-\cos\Omega) - u_z\sin\Omega & u_x u_z(1-\cos\Omega) + u_y\sin\Omega \\ u_y u_x(1-\cos\Omega) + u_z\sin\Omega & \cos\Omega + u_y^2(1-\cos\Omega) & u_y u_z(1-\cos\Omega) - u_x\sin\Omega \\ u_z u_x(1-\cos\Omega) - u_y\sin\Omega & u_z u_y(1-\cos\Omega) + u_x\sin\Omega & \cos\Omega + u_z^2(1-\cos\Omega) \end{pmatrix} \tag{3.4}$$

and for the polarization transformation at the detector, we have

$$\vec{\mathcal{E}}_{firn} = \mathbb{R}_\Omega \vec{\mathcal{E}}_{ice} \tag{3.5}$$

For reflected rays, the code is careful to assign a different rotation axis, which is reversed by 180° from the direct case axis. This is to account for the inversion of the polarization upon reflection of the signal at the ice-water boundary.

3.2.4 Index of Refraction Considerations

The ARIANNA simulation software implements a more accurate representation of the vertical index of refraction dependence at the ARIANNA site (see §2.3.5). The previous expression, in the *shelfmc v0.0*, was inherited from Equation 2.2 of Ref.[19] and was extension of ice-sheet studies in the context of ANITA:

$$n(z) = n_{firn}(0) + 0.463251(1 - e^{-0.0140157z}),\ 0 < z < 100$$

It has now been replaced with Equation 3.1, i.e.

$$n_{firn}(z) = 1.0 + 0.86(1.0 - 0.638e^{(-z/34.7)}).$$

The prior formulation, adopted from South Pole measurements, creates a mismatch at the shallower $\sim$ 100 m firn-depths; it produces an index of 1.67 that does not smoothly meet the ice index, n_{ice}, of 1.78. That expressions actually yields 1.78 at a depth of $\sim$ 290 m and that exceeds accepted values for firn depths on the ice shelf. As for the new dependence, it matches the ice at a depth of about 67 m. However, we currently use a value of 75 m in *shelfmc 1.0* as this is the quoted value of firn depth at the ARIANNA site in Ref.[85]. As discussed in §6.3.1, setting a firn thickness of between 65 m and 85 m does not change the aperture by less than 3%.

'Shadow' zones

In the **uniform ice + uniform firn** model, total internal reflections (TIR) apply for rays incident on firn boundary at angles greater than the critical angle, θ_{crit}, given by

$$\theta_{crit} = \sin^{-1}(n_{firn}/n_{ice}).$$

Therefore, rays originating in the ice with $\theta_{inc}^{vertex} > \theta_{crit}$ are to be excluded. For interaction vertices in the uniform firn, such limitations clearly do not apply; effectively implying that rays under such situations can travel far distances at near horizontal angles to the detector.

Under the **"uniform ice + graded firn"** model however, the continuous refraction of the ray through the firn layer results in a curved path for the signal and incident rays that do not satisfy certain particular geometries cannot reach the detector. This further excludes some regions in the firn as the source of the signal.

We leave the more detailed treatment of the ray tracing geometry under a graded medium to Appendix B.1. Here, the expression for determining the horizontal distance[1], r, at a given

[1]Note: r represents this variable only in the context of this discussion in this section (§3.2.4). Throughout this thesis, r represents the path distance from an interaction vertex to a station

depth z in the firn as

$$r(\theta_0, z) = \sin\theta_0 \left| \int_{z_0}^{z_r} \left[\frac{n_{firn}^2(z)}{n_{ice}^2} - \sin^2\theta_0 \right]^{-\frac{1}{2}} dz \right| + \sin\theta_0 \left| \int_{z}^{z_r} \left[\frac{n_{firn}^2(z)}{n_{ice}^2} - \sin^2\theta_0 \right]^{-\frac{1}{2}} dz \right| \quad (3.6)$$

The second term is a subtle refinement to the model and added for completeness. It accounts for the fact that rays can potentially turn once at the firn-air boundary due to the fact that the antennas extend downward from the surface to about $z_r = 2$ m into the snow. Based on the required level of precision, the user can decide about its inclusion in the derivations below.

Figure 3.4 illustrates how the effect is created. With $n_{firn}(z)$ as in Eqn 3.1, n_{ice} set at 1.78, and $\theta_0 = \theta_{crit} \approx 47°$, we can evaluate the horizontal range r for various depths ranging from $z = 0$ at the surface to $z = d_{firn}$, the firn-depth and tabulate r with depth, as in Table 3.2. From there, a functional dependence can be conveniently coded into the simulation. The locus of points (r, z) describe a 'dome' within the firn centered about the station. Direct rays originating from outside this dome will curve away from the station. In the denser ice, that 'excluded' zone is defined by extending a straight line inclined at θ_{crit} to the vertical and starting from the maximum extent r point at the firn depth d_{firn} (r=156 m at z=75 m in our default case). Within the 'dome', there is an admitted zone where the rays are processed for further consideration.

z(m)	r(m)
0	0
2	14
5	27
10	43
20	67
50	120
75	156

Table 3.2: Range of 'shadow zone' as a function of depth in the firn. It defines a 'dome' *shelfmc* uses a criteria for shadowing effects.

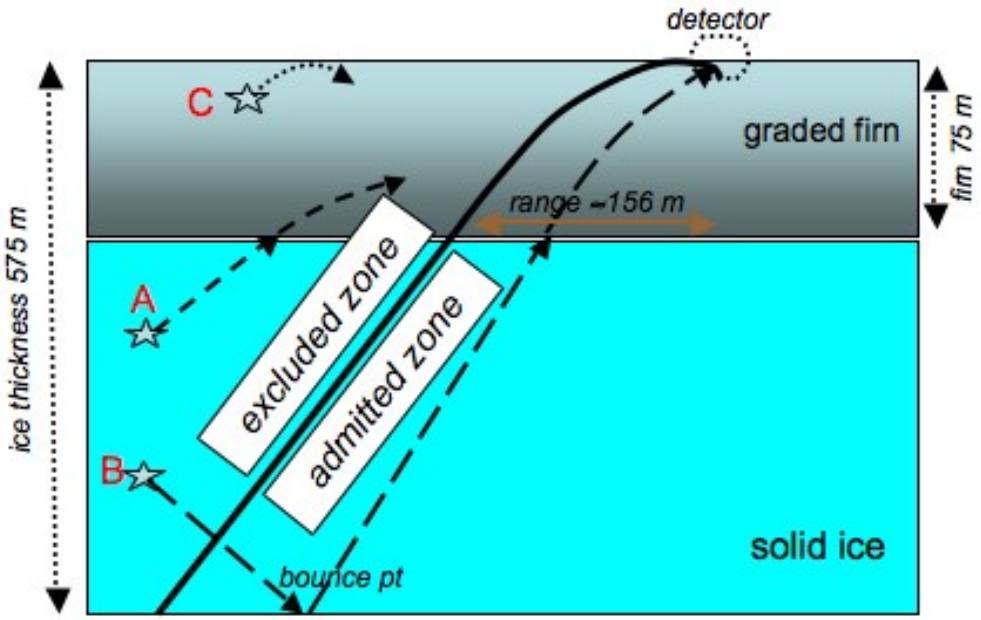

Figure 3.4: The scheme (not to scale) used for implementing a first-order correction due to 'shadowing' effects resulting from the graded index of the firn. The solid black line divides the 'excluded' zone from the 'admitted zone' . Rays from direct events A and C miss the detector. Shadowing for reflected events are included by considering the 'bounce point'; if it lies outside the limit of the zone, it is discarded, otherwise it is traced to detector. The solid line delimit the zones symmetrically around the detector and defines a 'dome' volume around.

Given that the geometrical constraints to be imposed depend on firn depth and index variations, modifications to the these two in the code will require re-computation of the functional dependence of r. Still, our above approach gives a first-order correction of the 'shadowing' effect.

Simulations which implements shadowing shows a $\sim 40\%$ drop in event rate. The suppression in far greater for direct events than for reflected (as discussed in §4.2 later). The decrease in the reflected events is equally applicable to firn- or ice-originating vertices and across all incoming neutrino angles. From Figure 3.4, we note that 'shadow zone' affects the direction of the reflected signal through the 'bounce point' location, and not the neutrino direction distribution. The greatest impact is on direct events that suffer a drop of about 80%, where almost all of the firn direct events disappear (outside the small 'dome' volume defined in firn) and about three-quarters of the ice direct events no longer trace to the detector. Further discussion of the 'shadowing' effect impact on event rates and profiles is given in the next chaper, §4.2.

3.2.5 Timing

The ray tracing geometry can also yield timing information from vertex to each individual antenna by considering the direct and/or reflected path distances with appropriate speed of electromagnetic wave propagation adjusted for varying indices of refraction.

For the **uniform ice + no firn** option, timing is generated in a straightforward way by using $t = l/c_{ice}$ where r is the traveled distance and c_{ice}, the speed of light in ice, is c/n_{ice}. The inclusion of **uniform ice + uniform firn** creates straight refracted ray for those paths that cross the ice-firn boundary and the modified travel time becomes

$$t = t_{ice} + t_{firn} = \frac{1}{c}(l_{ice}n_{ice} + l_{firn}n_{firn}) \tag{3.7}$$

where $t_{ice}[l_{ice}]$ and $t_{firn}[t_{ice}]$ are travel times[distances] in ice and firn respectively.

The **uniform ice + graded firn** requires a more sophisticated calculation of the travel time of the curved path in firn and that is not yet implemented in the simulation. Equation B.8 derived in Appendix B.1 gives

$$t_{firn}(\theta_0, z) = \frac{1}{c}\int_{z_0}^{z} n_{firn}(z)\cdot\sec\theta(z)dz = \frac{1}{c}\int_{z_0}^{z}\frac{n_{firn}^2(z)}{\sqrt{n_{firn}^2(z) - n_{ice}^2\sin^2\theta_0}}dz \tag{3.8}$$

that is to be added to t_{ice}. For reflected rays originating in the firn and traveling down first, the expression has to count all the path segments, namely two symmetric $t_{ice} = t_{ice}^{down} + t_{ice}^{up}$ from traveling down and up, and the two additional firn corrections:

$$t_{firn}(\theta_0, z) = \frac{1}{c}\int_{z_0}^{z_{int}} n_{firn}(z)\cdot\sec\theta(z)dz + \frac{1}{c}\int_{z_0}^{z} n_{firn}(z)\cdot\sec\theta(z)dz \tag{3.9}$$

where z_{int} is the interaction depth and z the detector depth. For reflected events occurring in the ice, the first term in Eqn 3.9 is not applicable and t_{ice}^{down} is $\leq t_{ice}^{up}$.

Arrival times, or more specifically differences between them, of the signal at the antennas are critical for direction reconstruction (see §5.1). Since angular reconstruction requires timing differences, implementation of the **uniform ice+uniform firn** model for timing (Eqn 3.7) is usually adequate. We are therefore able to carry out a first order investigation of events that can give rise to timing differences below 100 ps. For events with larger timing differences than 0.1 ns, it is possible that the vertex can be reconstructed. §4.3.1 in the next chapter discusses the simulation results pertaining to timing studies.

We note that shower development is assumed to be pointlike with vertex position associated with the maximum of the shower development. For the majority of the events, this approximation holds but it poorly represents LPM showers that can grow up to 100 m lengths (see also §3.4.2 later). However, the time profile of these showers is quite different from the

characteristic ones produced by hadronic showers, and this physics is not yet implemented given that time domain simulation is not yet implemented. Pointlike assumption for the vertex position also does not hold for vertices within 100 m of the station, but the fraction of events is miniscule.

3.3 Neutrino Properties

The neutrino direction is obtained by randomly picking $\cos\theta_\nu$ and ϕ_ν to represent isotropic incoming direction from all sky. Together with the previously generated interaction position data, the angle that the emerging interaction-to-station ray direction makes with the neutrino axis is determined; it is called the 'viewangle', θ_v. This is compared to the Cherenkov angle through $|\theta_v - \theta_c|$ and the code proceeds if that difference is less than a maximum angle imposed by the user. This loose cut, set by default at 20°, is imposed for speeding up the code since it is unlikely to detect the signals further away from the Cherenkov cone; the power being too weak to trigger.

The neutrino direction can then be traced back to find the ice and Earth entrance points. Neutrino characteristics like energy, E_ν,either fixed or chosen from a given spectrum, flavor and interaction type (charged or neutral current) and electromagnetic and hadronic fractions, f_{em} or f_{had} (see next section §3.4), are also generated at this point.

3.4 Modeling the Askaryan Signal

In the software, we use the parametrization outlined in Ref. [102] for the peak of the Askaryan signal:

$$\left(\frac{\mathcal{E}^{(@1\mathrm{m})}}{\mathrm{V/m/MHz}}\right)_{\theta_c} = 2.53 \times 10^{-7} \cdot \frac{E_\nu}{\mathrm{TeV}} \cdot \frac{\nu}{\nu_0} \cdot \frac{1}{1. + (\frac{\nu}{\nu_0})^{1.44}} \tag{3.10}$$

where $(\frac{\mathcal{E}^{(@1\mathrm{m})}}{\mathrm{V/m/MHz}})_{\theta_c}$ is the electric field on the Cherenkov cone at 1 m away from the interaction vertex, E_ν is the energy of neutrinos, $\nu_0 = 1.15$ GHz and ν is the frequency of the signal in the same unit as ν_0. For the electric field at some angle off the Cherenkov cone, at the so-called viewangle θ_v, it is calculated using a Gaussian distribution approximation, as illustrated in §3.4.2. This parametrization is valid up to frequencies below ~ 5 GHz. Above this frequency, the density of the shower particles means the wavelength is commensurate with mean separation between the particles and coherence is lost. Power begins to decrease.

At frequencies above 100 MHz and at the Cherenkov angle, the simulated frequency spectrum deviates from linear behavior because the wavelength becomes comparable to the transverse deviation of shower particles and to a lesser extent because of time delays. At angles away from the Cherenkov angle, the approximation becomes valid even to higher frequencies. Destructive interference in this case is due to the longitudinal excess charge distribution [102].

3.4.1 Electromagnetic and Hadronic Components of the Shower

The Askaryan signal for a given neutrino interaction includes both electromagnetic component and hadronic component. An inelasticity y is defined as the fraction of neutrino energy that goes into the hadronic part. According to Figure 7 of Ref. [104], the mean value of y for the ARIANNA energy regime is about 0.2 and we adopt the y distribution (parametrized

current	flavor	f_{em}	f_{had}
charged	ν_e	$1-y$	y
	ν_μ	-	y
	ν_τ	-	y (>0.5)
neutral	all	-	y

Table 3.3: Fractional distribution of electromagnetic and hadronic components of shower used in the simulation.

in our case by a double log) from Figure 6 of that reference in *shelfmc*. In later work of Ref. [13], the new calculations report modest changes and only noticeable at the highest energies (10^{21}eV). It should be noted that at the energy of interest for ARIANNA, the predictions rely in incompletely tested assumptions about the behavior of parton distributions at very small values of momentum transfer fraction. The calculations are extrapolated from standard model information about parton distribution functions at HERA [104]. Fig.3.5 here shows the distribution of the inelasticity of the triggered events in a typical simulation using a GZK ESS flux. The electromagnetic component (f_{em}) and the hadronic component (f_{had}) are driven by the y value, and the dependence varies for a charged current (CC) interaction and a neutral current (NC) interaction.

The outgoing lepton in CC ν_e events initiates a co-located electromagnetic shower that is modified by the LPM effect through a narrowing of the cone width (see §3.4.2 next). For CC ν_τ interactions, due to the double-bang mechanism, typically two hadronic showers are generated: one at the interaction vertex and another by the τ-decay (see §3.9.1). The simulation assumes (incorrectly) that both hadronic showers occur at the same position, selecting only the shower with the greatest energy, which is a somewhat conservative approximation of the ν_τ rates. In the simulation work for this dissertation, the outgoing muon in CC ν_μ is ignored because it loses energy by radiation and the contribution to the electromagnetic component of the shower is negligible. Table 3.3 summarizes the fractional assignment used in the simulation.

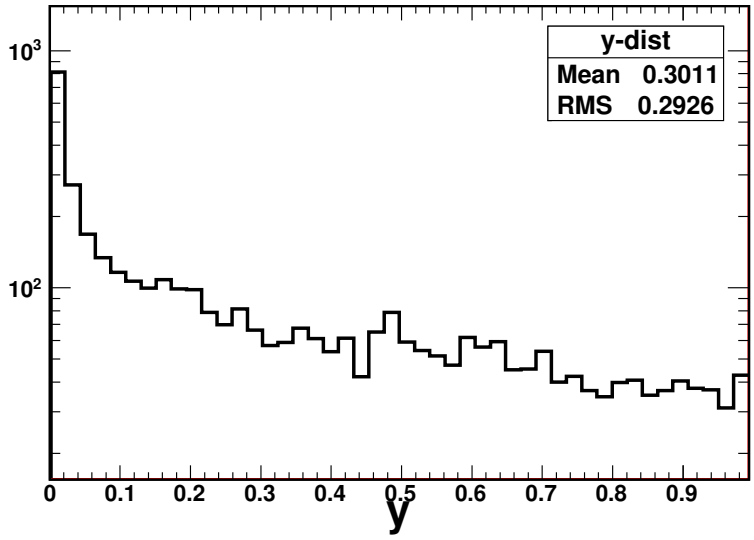

Figure 3.5: The inelasticity factor y in *shelfmc* is chosen from the distribution in Ref.[104] and parametrized by a double log. The distribution in y distribution of the triggered events, show here has a higher average value of $\sim$0.3 because it is biased from triggered events. It has the general feature of the exponential fall.

3.4.2 Width of Cherenkov Cone

In Ref.[102] and [105], the electric field amplitude around the Cherenkov cone is determined from 1-D and 3-D simulations as a function of energy and frequency in the Fraunhofer limit (far-zone). The angular distribution of the Askaryan pulse around the Cherenkov angle can be parametrized by a Gaussian peak modulated by a $\sin\theta_v$ which accounts for the angular behavior in the frequency region where the electric field behaves linearly with frequency:

$$\left(\frac{\mathcal{E}^{(@1\mathrm{m})}}{\mathrm{V/m/MHz}}\right)_{\theta_v} = \left(\frac{\mathcal{E}^{(@1\mathrm{m})}}{\mathrm{V/m/MHz}}\right)_{c} \frac{\sin\theta_v}{\sin\theta_c} \exp[-\ln 2 \cdot (\frac{\theta_v - \theta_c}{\Delta\theta})^2] \tag{3.11}$$

where:

θ_v is that 'viewangle' angle between the neutrino direction and the interaction-to-antenna ray [106, 107],

θ_c is the Cherenkov angle,

$(\frac{\mathcal{E}^{(@1\mathrm{m})}}{\mathrm{V/m/MHz}})_{\theta_v}$ is the electric field on the cone with half opening angle θ_v and same axis as the

Cherenkov cone at 1 m away from the vertex, and

$\Delta\theta$ describes the half width of Gaussian distribution of the pulse which we refer to as the width of the Cherenkov cone. As seen below, this width decreases as frequency increases. At low frequencies ($\lesssim$1 GHz), the angular distribution is pretty uniform for low frequencies showing an approximate $\sin\theta$ dependence which arises from the projection of the particle tracks on the celestial sphere of the observer [105]. The onset of destructive interference is associated with a peaking effect around the Cherenkov angle which narrows swiftly as the frequency increases. This is an analogy with the slit diffraction pattern where the shower length is treated as a single slit at large wavelengths, and as a series of finer slits at smaller wavelengths.

Electromagnetic and hadronic components of cone width The width of the Cherenkov cone ($\Delta\theta$ in radians) for electromagnetic components is calculated from Ref. [106] and that for hadronic components taken from Ref. [107].

(1) For electromagnetic shower $\Delta\theta$ in degrees is given in Ref. [106] as

$$\Delta\theta_{em}(\nu) = 2.7^\circ \cdot \frac{\nu_0}{\nu} \cdot \left(\frac{E_{LPM}}{0.14E_\nu + E_{LPM}}\right)^{0.3}, \tag{3.12}$$

where $\nu_0 = 115$ MHz, ν is the frequency of the signal, E_ν is the energy of neutrinos, and E_{LPM} is the energy above which the Landau-Pomeranchuk-Migdal effect (LPM) becomes important. The LPM effect causes the bremsstrahlung interaction and pair production to become suppressed because the momentum transfer ($\propto k/E^2$) becomes so small that the Heisenberg uncertainty causes the interaction to occur over many scattering centers, resulting in destructive interference. Showers of energy above E_{LPM} display an elongated depth distribution. This effect reduces the width of the Cherenkov cone, but not the magnitude of the electric field at the Cherenkov angle. According to Ref. [106], the value of E_{LPM} in ice

is 2 PeV, we scale this value based on the density at the interaction position as

$$E_{LPM} = 2 \times 10^{15} \cdot \frac{X_0(\text{Ice})}{X_0(\text{Depth})}. \tag{3.13}$$

Here X_0(Depth) refers to the refraction index, which is related to the density, of the interaction location, that varies in the firn but is constant in the ice.

(2) For the hadronic component of the shower the $\Delta\theta$ in degrees scales as, defining $\epsilon = \log_{10}\frac{E_\nu}{\text{TeV}}$,

$$\Delta\theta_{had} = \begin{cases} \frac{\nu_0}{\nu} \cdot (2.07 - 0.33\epsilon + 7.5 \times 10^{-2}\epsilon^2) & \text{for } 0 \leq \epsilon \leq 2 \\ \frac{\nu_0}{\nu} \cdot (1.74 - 1.21 \times 10^{-2}\epsilon) & \text{for } 2 \leq \epsilon \leq 5 \\ \frac{\nu_0}{\nu} \cdot (4.23 - 0.785\epsilon + 5.5 \times 10^{-2}\epsilon^2) & \text{for } 5 \leq \epsilon \leq 7 \\ \frac{\nu_0}{\nu} \cdot (4.23 - 0.785 \times 7 + 5.5 \times 10^{-2} \times 7^2) \times [1.0 + (\epsilon - 7) \times 0.075] & \text{for } \epsilon \geq 7. \end{cases} \tag{3.14}$$

The hadronic showers can be thought as having a hard penetrating central core containing mostly pions which feeds electromagnetic subshowers fundamentally through π^0 decay in two photons (if the π^0 energy is less that 6.7 PeV). As the primary energy rises, so will the energy of the first generation π^0's. However, they do not necessarily produce high energy photons because at these higher energies, interaction dominates over decay of π^0s. As a result, the showers can be expected to show LPM effects in a mitigated form, where even 100 EeV showers have small LPM elongation. EeV hadronic showers can look more like rescaled versions of lower energy showers while EeV electromagnetic showers are greatly distorted and elongated becaus of the LPM effect [107].

Combing the components Thus the $\mathcal{E}^{(@1m)}$ calculation for electromagnetic and hadronic showers is differentiated by the Cherenkov cone width $\Delta\theta$. Therefore, we note

$$\left(\frac{\mathcal{E}^{(@1m)}}{\mathrm{V/m/MHz}}\right)_{\theta_v}^{em} = \left(\frac{\mathcal{E}^{(@1m)}}{\mathrm{V/m/MHz}}\right)_{c} \frac{\sin\theta_v}{\sin\theta_c} \exp[-\ln 2 \cdot (\frac{\theta_v - \theta_c}{\Delta\theta_{em}})^2] \tag{3.15}$$

and

$$\left(\frac{\mathcal{E}^{(@1m)}}{\mathrm{V/m/MHz}}\right)_{\theta_v}^{had} = \left(\frac{\mathcal{E}^{(@1m)}}{\mathrm{V/m/MHz}}\right)_{c} \frac{\sin\theta_v}{\sin\theta_c} \exp[-\ln 2 \cdot (\frac{\theta_v - \theta_c}{\Delta\theta_{had}})^2]. \tag{3.16}$$

Eqn 3.11 now becomes, for the total electric field of the shower,

$$(\frac{\mathcal{E}^{(@1m)}}{\mathrm{V/m/MHz}})_{\theta_v}^{total} = f_{em} \cdot (\frac{\mathcal{E}^{(@1m)}}{\mathrm{V/m/MHz}})_{\theta_v}^{em} + f_{had} \cdot (\frac{\mathcal{E}^{(@1m)}}{\mathrm{V/m/MHz}})_{\theta_v}^{had} \tag{3.17}$$

where each type contribution is explicitly shown explicitly. As Table 3.3 shows, only ν_e interactions include the f_{em} term.

3.5 Propagation losses

3.5.1 Power losses

The surface area of the front surface of a conical geometry increases as the distance squared. Since energy is conserved, the radiated intensity will follow the usual $\frac{1}{r^2}$ dependence. The electric field scales as $\frac{1}{r}$, where r is defined as the geometric path length. *shelfmc* calculates the actual pathlength by including refraction with the firn layer, as previously discussed in §3.2.2.

3.5.2 Reflective losses at the ice-water boundary

A discussion of the reflective properties at the ice-water bottom boundary was given in §2.3.3. Signals that reflect from the water-ice surface are conservatively assumed to reflect with 50% power, although recent measurements [89] show that this surface may reflect more power. We also assume that polarization of the signal is preserved at the this surface, again, compatible with recent measurements. For reflected events, *shelfmc* modifies the amplitude of the electric field by the factor $\sqrt{R} = 0.707$.

3.5.3 Attenuation losses

The attenuation length of radiation propagating through Antarctic ice depends on frequency and temperature. Fortunately, it is possible to factor the two variables. In this section, we describe the rationale for the model of signal attenuation. The strategy is first outlined and then the detailed calculations are presented. We note that scattering is ignored in the current simulations; this is expected to be a small effect at the wavelengths relevant to ARIANNA.

Strategy We start with the temperature dependence, $\lambda(T)$. The temperature of the ice is a function of depth, $T(z)$, and thus the instantaneous attenuation length varies with the depth ($\lambda(T) \rightarrow \lambda(z)$) requiring an integration over the full pathlength to calculate signal attenuation. To reduce computation time, a mean attenuation length $\bar{\lambda}$ is computed by integrating over the pathlength from the interaction vertex to the station for both direct ($\bar{\lambda}_{dir}$) and reflected ($\bar{\lambda}_{ref}$)geometries.

The calculation begins with the inferred depth dependence of the attenuation length computed for thick ice at the South Pole [83]. One can obtain a similar prediction for shelf ice by adjusting two parameters: the surface temperature and the ice thickness. The temperature profile in shelf ice is far more linear than thick ice over the South Pole, and the temperature profile is assumed to follow a linear relationship between $-28°$ C at the surface and $-2°$ C at the ice-water boundary. The expression for the ice-shelf , as given in Ref.[19], is

$$\lambda(z) = 1250 \cdot 0.08886 \cdot \exp[-0.048827 \cdot (225.6746 - 86.517596 \cdot \log_{10}(848.870 - z))] \quad (3.18)$$

where z represents the depth in the ice with positive sign.

For a given interaction depth, z_{int}, the attenuation losses are integrated over two paths corresponding to direct and reflected rays. The average attenuation length for direct events near the bottom, or reflected events with vertices near the surface (it is the same for both cases) correspond to 1-way attenuation length measurements. The temperature dependence of the attenuation length in Antarctic ice is not well-known, and the calculation of Equation 3.18 has large systematic error. In fact, recent measurements of the 1-way attenuation length as discussed in §2.3.2 and Ref.[75] at the ARIANNA site indicate much longer attenuation lengths at all frequencies. The predicted variation of $\bar{\lambda}$ with depth is brought into agreement with these measurements by scaling the 1-way attenuation length averaged over frequency, and weighted by the A_e, the effective antenna area[2] .The weighting accounts for the strong

[2] $\bar{\lambda} = \int_{\nu_1}^{\nu_2} A_e \lambda(\nu) \mathrm{d}\nu / \int_{\nu_1}^{\nu_2} A_e \mathrm{d}\nu$ where antenna aperture $A_e \propto \nu^{-2}$ as in App. A. Thus $\bar{\lambda} =$

bias to larger wavelengths for the LPDA antenna in ARIANNA, and provides a better estimate of the average power detected by the antenna.

Calculations The detailed calculations of the steps outlined above are presented here. We consider the attenuation of the electric field as:

$$\mathcal{E} \rightarrow \mathcal{E} \cdot \exp(-r/\bar{\lambda}), \tag{3.19}$$

where r is the path that the signal travels through the ice and $\bar{\lambda}$ is the attenuation length averaged over the temperature profile during propagation. To obtain $\bar{\lambda}$, we evaluate $\left\langle \frac{1}{\lambda} \right\rangle$ and take its reciprocal.

To get values of $\langle 1/\lambda \rangle$ for upward direct rays, the integration carried out is

$$\langle 1/\lambda \rangle_{dir} = \frac{\int_{z_{int}^{eff}}^{0} 1/\lambda(z)\ \mathrm{d}z}{z_{int}^{eff}} \tag{3.20}$$

where z_{int}^{eff} is the *effective* interaction depth (positive). For reflected rays which first travel downward and then upward, the average attenuation length is calculated by

$$\langle 1/\lambda \rangle_{ref} = \frac{\int_{z_{int}^{eff}}^{z_{max}} 1/\lambda(z)\ \mathrm{d}z + \int_{z_{max}^{eff}}^{0} 1/\lambda(z)\ \mathrm{d}z}{2z_{max} - z_{int}^{eff}}. \tag{3.21}$$

For any given interaction depth, we now have two corresponding average attenuation lengths: one for direct and one for reflected. The use of *effective* interaction depth (z_{int}^{eff}) stems from the fact that the data for ice temperature profile adopted were from where the ice depth was 420 m in the Ross Ice Shelf [108]. The interaction depth is adjusted according to the local maximum ice thickness, z_{max}, to get a corresponding effective depth z_{int}^{eff}. In our current scenario, the shelf thickness, z_{max} is taken to be 575 m (the code obviously allows z_{max} to

$\int_{\nu_1}^{\nu_2} \nu^{-2}\lambda(\nu)\mathrm{d}\nu / \int_{\nu_1}^{\nu_2} \nu^{-2}\mathrm{d}\nu$. With $\lambda(\nu)$ as given by Eqn.2.1, $\bar{\lambda} \approx 425$m.

be modified) and the expression for effective depth is

$$z_{int}^{eff} = z_{int} \cdot \frac{420}{z_{max}} = z_{int} \cdot \frac{420}{575}. \tag{3.22}$$

As Figure 3.6 shows, the one-way attenuation length (which occurs for interactions at z_{max}) for "ice-shelf' is 262 m. As mentioned before, this is much smaller that recent measurements of $\bar{\lambda}_{up}$ [75] which, averaged over frequency weighted by the LPDA antenna area, is 425 m. We therefore apply a second modification to scale up the depth-dependent average attenuation lengths as

$$\bar{\lambda}'_{dir}(z_{int}) = \frac{425}{262} \cdot \bar{\lambda}_{dir} \qquad \bar{\lambda}'_{ref}(z_{int}) = \frac{425}{262} \cdot \bar{\lambda}_{ref}. \tag{3.23}$$

Hence we can compute a pair of *average* attenuation lengths for any interaction position in the ice and use the relevant direct or reflected one in the code. Figure 3.6 represents the functional dependence of $\bar{\lambda}$ on interaction depth. The "Moore's Bay" curves refer to values obtained by applying Eqn 3.23 to the "Ice Shelf" curve.

From this figure, we see that the $\bar{\lambda}(z_{int})$ for direct events decreases with depth of the interaction, as expected. This is because temperature of ice increases as it goes from ice surface to ice bottom, and field attenuation length decreases as temperature goes higher. So, as interaction position gets deeper in the ice, the average interaction length gets shorter. For reflected events, the $\bar{\lambda}(z_{int})$ of an interaction position near the surface is the same as that of near the bottom because as can be seen by setting $z_{eff}^{int} \to 0$ in Eqn. 3.21.

Additional remarks There is no explicit frequency dependence of $\bar{\lambda}$ in *shelfmc* though recent studies Eqn 2.1 from Ref.[75] provides this information. Since the details of the frequency dependence attenuation will affect the shape of the waveforms, future versions

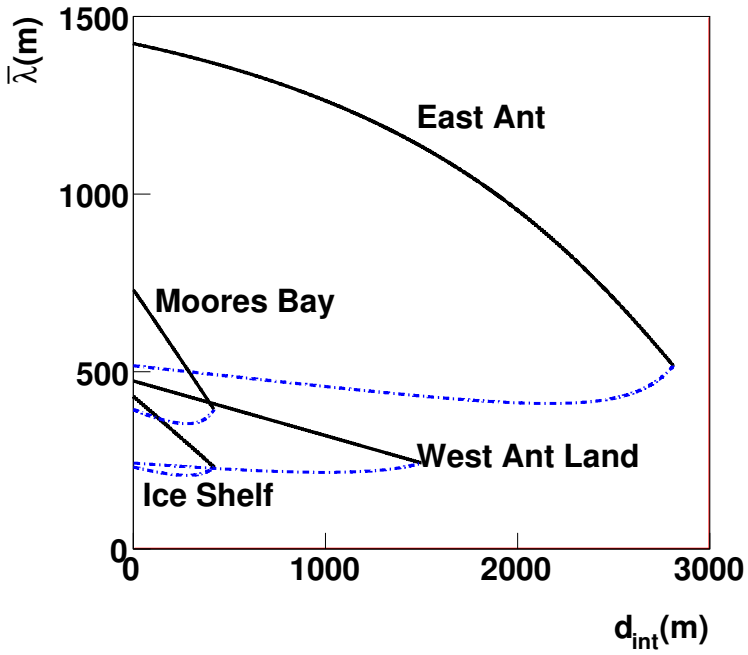

Figure 3.6: Representative values for average field attenuation length $\bar{\lambda}(z_{int})$ plotted as a function of depth for various geographical locations in Antarctica. Solid: for radio signals that travel upward directly from the neutrino interaction point. Dashed: for radio signals that first propagate down to the ice bottom and then reflect upward. The "East Ant" is for the $\bar{\lambda}(z_{int})$ of ice sheet in the east Antarctica, the "West Ant Land" is for the $\bar{\lambda}(z_{int})$ of the ice sheet in the west Antarctica, and the "Ice Shelf" is for the $\lambda(z_{int})$ of the ice shelves. All the three are derived from the South Pole measurements. The "Moores Bay" is the $\lambda(z_{int})$ derived from the Moores' Bay measurements, which indicates a larger $\bar{\lambda}(z_{int})$ for ice shelves. From Ref. [19]

of the *shelfmc* will include a detailed study of frequency-dependent attenuation Finally, we note that there is an option to bypass a depth-dependent attenuation in *shelfmc* and apply distinct and constant attenuation lengths for direct and reflect paths.

Including the propagation losses discussed in this section, Eqn 3.17 now becomes for the electric field at the surface

$$\left(\frac{\mathcal{E}^{(@\ \mathrm{z=0})}}{\mathrm{V/m/MHz}}\right)_{\theta_v}^{total} = \frac{e^{-r/\bar{\lambda}}}{r}\sqrt{R}\left[f_{em}\cdot\left(\frac{\mathcal{E}^{(@1\mathrm{m})}}{\mathrm{V/m/MHz}}\right)_{\theta_v}^{em} + f_{had}\cdot\left(\frac{\mathcal{E}^{(@1\mathrm{m})}}{\mathrm{V/m/MHz}}\right)_{\theta_v}^{had}\right] \quad (3.24)$$

where R=1 and $\bar{\lambda} = \bar{\lambda}_{up}$, and for reflected R=0.5 with $\bar{\lambda} = \bar{\lambda}_{down}$.

3.6 Antenna Response

A description of the antennas used in the ARIANNA station is given in §2.4.2 together with results of *in situ* studies. The baseline design of the ARIANNA station includes 4-8 log periodic antennas (LPDAs) arranged in a geometrically symmetric pattern, facing downward, and with the top of the antenna buried ∼1 m below the surface of the snow. Figure 3.7 shows a top view of the octagonal arrangement. In this section, we explain how we simulate the antenna response which is dependent on frequency and orientation with respect to the incoming signal.

Angular response of antennas One of the basic parameters of antenna response is gain which depends on the direction of the incoming radiation. The manufacturers supplies relative gain vs angle for E- and H-plane geometries at various frequencies. This data is valid for LPDA in air. In this work, the antenna response in low density firn is assumed to be a good approximation. This was supported by VSWR measurements, as described in §2.4.2 that showed very little changes between air and shallow firn.

As Figure 3.9 illustrates, the radiation pattern (and hence antenna response) at fixed frequency decreases as the angle relative to the nose of the LPDA increases. The relative gain is modeled by a Gaussian expression for both E- and H-plane geometries. Therefore, to characterize the angular response, relative orientations of the incident signal with respect to the antenna have to be considered and several planes and vectors are defined to facilitate the discussion[3]

The E-plane of the LPDA is the array plane that contains the tines of the antenna, and

[3]In this subsection, we use $\vec{n}$'s for directions of signal and polarizations, while throughout this dissertation, there are referred to as $\vec{P}$ and $\vec{\mathcal{E}}$ respectively. The reason for this notation here is for easy reference within *shelfmc*. Furthermore, unlike the convention used in Fig.3.8, in *shelfmc*, $\vec{n}_{E-plane}$ and $\vec{n}_{H-plane}$ are locally defined as unit vectors lying along the E- and H-planes respectively. This is an unusual notation that is a relic of quad horn antenna characterizations.

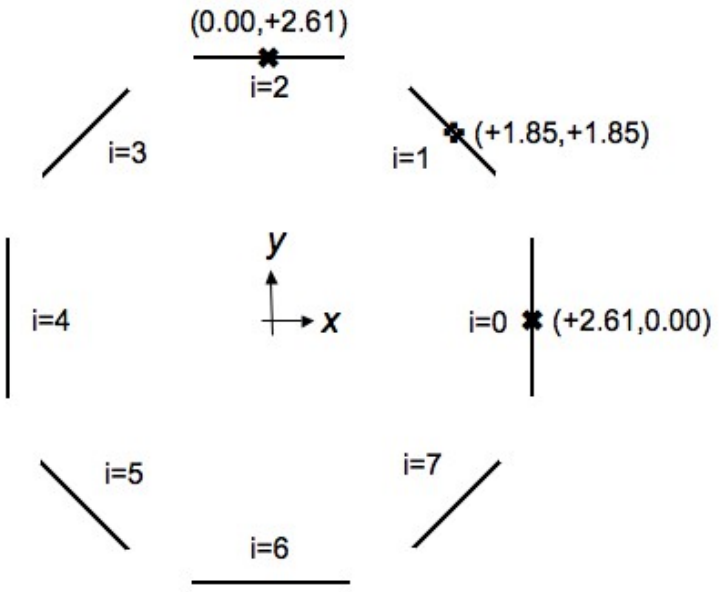

Figure 3.7: Top view representing symmetric antenna arrangement scheme and index label. The (x, y) coordinates of the mid-point lines are given in meters.

the H-plane lies perpendicular to that E-plane. $\vec{n}_{normal}$ is define as pointing away from the antenna nose as shown in Fig. 3.8. An incident signal, $\vec{n}_{signal} = \vec{P}$, defines a 'hitangle' θ^E_{inc} with respect to the E-plane and another θ^H_{inc} with respect to the H-plane. We note that these 'hitangles' can vary from antenna to antenna within the same station and are not to be confused with the angles defining the general direction of travel of the signal given by $\vec{P}(\hat{\theta},\hat{\phi})$.

frequency	beamwidth (θ_{hpbw})		gain
(MHz)	E-plane	H-plane	
<300	74°	144°	5.9
300-600	70°	128°	6.6
600-900	74°	134°	6.2
900-1200	78°	132°	6.0

Table 3.4: LPDA antenna parameters. For intermediate frequencies, the values are interpolated in *shelfmc*.

Together with the half-power beam-width, θ_{hpbw}, (see Appendix A for more details) and the incident angle, θ_{inc}, along a given plane, we can calculate the drop in voltage by a factor

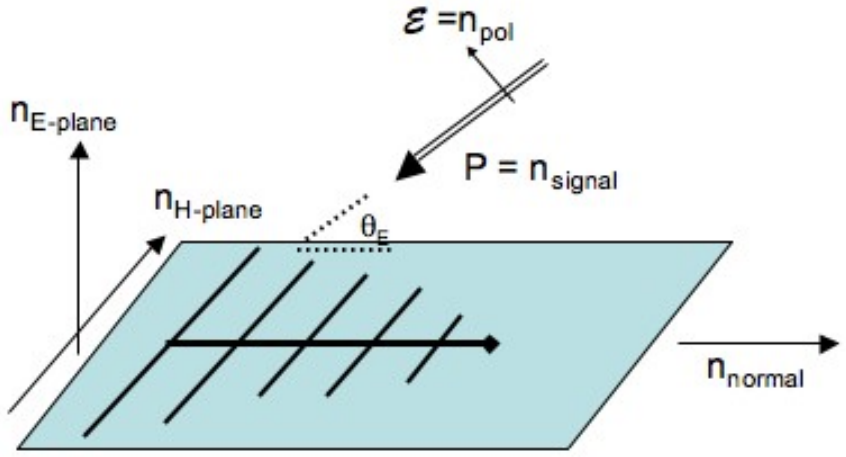

Figure 3.8: Diagram showing the vectors and angles defined in the code. The antenna is shown laying flat as opposed to pointing down, which is the default orientation. An incident signal will be incident at the antenna at an angle θ^E_{inc} off the E-plane of the antenna. The $\vec{n}_{E-plane}$, is perpendicular to the E-plane. Same applies for $\vec{n}_{H-plane}$ and H-plane.

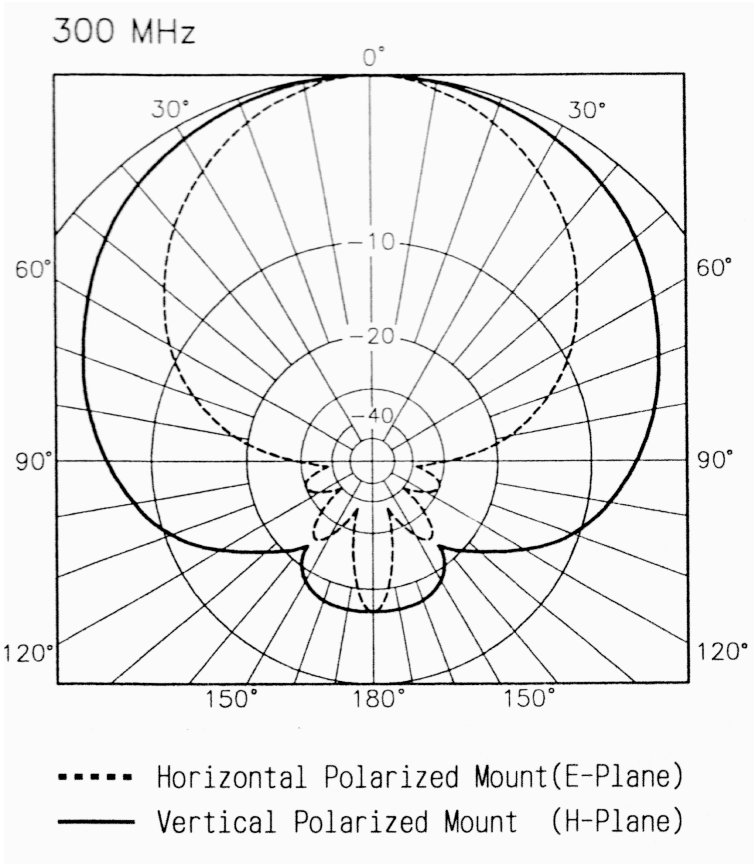

Figure 3.9: Average LPDA radiation pattern from manufacturer's manual shown for 300 MHz [96]. The gain on the antenna decreases as a function of angle.

from the Gaussian expression as

$$\exp[-2\ln 2(\frac{\theta_{inc}}{\theta_{hpbw}(\nu)})^2]. \tag{3.25}$$

Both θ_{inc} and θ_{hpbw} vary for each principal plane (see Fig 3.9) and in addition, is frequency dependent. We use the manufacturer's specification to obtain the frequency dependent angular response (and gain), and confirm the basic properties with a simulation package from [109]. The frequency-dependent properties are summarized in Table 3.4.

For arbitrary $\vec{n}_{signal}$, the approximate angular dependence by the LPDA antenna is obtained by averaging the E- and H- plane terms (also explicitly given in Eqn 3.29 (third line) of the next section)

$$\sqrt{\frac{1}{2}\left[\left(\mathrm{f}_{\mathcal{E}}\cdot\exp[-2\ln 2(\frac{\theta^E_{inc}}{\theta^E_{hpbw}(\nu_i)})^2]\right)^2+\left(\mathrm{f}_{\mathcal{E}}\cdot\exp[-2\ln 2(\frac{\theta^H_{inc}}{\theta^H_{hpbw}(\nu_i)})^2]\right)^2\right]}. \tag{3.26}$$

The individual terms are first squared to positive values and have the component of the electric field polarization, $\mathrm{f}_{\mathcal{E}}$ involved.

Specifically, $\mathrm{f}_{\mathcal{E}}$ is defined as

$$\mathrm{f}_{\mathcal{E}} = \vec{n}_{pol}\times\vec{n}_{E-plane} = \hat{\vec{\mathcal{E}}}\times\vec{n}_{E-plane} \tag{3.27}$$

and given that it can take negative values, the expressions get squared in Eqn.3.26.

Antenna height The effective height term that also appears in Eqn 3.29 is frequency-dependent and is related to gain[4] G (see also Appendix A for more details) by

$$h_{eff}(\nu) = 2 \times \sqrt{\frac{G}{4\pi} \cdot \frac{c^2}{\nu^2} \cdot \frac{Z_{rx} n_{ice}}{Z_0}} \tag{3.28}$$

where Z_{rx}=50 Ω is the impedance of the receiver antenna modified in ice(or firn) by n_{ice} (or n_{firn}) and Z_0= 377 Ω is the impedance of free space. The current simulations of ARIANNA assume that the antenna response in the firn are identical to the response in air. The tests described in §2.4.2 show that the approximation in good over most of the frequency band relevant to ARIANNA. However, the next version of the code will model the frequency response between 80-100 MHz to account for the added power detected by the LPDA.

In this section, we have focused on the LPDA simulation. However, *shelfmc* code has antenna options for quad-horn Seavey(as used in ANITA), and fat dipole. Any antenna can be studied as long as the relative gain of the E and H-plane as a function of angle and frequency between 50 MHz and 1GHz, and effective area as a function of frequency are given.

[4]We should be careful in distinguishing between raw gain G and the relative gain $G_{\mathrm{dBi}} = 10 \cdot \log_{10}(G)$ which are the usually the published technical figures and where dBi refers to antenna gains being compared to an isotropic radiator.

3.7 Signal Amplitude

Combining all the effects described in §3.4-3.6, starting from the generation of the electric field at the shower through propagation losses to finally the voltage conversion by LPDA by folding in the antenna response, we obtain the following expression for voltage amplitude of the time dependent pulse observed by the LPDA:

$$
\begin{aligned}
\mathrm{V_{LPDA}} \;=\; & \sum_j \Delta\nu_j \cdot 0.5 \cdot \frac{1}{\sqrt{2}} \cdot \frac{\sin\theta_v}{\sin\theta_c} \cdot h_{eff}(\nu_j) \cdot \frac{e^{-r/\bar{\lambda}}}{r}\sqrt{R}\cdot \\
& \sqrt{\frac{1}{2}\left[\left(f_E \cdot \exp[-2\ln 2(\frac{\theta^E_{inc}}{\theta^E_{hpbw}(\nu_j)})^2]\right)^2 + \left(f_E \cdot \exp[-2\ln 2(\frac{\theta^H_{inc}}{\theta^H_{hpbw}(\nu_j)})^2]\right)^2\right]} \;\times \\
\{ \quad & f_{em} \cdot \left(2.53\times 10^{-7} \cdot \frac{E_\nu}{\mathrm{TeV}} \cdot \frac{\nu_j}{\nu_0} \cdot \frac{1}{1.+(\frac{\nu_i}{\nu_0})^{1.44}}\right) \cdot \exp\left[-\ln 2 \cdot (\frac{\theta_v-\theta_c}{\Delta\theta_{em}(\nu_j)})^2\right] \\
+ \quad & f_{had} \cdot \left(2.53\times 10^{-7} \cdot \frac{E_\nu}{\mathrm{TeV}} \cdot \frac{\nu_j}{\nu_0} \cdot \frac{1}{1.+(\frac{\nu_i}{\nu_0})^{1.44}}\right) \cdot \exp\left[-\ln 2 \cdot (\frac{\theta_v-\theta_c}{\Delta\theta_{had}(\nu_j)})^2\right] \quad \}. \qquad (3.29)
\end{aligned}
$$

Equation 3.29 contains a summation over frequencies within the bandwidth assigned in the simulation (100-1000 MHZ). The low frequency cutoff is due to the response of the LPDA selected for the prototype station. The high frequency cutoff is due to decreasing h_{eff} at high frequencies, decreasing attenuation length, and rapidly decreasing width of the Cherenkov cone. Using 95 uniformly spread bins, j runs from 0 to 94 and the frequency bin is $\sim$ 9.5 MHz. Here, we distinguish the ν subscript in E_ν, the energy of the incoming neutrino, from ν_i which represents the center frequency of the jth bin.

Figure 3.10 shows an example of frequency-dependent voltage terms for various observations angles θ_v: on Cherenkov cone (i.e $\theta_v = \theta_c$), 2° off, and 5° off. It shows that the higher frequency terms are less relevant as we move away from the Cherenkov angle. As a reference,

Figure 3.11 gives shows the magnitude of the electric field as a function of the frequency for similar sets of angles off the Cherenkov angle. This is at a reference distance of 1 m from the vertex, before any propagation losses and antenna response. The plot represents Equation 3.11 for select θ_v.

The voltage computed as in Eqn.3.29 is compared to threshold values for triggering purposes, as elaborated in the next section §3.8.2. In this procedure, we implicitly take this sum of frequency components to correspond to the time dependent signal amplitude from the antenna. This approximation is justified as explained in the next section §3.8.2.

3.8 Noise and Trigger

3.8.1 Noise

In frequency domain simulation, we assume that an antenna will see noise due to the temperature of the ice (T_{ice}) and the temperature of the front-end electronics (T_{syst}). Taking $T_{ice} = 245$ K and $T_{syst} = 200$ K, we have $T_{noise} = 445$ K. With a bandwith, $(\nu_{max} - \nu_{min})$, of 900 MHz, we calculate r.m.s. voltage due to noise as follows:

$$\begin{aligned} \mathrm{V}_{\mathrm{noise}}^{\mathrm{rms}} &= \sqrt{4 \cdot T_{noise} \cdot 50\Omega \cdot k_B \cdot (\nu_{max} - \nu_{min})} \\ &= \sqrt{445\mathrm{K} \cdot 50\Omega \cdot 1.3806 \times 10^{-23}\mathrm{JK}^{-1} \cdot 900\mathrm{MHz}} \\ &= 3.32 \times 10^{-5}\mathrm{V} \end{aligned} \tag{3.30}$$

The trigger threshold can then be set with reference to this voltage level as seen in the next section. For instance, the nominal value at $5 \cdot \mathrm{V}_{\mathrm{rms}}^{\mathrm{noise}}$ corresponds to $\sim 166\mu$V.

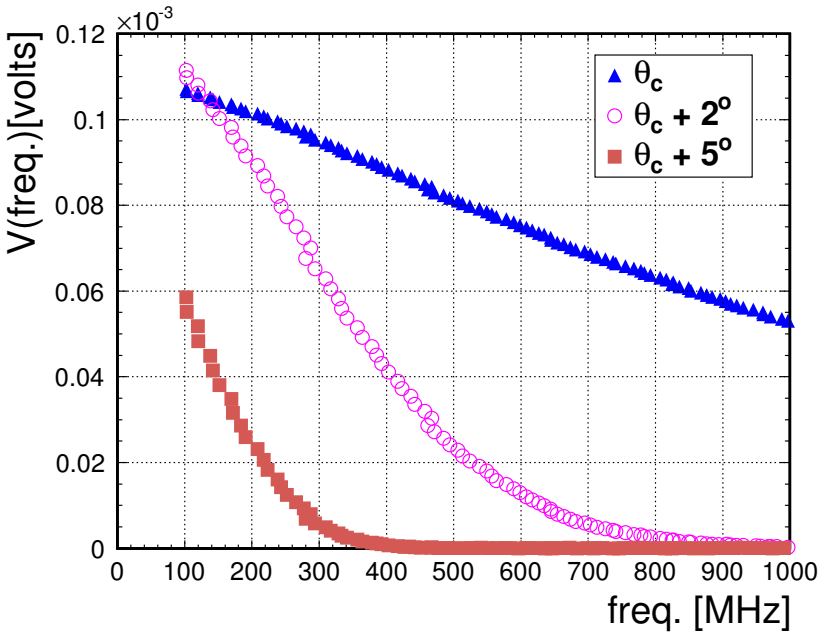

Figure 3.10: Voltage at LPDA antenna as a function of frequency and observation angles θ_v for an event with shower energy at 10^{18}eV. Distance r is 500 m, and $theta^E_{inc}$ and $theta^H_{inc}$ at 0°.

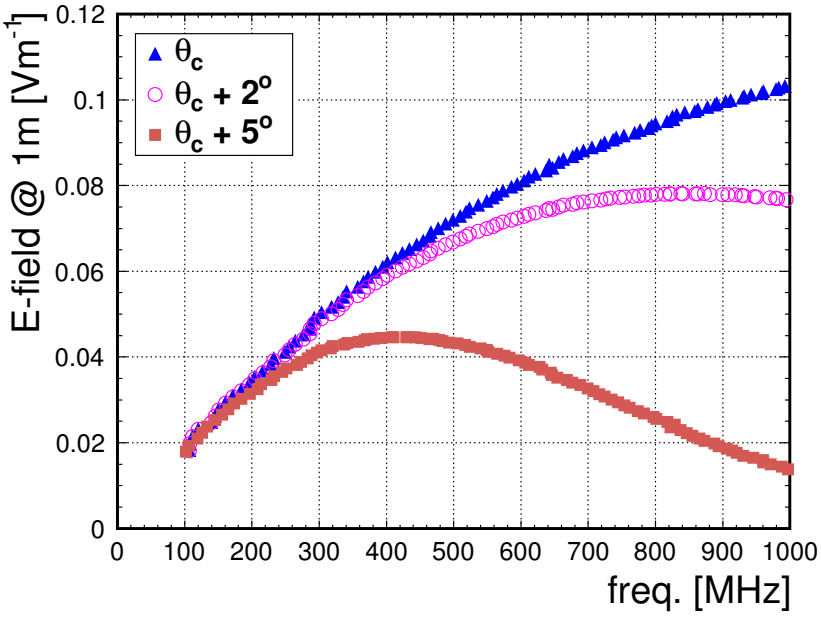

Figure 3.11: Electric field at reference point of 1m (as given by Equation 3.11), as a function of frequency and observation angles θ_v for an event with shower energy at 10^{18}eV.

In the prototype station, the electrical signals are amplified by ∼60 dB, corresponding to 10^3 factor in voltage. The $5{\cdot}V_{rms}$ thresholds are slightly larger than ∼166 mV due to the additional noise created by the amplifier. The noise created by the amplifier, characterized by a noise figure of ∼1.8 must be included by correcting the observed V_{rms}^{noise}. Roughly, $(V_{rms}^{noise})_{amp}$ $\sim \sqrt{1.8} V_{rms}^{noise}$ and so the simulated threshold of $5{\cdot}V_{rms}^{noise}$ corresponds to $3.6(V_{rms}^{noise})_{amp}$.

If the user activates the noise option for the signal, a value is randomly selected from a Gaussian distribution defined with the above V_{noise}^{rms} as root mean square, and added to V_{LPDA} from Eq 3.29. We note that this fluctuation can be positive or negative, serving to increase or decrease the final voltage that is compared to the threshold values.

3.8.2 Trigger

The trigger circuitry for the prototype station deployed in 2009 is described in §2.4.3 The total power in the high and low bands are integrated by a tunnel diode. The effective signal can be modeled by summing the voltage in Equation 3.29 over the frequency interval appropriate to the bands (130-460 MHz for the low band and 650-990 MHz for the high band). This approach has been utilized by the ANITA collaboration [110].

The new trigger circuit in the Hexagonal Radio Array (HRA) uses the time domain signal to compare to pattern trigger of controllable thresholds. Fortunately, the summed signal of Equation 3.29 provides a good estimate of the voltage amplitude in the time domain.

We illustrate this assertion by comparing to the maximum amplitude of the time domain signal computed by Alvarez-Muñiz et al.[111]. As shown in Table 3.5, the summed calculation of $\mathcal{E}^{(@1m)}$ in frequency domain from *shelfmc* replicates the time domain amplitude to good accuracy. At the Cherenkov angle, the simulation overestimates the amplitude; but the observation angles are on average 2-3° away from the peak and there, the program actually

underestimates the time-domain amplitude.

There has been further progress in the detailed calculation of the Askaryan time-domain pulse profile, as in Ref.[112]; the future implementation of time domain trigger into *shelfmc* will be facilitated by collaboration with the authors, who specialize in time domain pulse simulations. This will complement the hardware implementation of the new waveform digitizer.

$\lvert\theta_v - \theta_c\rvert$	$\mathcal{E}'_{max} = \sum_\nu \mathcal{E}(\nu)$	$\mathcal{E}_{max}$	$\lvert\mathcal{E}_{max}$ - $\mathcal{E}'_{max}\rvert / \mathcal{E}_{max}$
0°(on cone peak)	0.42	0.30	0.4
5°	3×10^{-3}	7×10^{-3}	0.6
10°	7×10^{-4}	1×10^{-3}	0.3

Table 3.5: Electric field amplitudes, at a reference point of 1 m, as simulated by *shelfmc* (denoted by prime, second column) and, as calculated in time domain (third column) taken from Fig. 2 (below)and 3 of Ref.[111]. Comparison is given for on cone peak power and two representative observation angles off cone. Electric field has been simulated for same shower energy and over similar frequency ranges of *10 to 5000 MHz*.

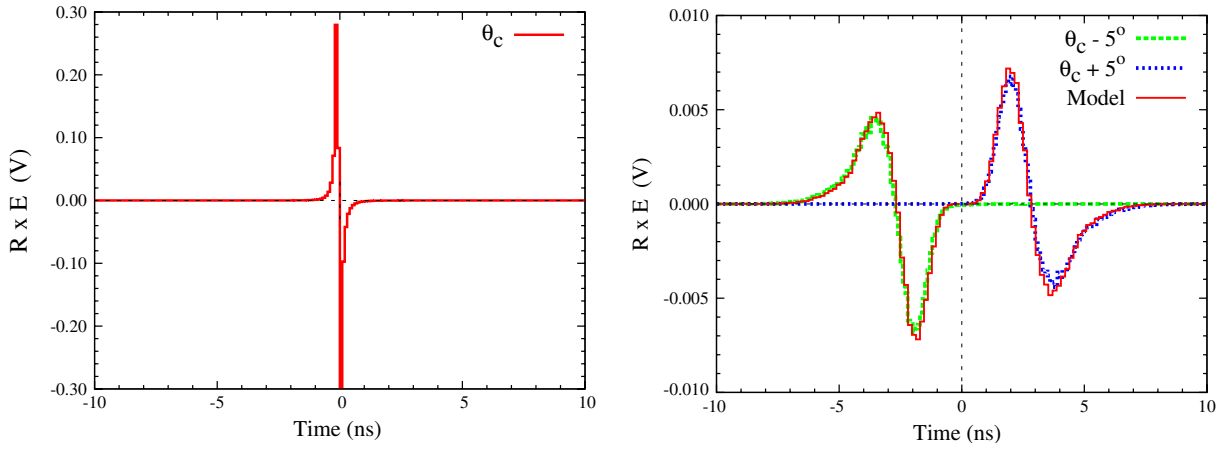

Figure 3.12: Electric field as a function of time for a 1 PeV electron induced shower in ice for different observations angles. Left panel is for the pulse at the Cherenkov angle; right panel is for 5° off the peak. From Fig 2. of Ref. [111].

For our concept study here, we use 8 antennas arranged symmetrically. The currently used trigger method is the more traditional method of triggering on a signal amplitude exceeding a specified level compared to the root mean square voltage fluctuations of the signal chain (as described in the previous subsection).

The simulation then counts the number of antennas passing the trigger condition in a particular station and stores the event if it passes the majority logic criterion for station level trigger. The default majority logic condition is a 3 out of 8 antenna. Other logic conditions where studied from 1 of 8 to 8 of 8; §4.1 discusses this.

There is no time window restriction imposed yet on the maximum time difference between the earliest and last antenna trigger. Simulation models only simplest pattern trigger - one condition that requires voltage amplitude to exceed a set value. That threshold is typically set to $5 \cdot V_{rms}$, but that factor is an adjustable parameter in the control script. Studies show that the threshold value causes modest modification to the station sensitivity (see Fig 3.13); however it has a dramatic impact on the rate of events induced by random thermal fluctuations.

With the advent of the new waveform digitizer previously explained in §2.5, the simulation code will be enhanced to replicate triggering based in time-domain. A first step in that process has been the investigation of noise suppression in each antenna channel. This is due to a specific pattern of trigger conditions that may be imposed. For example, we may require that a signal contain a large positive value followed by a large negative value, or vice-versa with the aim of having a pattern trigger that selects on general features of the expected Askaryan pulse from a neutrino interaction. Obviously, the more conditions in the pattern, the less sensitive is the instrument, but studies by J. Hanson[113] indicate that significant reduction of thermal trigger rates by several orders of magnitude can be obtained while retaining 90% signal sensitivity relative to a single threshold condition.

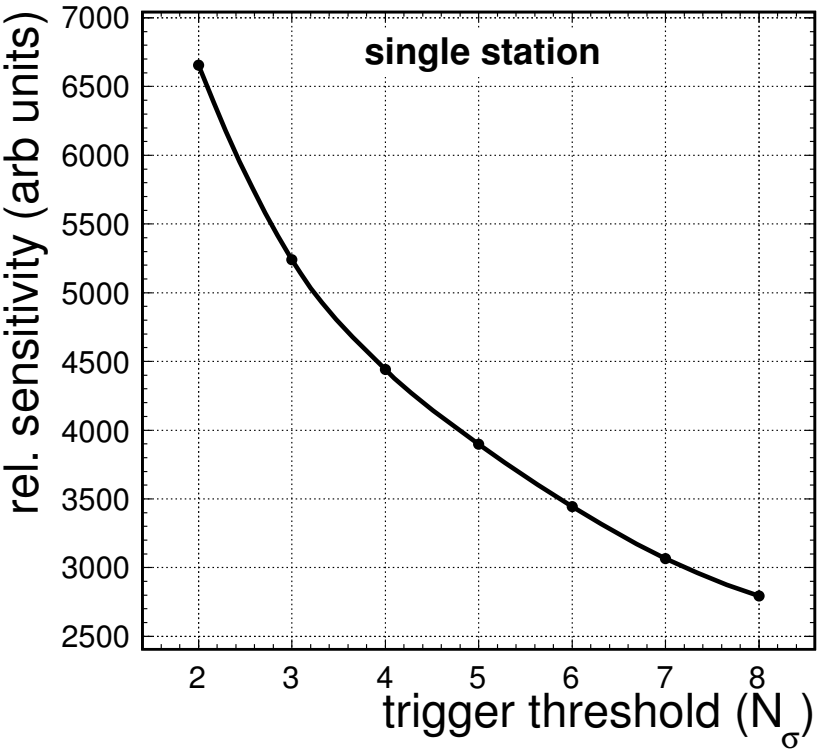

Figure 3.13: The voltage threshold is nominally set to $5{\cdot}V_{rms}$, but studies show that varying it from $3{\cdot}V_{rms}$ to $8{\cdot}V_{rms}$ causes the sensitivity to decrease by a factor 2 only.

3.9 Secondary Signals

3.9.1 Tau lepton effects

The ν_τ decay can lead to a couple of secondary effects that provides additional signatures for detection: ν_τ regeneration and double bang (see Ref.[114]). As discussed in this section, the latter is not fully implemented in the code yet but the first one is treated through a re-weighing of the tau flavor neutrinos.

Tau neutrino regeneration

Unlike other ν flavors, the Earth remains transparent to ν_τ above 10-100 TeV [115]. This is because a high-energy ν_τ will interact with the Earth and the outgoing τ-lepton will rapidly decay, before losing significant energy, mostly into ν_τ. For NC interactions, $E'_{\nu_\tau} \sim \frac{1}{2}E_{\nu_\tau}$ on average. In a CC interaction, a τ is produced which decays in a number of ways, yet there is always another ν_τ in the final state. So, high-energy ν_τ's will initiate a cascade in the Earth which will contain a ν_τ of reduced energy in each interaction. The energies involved are high enough so that the direction of ν'_τ is collinear with ν_τ. Unfortunately, the energy at which the Earth becomes transparent is too low for ARIANNA for most trajectories. However, near the horizon, the transparency energy remains large enough to be detected.

Our strategy to include tau-regeneration in *shelfmc* is to re-evaluate the weight assigned to the ν_τ's as a function of zenith angle. Due to the regeneration, there is now a new finite probability that a secondary neutrino, albeit at lower energies, will emerge along the direction of the original incident particle once the latter is absorbed. We can therefore apply a the correction to the original probability that was associated with the incoming neutrino. Using the dedicated simulation code employed in Ref.[115], we compute the weight (§3.10.2) as a function of zenith angle and energy for two neutrino energy input spectra, namely E^{-2} and

ESS GZK, and limit our energy range to the one relevant for ARIANNA.

The software from Ref.[115] randomly chooses a direction for an incoming ν_τ and randomly chooses an energy from an input spectrum of choice. From the selected zenith angle, it calculates a corresponding slab thickness through the Earth to a detector on the surface. It then propagates the ν_τ in finite steps, evaluating whether the particle will interact within each step. For the interaction probability calculation, the standard model cross-sections [13] and the density of the Earth crust at each location are used. The type of interaction (NC or CC) and the inelasticity factor are assigned and these determine whether a τ-lepton is emitted.The program tracks the secondary lepton along the original path and, using the lifetime of that τ and the γ factor, computes its decay coordinate and energy loss. The next calculation is selecting the branching mode of τ into ν_τ and the corresponding energy reduction. This process is iterated until a ν_τ emerges at the surface of the Earth. This final neutrino creates the interaction vertex within the ARIANNA fiducial volume. Figure 3.14 illustrates the concept of the regeneration effect.

For a specified energy interval, secondary ν_τ are counted and compared to the number observed without the regeneration effect. The ratio determines the weight as a function of neutrino direction and energy, as presented in Table 3.6.

If the event type is an upcoming ν_τ, *shelfmc* checks assigns a modified weight from the Table 3.6. In §4.3.2 and Fig.4.11 in the next chapter, we discuss the effect of implementing ν_τ regeneration on the angular sensitivity of the detector. We note that the current implementation of ν_τ regeneration was developed for two representative neutrino spectra. For GZK-like spectra, there is an enhancement at the lowest relevant energies, but there is a net reduction in the upgoing ν_τ flux. For power law spectra, due to the fact that the low energy neutrinos are quickly converted to energies that are below detection.

The current implementation does not include important effects, such as muon generation and

	zenith angle(degrees)								
$\log E_{\nu_\tau}$(eV)	60-65	65-70	70-75	75-80	80-82	82-84	84-86	86-88	88-90
15.0-15.5	3.58	3.01	2.38	1.94	1.63	1.43	1.29	1.16	1.05
15.5-16.0	2.92	2.94	2.65	2.28	1.87	1.74	1.47	1.27	1.07
16.0-16.5	1.33	1.89	2.23	2.22	2.11	1.89	1.69	1.42	1.13
16.5-17.0	0.26	0.57	0.97	1.27	1.46	1.51	1.48	1.37	1.14
17.0-17.5	0.02	0.06	0.17	0.34	0.52	0.65	0.80	0.92	0.98
17.5-18.0	0.00	0.00	0.02	0.08	0.17	0.28	0.43	0.64	0.87
18.0-18.5	0.00	0.00	0.00	0.01	0.03	0.07	0.17	0.36	0.77
18.5-19.0	0.00	0.00	0.00	0.00	0.00	0.01	0.05	0.22	0.74
19.0-19.5	0.00	0.00	0.00	0.00	0.00	0.00	0.01	0.15	0.73
>19.5	0.00	0.00	0.00	0.00	0.00	0.00	0.02	0.13	0.67

	zenith angle(degrees)								
$\log E_{\nu_\tau}$(eV)	60-65	65-70	70-75	75-80	80-82	82-84	84-86	86-88	88-90
15.0-16.0	0.59	0.69	0.78	0.84	0.89	0.90	0.93	0.96	0.99
16.0-17.0	0.19	0.33	0.49	0.60	0.70	0.79	0.84	0.91	0.97
17.0-18.0	0.01	0.03	0.08	0.22	0.35	0.39	0.66	0.75	0.93
18.0-19.0	0.00	0.00	0.00	0.01	0.04	0.07	0.15	0.36	0.77
19.0-20.0	0.00	0.00	0.00	0.00	0.00	0.00	0.01	0.21	0.73
20.0-21.0	0.00	0.00	0.00	0.00	0.00	0.00	0.00	0.35	0.90

Table 3.6: Modified weights implemented for ν_τ regeneration effects using GZK (top table) and E^{-2}(bottom) input spectra. Note that the energy bins are at half-decade for GZK. Numbers greater than 1 indicate an enhancement $\nu_\tau flux$.

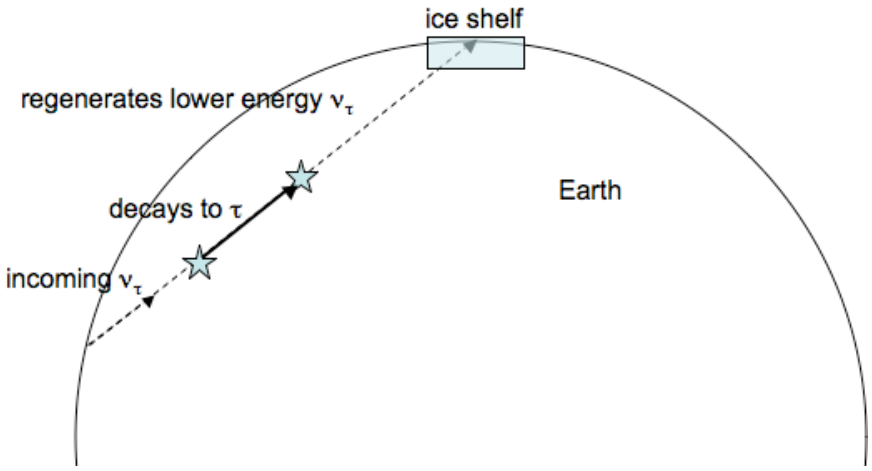

Figure 3.14: Sketch showing an incoming UHE ν_τ decaying to a τ that decays back to a lower energy ν_τ within the Earth.

photonuclear losses by the tau-lepton [116] which become important at the highest energies relevant to ARIANNA.

Double bang effect

A charged current interaction of ν_τ produces a τ that can carry most of the energy and decays over about 1 km, commensurate with the size of ARIANNA's fiducial volume. The first interaction produces a hadronic shower and so does the second tau decay that initiates a hadronic cascade through the main decay modes into pions, kaons and other mesons. Both interaction vertices initiate particles showers that be picked up by the detector array. This is obviously more probable the larger the fiducial volume and hence the larger the array. The 'double-bang' is characteristic of the tau flavor lepton and provides an avenue for flavor identification of the incoming neutrino if both interaction vertices occur within the fiducial volume of the detector. This is not yet considered in the ARIANNA analysis.

Even the case of the first decay occurring just outside the detection reach may lead to a secondary vertex within detection fiducial volume. This is more pronounced for horizontal neutrinos given the longer travel path through the ice. As mentioned in §3.4.1, we approxi-

mate the effect by choosing the higher energy shower from the tau decay taken to occur at a single vertex. Our current ν_τ calculations are therefore still on the conservative side as we are not counting those τ's being generated outside the detector volume.

Investigations of 'double-bang' effect have recently been carried out in concept studies of neutrino detection through mountain top antennas arrays overlooking the Ross Ice Shelf [117]. Future implementation of the effect into *shelfmc* can be based on that work.

3.9.2 Secondary Signals from Charged Leptons e and μ

The outgoing lepton in CC ν_e events is treated via an application of the LPM effect as described in §3.4.1. As for the outgoing muon in charged-current ν_μ, it loses most of energy through Bremsstrahlung and pair productions, with a small portion via photonuclear interaction, during the propagation within 10 km. We are yet to include the secondaries from the muon flavor neutrinos in *shelfmc*.

3.10 Effective Volume

3.10.1 How to Derive Effective Volume

Generally we use water-equivalent effective volume multiplied by the viewing solid angle $[V_{eff}\Omega]$ as the standard to evaluate the aperture of the detector. For ARIANNA, $[V_{eff}\Omega]$ is calculated using the following formula:

$$[V_{eff}\Omega] = V \cdot \frac{\rho_{ice}}{\rho_{H_2O}} \cdot 4\pi \cdot \frac{1}{n} \sum_{i=1}^{n_{success}} w_i \tag{3.31}$$

where the variables are:

- V is the fiducial volume over which neutrino interactions are generated, computed by the product of the area around a set of stations and the ice shelf thickness,
- ρ_{ice} and ρ_{H_2O} are the densities of ice and water, respectively,
- n is the number of neutrinos generated in the simulation,
- w_i is the probability that the i_{th} neutrino would have been absorbed by the Earth, given its path length through the Earth,
- $n_{success}$ is the number of events that succeed in passing the trigger requirements,

In the *shelfmc* code, set of individual neutrino flavors can be generated indepedently, but we currently assign flavors with equal probabilities. More generally, for any given ratio of $\nu_e : \nu_\mu : \nu_\tau$ of x:y:z, a random number, p, is generated between 0 and 1 and ν_e assigned if $0 < p \leq \frac{x}{x+y+z}$, ν_μ for $\frac{x}{x+y+z} < p \leq \frac{x+y}{x+y+z}$, and ν_τ for $\frac{x+y}{x+y+z} < p \leq 1$. With current simulations, we obtain $V_{eff}\Omega$, combined for all flavors, as will be discussed in §4.5.

3.10.2 Weighting the Events

Each event is assigned a weight according to the probability it interacts in the Earth before it reaches the ice. The Earth consists of a series of layers of increasing density to the core. Therefore, the general expression for the probability that a neutrino interacts on its way to the detector is

$$w = \prod_{i=0}^{n} \exp(\frac{-x_i}{L_i}) = \prod_{i=0}^{n} \exp(\frac{-x_i \rho_i}{l}) \tag{3.32}$$

where:

n is the number of layers the neutrino traverses,

x_i is the distance the neutrino travels through the i^{th} layer in meters,

ρ_i is the density of the i^{th} layer,

L_i is the interaction length of that layer in meters,

and l is the interaction length in kgm^{-2}.

For ARIANNA's energy regime, neutrinos will be typically absorbed beyond 30% below the horizon and upcoming neutrinos will encounter only the crust and potentially the upper mantle. We use an average density of 3500 kgm^{-3} for the top Earth layer; the ice density is set 917 kgm^{-3}.

3.10.3 Error on the Effective Volume $\times$ Steradians

Since $V_{eff}\Omega$ is derived from a sum of weights, the statistical error is non-trivial. Imagine we histogram all of the weights that are summed into M equally spaced bins between 0 and 1. Then the total number of events that pass our Monte-Carlo simulation is given by:

$$N_{tot} = \sum_{i=0}^{M} f_i \cdot \omega_i, \tag{3.33}$$

where f_i is the number of events fall in the i^{th} bin centered on weight ω_i. We define ϵ_i to be the error on f_i. When $f_i < 20$, we use the appropriate Poisson errors from Ref. [118], keeping track of asymmetric errors. When $f_i > 20$, $\epsilon = \sqrt{f_i}$. Then the total error on the sum of weights , $\sigma_{N_{tot}}$, is

$$\sigma_{N_{tot}} = \sqrt{\sum_{i=0}^{M} (\epsilon_i \cdot \omega_i)^2}. \tag{3.34}$$

3.11 Interaction Length

In Sect. 3.10.2, we mentioned that the interaction length directly affects the weight of each detected event. In this section we present more details on the standard way to derive the interaction length.

Interaction length, L_{int}, also called mean free path, of a particle in a medium can be derived from the cross section σ. In a simple material the number of atoms per volume is

$$n = \frac{N_A \rho}{A} \tag{3.35}$$

where:

N_A is the Avogadro's number, 6.02 $\times 10^{23}$ mol^{-1},

ρ is the density of the medium in [gcm^{-3}], and

A is the molar mass of the medium in [gmol^{-1}].

The units of n is then cm^{-3}.

The interaction length of a process can be given as

$$L_{int} = \frac{1}{n \cdot \sigma(Z, E)} \tag{3.36}$$

where $\sigma(Z, E)$ is the energy-dependent total cross section per atom of the process in units of cm^2 and L_{int} is in cm.

Combining the two above equations, we can express the interaction length as

$$L_{int} = \frac{A}{N_A \rho \cdot \sigma(Z, E)}. \tag{3.37}$$

Now, in a compound material the number of atoms per volume for the i^{th} element is

$$n_i = \frac{N_A \rho \omega_i}{A_i}, \tag{3.38}$$

where: N_A is the Avogadro's number,

ρ is the density of the medium,

ω_i is the proportion by mass of the i^{th} element,

A_i is the molar mass of the i^{th} element,

The interaction length of a process can be thus given as

$$L_{int} = \frac{1}{\sum_i [n_i \cdot \sigma(Z_i, E)]} \tag{3.39}$$

where $\sigma(Z_i, E)$ is the energy-dependent total cross section per atom of the process of the i^{th} element, and $\sum_i$ runs over all elements composing the material.

For the neutrino interaction in water, we use the neutrino-nucleon cross section, $\sigma_{\nu N}(E_\nu)$,

[ref QRGS] from which we get the total cross section per hydrogen atom $\sigma_H(E_\nu) = \sigma_{\nu N}(E_\nu)$, and that per oxygen atom $\sigma_O(E_\nu) = 16 \cdot \sigma_{\nu N}(E_\nu)$. According to Eq. 3.39, the interaction length in water, $L_{int}^{H_2O}$, becomes

$$L_{int} = \frac{1}{n_H \cdot \sigma_{\nu N}(E_\nu) + n_O \cdot 16 \cdot \sigma_{\nu N}(E_\nu)}, \tag{3.40}$$

where

$$n_H = \frac{N_A \rho_{H_2O} \cdot \frac{2}{18}}{1}, \tag{3.41}$$

and

$$n_O = \frac{N_A \rho_{H_2O} \cdot \frac{16}{18}}{16}. \tag{3.42}$$

Therefore,

$$L_{int}^{H_2O} = \frac{1}{N_A \rho_{H_2O} \sigma_{\nu N}(E_\nu)}, \tag{3.43}$$

where ρ_{H_2O} is in units of gcm^{-3}, $\sigma_{\nu N}$ is in cm^2, and $L_{int}^{H_2O}$ is in cm.

In ARIANNA's case, for the neutrino-nucleon interactions that take place in ice, we scale the interaction length as

$$L_{int}^{ice} = \frac{\rho_{H_2O}}{\rho_{ice}} \cdot L_{int}^{H_2O}. \tag{3.44}$$

Now, for interactions occuring in the less dense firn layer, we can also scale the interaction length accordingly

$$L_{int}^{firn} = \frac{\rho_{H_2O}}{\rho_{firn}} \cdot L_{int}^{H_2O}. \tag{3.45}$$

With $\rho_{ice} = 0.92$ gcm^{-3} and $\rho_{firn} = 0.55$ gcm^{-3} (on average) both being less than ρ_{H_2O} ($= 1.0$ gcm^{-3}), we see that the interaction lengths in ice and firn are longer than that in water. Since the average interaction length is used for interactions throughout the firn, the interaction rate will decrease discontinuously at the firn-ice boundary.

3.12 Expected Events Rate of a Detector

The expected number of events observed in an experiment is given by

$$N = \int \mathrm{d}N = \int \Phi(E) \cdot A(E) \cdot \mathrm{d}E \tag{3.46}$$

where

$\Phi(E)$ is the neutrino flux in the form of $\frac{dN}{\mathrm{d}E\mathrm{d}A}$, and

$A(E)$ is the exposure of the detector given in units of $area \times solid\ angle \times time$.

The $area \times solid\ angle$ equals $\frac{V_{eff}(E)}{L_{int}(E)}\Omega$, with $V_{eff}\Omega$ being the simulated effective volume $\times$ steradians of ARIANNA and L_{int} being the water-equivalent interaction length of neutrinos. The $time$ refers to the livetime, t_{live}, of the experiment. Then the differential part of Eq. 3.46, upon rewriting the exposure $A(E)$, becomes

$$dN = \Phi(E) \cdot \frac{V_{eff}(E)\Omega}{L_{int}} \cdot t_{live} \cdot \mathrm{d}E. \tag{3.47}$$

The water-equivalent interaction length of neutrinos, based on Eq. 3.36, is

$$L_{int} = \frac{m_{amu}}{\rho_{water} \cdot \sigma(E)}, \tag{3.48}$$

where:

m_{amu} is the atomic mass unit of $1.66053886 \times 10^{-27}$ kg,

ρ_{water} is density of water of 10^3 kgm^{-3},

with $\sigma(E)$ being the neutrino-nucleon cross section.

By plugging Eq. 3.48 into Eq. 3.47, we get

$$dN = \Phi(E) \cdot V_{eff}(E)\Omega \cdot \frac{\rho_{water} \cdot \sigma(E)}{m_{amu}} \cdot t_{live} \cdot \mathrm{d}E. \tag{3.49}$$

To facilitate integration of energies over several orders of magnitude, we convert $\mathrm{d}E$ to $\mathrm{dln}E$ or $\mathrm{dlog10}E$ as follows:

$$\mathrm{d}E = E \cdot \mathrm{dln}E, \tag{3.50}$$

or

$$\mathrm{d}E = E \cdot \mathrm{ln10} \cdot \mathrm{dlog}_{10}E. \tag{3.51}$$

Then Eq. 3.49 becomes

$$dN = E\Phi(E) \cdot V_{eff}(E)\Omega \cdot \frac{\rho_{water} \cdot \sigma(E)}{m_{amu}} \cdot t_{live} \cdot \mathrm{dln}E, \tag{3.52}$$

or

$$dN = E\Phi(E) \cdot V_{eff}(E)\Omega \cdot \frac{\rho_{water} \cdot \sigma(E)}{m_{amu}} \cdot t_{live} \cdot \mathrm{ln10} \cdot \mathrm{dlog}_{10}E. \tag{3.53}$$

The total number of events integrated over the energy regime of ARIANNA, N, becomes

$$N = \int E\Phi(E) \cdot V_{eff}(E)\Omega \cdot \frac{\rho_{water} \cdot \sigma(E)}{m_{amu}} \cdot t_{live} \cdot \mathrm{ln10} \cdot \mathrm{dlog}_{10}E. \tag{3.54}$$

By dividing the whole energy regime into several small logarithmic bins, we can get the number of events for each energy bin, so that the integration can be simplified to the summary of events over all bins. In this dissertation, we choose half decade logarithmic energy bin for our calculation of events rate. That means $\mathrm{dlog}_{10}E$ is set to 0.5, and the flux value of the center of the half decade energy interval is used for calculating the events for this interval.

3.13 Additional remarks

Multi-station set-up Almost no explicit mention has been made regarding simulation involving an array of stations. The first reason is that the focus of the dissertation has been an understanding of the single station capabilities and a concept study of the prototype station. Secondly, the code trivially incorporates multiple station by looping over a set of station locations. Consequently, the computing time is increased and the output variable tree becomes more involved as specific station information has to be recorded.

We note that *shelfmc 0.0* had already been designed for multi-station in square patterns with sizes a lattice size specified. This allowed studies of full scale 31×31 arrays. With the upcoming development of the Hexagonal Radio Array (§4.6), *shelfmc 1.0* now includes the option studying this configuration for a variety of separations.

Summary of Simulation We have described how the ARIANNA code generates isotropic neutrinos according to a specific flux, propagates them through the Earth and ice and simulates neutrino interactions within a specified volume. We then trace the signals generated through the ice and firn to the detector, accounting for losses along the way, and fold in the antenna response to calculate voltages generated that are compared to ambient noise for triggering. Events that successfully trigger a station through direct and/or reflected rays are assigned weights depending on the neutrino path through the Earth and/or ice, and effective aperture of the detector can be computed. Combined with a given flux, livetime of the experiment and interaction length (dependent on standard model cross-section at the relevant energies), we can obtain model-specific event rates for the detector, as will be discussed in the next chapter.

Several additions that significantly improve *shelfmc v0.0* have been documented here. A more accurate firn profile is now used. Effects due to graded index of refraction of the firn

on 'shadow' zones and polarization from ice to firn have now been introduced. The shadowing effect implemented in *shelfmc* is rather conservative with respect to signal sensitivity. The equations predict no propagation in the purely horizontal direction. However previous work at the South Pole [119] showed that antennas buried in the surface snow and pointed toward each other can transmit signals up to 100 m, presumably because the stratified layers of snow do not define a perfectly smooth function. Variation in the index of refraction could potentially create waveguides for grazing incident waves. This effect will be studied in future expeditions to the ARIANNA site.

The LPDA antenna response and ν_τ regeneration effects have been incorporated. Time-domain trigger as well as detailed inclusion of secondary effects like the double-bang for ν_τ will provide future refinement to the code.

The current version takes into account first-order corrections and is designed to be flexible to predicted fluxes considerations over a wide energy range as well as enable incorporation of new physics processes. Overall, *shelfmc (v1.0)* allows precise simulation for the ARIANNA concept study and provides a characterization of detector capabilities.

Chapter 4

Simulation Results

The ongoing development of the ARIANNA simulation, *shelfmc v1.0*, adopted and refined from previous software packages, provides the basis for understanding and evaluating the detection capabilities of the experiment. Chapter 3 extensively documents the physics behind and latest upgrades to the software.

In this chapter, we have organized several of the key findings. Our aim is to address the characteristics and profile of events and to provide quantitative understanding of the same.The results have been presented mainly for a single station; but multi-station data and comparisons are included where relevant.

Early concept studies were for 100×100 stations, with generic broadband antennas, arranged on a 30 km × 30 km square grid with a lattice separation of 300 m. Such work has been reported in Ref. [103] and [74] . Our focus here is on the single station capability and also new concept studies of the future commissioned expansion to a hexagonal array (HRA). Further, we also report on sensitivity from a full ARIANNA array in light of the recent simulation improvements.

The first set of sections (4.1 to 4.2) discusses the impact of modifications referred to in the last chapter. Sections 4.3 and 4.4 detail the event distributions and sensitivity, while Section 4.5 showcases the aperture of ARIANNA.

Throughout this Chapter, unless otherwise specified, results and plots are shown for ESS GZK input flux with all the described improvements like 'shadow zones' and ν_τ regeneration implemented. The default steering file for the simulation is given in Appendix C. We refer to this set of defined parameters as the standard configuration.

4.1 Antenna and Trigger conditions

The choice of antenna and trigger determines the sensitivity of ARIANNA to neutrino fluxes and accompanying signals. The simulation allows for the input of various antenna types through gain and angular response specifications.

Antenna choice

An investigation of the sensitivity of the station to a range of gains shows that the optimal detection rates lie in the region of the moderately high gain antennas. The log Periodic Dipole Array (LPDA) designed for use in the experiment has a nominal gain of ∼7-8 dBi in free space, and that suffers from little modification under in-ice conditions (as explained in §2.4.2). They are well suited for neutrino searches in the ARIANNA context, as we see from the dependence given in Figure 4.1. Here, we have run the simulations for various gain values G, with the angular response of an idealized antenna that follows an inverse relationship

$$G \propto \frac{1}{\theta^E_{hpbw}\theta^H_{hpbw}}$$

where θ^E_{hpbw} and θ^H_{hpbw} are the half-power beamwidths in the two principal planes. If we further assume the angular response is symmetric between the two principle planes and frequency independent over the range of interest (100-1000 MHz), then

$$\theta^E_{hpbw} \propto \sqrt{G}, \text{ and} \qquad \theta^H_{hpbw} \propto \sqrt{G}.$$

The optimum sensitivity occurs for $G = 8 - 11$ although the dependence is relatively weak. The decrease at small G is due to broad angle response implies that there is relatively more sensitivity looking horizontally into the shadow zone at the expense of sensitivity to reflected events. Conversely, the decrease at large G occurs because the viewing volume of the antenna is far smaller that the shadow zone, and the gain in sensitivity for a narrow viewing region cannot compete with losses due to reduction of solid angle.

Trigger conditions

Our single and multi-station studies use a nominal majority logic criteria of 3 out 8 antenna triggers. Studies of the varying trigger logic conditions, as in Figure 4.2, have confirmed that the similar sensitivities are obtained with a majority logic of 4/8 or above. This is due to symmetry that leads to parallel opposite antennas in the arrangement typically seeing the same signal amplitude.

One of the main changes to emulate the protostation is to modify this condition to a 2 out of 4. Figure 4.2 shows several features. There is relatively little difference in sensitivity between 3/8 and 4/8 ($\sim 10\%$) due to the fact that parallel antennas will observe about the same signal amplitude (modulated by thermal noise). In addition, triggering on half the antenna (2 of 4 vs 4 of 8) also produces a similar sensitivity, suggesting that using more than 4 antennas is to be justified by other properties, such as a reduction of thermal event rate, improvements in energy resolution or added redundancy to improve reliability. As will be

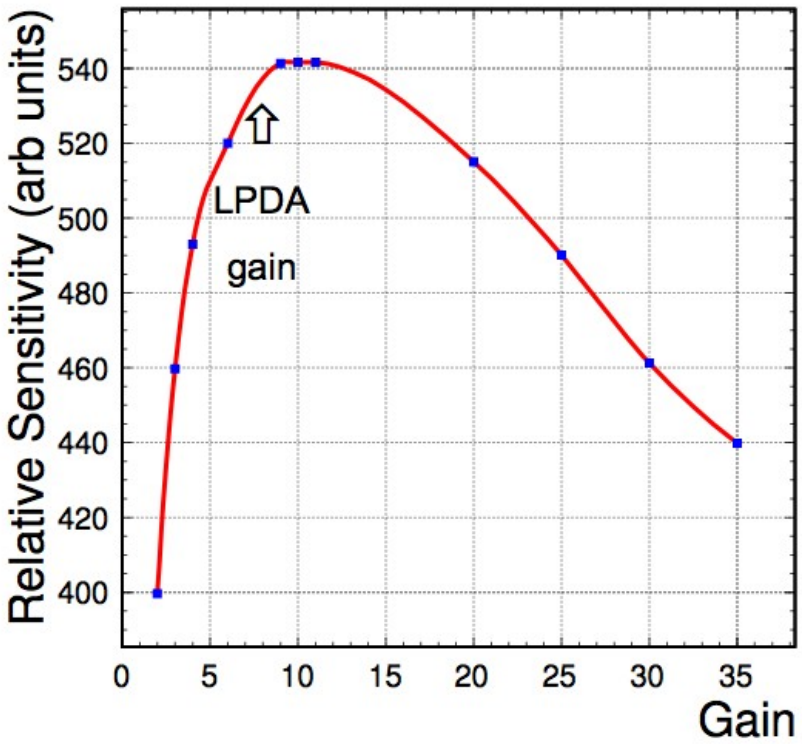

Figure 4.1: Sensitivity as a function of generic antenna gain, G(dimensionless). Dependence shows peak in the region of nominal LPDA gain indicating these types of antennas are well optimized for neutrino searches in ARIANNA.

discussed in §5.2, an octagonal antenna configuration provides better accuracy in angular resolution than a square configuration as it provides more basis for reconstruction.

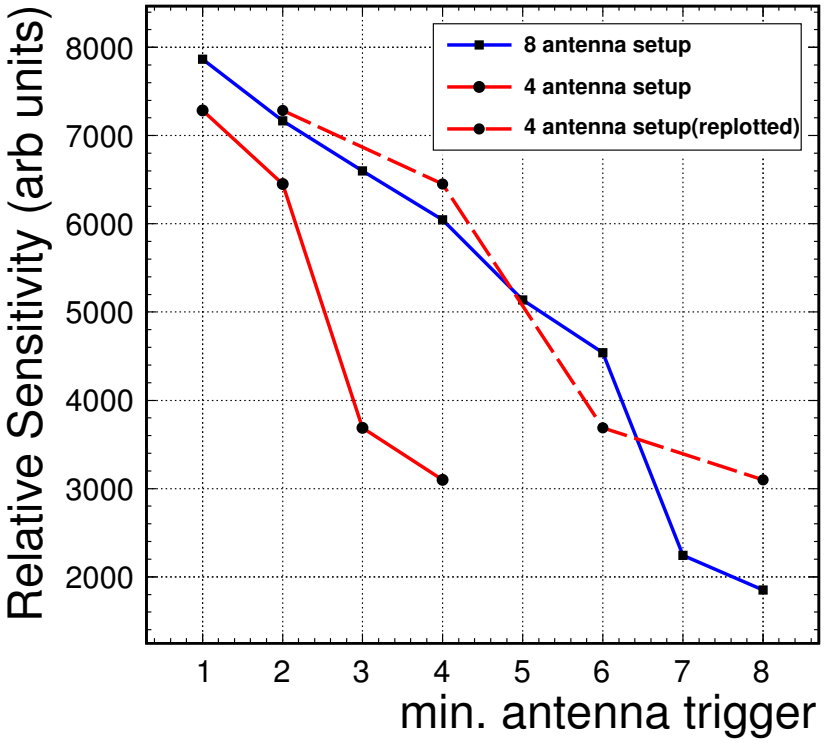

Figure 4.2: Sensitivity of ARIANNA station as a function of varying logic condition for an assumed symmetric arrangement of antennas. The dashed line (circles) is the same 4 antenna data as the solid line (circles) but stretched along the horizontal to visually compare to the 8 antenna station; for example, a 2/4 can be compared to 4/8 through this method.

4.2 'Shadowing' Effects

We see that introducing the 'shadowing effect'- a consequence of the graded refractive indices of the stratified firn- restricts some of angles of propagation to the station. This was discussed in §3.2.4; here we examine the quantitative impact of modeling the effect.

Table 4.1 shows the specific event rates that remains after implementing the shadow zones for two baseline neutrino models. The direct events, especially the firn ones, are most drastically affected by the consequence of the curved ray paths in a graded index firn.

Figure 4.3 gives the depth distribution with and without the shadowing effects and illustrates the depletion of the direct firn event rates. The bulk ice direct events get suppressed due Fresnel losses at the ice-firn boundary. The firn-originating direct signals will travel almost horizontally to the station, and would *a priori* traverse long distances. Figure 4.4 shows that without including the shadow effect, the detector would have picked up all these events (the spike for direct events in firn in the Figure) that produce incoming rays above 70°, that is near horizontal. Upon correcting for the curved paths through firn, these get largely suppressed.

From Figure 4.3, the suppression in the firn reflected events is due to the average density being lower in firn compared to ice. If we consider the solid angle acceptance at the station within a cone of half-opening angle of 46° (the critical angle from ice to firn), we would expect about $\frac{\rho_{ice}\delta\Omega}{\rho_{firn}2\pi} \approx 1.7(0.3) \approx 0.5$, which is the consistent with the drop between reflected bulk ice and reflected firn events.

Prior to implementing the shadowing effect, there was a strong increase in the event rate for events within the firn and from beneath the firn that required unrealistically large horizontal path lengths. With shadowing included, the total event rates decrease at firn depths due to the decrease in density and arrival angles at the antenna are restricted to 75° or smaller.

	Neutrino flux	
	ESS	$\mathbf{E^{-2}}$
direct in firn	2%	1%
direct in ice	22%	66%
reflected in firn	94%	99%
reflected in ice	85%	88%
all events	**57%**	**55%**

Table 4.1: Percentage of events surviving within different categories upon implementation of a shadowing effect, displayed here for the two representative neutrino fluxes. Only about 2% of the direct firn events survive when we simulate the shadow region. However, given that the overall share of the direct events is small compared to reflected events, the impact on the total event rate is less extreme but still significant as only over half the total events survive.

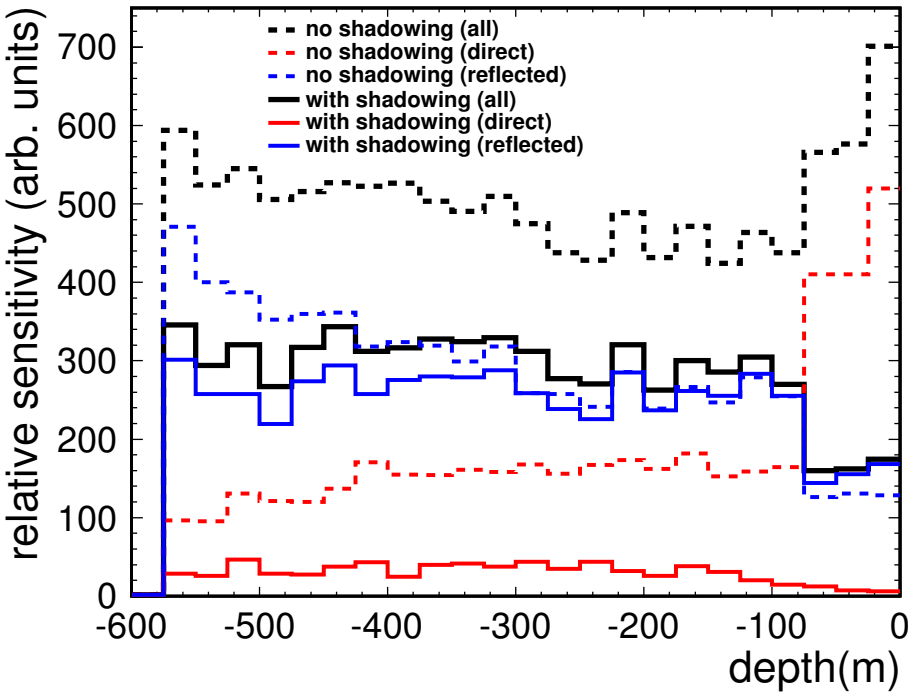

Figure 4.3: The depth distribution histograms illustrate the predominant suppression of direct firn events (depth > -75 m) under the shadowing effect. Neutrino input flux if from ESS GZK.

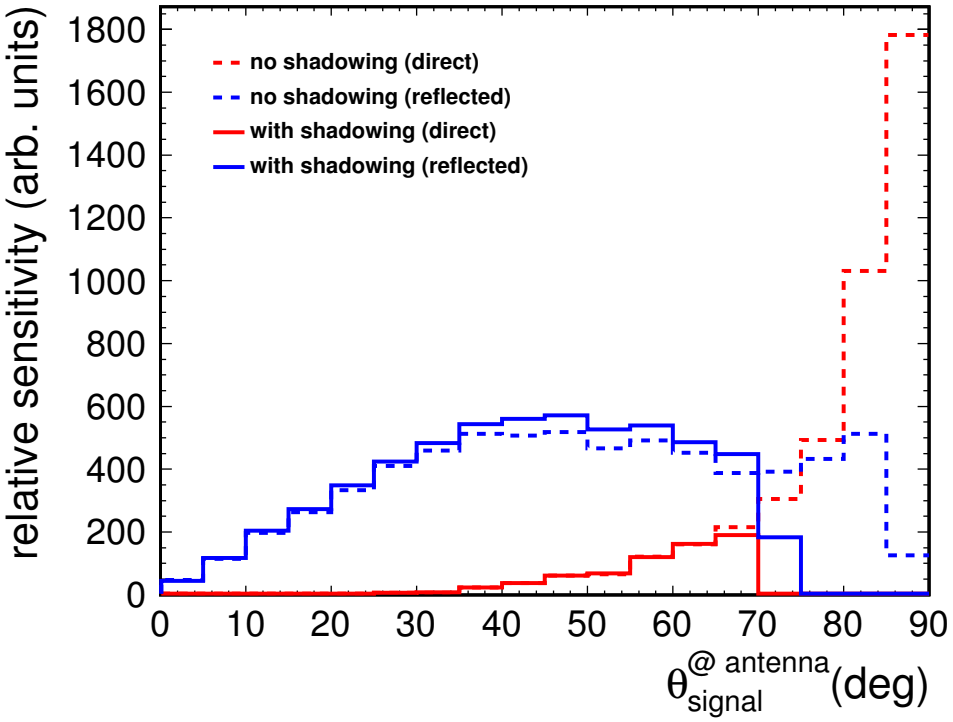

Figure 4.4: The zenith angle distribution of the incoming rays at the antenna, after they undergo refraction, shows that most of the direct rays arrive nearly horizontally and are therefore suppressed under the shadowing effect. The distribution of reflected ray angles at the station (blue lines) are not skewed to horizontal angles and hence less affected through shadow zones.

4.3 Characteristics of Event Distributions

In this section, we investigate several characteristics of the event distributions. In the first part, we compare profiles of direct to reflected events and present the vertical and horizontal distributions of interaction vertices. Angular distributions are also discussed but the angular coverage of ARIANNA is left to §4.3.2. We recall that the default configuration is a single station simulation with a ESS GZK neutrino input flux. Occasionally, we compare with data from E^{-2} input spectrum and with HRA numbers to provide a more comprehensive picture of the detection features of the experiment.

4.3.1 General Profiles

Event Types

ARIANNA capitalizes on the high-fidelity reflectivity at the bottom of the ice shelf to boost its solid angle coverage (§4.3.2). The majority of the detected events are reflected, whether for single or multi-station. Table 4.3.1 shows that reflected events dominate by over a factor of 8 for GZK spectrum; for a E^{-2} neutrino flux, they account for over 80% of events.

Note that it is possible for a small subset of events to trigger a *common station* through a combination of both direct and reflected rays (see also Figure 3.2). These usually account for $\leq 2\%$ of events and the simulation tags them as both a reflected and direct event. They constitute a negligible fraction, even in case of multi-station arrays (shown in Table 4.3.1 for HRA). We stress here that these 'combined' events are distinct from events that trigger multiple stations. In the case of the HRA, it is possible that the same event triggers one station directly and another one through a reflected ray. *The appropriate counting is done in this case*

	SINGLE		HRA	
type of events	GZK	E^{-2}	GZK	E^{-2}
direct	10%	17%	9%	16%
reflected	88%	81%	88%	81%
combined	2%	2%	3%	3%

Table 4.2: Relative (weighted) share of event types for single station and Hexagonal Radio Array using two baseline neutrino flux models. Combined events refer to those that trigger the station through both a direct and reflected ray. Errors on all values $\sim$ 1%.

type of events	upper firn	ice
direct	4%	96%
reflected	8%	92%
combined	2%	98%
all events	7%	93%

Table 4.3: Weighted fraction of events occurring in firn (center column) as opposed to bulk ice (right column) for each category of events. Errors on all values $\sim$1%.

Although the thickness of the firn is $\sim$13% of the thickness, its lower density ($\rho_{firn}^{ave} = 0.58 gcm^{-3}$) limits the firn to (13)(0.58)=7.8% of the nucleon number, which is compatible with the reflected numbers.

Depth Dependence

The depth dependence of the interaction positions gives a general flat distribution as profiled in Figure 4.5 for events originating in the lower ice layer. That drops to a smaller rate for sources in the upper firn layer. Table 4.3.1 quantifies the distribution. The attenuation dependence of the signal on distance is an exponential one (Eqn 3.19) and one may expect a similar trend on such a plot. However, this is mitigated by the fact that the ice shelf thickness is commensurate with the attenuation length.

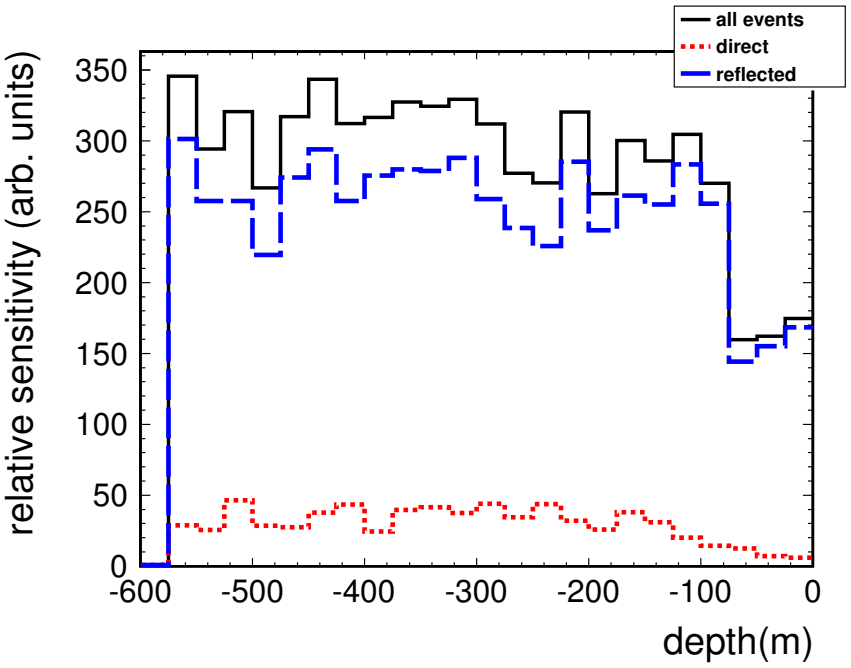

Figure 4.5: Depth distributions of interaction vertices show the firn (upper 75 m) as experiencing a drop in the event rate, whether for reflected or direct.

Horizontal Distributions

Interpretation of event vertices through top view projection maps provide useful insights. As Figure 4.6 visually indicates, direct events are on average clustered closer to the station, within about a 500 m radius. Reflected events are spread out over a larger area, extending up to 1000 m from the station. This is further confirmed by the distribution in Figure 4.8 that gives the distance traveled by the rays from the vertex to the station. Direct events are within 1000 m path distance. The reason for this is the effect of the shadow zone restricting the geometry of direct events (see also §4.2).

The handful of events that originate from beyond the 1 km horizontal extent on the projection plots are due to the largest signals, arising from a combination of high energy neutrinos and their rays to the station lying close to Cherenkov cone peak. As such, the x-y distributions of the vertices follow a general energy dependence in that events with the higher energies

can be located further away from the station. The comparison plots given in Figure 4.7 indicate that events with $E_\nu > 10^{19}$eV are spread over twice the distance than events with $E_\nu < 10^{17.5}$eV.

One important conclusion from these observations is that events will have less chance to overlap stations placed at least 1 km apart; that means that such widely spaced stations will tend to behave as independent detectors. We note that there are no events detected from 2 km away. This is expected, as seen in §3.2.1, we had determined and used a sufficiently large fiducial volume given by a square area of 4 km $\times$ 4 km $\times$ shelf-depth. The spacing between stations is a variable in *shelfmc*, and the sensitivity of the array as a function of spacing is investigated in§4.5.

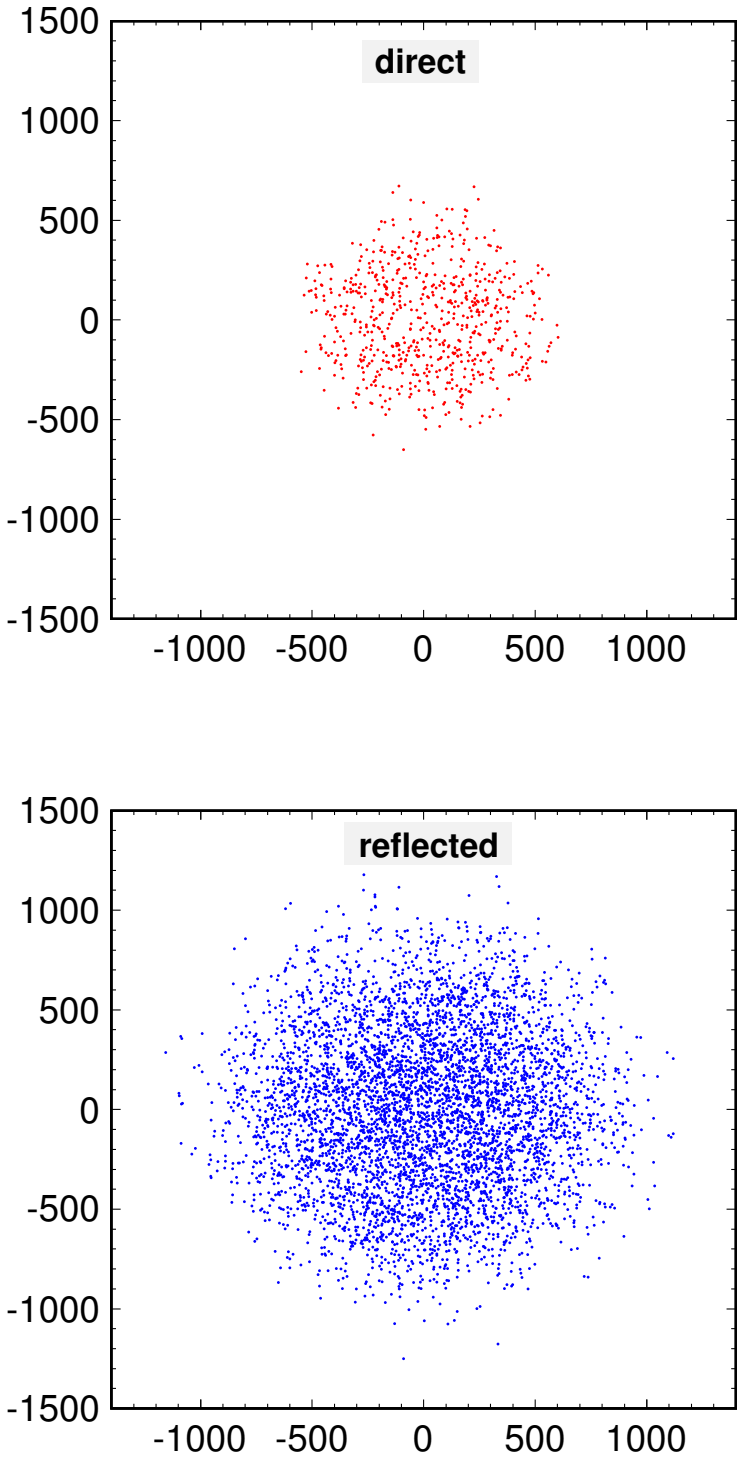

Figure 4.6: Horizontal distribution of direct (top panel) and reflected (bottom panel) event vertices around a single station located at the origin. Coordinates are in meters.

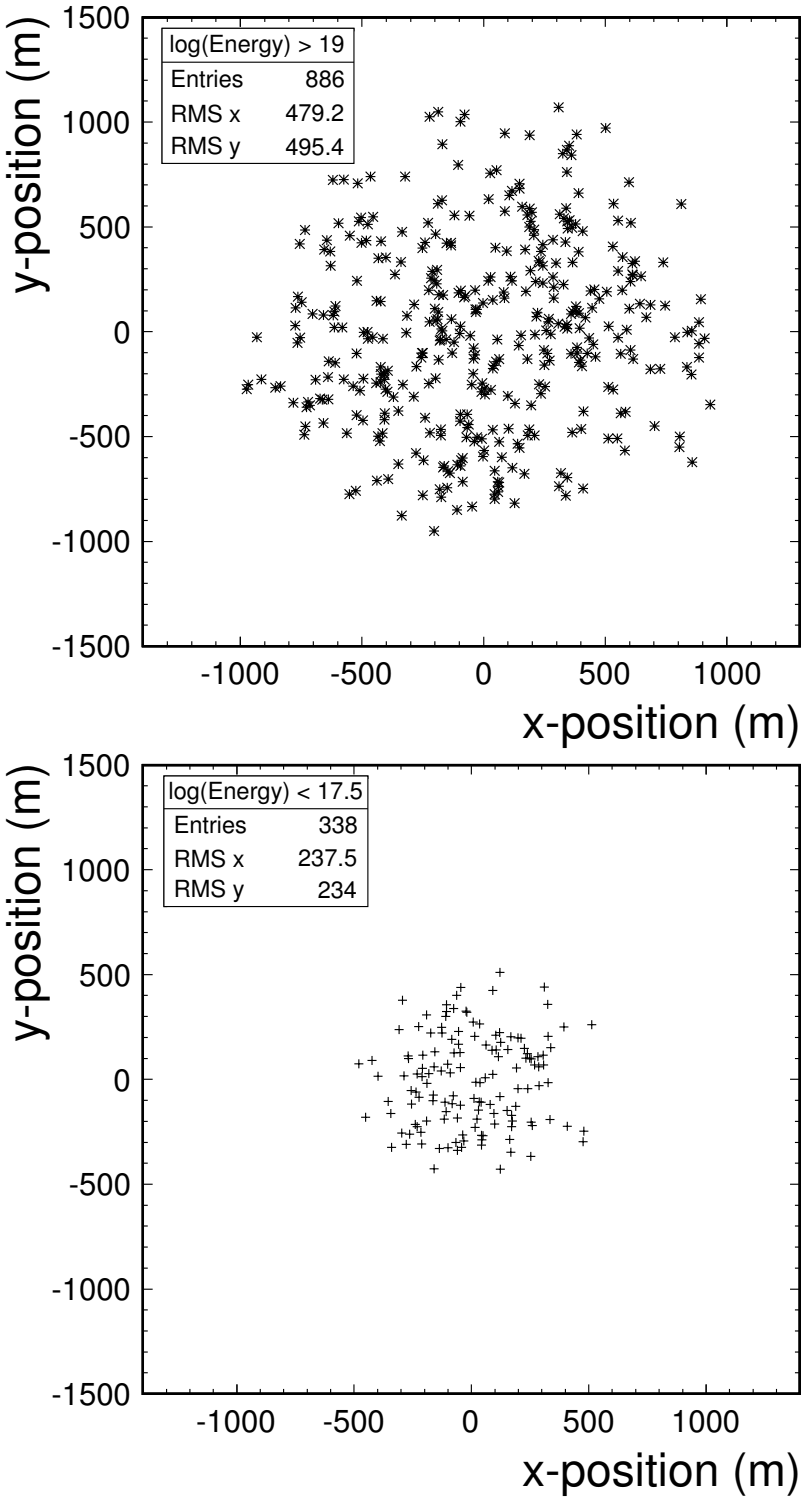

Figure 4.7: Horizontal distributions of higher energy (top panel) and lower energy (bottom panel) event vertices clearly show that the more powerful showers are located on average further away . Station is located at origin.

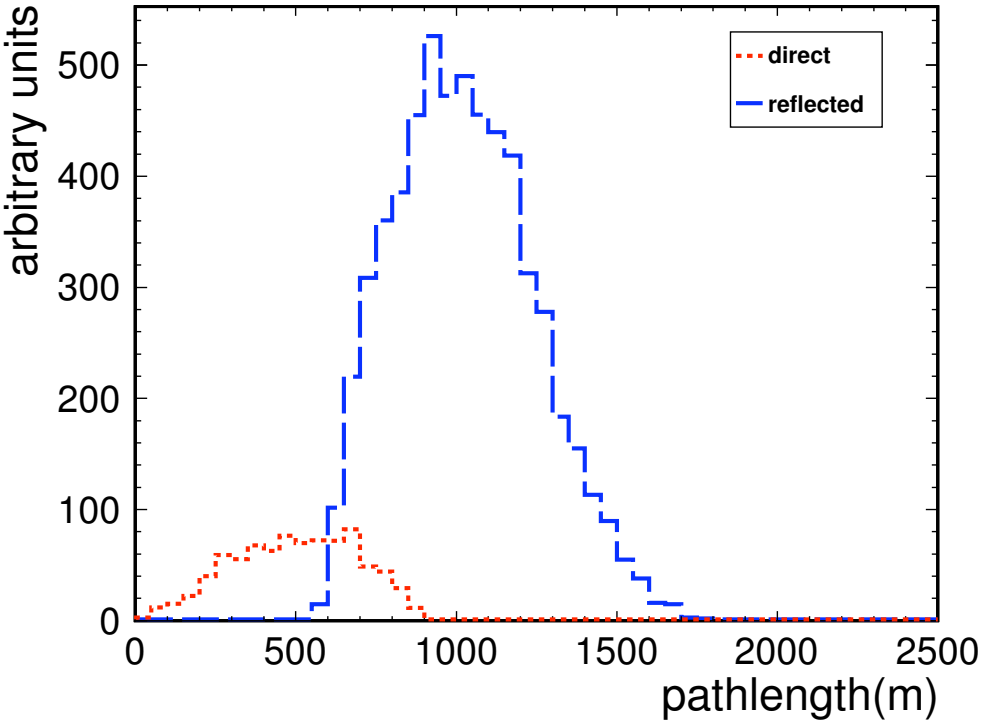

Figure 4.8: Pathlength distributions of direct and reflected events. This weighted histogram also illustrate the predominance of reflected events.

Pathlengths and Timing

Introduction Although the ray tracing in *shelfmc* provides an absolute time to each antenna of the station, it is nto a measurable quantity. Only relative times and geometrical information can be used to reconstruct the direction of the incoming signal. The method to reconstruct event directions is outlined in §5.1.

The absolute time calculation ignores the finite size of shower development at the interaction vertex and finite size of the LPDA, approximating both as points. In addition, the angular reconstruction assumes that the radio pulse propagates as a plane wave (rather than a conical sphere) in the vicinity of the station - a rather good approximation for interaction vertices at distances large compared to the dimensions of the station. In fact the approximation is excellent for all reflected events, but may be inadequate for a small subset of nearby direct events. In other words, it may be possible to determine the vertex of a nearby direct interaction due to timing differences incompatible with a plane wave. To get an idea of the maximum distance (and hence relative rates) of such events, the strategy is as follows.

Calculation details The time it takes an assumed plane wave to travel from vertex to antenna i is defined at $t^{[i]}_{planar}$. We first derive a ray from the interaction vertex to the center of the station and obtain the corresponding distance and time (t_{ST}). We recall that all the individual antennas are assumed symmetric at a given radius from this station center. We then define a plane perpendicular to that central incident ray and calculate the distance, $\Delta r^{[i]}_{AT}$, and corresponding timing offsets, $\Delta t^{[i]}_{AT}$, that each antenna i will make to that plane intersecting the station origin and perpendicular to the direction of travel of the signal. The combination

$$t^{[i]}_{planar} = t_{ST} + \Delta t^{[i]}_{AT} = t_{ST} + \Delta r^{[i]}_{AT} \cdot \frac{n}{c}$$

gives the duration for a plane wave leaving the vertex and hitting the ith antenna. n is the index of refraction of the firn and c the speed of light. We note that $\Delta t_{AT}^{[i]}$ can be a positive or negative offset, depending on whether the antenna is before the plane at the origin (center) of the station or behind.

Timing discussion The timing resolution for a given antenna, $\sigma(t_{AT}^{[i]})$ is an adjustable parameter in *shelfmc*. Previous studies of the ARIANNA prototype station indicate timing resolution of ~ 0.1ns, mostly limited by the digitization speed (2 GSa/s in HRA, 2.8 GSa/s in prototype station) of the waveform recording electronics, and thermal fluctuations (for low amplitude events). In this study, we adopt a resolution of 0.1 ns independent of amplitude[1].

The observed relative times between antennas i and j, $\Delta t_{ij} = t_{abs}^{[i]} - t_{abs}^{[j]}$, are related to time differences involving $t_{planar}^{[i]}$ and $t_{abs}^{[i]}$. Here, $t_{abs}^{[i]}$ is the absolute time from vertex to station, and $t_{planar}^{[i]}$ is the time from vertex to station if a plane wave is assumed. Two independent time differences involving three antenna measurements is sufficient to reconstruct angular direction of a plane wave and the remaining independent antenna measurements can be used to improve the fit and/or check for discrepancies from the plane wave approximation. To estimate the rate of events that produce times incompatible with the plane wave approximation, we compute the time difference between the plane wave approximation and the direct ray,

$$\Delta T_{ij} = |t_{planar}^{[i]} - t_{abs}^{[i]}| \tag{4.1}$$

for each antenna i. If

$$\Delta T_{ij} \leq \sigma_t \sim 0.1ns$$

[1] ARIANNA uses strong radio pulse which reflect from the bottom surface to establish precise time offsets due to cable and electronic delays; and a surface transmitter to provide "hearbeat" pulses to establish absolute locations which are refined from surface surveys. The periodic "heartbeat" pulses from a fixed location help to track time dependent drifts in the time-offsets.

then the plane wave approximation generates times whose precision is within the measurement uncertainty. As the results in Fig 4.9 show, only a small fraction of direct events generated at distances less than 100 m from the station produce ΔT greater than the timing resolution. Since direct events constitute only $\sim 10\%$ of the total event rate and only a small fraction of direct events have vertices sufficiently nearby, we conclude that vertex determination is not feasible with a single station.

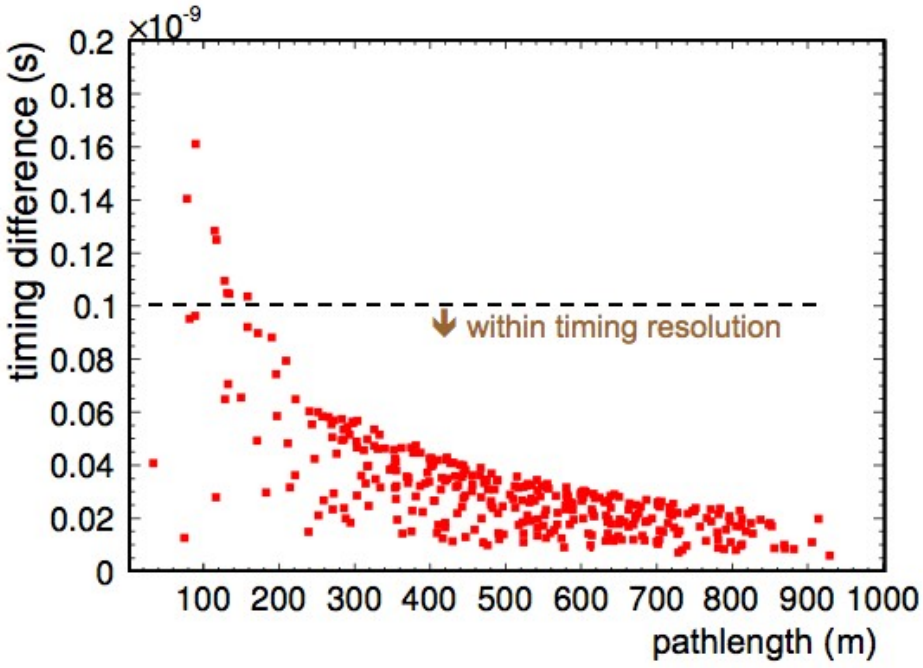

Figure 4.9: Timing discrepancy, ΔT between spherical and plane wave models against distance for direct events. With a timing resolution of 100 ps, nearby occurring direct events will be mis-reconstructed through plane wave assumption; but such events are rare.

Observation Angles

A critical factor for future implementations of time domain simulations of the Askaryan pulse is the understanding the angular distribution of the observed signals off the Cherenkov peak. We model this fall in power as a Gaussian [102] and from Figure 4.10, we see that the detected signals can lie up to 10° away from the peak. Reflected rays tend to be closer

to the maximum of the cone (average angle offset of $\sim 2.2°$). This is because these types of rays are subject to longer propagation distances and the signals that start off 'weaker' by virtue of lying further away from the Cherenkov angle do not survive the larger fractional attenuation losses on their way to the detector and fail to trigger upon arrival.

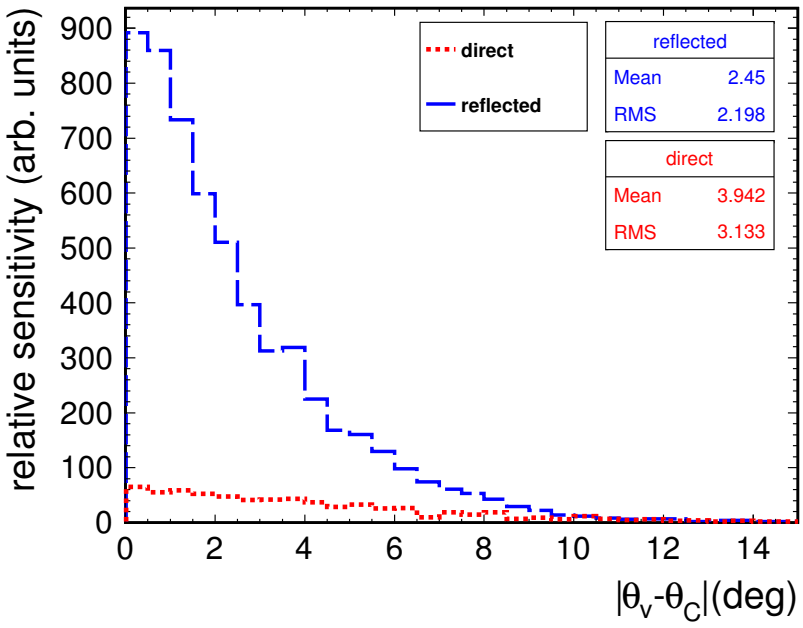

Figure 4.10: Distribution of angles off the Cherenkov maximum (i.e. the difference between observation angle θ_v and θ_c) shows that the direct rays can lie a bit further away on average from the peak of the cone. Since they travel smaller distances, they suffer less attenuation associated with propagation losses and hence those 'weaker' off-peak signals still trigger the station.

4.3.2 Angular coverage

One critical advantage of the ARIANNA detector is its large field of view by virtue of it being sensitive to reflected pulses from the ice-water bottom. The geometry of the Cherenkov cone implies that generally downgoing neutrinos are the main source of such reflected rays. The angular distribution of the incoming neutrino zenith angles gives the full picture of the sensitivity to neutrino directions.

As seen from the series of plots[2] in this subsection, the station views more than half the sky, with a solid angle coverage Ω of 3.0π. The predominance of reflected events is again obvious from Figures 4.11 and 4.13, and we now see that their neutrino directions span the whole southern celestial hemisphere with even some originating from slightly below the horizon. On the other hand, the direct events are mainly confined around the horizon in the range $60^\circ < \theta_\nu < 130^\circ$. As evidenced in Figure 4.13, the inclusion of the ν_τ regeneration effects (§3.9.1) significantly enhances their rate as they travel the Earth. In fact, as the flavor dependent distribution of Figure 4.12 shows, the tau neutrinos are more likely to be observed over all incoming neutrino angles because of the secondary effects associated with their interactions. Detection probability of electron neutrinos is boosted due to the possibility of additional electromagnetic shower from the outgoing lepton in a charged-current interaction. The electron usually carries most of the energy and hence the contribution from that type of shower is non-trivial.

Comparison the angular sensitivity with and without the shadowing effect (§3.2.4) as done in Figure 4.14 provides a further insight into its impact. The inclusion of this correction due to the firn layer suppresses direct events and restricts them to near horizontal neutrinos. The shadow correction applies more or less uniformly across all downgoing neutrinos that trigger through reflection.

[2] where $\cos\theta = 0$ is the horizon and negative values represent downgoing neutrinos

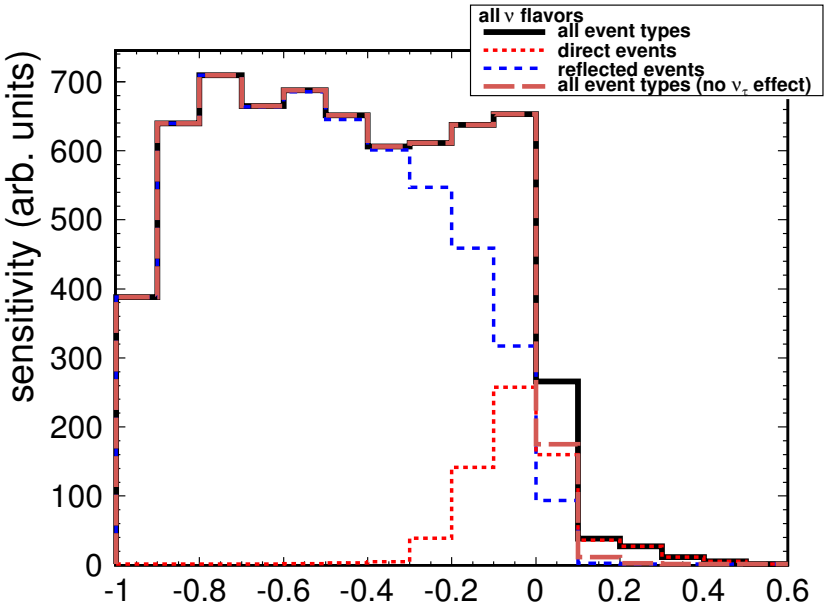

Figure 4.11: Angular sensitivity from *shelfmc 1.0*. On the horizontal axis, 0 is the horizon, and negative values are downgoing neutrinos. The solid black line shows an enhancement of events around the horizon due to ν_τ regeneration effects. The dotted black line is the same simulation without the effect.

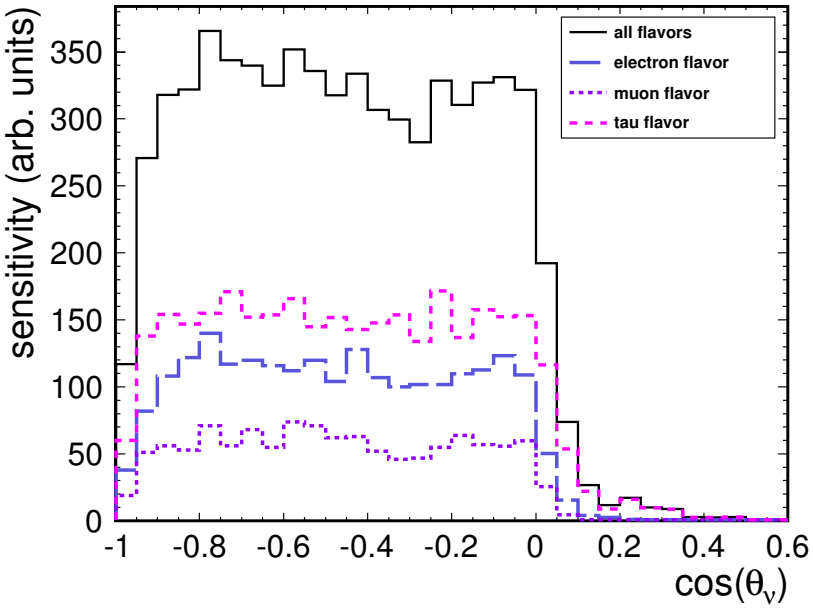

Figure 4.12: Angular coverage shown for individual flavors. Tau neutrinos are more likely to be detected due to their secondary effects.

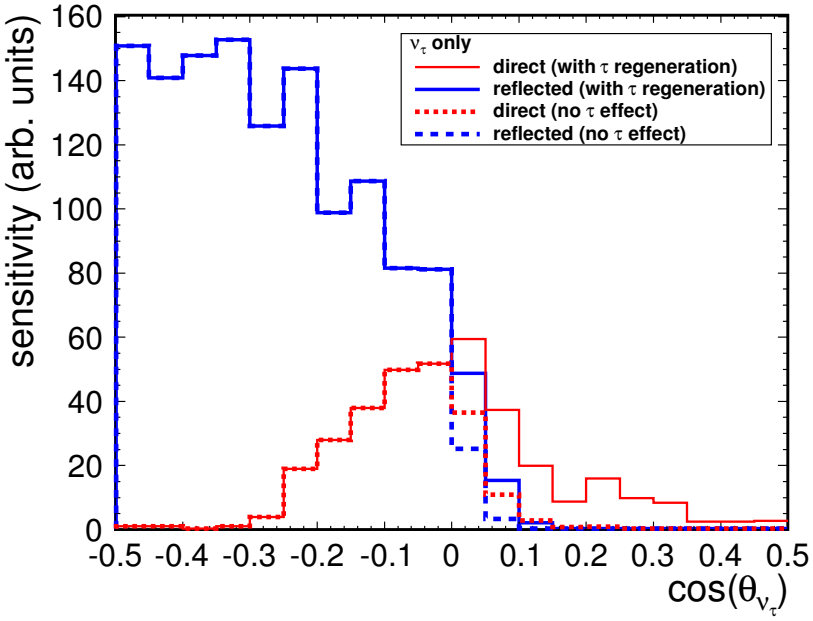

Figure 4.13: Angular distributions of tau flavor neutrinos show that the regeneration effects boosts the detection rates around the horizon for both direct and reflected events.

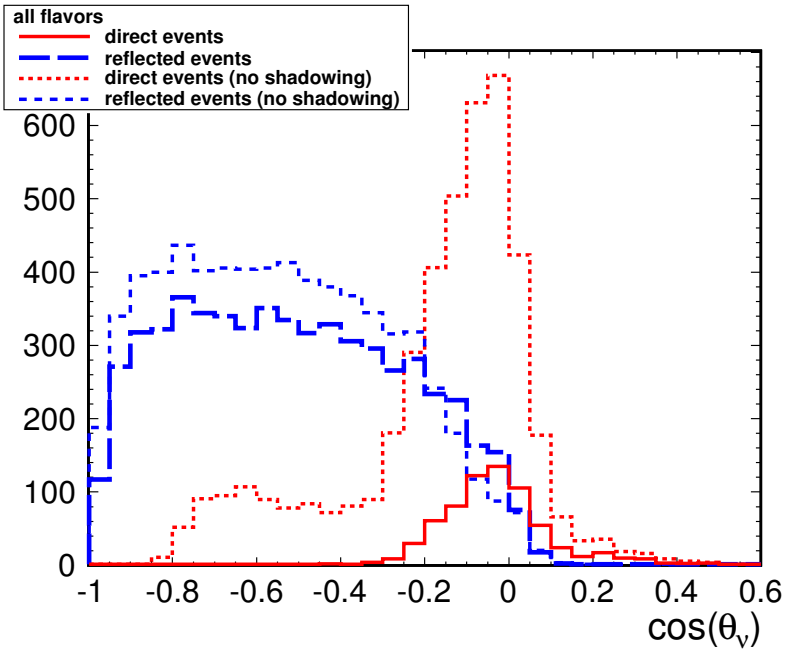

Figure 4.14: Shadowing effects changes the angular profile of direct events significantly but do not modify the reflected events neutrino distribution drastically.

4.4 Energy Dependence

As was pointed out in §1.5, ARIANNA is designed to provide sufficient sensitivity to bridge the energy gap in sensitivity by currently operating instruments between 10^{17} eV and $\sim 3 \times 10^{20}$ eV. With all the standard parameters implemented in *shelfmc 1.0*, we can obtain its simulated energy sensitivity to a neutrino flux model. For a GZK predicted spectrum (ESS standard), this is given in Figure 4.16. We see that the detector has a low energy threshold, starting at $\sim 10^{17}$ eV and spanning three decades of energy up to 10^{20} eV. The peak response lies in the "sweet spot" of GZK spectrum, where $E \cdot \Phi$, the product of energy and neutrino flux, is maximal. In many detectors, the quantity $E \cdot \Phi$ is proportional to event rate, as is the case for ARIANNA. In Figure 4.17, energy response to the E^{-2} flux prediction, and decreases smoothly with energy as expected.

ARIANNA is sensitive to all neutrino flavors as seen in both plots. The tau neutrino dominates for the following reasons: (1) selection of the larger of the two cascade energies between the hadronic shower and the τ-decay. As argued previously, this is justified by the novel physics of the double bang mechanism and (2) tau regeneration. The electron neutrino signal is generated by adding the signals from both the hadronic and electromagnetic shower. However, over most of the energy interval relevant to ARIANNA, the LPM effect restricts the width of the Cherenkov cone and thereby reducing the detection probability.

Figure 4.16 shows that the relative sensitivity between ν_e and ν_τ is about the same at energies below 10^{18}eV where the LPM effect is less pronounced. However, for $E_\nu > 10^{19}$ eV, the relative sensitivity of ν_e decreases to that of ν_μ (which produces NC interactions in *shelfmc 1.0*) because LPM effectively eliminates the additional events due to the electromagnetic cascade produced by the outgoing lepton in CC events.

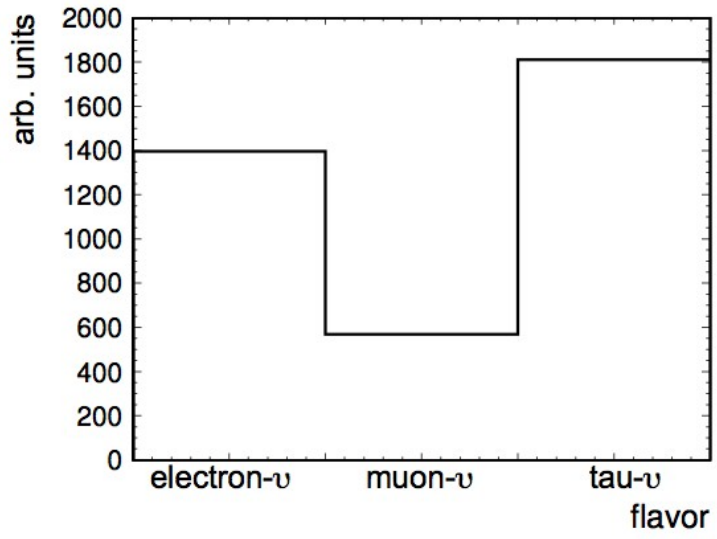

Figure 4.15: Flavor distribution histogram establishes the higher detection rate for tau neutrinos.

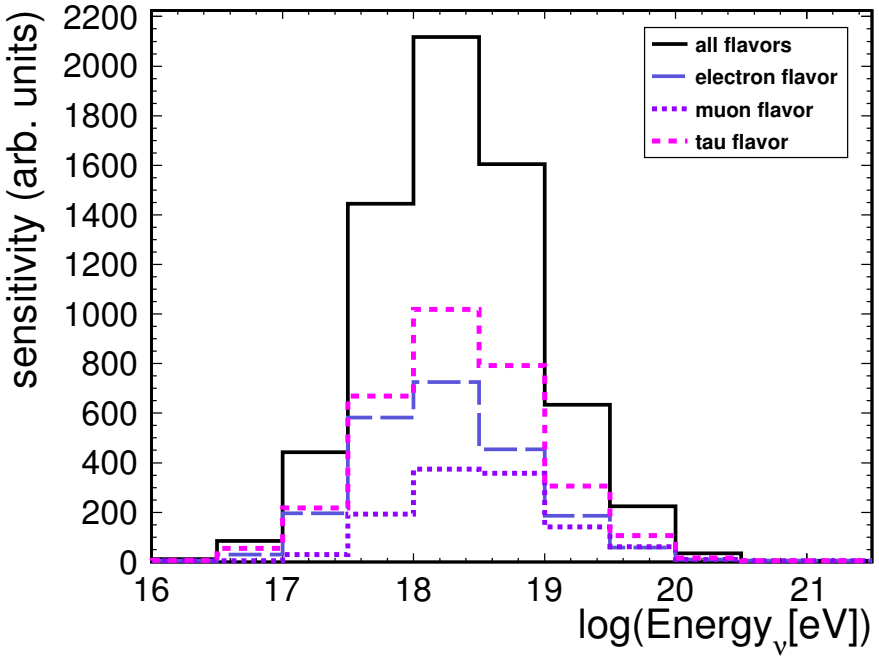

Figure 4.16: Flavor sensitivity based on ESS (std) GZK flux as simulated over a wider range of $10^{16} - 10^{21.5}$ eV. Errors are $\sim 6\%$.

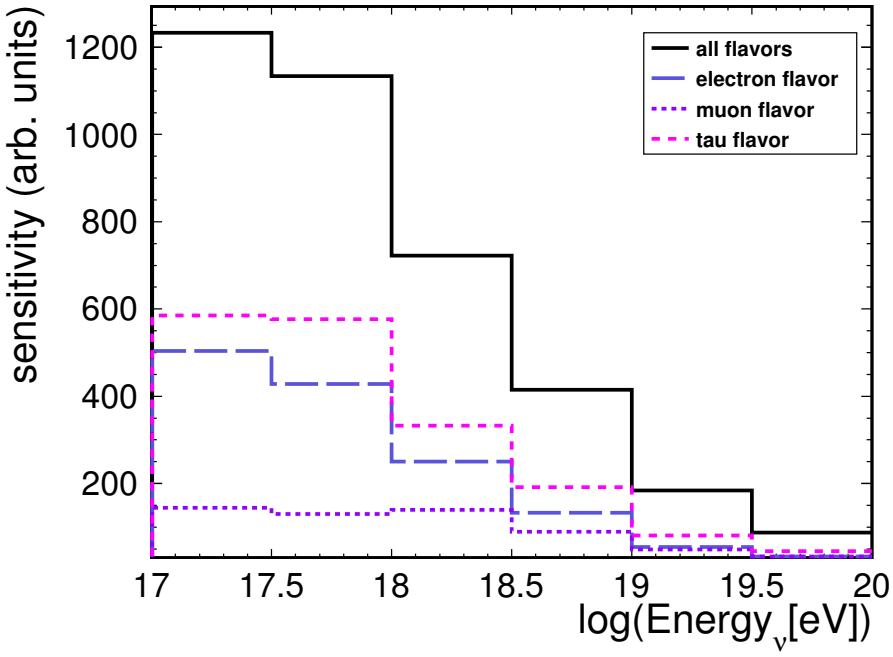

Figure 4.17: Flavor sensitivity based on E^{-2} flux over $10^{17} - 10^{20}$ eV range. Errors are $\sim 6\%$.

4.5 Aperture: $V_{eff}\Omega$ vs E_ν

Calculation of the expected number of events was described in §3.12. It depends on the experimental aperture, or $V_{eff}(E_\nu)\Omega$; where V_{eff}, the effective volume, is computed in the simulation as in §3.10.1.

With a choice of parameters, *shelfmc* predicts $V_{eff}\Omega$ for each of the three neutrino flavors (ν_e, ν_μ and ν_τ). For the standard configuration (given in Appendix C), Figure 4.18 displays the simulated single-station aperture for each flavor.

At lower energies, ν_e has the largest contribution but declines at the higher energies; there it tends to the ν_μ curve. At lower energies, ν_e can initiate both electromagnetic and hadronic showers via $\nu_e + N \rightarrow e^- + X$, and both types are detectable. However, at higher energies, the Landau-Pomeranchuk-Migdal (LPM) effect [120, 121, 122] turns on and suppresses bremsstrahlung of electrons and hence the associated electromagnetic showers For CC ν_μ interactions, muon radiation is ignored because the muon has much larger mass than electron. Considering that total radiated power by bremsstrahlung goes as m^{-4} or m^{-6} depending on the relative direction of velocity and acceleration of the charged particle, the probability for muon to create an electromagnetic shower with large fraction of the lepton energy is much smaller than electron. Therefore only the hadronic shower from ν_μ CC interaction is expected to be detected by ARIANNA. The stochastic radiation losses from high energy muons will be added in future versions of *shelfmc*.

A similar argument for the tauon from the ν_τ interaction applies, and the outgoing lepton has a negligible probability of inducing electromagnetic showers. However, we take into account the double-bang mechanism whereby two hadronic showers are generated: one at the interaction vertex and another by the τ-decay. The simulation selects the shower with the greatest energy, and, since on average 80% of the neutrino energy goes to the leptons in a charged-current interaction, there is higher chance of triggering on tau flavor events due

to the second 'bang'. In addition, *shelfmc 1.0* now includes the ν_τ regeneration effects that enhances the detectability of tau neutrinos from trajectories near the horizon. The main consequence is that the aperture for ν_τ is larger than ν_μ and ν_e for E_ν above 10^{18} eV.

Figure 4.18 provides the apertures for all flavors and the flavor-averaged aperture assuming 1:1:1 flavor mix.

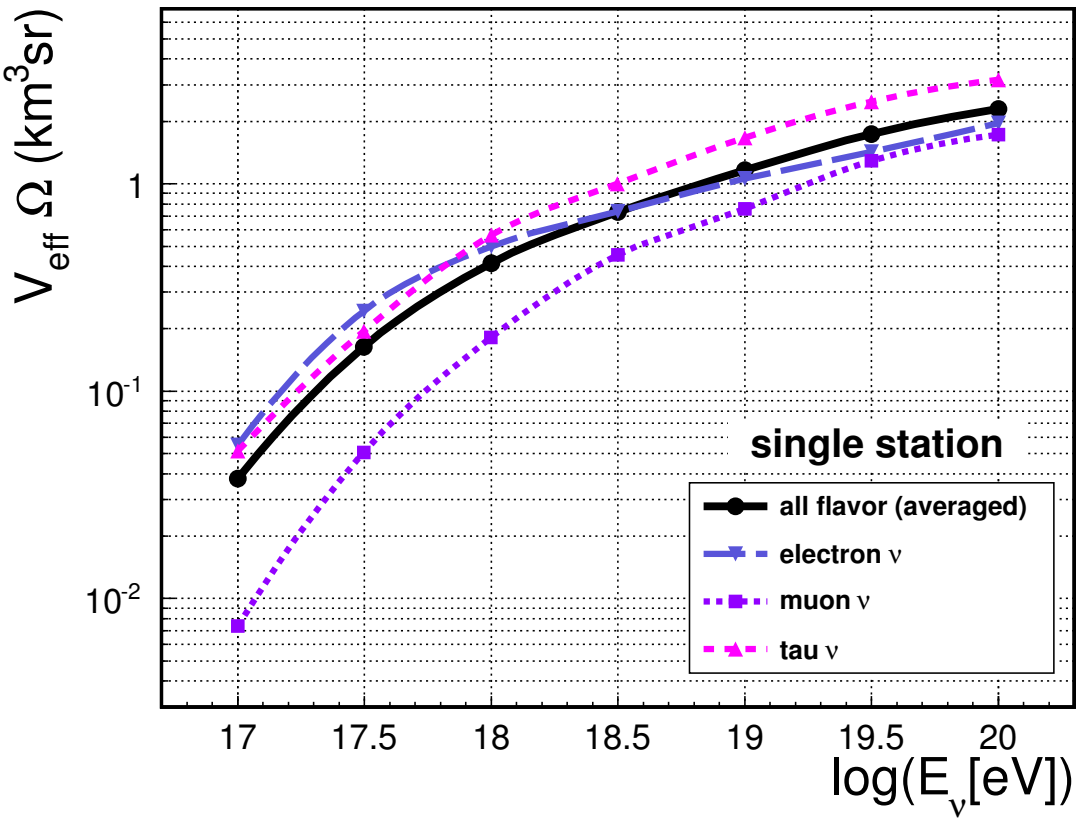

Figure 4.18: ARIANNA single station aperture shown for individual flavors and averaged over all three. Each point has $\sim 2\%$ error.

Multi-station comparison In addition to single station station studies, *shelfmc* was used to generate data for the Hexagonal Radio Array and a 31 $\times$ 31 square array with a nominal 1 km lattice separation. We compare the apertures in Figure 4.19 as a function of energy. At the highest energies, the effective volume $\times$ steradians for the 31$\times$31 array starts to saturate

because it is approaching the maximum fiducial volume $\times$ steradians of the detector at approximately 900 km$^2\cdot$ 0.575 km $\times$ 2π steradians $\approx$ 3000 km^{3}sr. For the single station, the saturation effective volume is dominated by the attenuation lengths of radio in ice.

Clearly, the aperture increases with fiducial volume of the detector and a function for scaling the aperture with the number of stations, N, can be derived. This is shown through Figure 4.20 where the ratio of $\frac{(V_{eff}\Omega)_N}{(V_{eff}\Omega)_1}$ as a function of N is given for three different lattice sizes: 1000 m, 500 m and 300 m. $(V_{eff}\Omega)_1$ is the aperture for a single station and $(V_{eff}\Omega)_N$ for N stations.

As seen in Eqn. 4.3, a linear scaling can be applied for different lattice sizes to estimate the aperture for different number of stations. For 1 km spacing, we can approximate a linear relationship as $V_{eff}\Omega \approx 0.94N$ for large N. This follows from an argument laid out earlier in §4.3 where stations $\geq$ 1 km apart behave independently, and so the aperture behaves almost linearly with N. The reason the coefficient is not exactly unity is due to the fraction of overlapping events at the highest energies (see also §4.6 next). The rate of overlapping goes up with decreasing lattice size and the slope of the linear relations gets even smaller.

$$
\begin{aligned}
(V_{eff}\Omega)_N &\approx 0.94 \cdot N \cdot (V_{eff}\Omega)_1 \quad \text{for 1000 m lattice} \\
(V_{eff}\Omega)_N &\approx 0.68 \cdot N \cdot (V_{eff}\Omega)_1 \quad \text{for 500 m lattice} \\
(V_{eff}\Omega)_N &\approx 0.45 \cdot N \cdot (V_{eff}\Omega)_1 \quad \text{for 300 m lattice}
\end{aligned}
\tag{4.2}
$$

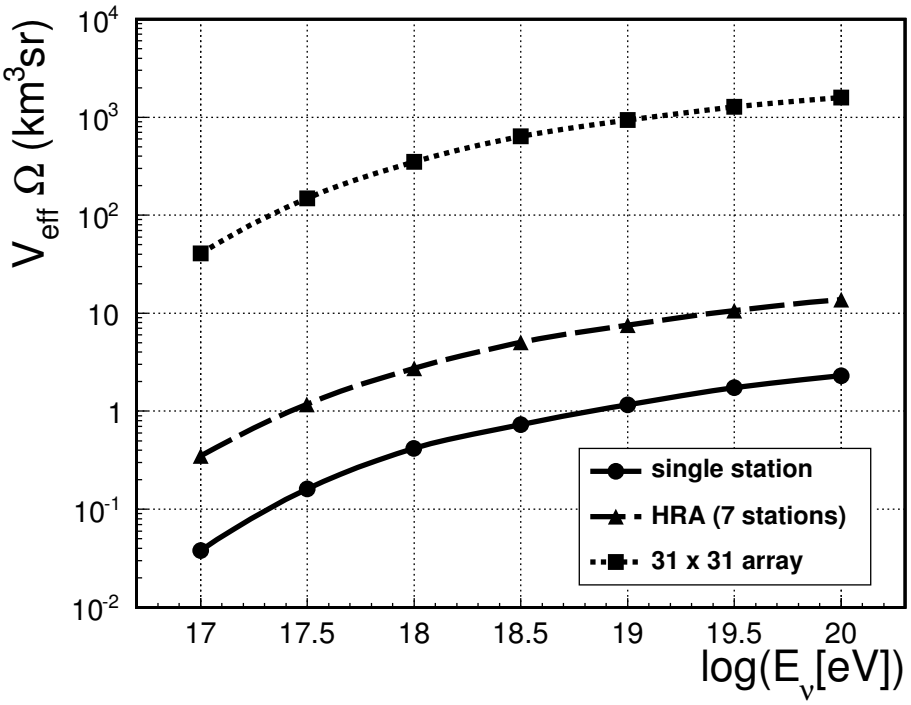

Figure 4.19: Effective volume × steradians, averaged over neutrino flavor, as a function of energy for a single station, Hexagonal Radio Array and 31 × 31 array. The lattice size for both the HRA and the array is 1 km. Each point has $\sim 2\%$ error.

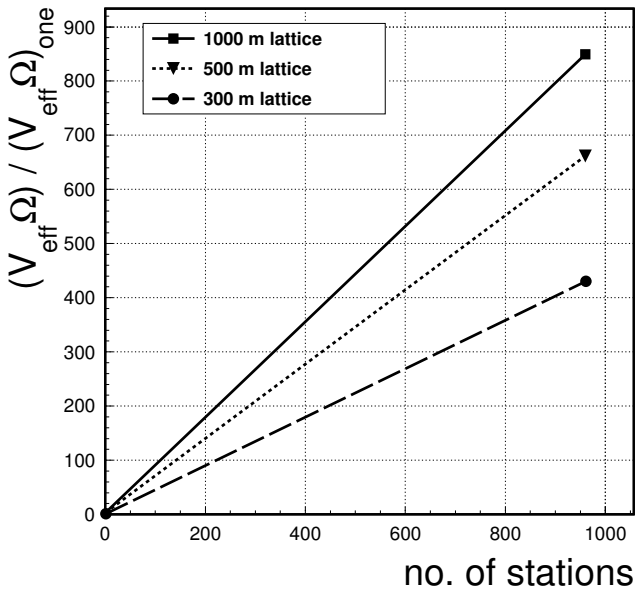

Figure 4.20: Ratio of $(V_{eff}\Omega)_N$, array aperture, to $(V_{eff}\Omega)_1$, single station aperture, as a function of number of stations for different lattice sizes and averaged over all energies. The aperture scales linearly with the number of stations (see text).

4.6 Prospects with Hexagonal Radio Array

The physics promise of a multi-station ARIANNA is very compelling given the dramatic increase in aperture achieved, as discussed in the preceding section. *shelfmc 1.0* now includes the Hexagonal Radio Array (HRA) option to complement the existing square array option. HRA consists of six stations symmetrically distributed around a central one at nominal distance of 1 km from one another. Figure 4.21 overlays the HRA over a conceptual square lattice that is envisaged to extend up to 15 km in each direction (thus covering a 900 km^2 area).

In a square lattice, a single variable defines the intra-station separation. For a hexagonal array (see Fig.4.21, it is necessary to alter the separations along the x and y directions to create the requisite station gap (for 1 km, the y-distance becomes 866 m). The fiducial volume used for a square lattice is obtained by adding a fixed 2 km^3 margin around the perimeter of the stations and multiplying the resulting area by the shelf thickness. In the hexagonal set-up, *shelfmc* uses a rectangular area that extends 2 km further from the outermost stations, which results in a fiducial volume of

$$(2 \cdot 1000 \text{ m} + 2 \cdot 2000 \text{ m}) \times (2 \cdot 866 \text{ m} + 2 \cdot 2000 \text{ m}) \times 575 \text{ m} = 19.7754 \text{ km}^3.$$

The same idea of a rectangular extension of 2 km on each side applies for various hexagonal separations.

Conceptual studies of scaling the HRA from 1 km to smaller separations yield important physics insight with regards to neutrino energy determination. Based on the earlier observation (§4.3.1) of a general energy dependence of vertex distribution, we can speculate that the most energetic events will have an enhanced probability of triggering multiple stations. Simulations show that this is the indeed the case and a multi-station trigger requires a min-

[3]This distance was motivated by a discussion presented in §3.2.1

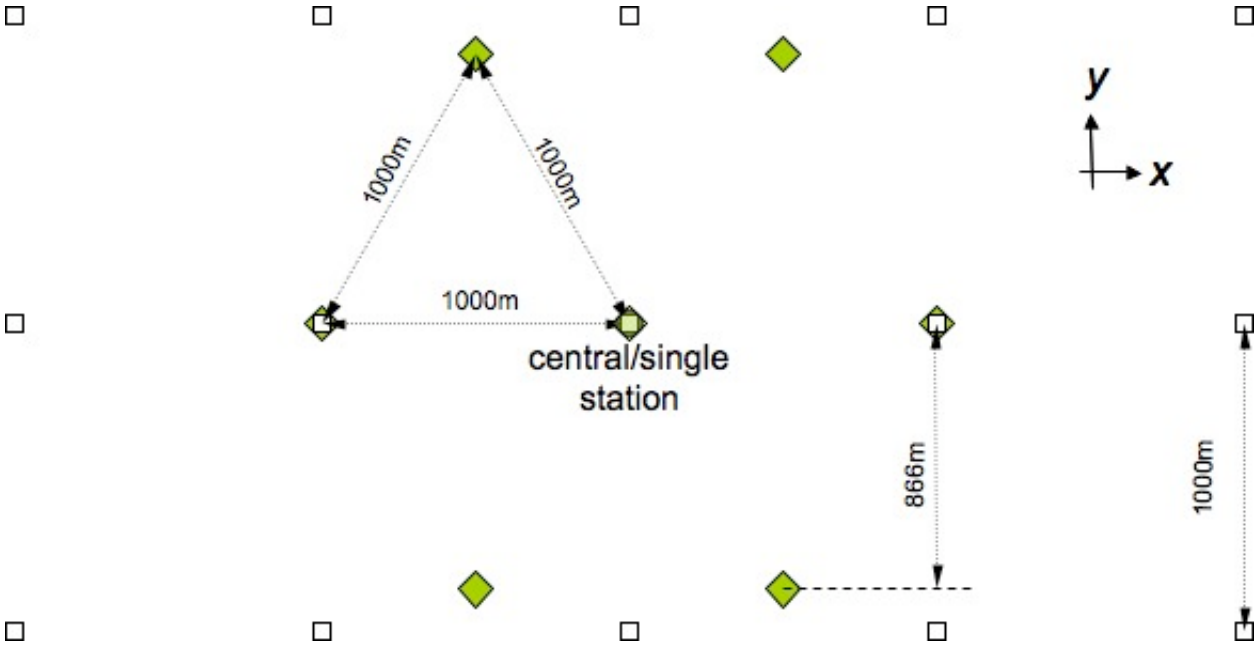

Figure 4.21: Sketch showing relative position of a central station within the Hexagonal Radio Array (green diamonds) and a square array (black squares) than can extend up to 31 × 31 in both directions. The nominal separation shown in 1 km.

imum energy threshold that is higher than a single station detection threshold and which varies with intra-station spacing. This is shown in Figure 4.22 where we have plotted two energy distributions of HRA events: one that involves the central station exclusively, and another with the central station + at least a peripheral one. We display the data for three separations at 900 m, 600 m and 300 m. For the largest spacings, simulation shows that such a multi-station trigger is more likely for a neutrino of least $\sim 10^{19.5}$ eV. Below that energy, single station trigger dominates. Decreasing the station distance to 600 m reduces that energy level to $\sim 10^{18.2}$ eV. At even smaller lattice size of 300 m, multi-station trigger means that the neutrino is likely to be above $\sim 10^{17.2}$.

Hexagonal Radio Array already possesses some intrinsic way for energy discrimination and it can be optimized to follow the physics goal of neutrino detection.

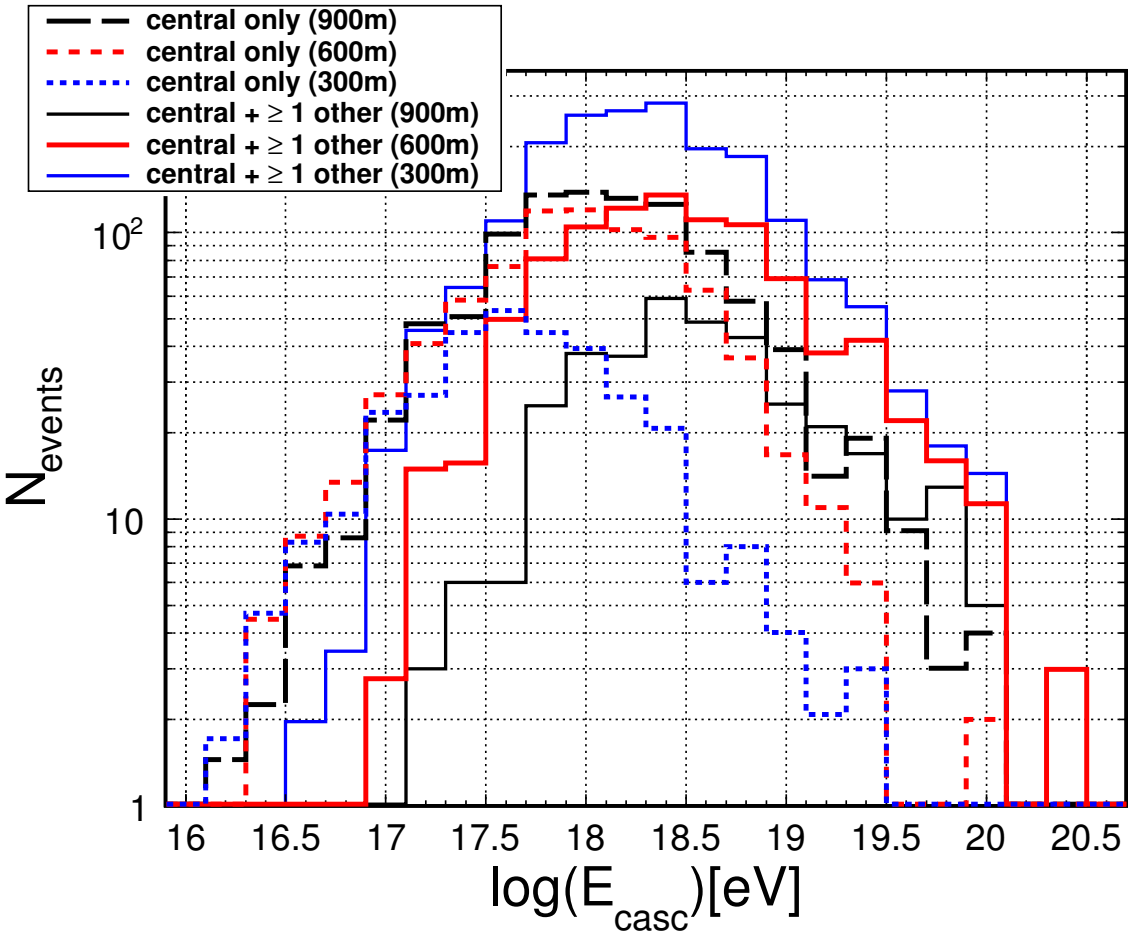

Figure 4.22: Number of events triggered against shower (or cascade) energy. Multi-station trigger that involves the central station in HRA provides a way to discriminate on neutrino energies. At smaller separations, lower energy events are already triggering multiple stations, but at larger lattice sizes, only the highest energy events have the larger probability of triggering more than 1 station.

4.7 Limits on Diffuse Neutrino Flux

In this section, armed with the previously derived $V_{eff}(E_\nu) \times \Omega$, we work through the exercise of setting limits on diffuse neutrino flux based on an assumed null result from ARIANNA.

Calculations as set out in §3.12 and [19] serve as basis for the flux limit studies presented here. We also assess the event rates from several cosmological flux models.

4.7.1 Calculation of Flux Limits

Based on the assumed case of zero detection of neutrinos, we can set limits on neutrino flux to each energy bin with the method approached in Ref [58].According to Sec. 3.12 the expected number of detected events by a detector is

$$\begin{aligned} N &= \int \Phi(E) \cdot A(E) \cdot \mathrm{d}E \\ &= \int E\Phi(E) \cdot V_{eff}(E)\Omega \cdot \frac{\rho_{water} \cdot \sigma(E)}{m_{amu}} \cdot t_{live} \cdot \ln 10 \cdot \mathrm{dlog}_{10}E, \end{aligned} \tag{4.3}$$

where $\Phi(E)$ is the differential neutrino flux (per unit time, area, solid angle and energy), and $A(E)$ is the exposure of the detector. The number of detected events is a Poisson distributed random number with expectation N. If no events observed we can set an upper limit on N:

$$N \leq N_{max} = -\log\alpha, \tag{4.4}$$

where $1-\alpha$ is the confidence level. For example, for a 90% confidence level ($\alpha = 0.1$), $N_{max} = -\log 0.1 \simeq 2.3$, then

$$N = \int \Phi(E) A(E) \mathrm{d}E \leq N_{max} \simeq 2.3. \tag{4.5}$$

If n events detected, the confidence level, α, of setting upper limit at N_{max} is

$$\alpha = Q(n+1, N_{max}), \tag{4.6}$$

where $Q(n+1, N_{max}) = (\int_{N_{max}}^{\infty} x^n e^{-x} \mathrm{d}x)/(\int_0^{\infty} x^n e^{-x} \mathrm{d}x)$ is the regularized incomplete gamma function. If $n = 1$, for instance, at a confidence level of 90% ($\alpha = 0.1$), we have $N_{max} \simeq 3.89$.

Combining Eq. 4.5 with Eq. 4.3, we get

$$\int E\Phi(E) \cdot V_{eff}(E)\Omega \cdot \frac{\rho_{water} \cdot \sigma(E)}{m_{amu}} \cdot t_{live} \cdot \ln 10 \cdot \mathrm{dlog}_{10}E \leq N_{max} \tag{4.7}$$

from which we can derive the differential flux limit

$$\Phi(E) \leq \frac{N_{max} \cdot L_{int}(E)}{E \cdot V_{eff}(E)\Omega \cdot t_{live} \cdot \ln 10 \cdot \mathrm{dlog}_{10}E} \tag{4.8}$$

with $L_{int}(E) = \frac{m_{amu}}{\rho_{water}\sigma(E)}$ representing the interaction length of neutrino and all the other variables defined as before. If an analysis efficiency, ϵ, is taken into account, the flux limits are

$$\Phi(E) \leq \frac{N_{max} \cdot L_{int}(E)}{E \cdot V_{eff}(E)\Omega \cdot t_{live} \cdot \epsilon \cdot \ln 10 \cdot \mathrm{dlog}_{10}E}. \tag{4.9}$$

Since this limit does not assume any particular model except that it is sufficiently smooth, we will define it as the model-independent limit.

In our calculations, we choose half decade as the width of each energy bin ($\mathrm{dlog}_{10}E = 0.5$), and $N_{max}/2$ as the upper limit of the observed events with energies within each energy bin. This is basically scaling the limits such that a model spectrum that matches the limit over one decade of energy would yield approximately 2.3 events.

Using a null result from ARIANNA, N_{max} is 2.3 for each energy decade at 90% C. L. We take a live time of $t_{live} = 180$ days, and we assume an ideal analysis efficiency of unity. With all the parameters plugged into Eq. 4.9, we get the upper limits on neutrino flux shown in Fig. 4.23. We present the data for three stages of ARIANNA: single station, Hexagonal Radio Array and the full 31 $\times$ 31 array. Clearly, the differential limits will get more stringent as the live times increase; ARIANNA is expected to run for at least a decade.

The 7 station Hexagonal Radio Array (HRA) will have sensitivity to cosmological neutrinos predicted from more optimistic neutrino models assuming pure proton injection. For the full 961 station ARIANNA, we estimate the total number of events expected from selected individual UHE neutrino fluxes which are representative of GZK neutrino models. Table 4.4 displays the numbers for 1 year of operation and their corresponding model rejection factors ($MRF = 2.3/N_\nu$). ARIANNA is expected to detect about 35 cosmological neutrinos per year using the ESS model with strong evolution.

Model & references	predicted N_ν	MRF
Cosmogenic (GZK):		
Engel, Seckel, Stanev 2001 (strong evolution) [20]	35	0.05
Yuksel & Kistler 2007 (GRB evolution, $\alpha = 2$) [24]	51	0.044
M. Ahlers et al. 2005 [22]	12	0.19
M. Ave et al. 2004 ($E_{max} = 10^{22}$ eV) [21]	3	0.75
Non-cosmogenic:		
AGN-MPR [38]	154	0.0015
AGN-M [44]	62	0.037

Table 4.4: Expected total events numbers N_ν from selected neutrino flux models and the model rejection factor (MRF) by ARIANNA's non-observation of neutrinos. Also included is a short, representative set of AGN and GRB models. Predictions are excluded for MRF<1.

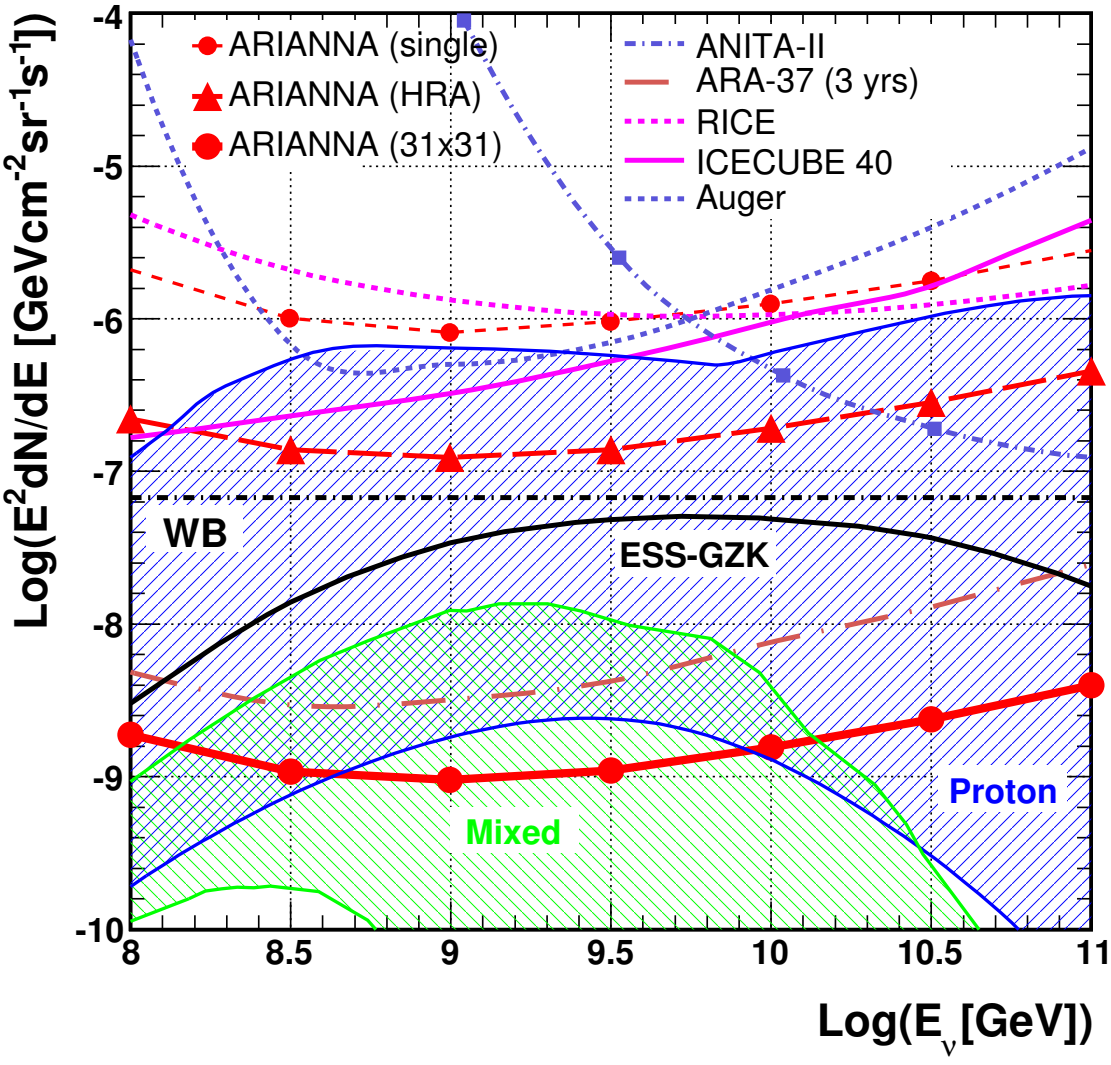

Figure 4.23: ARIANNA differential flux limits projection based on livetime of 180 days, shown for full 31×31 array (red solid line with dots), HRA (red dash with triangles). Included are limits on GZK neutrino fluxes from the Pierre Auger Observatory [47], RICE [48], ICECUBE (IC-40) [46], ANITA-2 [49] and project limits from 3 years of ARA (brown dot-dash curve)[66]. The black solid curve shows the expected flux of GZK neutrinos from Ref. [20], generally called ESS_{std}. Models shown include Ref. [17] [21] [22] [23] [24].

4.8 Discussion on Simulation Results

In this chapter, we found that the preferred gain of an antenna for ARIANNA was between 6-17. The baseline design of the ARIANNA station selects the Log Periodic Dipole Array antenna because of its low cost, high durability, light weight, broad bandwidth and gain in the appropriate range. An array of 961 stations covering a surface area of $30 \times 30\text{km}^2$ will detect $\sim$35 cosmological neutrinos per live year. Shadowing effects emphasize the role of reflected events by dramatically reducing the effective volume for direct events. In fact, the role of shadowing is likely overestimated in *shelfmc 1.0* if signals can propagate horizontally in the firn.

Tau-neutrino regeneration produces significant enhancements in the detection rate of ν_τ, especially below the horizon, for GZK like spectra. For power law spectra, there is generally a decrease of ν_τ events since the lowest energies quickly evolve downward to energies undetectable by ARIANNA. This effect must be carefully studied to disentangle ν_τ regeneration from energy dependent changes in the neutrino cross-section. It appears that the regeneration events can be subtracted as they appear from much larger zenith angles below the horizon (up to 30° as is shown in Fig.4.13).

At separations of 1 km, only the very highest energy neutrinos are likely to trigger 2 or more stations. This does not depend strongly on the threshold, but does depend on station separation. If station spacing is 300 m, then $\sim$80% of the events trigger 2 or more stations, greatly simplifying vertex reconstruction. There are discussions of several configuration modifications to enhance vertex reconstruction. For example, it is possible to trigger the HRA electronics at very high rates, corresponding to very low thresholds. Event information can be stored in a temporary buffer waiting for coincident signals from nearest neighbor stations, which transmit event times over the wireless LAN. In addition, it is possible to reconfigure the station to extend 4 of the 8 antenna to half the station separation ($\sim$500 m).

Signals would be significantly degraded after propagation over light weight coaxial cable, but limited information such as start time with 25 ns accuracy would be sufficient to reconstruct a vertex by triangulation of signals from short distance and long distance antenna.

Chapter 5

Data Analysis

Earlier, in Chapter 3, we have seen how the electric field amplitude is parametrized from a shower energy, and turned into a voltage at the antenna. In this chapter, we describe reconstruction techniques for the direction and energy of the neutrinos, based on waveform information such as maximum amplitude, relative timing between receivers, and polarization We restrict our study to single station with 8 antennas. Prior reconstruction studies have been carried out for densely packed array of stations and have reported energy and angular resolutions using vertex information from triangulation with multi-station hits[103].

We first briefly present a scheme that uses relative timing information to determine signal arrival direction. The reconstruction techniques are then discussed. Using simulated data, we also derive the energy and angular resolution of a single ARIANNA station. Throughout this chapter, unless otherwise noted, the variables used are as in Chapter 3.

5.1 Event Reconstruction

Reconstruction of the neutrino direction,$\vec{D}$, relies on knowledge of the arrival direction of the signal at the station, $\vec{P}$, to high accuracy. This is achieved by considering signal arrival time differences between different antennas and will be described in detail in future data analysis documentation of ARIANNA (for example Ref.[100]).

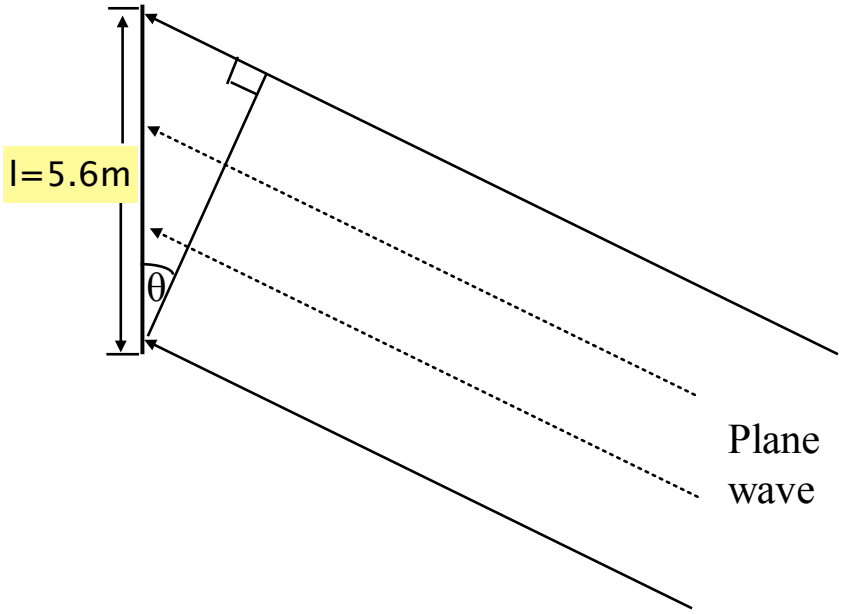

Figure 5.1: Scheme for roughly deriving the relationship between angular resolution and time resolution using two antenna positions. From Ref.[19].

Fig. 5.1 illustrates the simple scheme that is used to estimate the relationship between angular resolution and time resolution. We assume that the radio pulse propagates as a plane wave, as discussed in §4.3.1. Using the horizontal separation between two antennas l, we define a time baseline as

$$t_{baseline} = \frac{l}{c/n} = \frac{5.6\text{m} \times 1.325}{3 \times 10^8 \text{ ms}^{-1}} \approx 25 \text{ ns} \tag{5.1}$$

where we have used the nominal distance between opposite antenna as given in Fig. 3.7, and set n_{firn} as 1.325 at the surface. If the plane wave comes aligned with the pair of antennas,

the expected arrival time difference is zero. For a plane wave at an angle θ, the arrival time difference is expected to be

$$\Delta t = t_{baseline} \cdot \sin\theta = \frac{l \cdot n}{c} \sin\theta. \tag{5.2}$$

The time difference is a function of l and θ and we calculate the relationship between the angular and timing resolutions as follows:

$$\begin{aligned}
\sin\theta &= \sqrt{\frac{c\Delta t}{l \cdot n}} \\
\cos\theta\delta\theta &= \sqrt{\left(\frac{c}{l \cdot n}\delta(\Delta t)\right)^2 + \left(\frac{c\Delta t}{n} l^{-2}\delta l\right)^2} \\
\frac{\cos\theta\delta\theta}{\sin\theta} &= \sqrt{\left(\frac{\delta(\Delta t)}{\Delta t}\right)^2 + \left(\frac{\delta l}{l}\right)^2} \\
\delta\theta &= \tan\theta\sqrt{\left(\frac{\delta(\Delta t)}{\Delta t}\right)^2 + \left(\frac{\delta l}{l}\right)^2}.
\end{aligned} \tag{5.3}$$

From Eqn 5.3, we see that $\frac{\delta l}{l}$ has to be comparable or less that $\frac{\delta(\Delta t)}{(\Delta t)}$, or else this error will dominate. In practice, this gives

$$\delta l \sim \frac{l \cdot \delta(\Delta t)}{(\Delta t)} \approx (5.6\text{m})(\frac{0.14}{25}) \approx 3\text{cm}$$

or roughly $(3/\sqrt{2})$cm per location measurement. This estimate for $\delta\theta$ is valid for $\theta < 45°$. For larger angles, the angular calculation is based on the complementary angle to the one shown in Figure 5.1.

For small angles, we can approximate Eqn.5.2 to $\Delta t \approx t_{baseline} \cdot \theta$. The relationship between

angular resolution and timing resolution becomes

$$\sigma(\Delta t) = t_{baseline}\ \sigma(\theta). \tag{5.4}$$

Waveform cross-correlation information is used to get baseline delays between pairs of antennas. As seen in §4.3.1, timing resolution of 100 ps per antenna is achievable in ARIANNA, or 0.14 ns for Δt. With this value of Δt, we can expect to determine the signal arrival direction with a resolution

$$\sigma(\theta) \approx \frac{\sigma(\Delta t)}{t_{baseline}} \approx \frac{0.14ns}{25ns} \approx 0.006 \text{ rad} = 0.3^{\circ}.$$

In the neutrino angular and energy reconstruction described in the following sections, the angular uncertainty of the arrival direction of the signal at station is ignored. This assumption is justified because the dominant uncertainty contributing to the angular resolution of the neutrino direction is due to imprecise knowledge of the angular offset between the observation angle, θ_v, and the Cherenkov cone angle θ_c.

5.2 Angular Reconstruction

The direction of a neutrino $\vec{D}$ is related to the signal propagation direction (Poynting vector), $\vec{P}$ and the polarization vector, $\vec{\mathcal{E}}$, of the pulse observed at the station, as mentioned in §3.2.3,. In the previous section, §5.1, we have seen how directional information $\vec{P}$ is derived from timing considerations.

The polarization can be obtained with greatest accuracy by maximum likelihood methods incorporating all information gathered by station antennas. However, this procedure is complex and initially we seek a simpler method to estimate the direction of the polarization vector. Two methods can be investigated as follows:

(1) Adjacent antenna method, where we
- identify antenna i with maximum amplitude $V_{max}^{[i]}$,
- select neighboring adjacent antennas to $V_{max}^{[i]}$, namely $V_{max}^{[i-1]}$, $V_{max}^{[i+1]}$,
- use average amplitudes for each pair of opposite antenna in the calculation.

(2) Orthogonal antenna method, where we
- select the antenna with the maximum amplitude $V_{max}^{[i]}$ and average it with its opposite pair, and use average amplitude from the orthogonal pair to these two antennas.[1]

The two methods are distinct for a 8 antenna station but not for a 4 antenna station. As we have seen in §4.1, both 4 or 8 antenna configurations provide similar sensitivities under similar majority logic conditions. In our study here, only the octagonal antenna configuration is considered. We first describe how signal arrival information and known antenna response can be accounted for in the voltage measurements. We then show that either methods above can be used to get a polarization component but to different accuracy. With the signal vector $\vec{P}$, and the polarization vector $\vec{\mathcal{E}}$ thus know, a neutrino direction $\vec{D}$ is derived.

[1]Note that the usual trigger condition of 3-fold majority logic does not demand orthogonal antennas, but all antenna waveforms are recorded and can be saved.

5.2.1 Strategy

Equation 3.29 gives the voltage observed at an antenna i as a sum over frequency components j: $V^{[i]}=\sum_j V^{[i]}(\nu_j)\Delta\nu_j$. The summation over frequency, as discussed in §3.8.2, is an adequate approximation of the time-dependent signal amplitude in *shelfmc*.

The frequency-dependent voltage amplitude is obtained from the magnitude of the electric field at the surface, $\mathcal{E}_s$, as

$$V^{[i]}(\nu) = \mathcal{E}_s(\nu) \times \left[\frac{1}{2\sqrt{2}} h_{eff}(\nu) \cdot \mathrm{f}_{\mathcal{E}}^{[i]} \cdot \exp\left(-2\ln 2(\frac{\theta_{\mathrm{inc}}^{[i]}}{\langle\theta_{\mathrm{hpbw}}(\nu)\rangle})^2\right)\right] \tag{5.5}$$

where the frequency dependence on ν is explicity given, the superscripts $[i]$ refer to the antenna index, and the subscript s indicates to surface value of the electric field. The effective height term $h_{eff}(\nu)$ is related to antenna gain as seen in Eqn.3.28 before. The component of the signal polarization along the E-plane of the LPDA (the tines of the antenna) is given by $\mathrm{f}_{\mathcal{E}}$ $(= \vec{\mathcal{E}} \cdot \vec{n}_{E-plane}^{[i]})$. The term in the square bracket represents the overall antenna response.

The exponential term represents the angular response of the LPDA. It is shown as a single term for convenience. Explicitly, it contains terms for response along both principal planes of an ith antenna and in *shelfmc*, it is averaged as follows:

$$\sqrt{\frac{1}{2}}\left[\left(\exp[-2\ln 2(\frac{(\theta_{inc}^{E})^{[i]}}{\theta_{hpbw}^{E}(\nu)})^2]\right)^2 + \left(\exp[-2\ln 2(\frac{(\theta_{inc}^{H})^{[i]}}{\theta_{hpbw}^{H}(\nu)})^2]\right)^2\right]^{\frac{1}{2}}. \tag{5.6}$$

The half power beamwidths θ_{hpbw} is taken from Table 3.4. The angles θ_{inc}^{E} and θ_{inc}^{E} refer to the angle the incoming signal makes with respect to the E and H- antenna planes respectively (see Fig.3.8). They are defined by the signal direction and antenna orientation.

The full antenna response, through its frequency dependent beam widths (θ_{hpbw}) and the effective height $h_{eff}(\nu)$, can be measured in detail and can be accounted for. We therefore

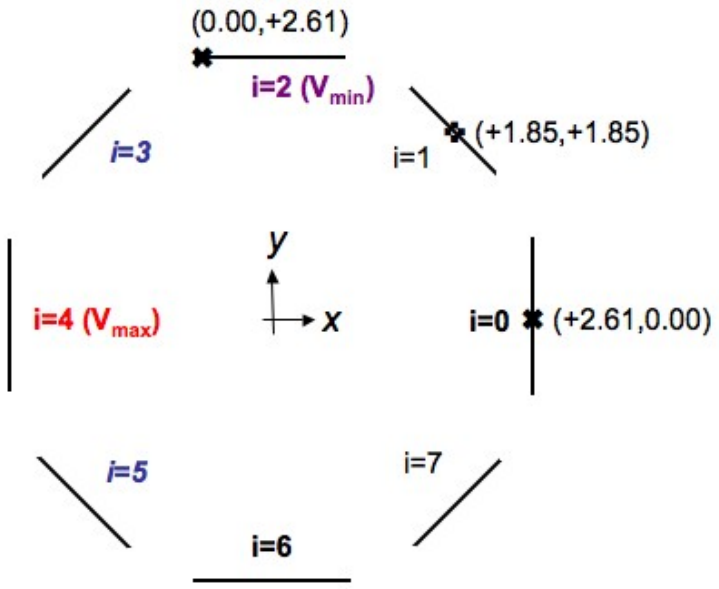

Figure 5.2: Same as Fig.3.7 but here,we show a specific example of the 4^{th} antenna registering the maximum voltage; antenna $i = 2$ records the minimum voltage. The (x, y) coordinates of the mid-point lines are given in meters.

obtain an expression that gives the fractional component of $\vec{\mathcal{E}}_s$ (the surface electric field) along the E-plane of each antenna i in the station:

$$\mathrm{f}_{\mathcal{E}}^{[\mathrm{i}]} \cdot \mathcal{E}_s(\nu) = \frac{2\sqrt{2} \cdot V^{[i]}(\nu)}{\left[h_{eff}(\nu) \cdot \exp\left(-2 \ln 2 (\frac{\theta_{inc}^{[i]}}{\langle \theta_{hpbw}(\nu) \rangle})^2\right)\right]} \tag{5.7}$$

where, we have again expressed the angular response by a single exponential term for convenience.

Given that each measured voltage is subject to noise, we improve the accuracy of $\mathrm{f}_{\mathcal{E}}^{[\mathrm{i}]} \cdot \mathcal{E}_{\mathrm{s}}(\nu)$ by averaging the $V^{[i]}(\nu)$ for opposite pairs of antenna in a symmetric arrangement. We denote the averaged values with primes, $\mathrm{f}_{\mathcal{E}}^{[\mathrm{i}]'} \cdot \mathcal{E}_{\mathrm{s}}(\nu)$. In the situation depicted in Fig. 5.2, we have, for example,

$$V^{[i=4]'}(\nu) = \frac{V^{[i=4]}(\nu) + V^{[i=0]}(\nu)}{2} \tag{5.8}$$

Applying our two methods To obtain the polarization vector

$$\vec{\mathcal{E}} = \mathcal{E}_\theta\hat{\theta} + \mathcal{E}_\phi\hat{\phi} + \mathcal{E}_r\hat{r} = \mathcal{E}_x\hat{x} + \mathcal{E}_y\hat{y} + \mathcal{E}_z\hat{z}$$

we first use the information from Eqn.5.7 to calculate the azimuth component of the polarization, $\mathcal{E}_\phi$. The two methods outlined in the beginning of this subsection are now used for that derivation. We drop the frequency dependence of $\mathcal{E}_s$ on ν from this point onwards.

In method (1), we select the adjacent antennas to $V_{max}^{[i]}$ as our basis for the calculation. With V_{max} in the ith antenna, we use antennas $[i-1]$ and $[i+1]$ for determining the azimuth angle

$$\mathcal{E}_\phi = \tan^{-1}\left[\frac{\mathrm{f}_{\mathcal{E}}^{[\mathrm{i}-1]'}\cdot\mathcal{E}_\mathrm{s}}{\mathrm{f}_{\mathcal{E}}^{[\mathrm{i}+1]'}\cdot\mathcal{E}_\mathrm{s}}\right] \tag{5.9}$$

where the primes are included to specify that we are using the opposite pair averages. $\mathcal{E}_s$ is nearly equal for neighboring antennas provided the pathlength of the signal vertex to the station is large. This is the case for the majority of events as seen in Figure 4.8. This approximation introduces a source of error.

In the specific example shown in Fig.5.2, V_{max} occurs at $i = 4$, and Eqn.5.9 becomes

$$\mathcal{E}_\phi \approx \tan^{-1}\left[\frac{\mathrm{f}_{\mathcal{E}}^{[3]'}}{\mathrm{f}_{\mathcal{E}}^{[5]'}}\right]$$

where again, averaged values are used:

$$\mathrm{f}_{\mathcal{E}}^{[3]'}\cdot\mathcal{E}_\mathrm{s} = \frac{1}{2}(\mathrm{f}_{\mathcal{E}}^{[3]}\cdot\mathcal{E}_\mathrm{s} + \mathrm{f}_{\mathcal{E}}^{[7]}\cdot\mathcal{E}_\mathrm{s}) \qquad \text{and} \qquad \mathrm{f}_{\mathcal{E}}^{[5]'}\cdot\mathcal{E}_\mathrm{s} = \frac{1}{2}(\mathrm{f}_{\mathcal{E}}^{[5]}\cdot\mathcal{E}_\mathrm{s} + \mathrm{f}_{\mathcal{E}}^{[1]}\cdot\mathcal{E}_\mathrm{s}).$$

In method (2), we select $V_{max}^{[i]}$ and average it with its opposite pair to give $V_{max}^{[i]'}$. This averaged value, together with the orthogonal antenna pair averaged values, are used as the

basis to evaluate $\mathcal{E}_\phi$. The equation is

$$\mathcal{E}_\phi = \tan^{-1}\left[\frac{\mathrm{f}_{\mathcal{E}}^{[\mathrm{i}]'} \cdot \mathcal{E}_\mathrm{s}}{\mathrm{f}_{\mathcal{E}}^{[\mathrm{i}+2]'} \cdot \mathcal{E}_\mathrm{s}}\right]. \tag{5.10}$$

In our example from Fig.5.2, V_{max} occurs at $i = 4$, and Eqn.5.10 becomes

$$\mathcal{E}_\phi = \tan^{-1}\left[\frac{\mathrm{f}_{\mathcal{E}}^{[4]'} \cdot \mathcal{E}_\mathrm{s}}{\mathrm{f}_{\mathcal{E}}^{[2]'} \cdot \mathcal{E}_\mathrm{s}}\right]$$

The explicit expressions for the averages are:

$$\mathrm{f}_{\mathcal{E}}^{[4]'} \cdot \mathcal{E}_\mathrm{s} = \frac{1}{2}(\mathrm{f}_{\mathcal{E}}^{[4]} \cdot \mathcal{E}_\mathrm{s} + \mathrm{f}_{\mathcal{E}}^{[0]} \cdot \mathcal{E}_\mathrm{s}) \qquad \text{and} \qquad \mathrm{f}_{\mathcal{E}}^{[2]'} \cdot \mathcal{E}_\mathrm{s} = \frac{1}{2}(\mathrm{f}_{\mathcal{E}}^{[2]} \cdot \mathcal{E}_\mathrm{s} + \mathrm{f}_{\mathcal{E}}^{[6]} \cdot \mathcal{E}_\mathrm{s}).$$

Two methods have been used to obtain the polarization vector. We compare their relative accuracy for determining $\mathcal{E}_\phi$ in Fig.5.3. Method (1), the adjacent antenna method, produces a better estimate and this method is used to compute polarization. Method (2) usually involves antenna pairs with the largest and smallest average amplitudes. While the largest amplitude pair produces the most accurate information, the smallest provides the least accurate value in the presence of thermal noise fluctuations. The smallest amplitude pair will dominate the uncertainty and broaden the neutrino resolution $(\delta\theta_\nu, \delta\phi_\nu)$ distributions. Method (1) typically avoids the extreme pairs and provides a more consistent estimate of polarization vector $\vec{\mathcal{E}}$.

Reconstructing $\vec{\mathcal{E}}$ So far, with Eqn.5.9, we obtain the azimuth component of the polarization vector, $\vec{\mathcal{E}}$. The zenith component $\mathcal{E}_\theta$ is required to fully define $\vec{\mathcal{E}}$. The polarization vector is perpendicular to the signal direction, $\vec{P}$, and $\vec{P}$ can be derived to within 1° from timing considerations, as seen in §5.1. We use the orthogonality between $\vec{\mathcal{E}}$ and $\vec{P}$ to obtain the remaining component of the polarization vector, and in cartesian representation, we have

$$\vec{P} \cdot \vec{\mathcal{E}} = P_x \mathcal{E}_x + P_y \mathcal{E}_y + P_z \mathcal{E}_z = 0, \tag{5.11}$$

Solving for the vertical component of polarization gives

$$\mathcal{E}_z = (P_x \mathcal{E}_x + P_y \mathcal{E}_y)/P_z. \tag{5.12}$$

With $\mathcal{E}_z$ known and with $\mathcal{E}_\theta = \cos^{-1} \mathcal{E}_z$, the polarization vector is given by

$$\vec{\mathcal{E}} = \mathcal{E}_\theta \hat{\theta} + \mathcal{E}_\phi \hat{\phi} + \mathcal{E}_r \hat{r}. \tag{5.13}$$

where we set $\mathcal{E}_r = 1$ since we are interested in the angular direction of the polarization.

Remarks A polarization vector $\vec{\mathcal{E}}$ has been derived using information from the signal direction, $\vec{P}$. We note the following at this point:

(a) The calculation is limited because it is not possible to distinguish the reconstructed polarization vector from its degenerate counterpart, which points along the opposite direction on the plane perpendicular to the signal direction. We thus obtain a pair of polarization vectors that will reconstruct to degenerate neutrino directions. This is treated is §5.2.2.

(b) The reconstructed signal and polarization, $\vec{P}$ and $\vec{\mathcal{E}}$, are the vectors at the station that is at the surface, i.e. in the firn. Most of the interactions occur in the lower bulk ice, as seen in §4.3.1. The vectors derived here would then be the refracted components of the vectors originating in ice. To reconstruct neutrino direction, $\vec{D}$, for those events, one needs to recover the original $\vec{P}$ and $\vec{\mathcal{E}}$. This procedure is described next.

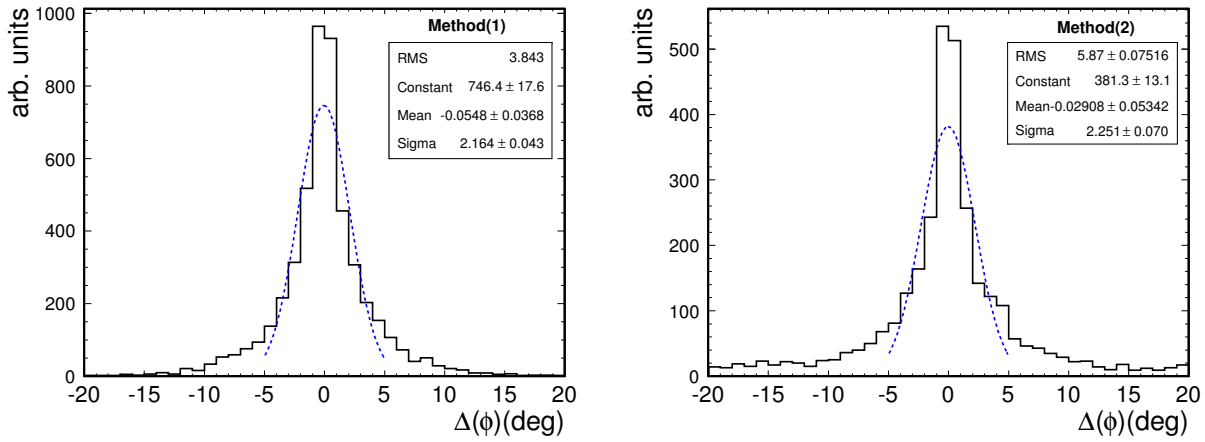

Figure 5.3: Comparison of polarization azimuth reconstruction $\mathcal{E}_\phi$ using two methods to derive polarization direction. The plots give the distribution of $\delta\mathcal{E}_\phi$, the difference between the reconstructed and the true polarization angles. Method(1), that uses neighboring antennas to the maximum voltage antenna, gives a smaller resolution and RMS value than Method(2) that involves using the maximum voltage antenna and its orthogonal pair (see text).

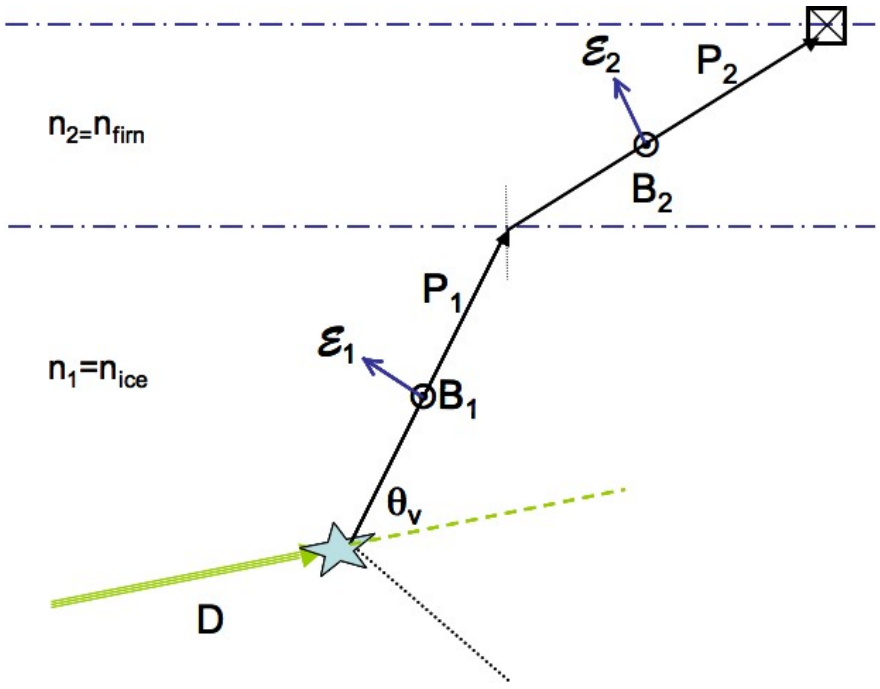

Figure 5.4: A schematic depiction (not to scale) of the signal vector from a neutrino interaction in ice, and observed at an angle θ_v, getting refracted at the firn-ice boundary. The firn layer is shown as uniform but it is modeled with a graded index of refraction. The polarization vector, $\vec{\mathcal{E}}$, is always perpendicular to the Poynting vector $\vec{P}$ and under a graded index, is rotated through the firn.

Firn transform In this dissertation, the shelf is modeled as a uniform ice layer and a top firn layer with a graded index of refraction. This was described in §3.1 For our discussion in this section, we introduce numeric labels to differentiate between the firn and ice variables, as illustrated in Fig.§5.4. The signal direction (Poynting vector) and polarization in firn becomes $\vec{P}_2$ and $\vec{\mathcal{E}}_2$ respectively. With the firn values known, we derive the $\vec{P}_1$ and $\vec{\mathcal{E}}_1$ vectors in ice as follows.

First, Snell's Law is used to transform the signal vector $\vec{P}_2$ back to the incident signal $\vec{P}_1$ in ice with a chance in the zenith angle:

$$n_1 \sin[(P_1)_\theta] = n_2 \sin[(P_2)_\theta] \tag{5.14}$$

$$(P_1)_\theta = \sin^{-1}\left[\frac{n_2}{n_1}\sin[(P_2)_\theta]\right] \tag{5.15}$$

In §3.2.3, it was shown that under a graded firn layer, a 3-D rotation (as in Eqn.3.5) is applied to obtain the polarization vector $\vec{\mathcal{E}}_2$ from the incident $\vec{\mathcal{E}}_1$ in ice. This procedure is simply reversed here to get from $\vec{\mathcal{E}}_2$ to $\vec{\mathcal{E}}_1$. Equation 3.5 becomes

$$\vec{\mathcal{E}}_1 = \mathbb{R}_\Omega^{-1}\vec{\mathcal{E}}_2 \tag{5.16}$$

where the angle of rotation Ω is given by $|(P_1)_\theta - (P_2)_\theta|$, and the rotation axis is a unit vector perpendicular to both $\vec{P}_1$ and $\vec{P}_2$ and lies along the horizontal plane of the ice-firn boundary. Note that change in angle, Ω, due to refraction only depend on the initial and final indices of refraction.

With $\vec{P}_1$ and $\vec{\mathcal{E}}_1$ now known, we can recover the neutrino direction $\vec{D}$ by using the pair of

relationships given in Eqn.3.3 and reproduced here:

$$\vec{B_1} = \vec{P_1} \times \vec{\mathcal{E}_1} \tag{5.17}$$

$$\vec{B_1} = \vec{D} \times \vec{P_1} \tag{5.18}$$

and applying a third relation

$$\vec{D} \cdot \vec{P_1} = |\vec{D}||\vec{P_1}| \cos\theta_c. \tag{5.19}$$

By Eqn.5.19, it is implicitly assumed here that the signal lies along the Cherenkov angle, $\theta_c = \cos^{-1}(n_1^{-1})$. However, the signal lies along an observation angle θ_v that can be up to 15° off from θ_c (see Fig.4.10). This is a major source of error introduced in the reconstruction procedure and is addressed later in §5.2.3.

Equations 5.17-5.19 give a set of four linear equations than can be used to solve for the components of $\vec{D}$. In the following set of equations, we temporarily drop the numerical subscript that refers to the ice to recognize the fact that they apply to either medium. First, from Eqn. 5.17, $\vec{B}$ is evaluated:

$$\begin{aligned}
0 + P_z D_y - P_y D_z &= B_x = P_y \mathcal{E}_z - P_z \mathcal{E}_y \\
-P_z D_x + 0 + P_x D_z &= B_y = P_z \mathcal{E}_x - P_x \mathcal{E}_z \\
P_y D_x - P_x D_y + 0 &= B_z = P_x \mathcal{E}_y - P_y \mathcal{E}_x \\
P_x D_x + P_y D_y + P_z D_z &= \cos\theta_c.
\end{aligned} \tag{5.20}$$

These equations are coded in to the reconstruction software to obtain D_x, D_y and D_z, the

components of the neutrino direction vector $\vec{D}$.

For interaction vertices in the firn, our procedure incorrectly reconstructs the neutrino direction because we assume the events originate in ice. For firn events, $\vec{P}_2$, $\vec{\mathcal{E}}_2$ and θ_c corresponding to the appropriate index of refraction at the depth of interaction should be used, instead of the values transformed to ice. This is an additional source of error in our estimate; but given that firn events account for less that 7% of the total (see §4.3.1), it is not expected to be significant.

5.2.2 Choosing Reconstructed Angles

As discussed in "note (a)" of §5.2.1 above, two degenerate polarization vectors are obtained for a given signal direction. That translates into two derived neutrino directions. For each neutrino azimuth, D_θ ($=\theta_\nu$), a weight corresponding to the incoming direction is evaluated (see also §3.10.2). This parameter provides a way to favor one calculated neutrino azimuth over the other.

Fig. 5.5 gives the distribution of the reconstructed neutrino zenith angles from a typical simulated data set. The unweighted distribution has zenith angles down to 60°; but upon applying a weight, neutrino directions below 75° are suppressed. This favors the higher weighted reconstructed neutrino direction and improve the choice between the degenerate neutrino directions for those fraction of incoming neutrino directions just below the horizon.

For the remaining angles, there is an ambiguity in selecting the correct neutrino direction. For point source searches, each event will consist of a true direction and a false one at a random location on the sky. A source will be identified by the usual methods of requiring several neutrinos from the same direction. The probability of the random (false) directions co-aligning is very small. For a diffuse flux spectrum, the ambiguity cannot be resolved.

However, in the energy reconstruction discussed in the next section (§5.3), the reconstructed energy of the neutrino does not depend on the incoming neutrino direction (only on the well measured direction of the signal at the station). Therefore, the energy distribution derived from a diffuse neutrino search will not be biased by the degeneracy.

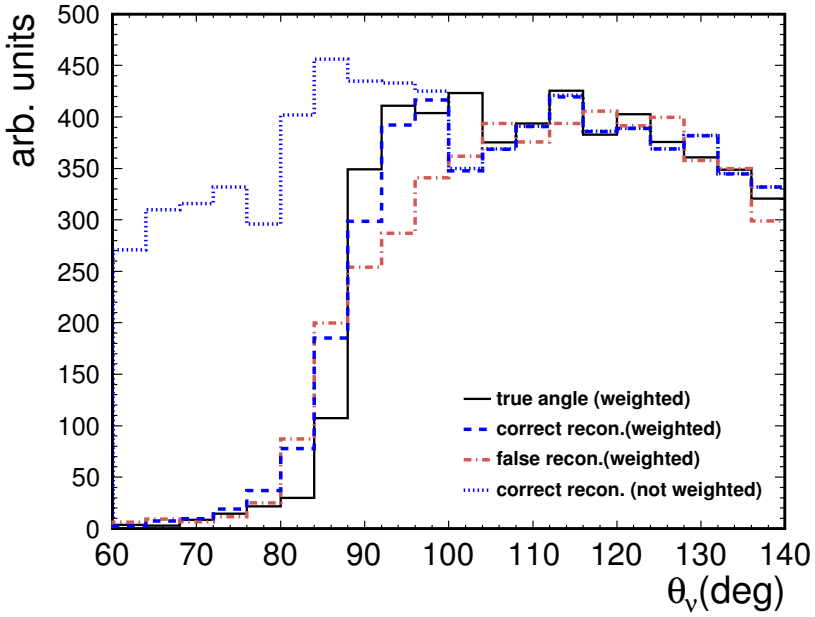

Figure 5.5: Distribution of neutrino zenith angles around the horizon ($60° < \theta_\nu < 140°$). Solid black line represents true neutrino direction. Dashed blue line is the 'correct' reconstructed angle matching the true neutrino angle; dashed-dot brown line is the degenerate 'false' reconstructed angle. Dotted blue line is the un-weighted distribution of the 'correct' reconstructed neutrino direction matching the true direction.

5.2.3 Angular Resolution

The previous subsections (§5.2.1-5.2.2) describe the reconstruction technique and discuss the degeneracy inherent in the polarization vector determination. Using a simulated data set, we apply the reconstruction procedure to obtain a pair of degenerate angles for the neutrino direction. Since the true neutrino angle is known, we get the 'correct' angle between the degenerate pair by simply choosing the one lying closest to the true neutrino angle. The dif-

ferences between the reconstructed and true zenith and azimuth angles are histrogrammed. The width of that distribution quantifies the 'intrinsic' angular resolution of a single ARIANNA station. In Figures 5.6 and 5.7, the distributions are shown for a sample data set from a GZK ESS spectrum. Applying a gaussian fit, we obtain

$$\sigma_{\theta_\nu} = 2.868^\circ \pm 0.046^\circ \qquad \sigma_{\phi_\nu} = 2.528^\circ \pm 0.038^\circ. \tag{5.21}$$

As mentioned earlier, due to lack of vertex determination, we are unable to identify the small subset of firn events and have treated them as originating from the ice. This wrongly corrects for the signal and polarization. By removing the firn events from the distributions, the resolutions are slightly improved to $\sigma_{\theta_\nu} = 2.838^\circ \pm 0.045^\circ$ and $\sigma_{\phi_\nu} = 2.491^\circ \pm 0.038^\circ$. The impact of firn events mis-reconstruction is less than 3% on the resolution and is small as expected.

The major source of error is the assumption that the signal lies on the Cherenkov angle, but the observation angles, θ_v can up to 15 degrees off the peak ($|\theta_v - \theta_c| \lesssim 15^\circ$) as shown in Fig.4.10. Our analysis shows, for example, that determining $|\theta_v - \theta_c|$ to within 1.5° yields $\sigma_{\theta_\nu} = 1.32^\circ \pm 0.03^\circ$ and $\sigma_{\phi_\nu} = 1.96^\circ \pm 0.06^\circ$, that is, a 54% and 22% improvement respectively. Therefore, the angular resolution of a single ARIANNA station hinges on the angular resolution of$|\theta_v - \theta_c|$. Recent and ongoing simulation work as in Ref.[111] has shed light on the time domain profile of the pulse at various angles off the Cherenkov angle (see also Fig.3.12). The waveform pattern recognition chip that is being implemented in ARIANNA can provide a way to constrain $|\theta_v - \theta_c|$ based on recorded pulse shapes.

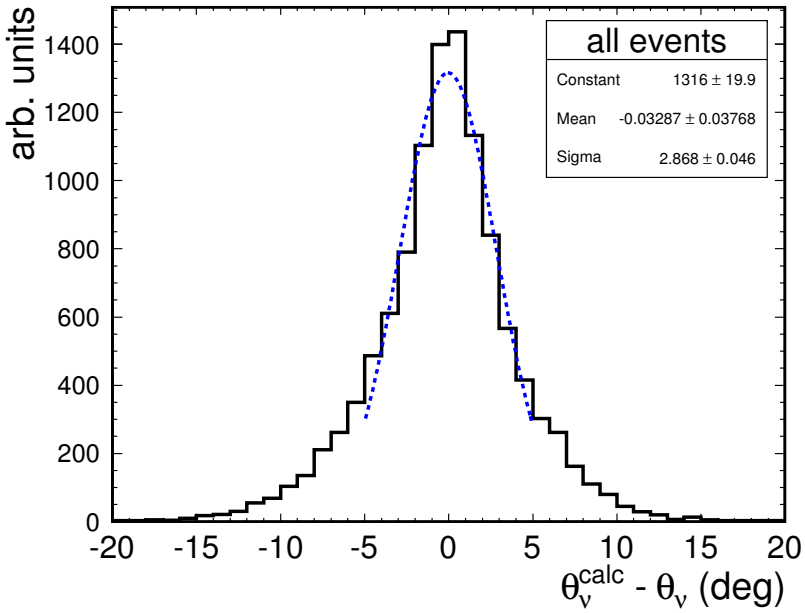

Figure 5.6: Distribution of reconstructed neutrino zenith (θ_ν^{calc}) with true neutrino zenith(θ_ν) gives intrinsic resolution of neutrino zenith for a single ARIANNA station, with $\sigma_{\theta_\nu} = 2.9°$ for all events. No distinction is made on event types (reflected or direct) or flavor. Plot includes mis-reconstructed firn events.

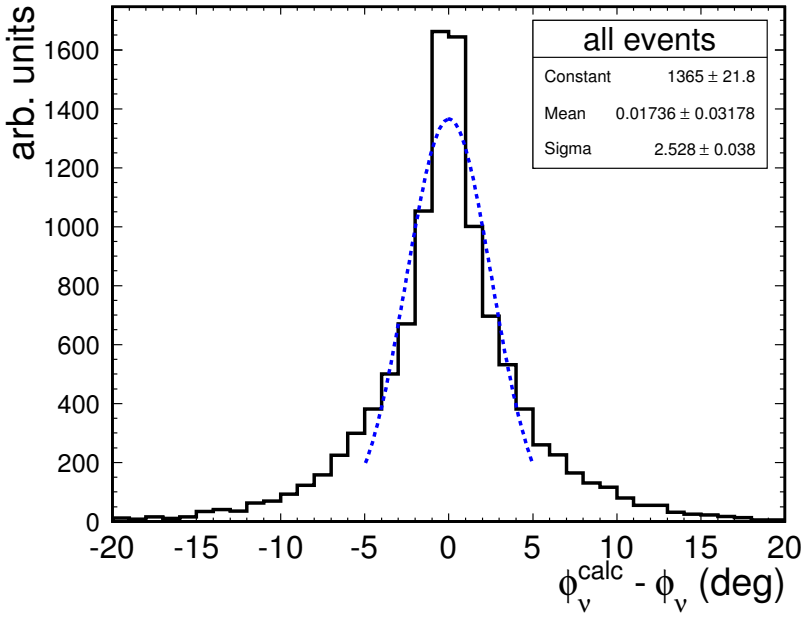

Figure 5.7: Distribution of reconstructed neutrino azimuth (ϕ_ν^{calc}) with true neutrino zenith(ϕ_ν) gives intrinsic resolution of neutrino azimuth for a single ARIANNA station with $\sigma_{\phi_\nu} = 2.5°$ for all events. No distinction is made on event types (reflected or direct) or flavor. Plot includes mis-reconstructed firn events.

5.3 Energy Reconstruction

Section 5.2 has described an approach that uses voltage measured by the antennas and incoming signal direction derived from relative timing delays to obtain the direction of the polarization vector ($\vec{\mathcal{E}}_s/|\vec{\mathcal{E}}_s|$) and neutrino direction.

In this section, we describe a method to determine the neutrino energy, E_ν, from the measured quantities by an ARIANNA station. The calculation reveals that the uncertainty in the energy is dominated by the uncertainty in the deviation angle $\delta\theta_v = |\theta_v - \theta_c|$, and the uncertainty in the fraction of the neutrino energy carried by the cascade at the interaction vertex. In fact, the uncertainty in $\delta\theta_v$ alone leads to an energy resolution of $\sigma(\frac{E_\nu^{meas.}}{E_\nu}) \sim 5$, due to the gaussian-like dependence of energy on $\delta\theta_v$.

Given the strong dependence of a few terms in the expression for E_ν, the uncertainty of several of the linear terms is ignored in the calculation, such as the errors in the signal amplitude at each antenna which are measured to 20%. We also ignore systematic errors associated with reflectivity, R, which is related to E_ν by a power-law because the measured uncertainty is a modest $\pm 25\%$. Other parameters associated with the losses due to propagation, such as the distance and depth of the interaction vertex are unknowable without vertex reconstruction and therefore estimated by statistical averages obtained from *shelfmc* simulation. Lastly, errors associated with the direction of the radio pulse at the station, and consequent errors associated with the antenna corrections are ignored. This too is justified because the expected errors are small ($\sigma(P_\theta) \sim 0.3^\circ$) and antenna corrections can be measured in the lab with great precision.

The calculation begins with the time dependent waveforms that are measured by each antenna, which are converted into frequency domain components by the usual FFT techniques $V_{obs}^{[i]}(\nu_j)$, where j indexes the frequency bin and $[i]$ indexes the antenna. The frequency dependent electric field at the surface, $\mathcal{E}_s^{[i]}$, is obtained from Equation 5.23 which used the

antenna response of the LPDA to convert electric field to electric potential. If errors are ignored in the voltage components and in the direction of the radio pulse $\vec{P}$, then θ^E_{inc}, θ^H_{inc} and $f_{\mathcal{E}}$ are exactly calculable and taken from simulation. Under these circumstances, $\mathcal{E}_s^{[i]}$ will be identical for all antenna. For concreteness, the antenna with the maximum voltage amplitude in the time domain is selected. The calculation can be improved if errors are included, but that remains a future activity.

Once the $\mathcal{E}(\nu)$ are determined (at the surface), Eqn. 5.24 corrects for attenuation and geometric ($\frac{1}{r}$) losses and reflective losses to obtain the electric field components at 1 m from the vertex, $(\mathcal{E}(\nu))_{\theta_v}$.

The electric field components $(\mathcal{E}_0(\nu))_{\theta_v}$ are corrected for the deviation angle, $\delta\theta_v(=|\theta_v-\theta_c|)$, which is the relative angle from the Cherenkov angle that is viewed by the antenna, and other geometric quantities associated with the Cherenkov cone produced by the Askaryan effect. This correction is computed in Equation 5.27. In this correction, the frequency dependent cone width, $\Delta\theta(\nu)$ assumes that the signal is produced by hadronic cascade and is given by Eqn.3.14. Obviously, this will not be correct for low energy ν_e events, where there is a significant contribution by the EM cascade induced by the outgoing lepton, but in the absence of flavor identification, there is no way to insert a more accurate expression. We note that substituting the electromagnetic expression for $\Delta\theta(\nu)$ (Equation 3.12), has little effect on the energy resolution. In addition, as previously discussed, relatively few events are detected at low energies. At most energies, LPM effects suppress the contribution from the electromagnetic cascade, so most of the observed signal is due to the hadronic cascade.

Next, Equation 5.28 sums the components $(\mathcal{E}_0(\nu))_{\theta_c}$ to determine the shower energy, E_{sh}, using standard parametrizations as in Ref.[102].

Finally, E_ν is determined from the effective inelasticity $\langle y_{eff} \rangle$ over energy and flavor, so

$$E_\nu = E_{sh}/\langle y_{eff} \rangle \tag{5.22}$$

where *shelfmc* was used to determine $\langle y_{eff} \rangle = 0.8$ (see also Figure 5.9).

5.3.1 Reconstruction details

To determine neutrino energy E_ν, the electric field amplitude at the antenna receiver $\mathcal{E}_s$ is required. The neutrino energy is calculated by sequence of steps:
(1) use waveform information to compute the amplitude of the Askaryan signal at a reference distance of 1 m from the vertex, which is related to shower energy by standard parameterization as in Eqn.3.10 from Ref.[102], and
(2) the neutrino energy is computed by dividing the shower energy by the effective inelasticity, averaged over neutrino energy and neutrino flavor. The inelasticity y is related to the fraction of neutrino energy that goes into the hadronic shower as was described in §3.4.1, but it also includes the energy from the lepton in the cases of ν_e and ν_τ. For the specific case of ν_e, where the electromagnetic component includes strong effects due to LPM, the inelasticity is the average of the cascade energy contributing to the signal at the particular observation angle θ_v. The reason for this is that the LPM effect significantly narrows the width of the Cherenkov cone, so the relative contributions from the hadronic and electromagnetic showers are strongly altered.

In the following paragraphs, we expand on the procedure outlined above, and discuss the averaging and approximations used. To derive $\mathcal{E}_s$, we start with the measured voltage amplitude at the LPDA antenna i, which is the sum over the frequency components j: $V^{[i]}=\sum_j V_{obs}(\nu_j)\Delta\nu_j$ (see Equation 3.29). We have seen before (§3.8.2) that a summation of the frequency components, as currently implemented in our simulation, is an adequate

representation of the time-domain voltage amplitude measured by the ARIANNA station.

Step (1a) : Antenna response As seen in Chapter 3, the signal observed by LPDA antenna of the station is the electric field signal convolved with the antenna response in the time domain. In frequency domain, the voltage dependence at the ith antenna becomes

$$V_{obs}^{[i]}(\nu) = \mathcal{E}_s(\nu) \cdot \left[\frac{1}{2\sqrt{2}} h_{eff}(\nu) \cdot \mathrm{f}_{\mathcal{E}}^{[i]} \cdot \exp\left(-2\ln 2 (\frac{\theta_{\mathrm{inc}}^{[i]}}{\theta_{\mathrm{hpbw}}(\nu)})^2\right) \right] \tag{5.23}$$

where $h_{eff}(\nu)$ is the effective height related to the antenna gain and $\mathrm{f}_{\mathcal{E}}$ is the component of the polarization vector along the E-plane of the ith antenna. The single exponential term represents the averaged angular responses along the two LPDA principal planes, as already shown in Eqn.5.6).

The antenna response (the term indicated by the square bracket in Eqn.5.23) depends on beamwidths $\theta_{hpbw}(\nu)$ which can be precisely measured as function of frequency. The geometry is determined by the signal arrival direction $\vec{P}$ and the polarization vector $\vec{\mathcal{E}}$. Section 5.1 has shown that timing delays between antennas gives $\vec{P}$ to high accuracy and in this calculation, assumed to exactly calculated. This vector $\vec{P}$ defines the incident angles θ_{inc}^{E} and θ_{inc}^{H} at the ith antenna, as described in §3.6. The reconstruction of the polarization, $\vec{\mathcal{E}}$, has been detailed in the previous section, §5.2, and it gives the value of $\mathrm{f}_{\mathcal{E}}^{[\mathrm{i}]}$. In this calculation, we take the exact values of $\mathrm{f}_{\mathcal{E}}^{[\mathrm{i}]}$ from the simulation data.

Therefore, with $V^{[i]}(\nu)$ and the known antenna response, the electric field at the surface, $\mathcal{E}_s$ is obtained as

$$\mathcal{E}_s(\nu) = \frac{2\sqrt{2} \cdot V_{obs}^{[i]}(\nu)}{\left[h_{eff}(\nu) \cdot \mathrm{f}_{\mathcal{E}}^{[i]} \cdot \exp\left(-2\ln 2 (\frac{\theta_{inc}^{[i]}}{\theta_{hpbw}(\nu)})^2\right) \right]} \tag{5.24}$$

where the averaged angular response along the two principal planes is again expressed by a

single exponential term for convenience.

Step (1b): Propagation losses The electric field at the surface, $\mathcal{E}_s$, is related to the benchmark field at 1 m from the interaction, $\mathcal{E}_0$ through a series of factors. Without vertex information, a precise calculation of propagation losses is not possible. Instead, we use computer simulation to determine the average distance to a vertex as a function of signal zenith angle, $\langle r(P_\theta)\rangle$. The average is determined for all flavors and averaged over all energies.

This electric field expression, given in Eqn.3.24, is rewritten here as:

$$(\mathcal{E}_s)_{\theta_v} = \frac{e^{-\langle r(P_\theta)\rangle/\bar{\lambda}}}{\langle r(P_\theta)\rangle}\sqrt{R}\cdot(\mathcal{E}_0)_{\theta_v} \tag{5.25}$$

where $\langle r(P_\theta)\rangle$ is the average distance to the vertex. The subscript θ_v has been added to specify that the electric fields are being considered at any observation angle (or 'viewangle') θ_v. It is the angle between the incoming neutrino direction and the signal direction to the station. This dependence is addressed in the "neutrino energy estimate" paragraph later.

The losses are through $\frac{1}{r}$ propagation loss, attenuation by ice and firn and reflective losses at ice-water boundary. As seen in §4.3.1, for a single station, the spatial location of the vertex can only be determined for nearby interactions (the tiny fraction of direct events occurring at $r \lesssim 100$m). However, for the majority of events, the direction to the shower constrains the maximum distance to the vertex, and simulations are used to determine a mean distance, averaged over all events, for a given measured propagation direction ($\vec{P}$) of the Askaryan pulse. A parametrization for $\langle r(P_\theta)\rangle$ is determined, as shown in Fig.5.8. The average pathlength distance r is determined for 10 bins of the cosine of the zenith angle of the signal, and the equation used for the reconstruction is

$$\langle r\rangle \approx 992(\cos P_\theta)^{-0.27} \tag{5.26}$$

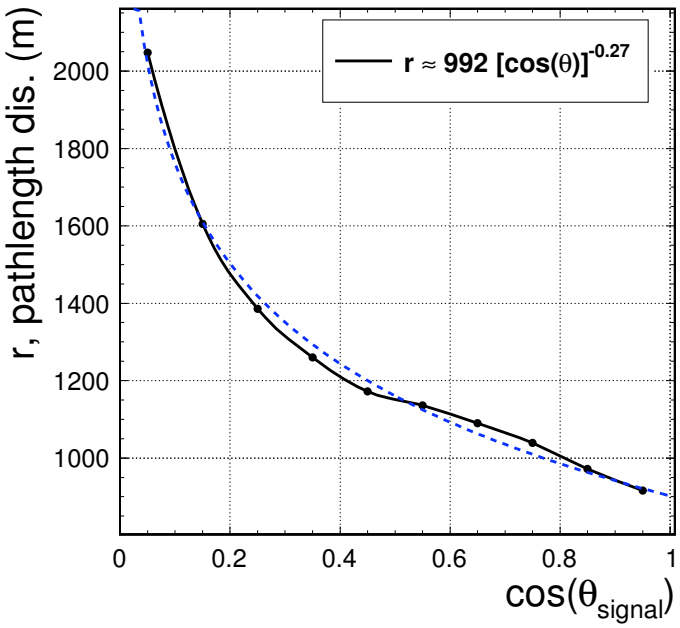

Figure 5.8: Average pathlength distance r as a function of incoming signal angle, P_θ, for reflected events. The parametrization is used for estimating the propagation loss factors as a function of zenith angle.

Since the vertex position is not reconstructed, the depth dependent attenuation length must be averaged over the ice thickness; the global value of $\langle\lambda\rangle$ used is 420 m.

The reflectivity factor, R, which accounts for reflective losses in power for events that reflect from the water-ice boundary is assumed to be independent of frequency [91]. The canonical value of R used here is 0.5 as discussed in §3.5. As the ARIANNA site is better studied, the reflectivity factor will be determined with greater precision, reducing the potential systematic error. At this stage of the development of the analysis, there is no effort to distinguish between reflected and the small admixture of direct events. Obviously for these events, the assumed value of $R = 0.5$ will cause $\mathcal{E}_s$ to be over-estimated.

In Equation 5.25, instead of averaging each individual variable in the correction coefficient in front of $(\mathcal{E}_0)_{\theta_v}$, the whole expression may also be averaged but it is not expected to significantly affect the overall resolution determination.

Step 2: Neutrino energy estimate Table 3.3 gives the assignment of the inelasticity factor y to the electromagnetic (f_{em}) and hadronic (f_{had}) fractions in the simulation. In *shelfmc*, the electromagnetic component is ignored for all but the charged-current ν_e interactions. In our reconstruction study, there is no attempt of flavor identification and the electromagnetic contribution in Equation 5.25 cannot be considered at this point. Given that the LPM effect suppresses the electromagnetic contribution from the outgoing electron in the ν_e interaction in the energy range of interest (see also §3.4.2), this approximation is partially justified.

The electric field at 1 m, $(\mathcal{E}_0)_{\theta_v}$, is also dependent on the observation or 'viewangle', θ_v, between the neutrino direction and the signal direction to antenna. As explained in §3.4.2, the fall in electric field away from the peak Cherenkov angle is modeled by a modulated Gaussian expression (see also Eqn.3.11):

$$(\mathcal{E}_0(\nu))_{\theta_v} = (\mathcal{E}_0(\nu))_{\theta_c} \cdot \frac{\sin\theta_v}{\sin\theta_c} \cdot \exp[-\ln 2 \cdot (\frac{\theta_v - \theta_c}{\Delta\theta(\nu)})^2] \tag{5.27}$$

where, from §3.4.2, we recognize that the width of the Cherenkov cone, $\Delta\theta$, is different between electromagnetic and hadronic components. In our approximation here, $\Delta\theta_{had}(\nu)$ is used and $\Delta\theta_{em}(\nu)$ is ignored. The angle difference $|\theta_v - \theta_c|$ is not precisely known and estimating its average value $\langle|\theta_v - \theta_c|\rangle$ introduces a large source of error in the energy reconstruction. However, with new simulation techniques for time profile information, as seen in §3.8.2 and Ref.[111], the pulse shape depends on the angle difference. Waveform pattern information from future ARIANNA stations can provide a more accurate estimate of $|\theta_v - \theta_c|$. In our reconstruction, we assume that $\theta_v - \theta_c$ can be known to the within $\sim 0.4^\circ$ close to Cherenkov angle, and slightly less accurately at large angle differences as in the following relationship:

$$\sigma(\theta_v - \theta_c) \approx 0.1|\theta_v - \theta_c| + 0.3^\circ.$$

From Equation 5.27, $(\mathcal{E}_0(\nu))_{\theta_c}$ is known and is plugged into the following equation using standard parametrizations as mentioned before:

$$(\mathcal{E}_0(\nu))_{\theta_c} = 2.53 \times 10^{-7} \cdot \frac{E_{sh}}{\text{TeV}} \cdot \frac{\nu}{\nu_0} \cdot \frac{1}{1. + (\frac{\nu}{\nu_0})^{1.44}} \tag{5.28}$$

where ν_0=1.15 GHz. It is summed over frequencies to give the shower energy E_{sh} as

$$\frac{E_{sh}}{\text{TeV}} = \sum_v (\mathcal{E}_0(\nu))_{\theta_c} \cdot \frac{\nu_0}{\nu} \cdot \frac{1 + (\frac{\nu}{\nu_0})^{1.44}}{2.53 \times 10^{-7}} \tag{5.29}$$

Finally, as in Equation 5.22, an estimate for neutrino energy is obtained through

$$E_\nu = E_{sh}/\langle y_{eff} \rangle$$

where we refer to reconstructed E_ν as $E_\nu^{meas.}$.

Simulations were used to obtain the inelasticty $\langle y_{eff} \rangle \approx 0.8$, averaged over flavor and energy spectrum, as shown in Fig 5.9. The distribution shows that for τ flavor, the value is higher above 0.5, and this because the higher value of the electromagnetic or hadronic component of the shower was chosen in *shelfmc*. This was an approximation to account for the fact that in charged-current interaction, the outgoing lepton carrying most of the energy can initiate a hadronic shower that is detectable. For the electron flavor, the ratio of shower energy to neutrino energy is closer to 1 on average because for the charged-current(CC) interactions (which occur on average twice for frequently that neutral current interactions), both the electromagnetic and hadronic components contribute to the shower energy. This will cause the procedure to overestimate ν_e energies from CC interactions, i.e. about $\sim$ 30% of the triggered events.

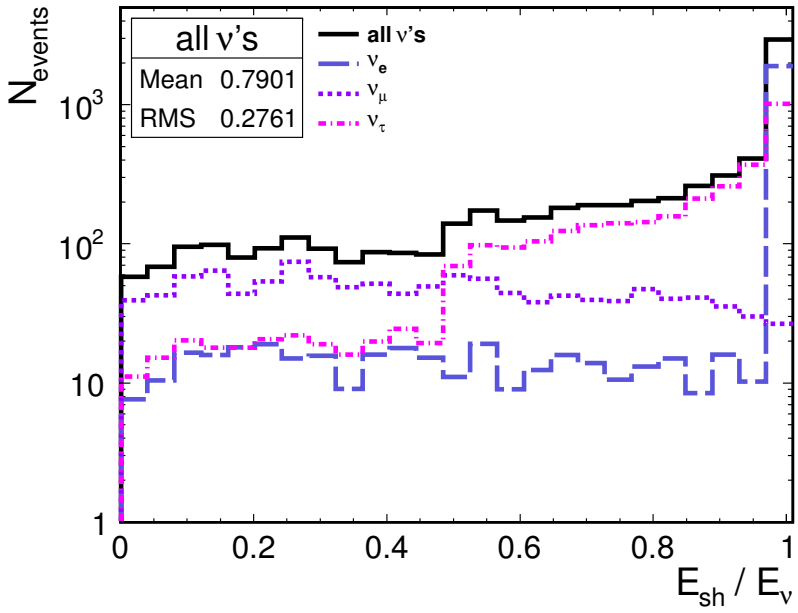

Figure 5.9: Ratio of shower energy (E_{sh}) to neutrino energy(E_ν) for all flavors, and each flavor separately, and over all energy. The average value of ∼0.8 for the inelasticity factor is used in the energy reconstruction.

5.3.2 E_ν resolution

The energy reconstruction procedure described is applied to a set of simulated data assuming ESS GZK flux. Fig. 5.10 shows the distribution on a log scale of the ratio of the reconstructed neutrino energy ($E_\nu^{meas.}$) to the true neutrino energy, E_ν, for all flavors and for each flavor separately. Applying a Gaussian fit to the all flavor data gives a standard deviation, σ, of ∼0.34 on the log scale of the ratio. This translates into a factor of ∼2.2 for the neutrino energy estimate. A positive value on the x-axis means that it is an overestimate and negative values means an underestimate.

The ν_e distribution has a peak around a x-value of 0.1, implying an overestimate of ν_e energies by a factor of about 1.26. This is consistent with what is expected from Figure 5.9 where almost of all the electron neutrino energy is seen to go into the shower ($(E_{sh})_{\nu_e} \approx E_{\nu_e}$). In our reconstruction method, the average fraction assigned to the shower was 0.8 (i.e.

$(E_{sh})_{\nu_e} \approx 0.8 E_{\nu_e}$), and with this choice of value, we would indeed expect an overestimate of about $\frac{1}{0.8} \approx 1.25$ for ν_e events.

A similar argument applies for tau-neutrinos, where, again from Fig. 5.9, we see that $(E_{sh})_{\nu_\tau}/E_{\nu_\tau}$ mostly lies above 0.5 and peaks above 0.8. Upon reconstruction, those values with ratio above 0.8 will be overestimated, and that explains the peak for ν_τ around x-value of about 0.1 in Figure 5.10. No such peak seems to occur for muon neutrinos; the distribution of the ratio of $(E_{sh})_{\nu_\mu}/E_{\nu_\mu}$ is more or less flat in Figure 5.9.

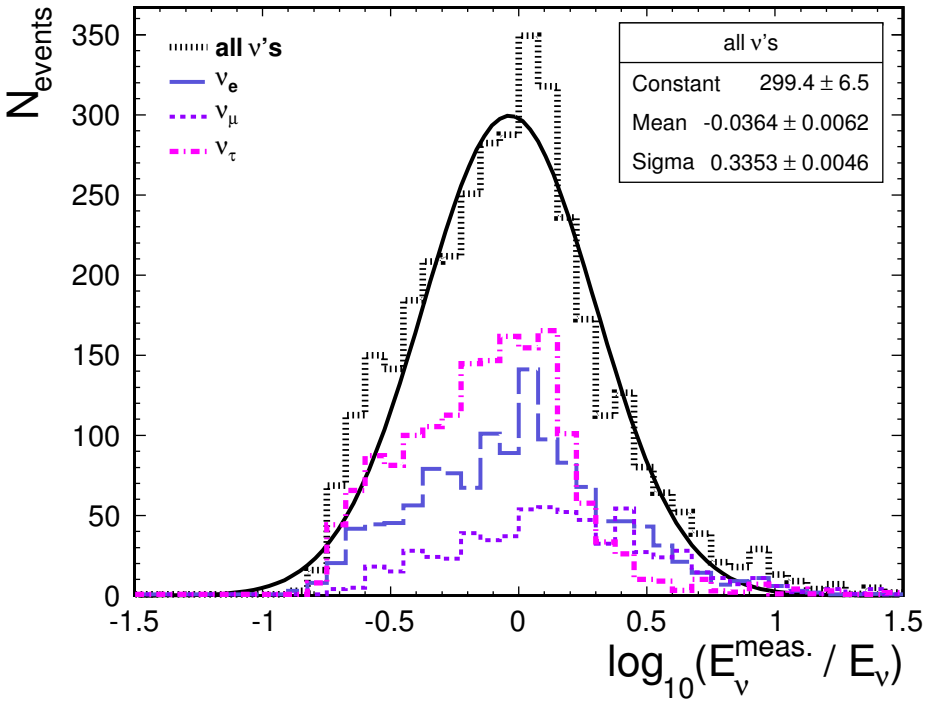

Figure 5.10: Energy resolution of reflected events with a reconstruction procedure using single station data. The σ value of the Gaussian fit at 0.34 to the log x-axis scale means a resolution of $\sim$2.2 for the ratio $E_\nu^{meas.}/E_\nu$, i.e. the energy of the neutrino can be estimated to within a factor of $\sim$2.2.

Flavor identification with ARIANNA will provide a way to improve on the neutrino energy estimate because the shower energy dependence varies with flavor type. This is illustrated in Figure 5.11. The reconstruction method uses an average value of 0.8 for $(E_{sh})_\nu/E_\nu$ over all energies and all flavors, but these values show an actual variation with the neutrino

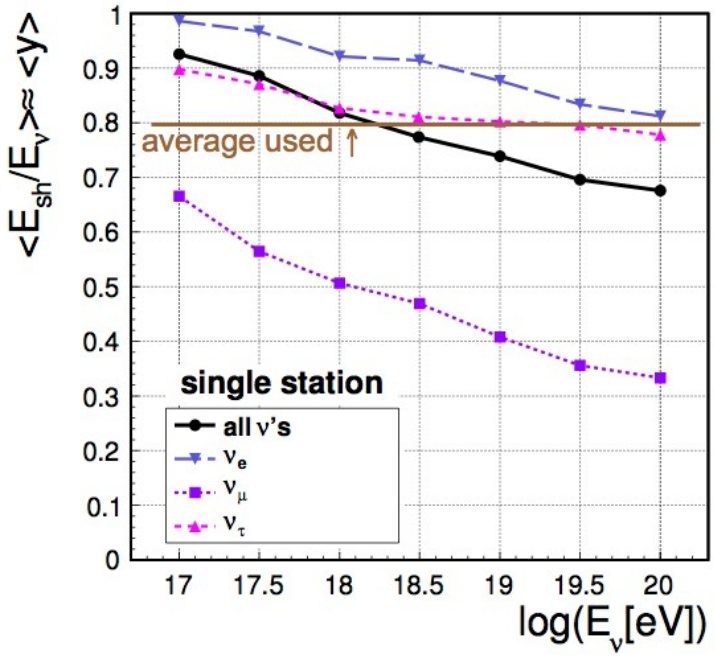

Figure 5.11: Average ratio of shower energy to E_ν as function of neutrino energy, E_ν for each individual and all flavors. The reconstruction method uses a constant value of 0.8 for the average inelasticity factor for all energies and flavors.

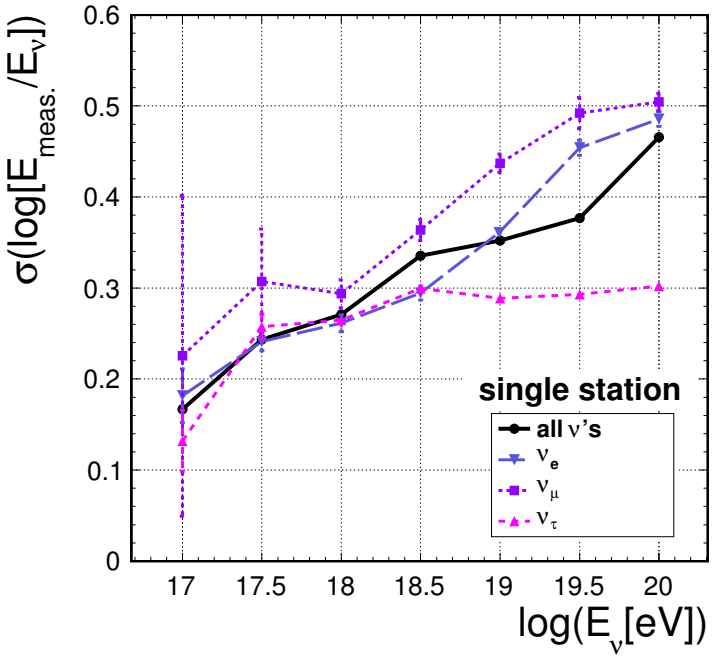

Figure 5.12: Neutrino energy resolution as a function of energy and flavor. The errors bars on the standard deviation values indicate that low energy events suffer from low statistics.

energy (the all flavor average is the black line). For a given flavor and energy, the further its average inelasticity value lies from 0.8, the less accurate will be the energy estimate. This is confirmed by Figure 5.12 where the energy resolution, characterized by the standard deviation of the $\log(E_{meas.}/E_\nu)$ distribution, is given as a function of energy and flavor. The error on the resolution itself is large for the lowest energies due to small statistics, but some general explanations can be provided for the overall trends observed.

The τ-neutrino ratio from Fig.5.11 approaches 0.8 for above 10^{18}eV, and therefore, its energy resolution is flat above that energy. The $\langle y \rangle$ for the ν_μ starts at 0.66 at 10^{17} eV and decreases to about 0.3 at 10^{20}eV. Therefore the energy resolution for the ν_μ gets less accurate with energy, as seen in Figure 5.12. The energy resolution on the ν_e flavor also gets worse with increasing energy but the connection with the shower energy ratio in Figure 5.11 is less clear. This is due to the subtle effect of the combination of electromagnetic and hadronic showers that have different profiles for their Cherenkov cone widths (see §3.4.2). As the LPM effect turns on, the electromagnetic shower is suppressed through a narrowing of the cone, and the hadronic shower is the main contributor to the signal strength, especially at observation angles far from the Cherenkov angle.

At energies below 10^{18}eV, the energy resolution seems to improve for all flavors. This can explained through the other major determining factor to the energy estimate: the difference between the observation angle, θ_v, and the Cherenkov angle θ_c. Equation 5.27 showed that the electric field falls by a Gaussian determined by the size of $|\theta_v - \theta_c|$. Lower energy events will typically trigger through signals lying closer to the Cherenkov angle and this is evidenced by the plot in Figure 5.13. Due to the significant electric field strength drop at observation angles further away from the Cherenkov angle, only the highest energy events can trigger at large $|\theta_v - \theta_c|$. However, as pointed out in the previous subsection, we assume that our resolution on estimating $|\theta_v - \theta_c|$ is coarser at larger deviations, and therefore, at the highest neutrino energies, the resolution on $\log(E_{meas.}/E_\nu)$ gets larger, as seen in Figure 5.12.

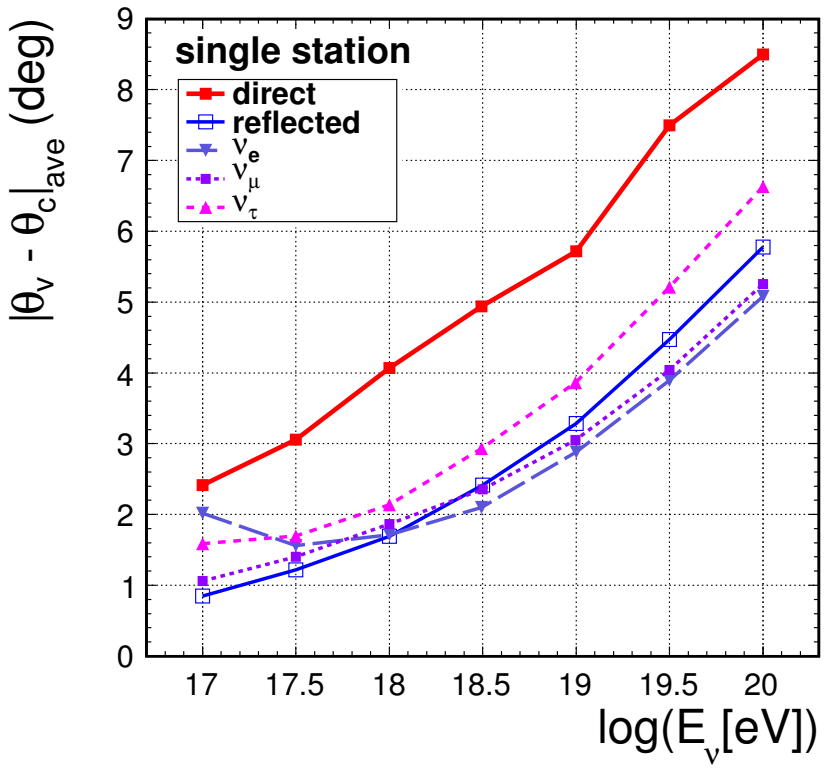

Figure 5.13: Mean value of $|\theta_v - \theta_c|$ as function of energy and flavor. Shown also for direct and reflected events.

Overall, we have seen that the reconstruction method can estimate neutrino energy to within a factor of ~ 2.2. This resolution has an energy and flavor dependence. The main source of uncertainty is the inelasticity factor y and the observation angle(θ_v) deviation from the Cherenkov angle(θ_c).

5.4 Summary on Reconstruction Studies

In this chapter, we have presented a method to reconstruct the neutrino direction and energy using information such as relative voltage amplitudes and high precision timing delays between antennas from an ARIANNA single station. The reconstruction procedure takes into account the angular response of the LPDA antenna.

Prior studies in Ref.[103] considered multi-station hits within a densely-packed array for event reconstruction and assessing the energy and angular resolution . The techniques are developed for single station and are applicable to arrays with spacings of 1 km, where each station acts as an independent radiodetector, except at the highest energies.

The neutrino direction can be determined with resolution of $\sigma_\theta = 2.87^\circ \pm 0.05^\circ$ and $\sigma_\phi = 2.53^\circ \pm 0.04^\circ$. This angular reconstruction assumes that the observation angle θ_v is unknown, i.e. there is no use of waveforms to obtain this information. The imprecision in the observation angle deviation from the Cherenkov angle is the dominant factor behind the imprecision in neutrino direction.

The neutrino energy for reflected events, which constitute the vast majority of detected events, can be estimated to within a factor of 2.2 irrespective of flavor and independent of vertex reconstruction. The deviation angle $\delta\theta_v{=}\theta_v - \theta_c$ to be known within $0.3 - 1.3^\circ$, which we argued is achievable with the time profiles of the pulse through the waveform digitizer technology being implemented in ARIANNA data acquisition systems. Without knowledge of the deviation from the Cherenkov cone, the energy resolution was determined to be within a factor of 5. Obviously, the energy resolution is completely dominated by the uncertainty in the deviation angle $\theta_v - \theta_c$. Even if waveform information can be used to determine the deviation angle to $\sim 1^\circ$, it still dominates the energy resolution, although uncertainty in the effective inelasticity is also significant. However, this latter term can be improved by flavor identification.

Chapter 6

Systematic Uncertainties

The calculations presented in Chapter 4, specifically the aperture determination, depend on a choice of values and conditions based on *in situ* measurements and results from other published results.

In this chapter, we discuss the potential repercussions on our studies for deviations from these conditions, making quantitative assessments where possible.

6.1 Roughness

In *shelfmc*, there are two discrete boundaries, and a firn region where the density $\rho(z)$ and index of refraction $n(z)$ change continuously. This is modeled in two ways (see also §3.1: (1) a 'uniform ice + uniform firn' model with a constant n_{ice} and n_{firn} and (2) a continuous variation for index of refraction, with $n_{firn}(z)$ given in Eqn.3.1. The two discrete boundaries occur at the firn-air and the ice-seawater surface. The simulation of ARIANNA implicitly assumes that the two discrete boundaries are characterized as follows:

air-firn: surface is flat. No power reflected by total internal reflection is added to the signal observed by the antenna. Since the antennas are only buried to a depth of 1 m, there is little delay between the signals that reflect from the firn-air boundary and those that do not. This discussion is detailed in later in §6.4.1 and we simply note here that *shelfmc* ignores effects from air-firn interface.

ice-seawater: Due to the high conductivity of sea-water, very little radio power is lost due to absorption. Therefore *shelfmc* only considers reflective losses by scattering from a rough surface. Currently, scattering losses are approximated by a constant value of 0.5 in power (although this is adjustable) independent of frequency. In fact, recent measurements [89] are consistent with this value, but also compatible with much smaller losses which are characteristic of an idealized smooth surface. There are three confirming pieces of evidence that suggests a very smooth surface.

(i) In reflection studies, there is little distortion of the observed pulse in the time domain. As we discuss later in this chapter, significant reduction in amplitude due to scattering is also accompanied by strong modifications in the time domain.

(ii) Reflected pulses preserve polarization. In computer simulation of the effects of rough surfaces, strong losses in signal intensity of linear polarized signals are correlated with significant power transferred to the cross-polarization direction.

(iii) The reflected signal strength for vertical directions is observed to be similar at three different locations separated by $\sim$ 1 km.

Therefore, the approximate loss of a factor of 2, independent of frequency, is thought to be sufficient, if slightly conservative. As discussed later in §6.2, the sensitivity of ARIANNA depends weakly on the combined effects of reflective losses and 1-way attenuation. The effect of larger reflective loses is compensated by the increased attenuation length (the 1-way reflection measurement constrains the combination of both parameters).

Computer simulations of the impact of surface roughness provide the following results.

- Strong modification of the time dependent pulse are observed for trajectories that skim the surface ("grazing angles").
- Very little distortion is seen for vertically incident waves, even for surface roughness comparable or larger than the relevant wavelengths in the Fourier transform of the time-dependent pulse.
- Strong modification of the linearly polarized time-dependent pulse is correlated with power transfer to the cross-polarized component.

Given the importance of the characteristics of the bottom surface, we describe the simulation studies in the next subsections. We also note that surface roughness impact is of concern in detection methods that involve exit angles near grazing, which is the case in ANITA with observation of Antarctic ice [110] or experiments that monitor the moon for Askaryan pulses. For instance, Ref [65] details attempts to include small-scale lunar roughness in their aperture calculation. We remark that presence of roughness, depending on the relative scales involved, may not *a priori* negatively affect detection efficiency; they might favor transmission beyond critical angles. However, effect of rough surfaces on the coherence of pulse transmission are still to be fully understood.

The application of this work to ARIANNA surface is not straightforward. In these studies, the index of refraction in the incident media is higher than in the transmission media. At the ice-seawater interface, the seawater has very large effective index of refraction with little power transmitted and the reflected pulses have inverted phase. However the key observation in this work shows that significant distortion occurs for grazing angles (which are produced for incident angle close to critical angles). This suggests that strong distortions in reflected signals are possible for grazing paths ($\theta_{inc} \geq 75^{\circ}$). This will also be discussed in §6.1.3 later.

6.1.1 Effects on Transmittance

Modeling a rough surface gets simplified in two limiting cases. If the wavelength components of the signal is much smaller than the size of the surface roughness, then geometrical ray tracing suffice. If the wavelengths are much larger than the undulations, a flat surface approximation holds. In between, the situation gets more complex, especially where the wavelengths of interest are similar in size to the roughness features. The following subsections describe prior studies that were carried out to understand and characterize effects of surface features commensurate with the relevant regime of wavelengths on radio pulse refraction at a firn-air interface.

Prior work through numerical simulations, for eg [123], have improved on and confirmed previous analytical work (for eg. Ref.[124]) which established that the transmitted power through a rough surface undergoes significant deviations from Fresnel predictions as a function of incident angles, polarization and varying roughness scales. Experimental observations have subsequently confirmed deviations from flat surface behavior. For instance, Griswold et al [125] used an optical laser of wavelength 600 nm on ground glass diffuser at various incident angles. One of the main observations was that for incidence near critical angle[1], there was a broadening in the angular distribution of the transmitted power. In addition, the peak of the distribution shifts towards normal.

The experimental results were reproduced in simulation by using ASAP (Advanced System Analysis Program), a commercial optical analysis software developed by Breault Research Organization[126]. The surface roughness was determined from a high resolution scan of the glass surface and this data imported into ASAP. As Figure 6.1 shows, the same shift from Fresnel prediction is observed and the FWHM is slight narrower. The tails of the experimental distribution are not well reproduced, presumably due to non-gaussian fluctuations

[1]Since it is the angle above which total internal reflection occurs, it is also sometimes referred to as *TIR angle*.

in the regions not measured by the surface scan. The simulation also gave deviations from Fresnel behavior in the vicinity of critical angles: loss of transmission power occurred below critical angles but there were some transmission just above. This geometrical ray tracing method reproduced the general features observed by [125].

Scaling to radio waves Due to the large scale of radio waves, it is difficult to experimentally study surface roughness. Rather, it is common to use visible light as a proxy for longer wavelengths. The ratio of the micrometer size of the glass roughness[2] to the laser wavelength used could be compared to radio wavelengths to decimeter size surface features on Antarctica. Based on such scaling, one could draw conclusions about the transmission of radio power through rough surfaces based on the experiment.

6.1.2 Time-Domain Effects

In geometrical ray tracing, where the size of the incident wavelength is much smaller than the roughness values, it might be sufficient to characterize the roughness of the surface by a single slope value. However, in the time-domain approach, defining the rough surface of interest by a slope ratio or angle is not adequate. For example, let us visualize a situation where the incident wavelength is $\mathcal{O}(1)$ m. Intuitively, r.m.s heights (σ_h) and correlation lengths (Λ) of order mm or smaller do not produce the same effect on its transmittance as does a rough surface with those pair of parameters of the order of 1 m (i.e. commensurate with the wavelength), even though the two roughness contrive to give similar slope values. We therefore emphasize that, in the time domain, the dimensionless slope ratio does not

[2]In such studies, it is common to quantify the degree surface roughness with a dimensionless slope given by a ratio of a vertical to a horizontal parameter. R.m.s height (σ_h) is a useful measure of the average vertical fluctuations about a mean plane while correlation length (Λ) is a measure of horizontal roughness scale. A larger correlation length means that peaks and troughs are on average further apart. Correlation distance is to a certain extent an analogy of the period of a periodic surface, just as the r.m.s height or standard deviation is an analogy to the amplitude.

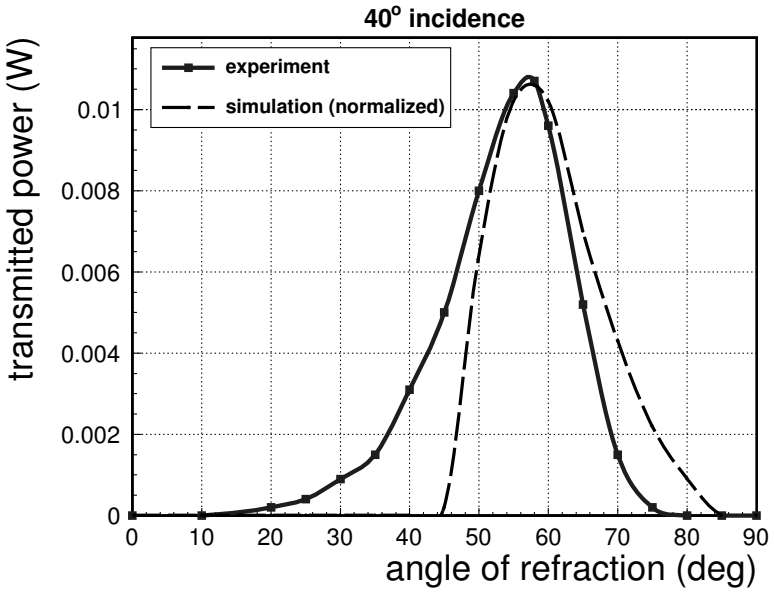

Figure 6.1: A representative comparison of data from Ref [125] vs. ASAP ray tracing simulation. The x-axis denotes the angle of transmission relative to the normal of the (flat) exit surface. The rough surface used has a r.ms height of 1 μm and correlation length of 5.1 μm, with index of refraction of $n = 1.5$. That implies a specular angle of refraction at 74.6°.

uniquely allow us to assess and compare a rough surface impact in the time domain; it has to be used in conjunction with at least one of the length parameters, σ_h or Λ.

The optics test in Ref [125] used a continuous-wave source rather than an impulse. Even though it provides an insight into transmission near grazing angles under rough conditions, it does not address the coherent wave behavior of the transmitted pulse. We develop a model for investigating this using a computational electrodynamics tool known as "finite-difference time-domain". We chose a commercial software called FDTD Solutions by Lumerical [127] for that purpose.

Considering radio wavelengths in the regime of interest, i.e. ranging from $\sim$3 m (ν = 100 MHz) to 30 cm (ν = 1 GHz) in air, we create gaussian random surfaces with r.m.s heights and correlation lengths within the same range. We employ the following strategy to emulate the effect a short duration ($\sim$2ns long) bimodal pulse. We decompose the signal into its

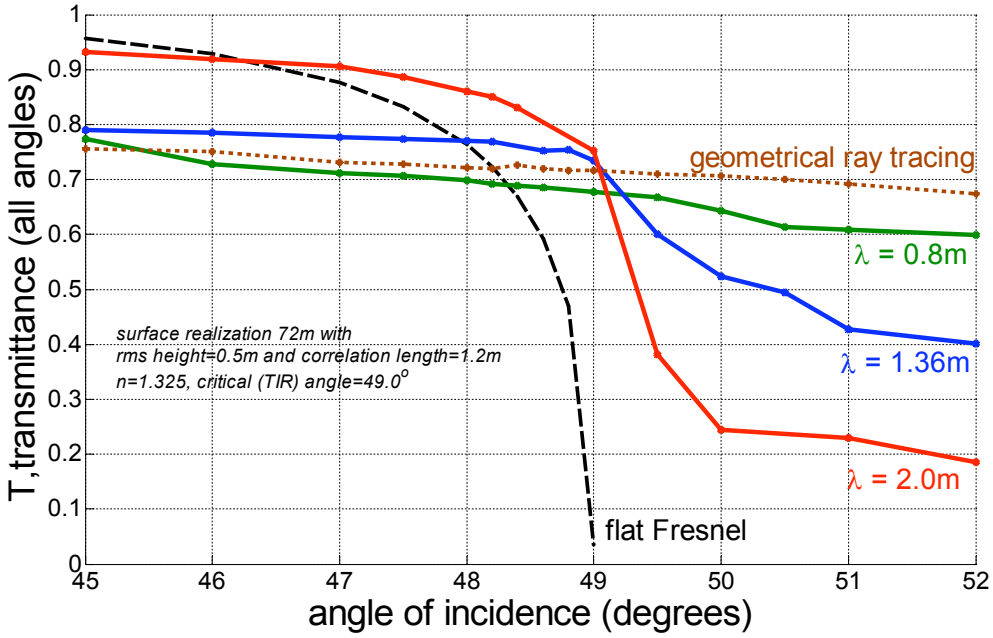

Figure 6.2: Transmittance, T, as a function of incident angle shows deviations away from Fresnel equations applied to a flat surface. However, the behavior depends on the relative sizes of the roughness features and wavelengths. In the limit of large wavelengths, it approaches a flat surface behavior; while in the limit of small wavelength, geometrical ray tracing applies.

Fourier frequency components and input a series of monochromatic plane waves with the appropriate amplitudes (given by the power spectrum of the pulse) into the software. The plane waves are all incident at a set angle over a limited patch of the rough surface (about 10 $\Lambda's$). This is to mimic the finite size of a plane wave from an Askaryan pulse. At observation points in Fraunhofer limit (sufficiently far from the surface), we record the transmitted plane waves. The software would have properly taken into account the electrodynamic effect of the rough slopes on each wave at they refract through the interface. Applying the correct phase information from the original Fourier transform, we recombine the outgoing wave profiles to create the simulated transmitted wave at those observation points.

The results are presented in Figures 6.4. For incidence angles less than critical angle (difference of $\gtrsim 5^\circ$), the impact on the pulse coherence is small, even for relatively severe roughness. In addition, the distortion in the time domain gets less pronounced for nearly normal incidence. At angles close to the critical angles and larger, the distortions of the pulse become more significant. Interestingly, power is transmitted through rough surfaces at incident angles larger than critical angle but pulse shape is strongly distorted.

6.1.3 Applicability to ARIANNA

Surface with roughness parameters comparable to the maximum wavelength in the power spectra of a pulse can lead to distortions of the transmission pulse at refraction near grazing angles. In contrast, the coherence of a bimodal pulse is preserved for incidence angles small compared to the critical angle.

In the case of ARIANNA, refraction from ice to air are not applicable nor does the refraction from ice to firn involve grazing angles. Further at a depth of 75 m, beneath the firn layer, any decimeter scale undulations that may be present will be compacted away to a flatter interface. Still, we can pull some general conclusions from the above studies and use them

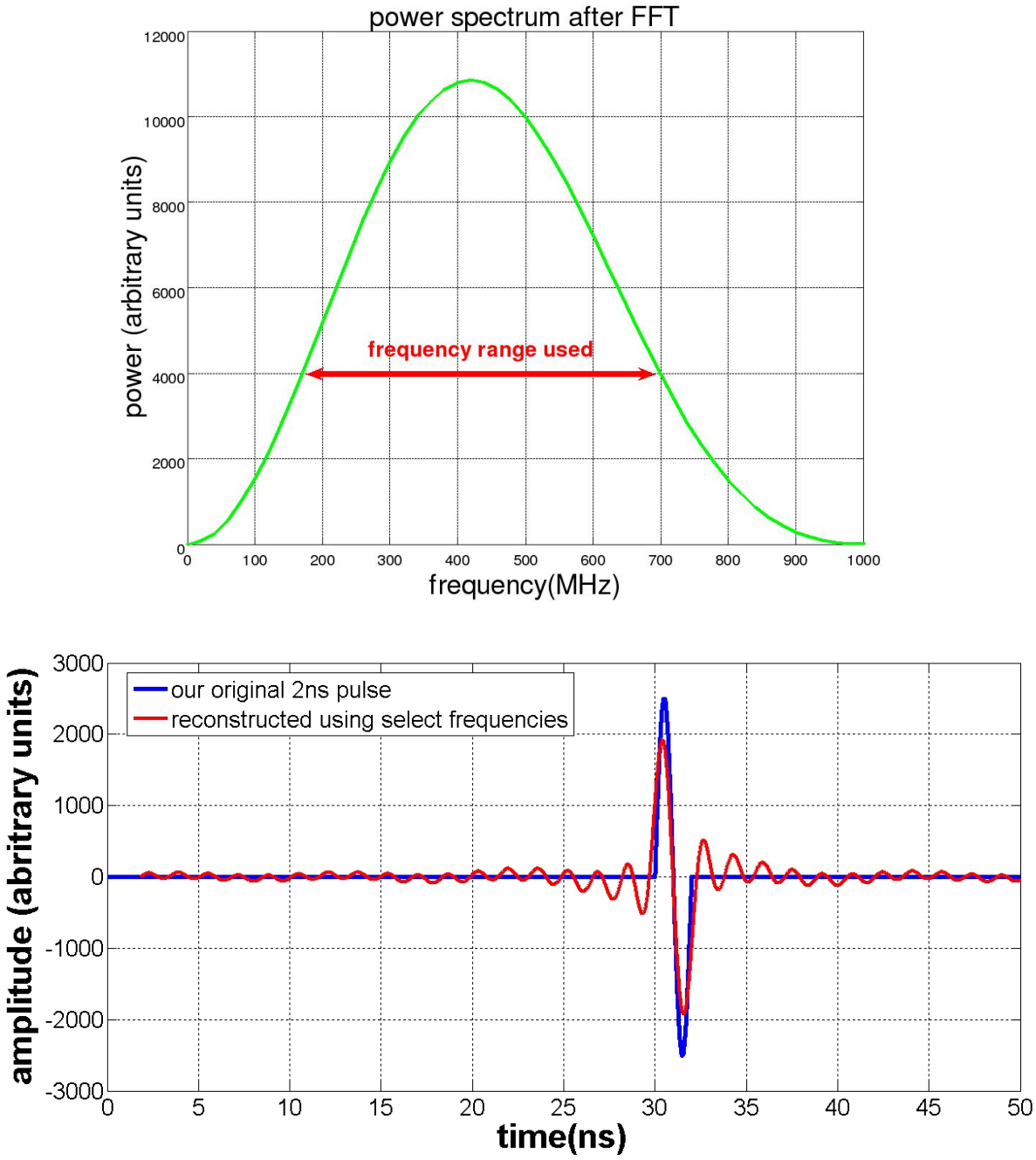

Figure 6.3: A sharp bimodal pulse can be created by superimposing a set of Fourier components. A selected number of frequencies are used to speed up the simulation in FDTD.

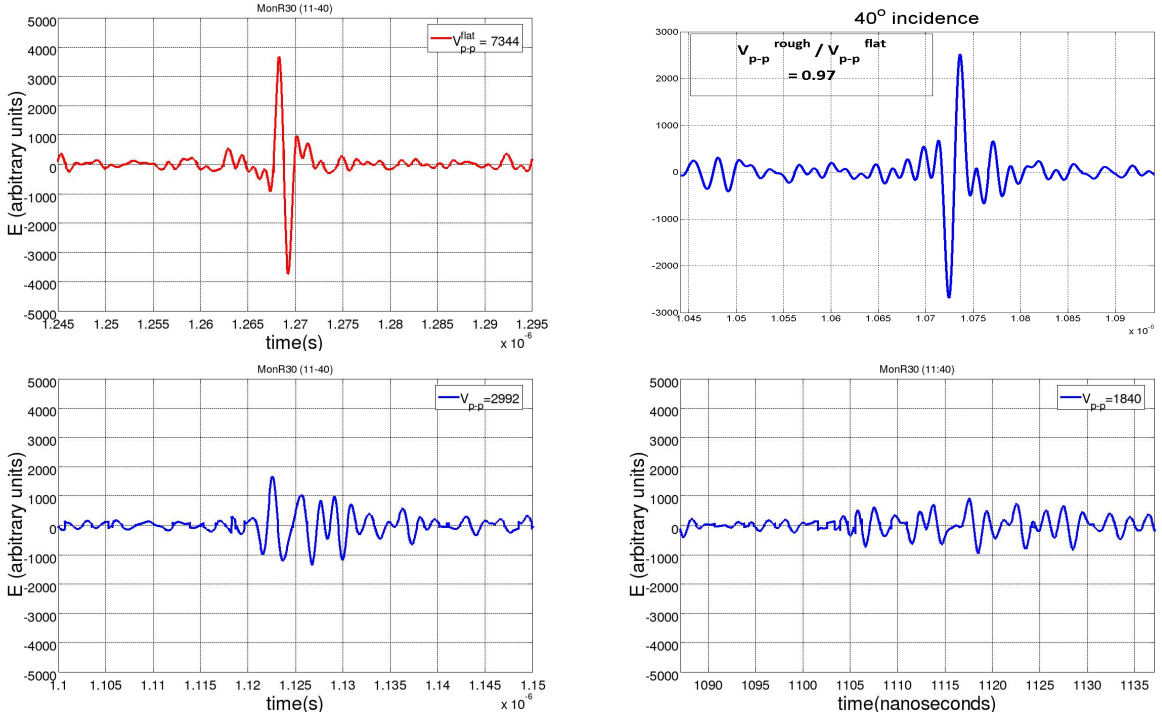

Figure 6.4: Select time profiles of transmitted pulses in air through different surface roughness ($n = 1.325$) and incidence angles. Top left panel indicates that the bimodal pulse shape is preserved through a flat surface, as expected. For incidence smaller than the critical angle of 49°, the coherence still survives as shown for 40° incidence in the top right panel. Just below the critical angle, at 46.8° incidence, decoherence start to occur (bottom left panel) and beyond that at 50° incidence, there is still some transmitted power but it is spread out in time and the pulse shape is completely lost.

for reflection even though any phase change is two times bigger than for transmission.

Firstly, nearly vertical incidence (rays away from critical angle and closer to the surface normal) change very little, even for relatively large roughness ($\sigma_h \sim$ largest wavelength in pulse). Secondly, as we previously saw, significant spreading in time occurs in the vicinity of the critical angle, where the transmitted wave grazes the surface, effectively creating multiple chances to scatter as it propagates and spreads. The equivalent for reflection on the bottom would be rays that skim in the incoming direction, but those will generally miss the surface detectors or get absorbed. This is confirmed by Figure 6.5, where the rays angles near horizontal would suffer total internal reflection upon hitting the ice-firn interface.

In addition, empirical measurements as reported in the literature [84] suggest a smooth surface with variation of order cm, as mentioned in Chapter 2. The decimeter scale radio wavelengths will not 'see' such undulations and the flat surface approximation holds. Furthermore, macroscopic roughness, as in a situation depicted in Figure 6.6 and that would warrant geometrical ray tracing to determine whether reflected rays will hit or miss the station, is unlikely for ARIANNA. This is due to the absence of crevasses at the site and the fact that the surface melts that would result in smoother interfaces. We therefore infer that the ice-water boundary will not play a big role in affecting the time dependence of the pulse through surface roughness.

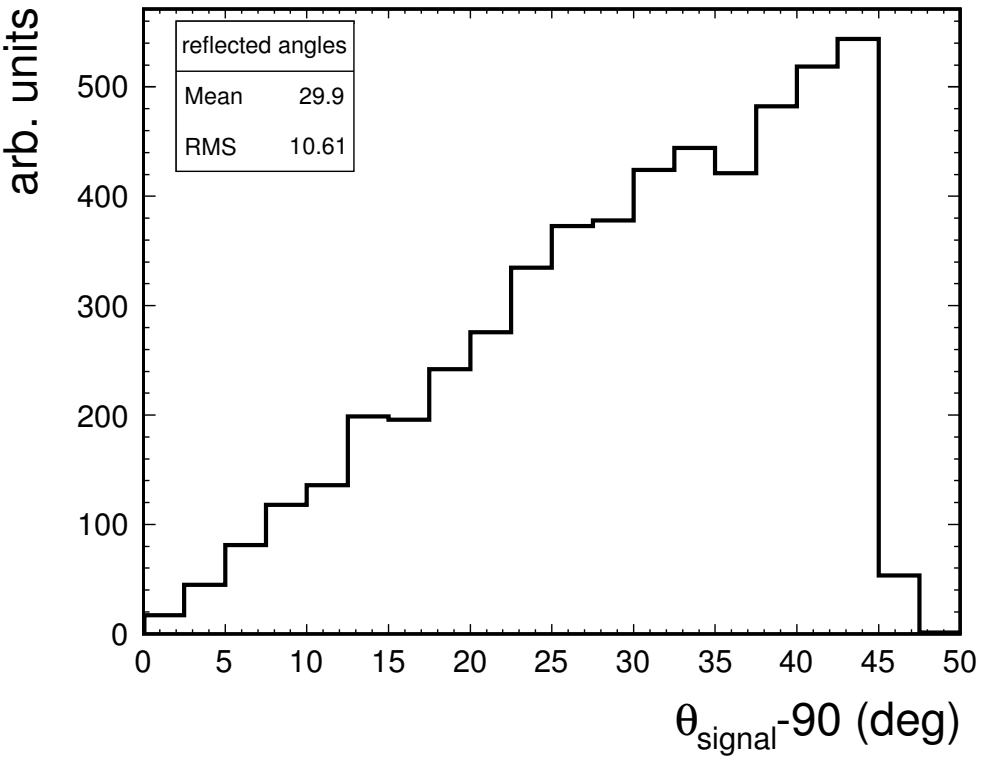

Figure 6.5: Distribution of reflection angles for rays at ice-water interface, where we have re-expressed the incident angles with respect to the local normal. The cut-off at the critical angle of 48.1° from ice to firn surface places an upper limit on the distribution. The average value of 30° means that the reflection are not occurring near grazing angles.

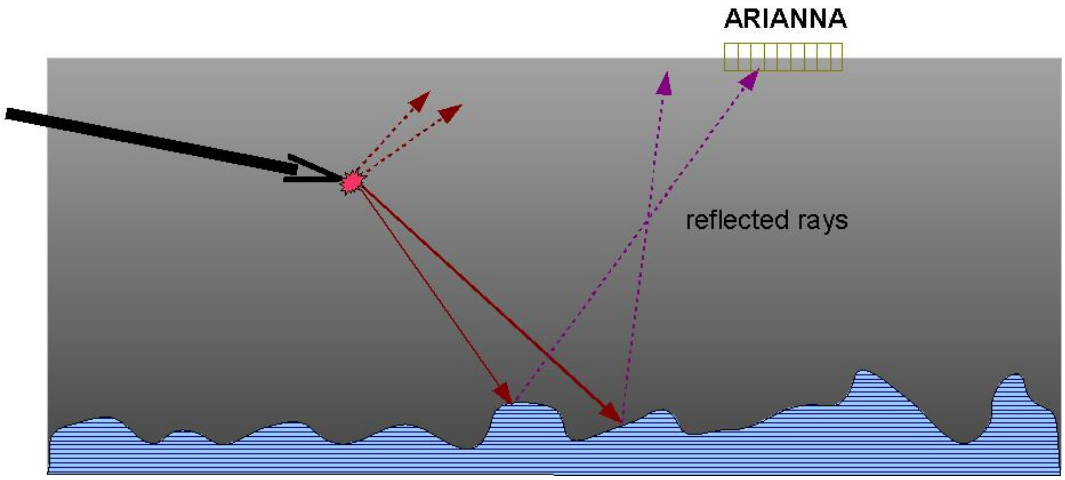

Figure 6.6: Based on time domain considerations of reflected pulses, presence of extreme ice-seawater roughness that distorts time domain profile for radio wave pulses is unlikely at the ARIANNA site.

6.2 Reflectivity

Measurements of the fraction of power reflected, or reflectivity R, have been discussed in Chapter2. In Chapter 4, we specify that the nominal reflectivity in *shelfmc* is set to 0.5, implying electric field amplitude modifications of $\sqrt{\mathrm{R}} = 0.71$. Recent and ongoing *in situ* measurements point to the possibility of even higher reflectivity; data from the latest season yield R=0.64±0.16 at 65% C.L [89] but we note that the measurements were restricted to lower frequency range. From the graph presented in Figure 2.6, we see that the empirical determination of depth-averaged attenuation length, $\langle \mathrm{L} \rangle$, is coupled to the reflectivity. In our simulation, we have kept the (wider) frequency-averaged value of ∼450 m for $\langle \mathrm{L} \rangle$ while fixing R at 0.5.

However, we can investigate the variation in V_{eff} as a function of R and its corresponding attenuation length values, as given in the dependence in Figure 2.6. For additional comparison, $\langle \mathrm{L} \rangle$ is also kept constant at our nominal value of 450 m for all R's. Both results are plotted in Figure 6.7. They show that the current value of 450 m as attenuation length underestimates the aperture by nearly 30% compared to using a broader frequency-averaged value of 520 m for R=0.5. The upper curve that takes into account the dependence of $\langle \mathrm{L} \rangle$ on R gives a rather flat trend between R=0.5 and R=0.64 and even up to the upper theoretical limit of R=0.8281; the overall change is less than 5%. The net effect on aperture is an interplay between R and $\langle \mathrm{L} \rangle$. In both cases, for lower values of reflectivity (R<0.5), the aperture drops because the smaller reflected amplitudes are not able to trigger the detector.

6.3 Ice Thickness

Early work on ARIANNA simulations (for example Ref.[103]) have used a smaller thickness (500 m) for the ice shelf than recently published values in Ref.[85]. It is also assumed in §3.1

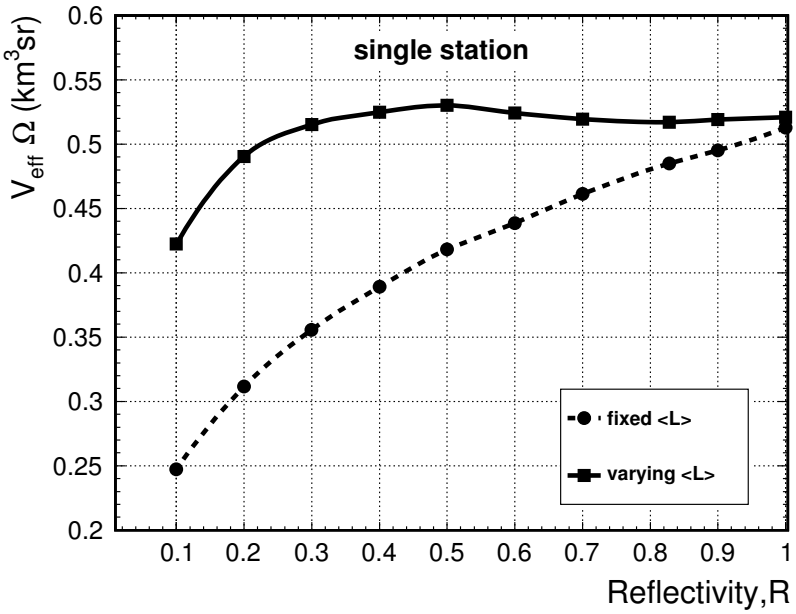

Figure 6.7: Aperture dependence on reflectivity for the case where depth-average attenuation length is kept constant (dashed line) and varied (solid line) as in Figure 2.6.

that the depth is kept uniform over a 900 km^2 area for the array simulation, but it is worth examining the impact of different ice thicknesses on V_{eff}. For instance, this may provide a quick assessment in a scenario where the shelf depth varies linearly from say 550 m to 600 m over kilometer scale distances spanning several stations.

A first order calculation follows from the fact that the fiducial volume, $\mathcal{V}$, depends linearly on the depth, so an increase from 500 m to 600 m implies a 20% increase in $\mathcal{V}$. Equation 3.31 indicates that a similar increase should also result in $V_{eff} \times \Omega$. The simulated dependence of aperture on depth shown Figure 6.8 shows that our first order estimate is a maximum correction. Due to attenuation length and geometric considerations, the impact of decreasing fiducial volume through smaller depth is mitigated. Interestingly, above 600 m depth, the trend in the aperture increase is that it starts to plateau out indicating that fewer events are originating from the deeper reaches of the ice, and that the extra pathlengths being added by the extra depth margin is contributing to propagation losses of a larger share of events.

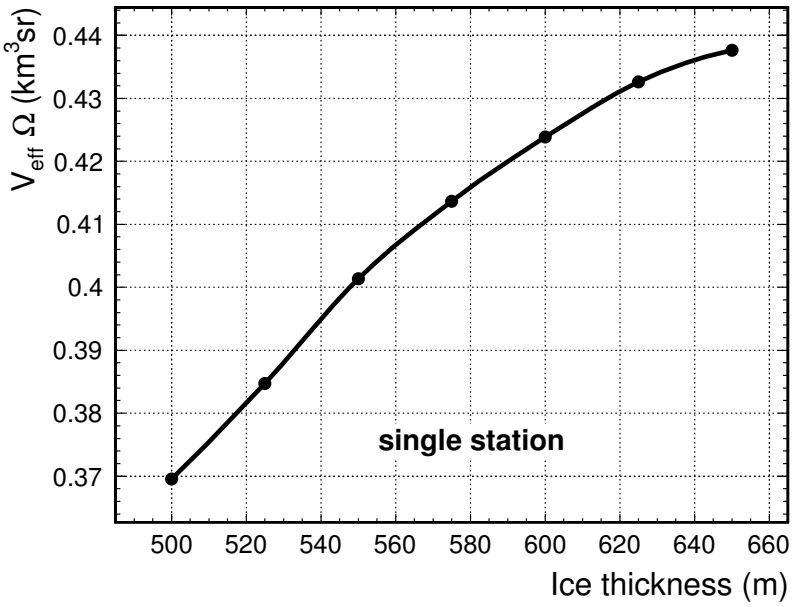

Figure 6.8: Variation in ARIANNA aperture as a function of ice depth. A 20% increase from 500 m does not result in a corresponding increase in aperture due to mitigating factors from attenuation lengths and geometric considerations.The firn depth is kept uniform at 75 m and other parameters are standard.

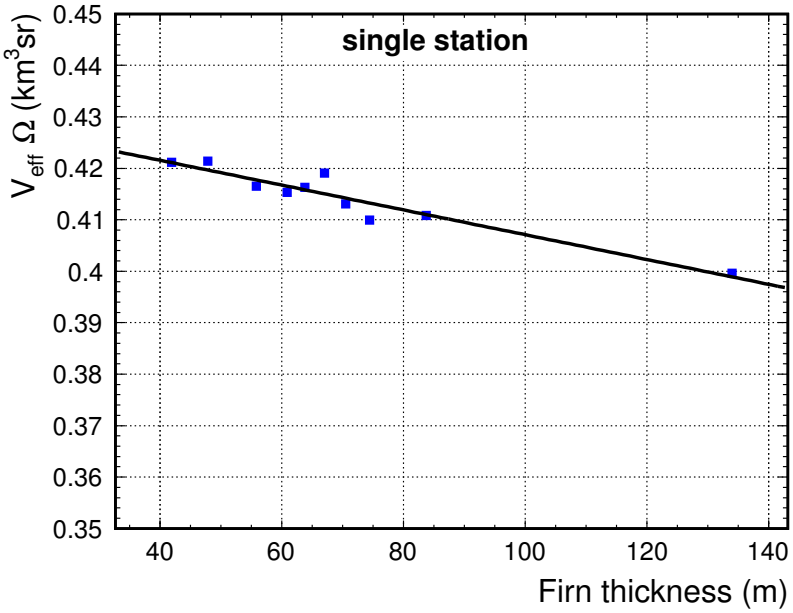

Figure 6.9: Aperture as a function of firn depth. The total shelf ice thickness is kept constant at 575 m. The depth-dependent index of refraction of the firn was scaled so that it matched the boundary values of 1.325 at the surface and 1.78 at the ice-firn interface. Error on each point $\sim 2\%$.

6.3.1 Firn Thickness

We also investigated the impact of the firn thickness on aperture. For a range of firn depths, we kept the firn index of refraction dependence with depth as in Eqn.3.1 but depth variable,z, was scaled accordingly so that $n_{firn}(z)$ matches the boundary values of 1.325 at the surface and 1.78 at the ice-firn interface. The overall ice thickness remained constant at 575m.

The results, shown in Figure 6.9, indicate that the firn depth does not affect the aperture significantly. An increase of the firn thickness by a factor of 3 from $\sim$40 m to $\sim$120 m decreases the aperture by only about 6%. The mild increase in detection rates due to a thinner firn layer can be attributed to the fact that the shadowing effect is reduced. From §4.2, we saw that shadowing impacts firn events more than bulk ice events.

6.4 Additional Signals

Our simulation treats an individual direct or reflected ray from its interaction vertex to the station where it hits the antenna and generates a voltage that is contaminated by thermal noise. Here, we briefly consider here two situations that may further complicate the above picture: (a) reflections from the firn-air surface and (b) noise from cosmic rays that may trigger our stations.

6.4.1 Surface Reflections

As depicted in Figure 6.10, the reflection off the firn-air boundary of an incoming plane way may play a role. Further, the fact that the surface at the ARIANNA site has been observed to be flat and relatively featureless [85] implies that such rays will undergo specular reflections at that interface. However, since the antenna is within about 1 m of the surface, the new reflected ray only acts as an interfering term to the main incoming 'direct' [3] ray. The amplitude of the reflecting pulse is reduced compared to the direct, and only comparable in amplitude for nearly grazing incident angles. For instance, the mean zenith angles of the incoming signals at the antenna are $\sim 43°$, and applying an average on both polarization-dependent reflectance given by Fresnel's equations yields $\sim 8\%$ of reflected power. The amplitude of this minor reflected signals will typically be a third of the main one.

Further, at incidence angles closer to the normal, the reflected pulse is observed by the back of the antenna with far poorer gain (see Figure 3.9 for the LPDA antenna pattern) than in the direction of the direct pulse. Overall, the firn-air interface should not have a significant impact but needs to be included in an even more detailed simulation study.

[3] We note that in this discussion, the direct ray refers to either the one coming straight from the vertex (direct events) and the ones from a reflection off the ice-water bottom (reflected events). It is not to be confused with direct type events as used throughout the rest of this dissertation.

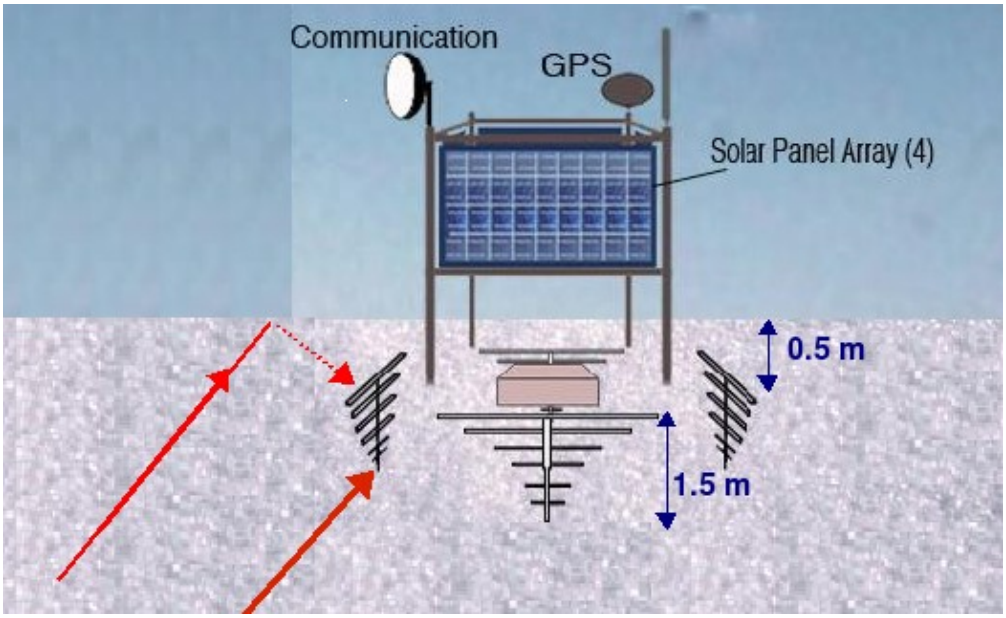

Figure 6.10: Scheme depicting surface reflection from parts of the incident plane wave can hit the antenna. The gain of the antenna at the back is smaller and the reflected signal may not contribute significantly to the voltage.

6.4.2 Cosmic Rays

The high threshold of radio detection offers the advantage of low backgrounds due to atmospheric neutrinos generated by cosmic rays. However, the latter give rise to Extensive Air Showers (EAS) with an electromagnetic core that may, upon impact with the ice, propagate into the upper 10-20 m of the firn and produce an ice-shower. This will generate coherent radio-wave in the frequency range to which ARIANNA is sensitive.

The antenna angular response, as illustrated in Figure 3.9, shows that in the back of the LPDA (which is the general direction in which such signals will hit), the gain is extremely small. The voltage measured may not be high enough for triggering, but inclusion of such background into future versions of the simulation software will provide a more accurate understanding of the cosmic ray effect on noise and triggering.

The advent of time domain triggering and its inclusion in *shelfmc* will also help discrimi-

nate against such signals, because as Figure 6.11 shows, there are characteristic differences between a typical neutrino induced Askaryan pulse and an air shower emission. The latter contains lower frequency components and is more spread out in time, while our signal contains higher frequency components up to GHz, resulting in the sharper pulse shape.

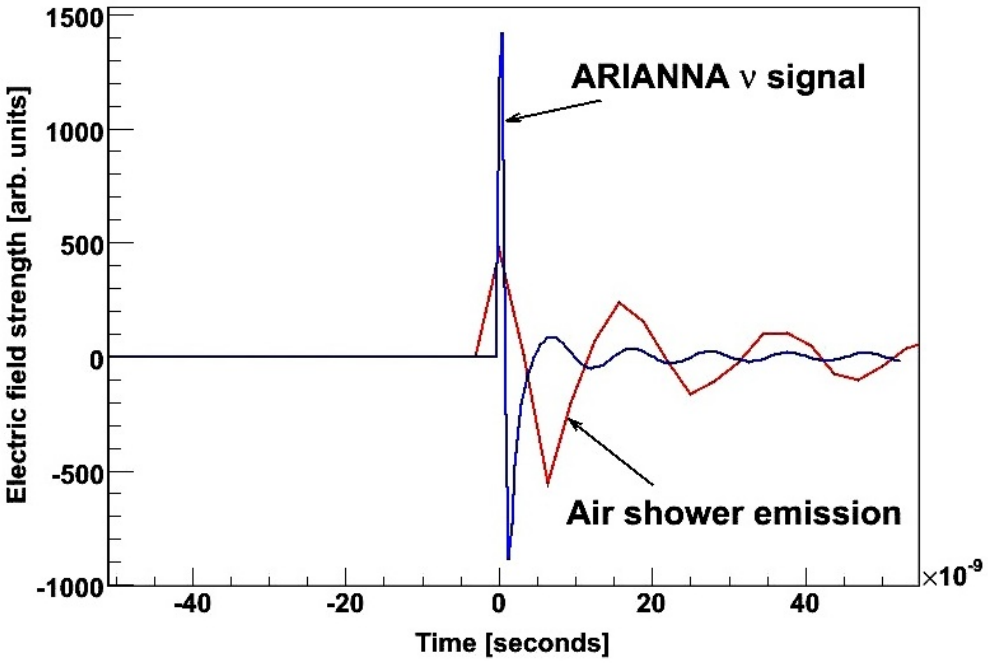

Figure 6.11: Simulation shows that the time-domain shower profile of an air shower is distinct from an Askaryan pulse that is a short bimodal pulse. From [128].

Chapter 7

Conclusions

7.1 Summary

When one considers the paradigm shift that ensued in both astrophysics and particle physics as a result of the detection of handful of neutrinos from Supernova 1987A [129], one can only imagine what richness of information could extragalactic and cosmogenic neutrinos herald us into. The Antarctic Ross Ice-shelf Antenna Neutrino Array is a next-generation ultra-high energy neutrino radiodetector that is designed to capture enough neutrinos to establish the absolute flux and carry out particle physics studies at the EeV range.

This dissertation has described the design of the prototype and initial performance of ARIANNA. The simulation software, *shelfmc*, and the new physics implemented have been documented and is summarized as follows:

- more accurate firn profile and ice thickness based on latest *in situ* measurements
- consideration of the subtle effects of the graded firn index on signal propagation ('shadowing') and polarization

- inclusion of the ν_τ regeneration effect and an approximation of the 'double-bang' for ν_τ interactions
- averaging of E- and H-planes angular response in the LPDA antenna
- added options for the hexagonal array for concept study of Hexagonal Radio Array.

Numerical simulations have shown that

- the LPDA antenna used in ARIANNA has a gain which is close to the optimum gain for sensitivity
- reflected event types account for almost 90% of the events
- more than 90% of the events occur in ice as opposed to the top firn layer
- 'shadow effects' suppress mainly direct events geometries, and is more pronounced for the firn direct events.
- the detector has a view of over 3π steradians of the Southern sky
- the aperture of ARIANNA grows almost linearly with the number of stations.

The *shelfmc* software provides the effective aperture of the telescope and give the energy-dependent sensitivity to all neutrino flavors in the energy range $10^{17.5} - 10^{20}$eV and it shows that ARIANNA is optimized for cosmogological neutrino detection.

Expected event rates for a variety of flux models can be also evaluated: a 31×31 station array spread over 900 km^2 has the potential to observe $\sim$35 GZK ν's/year from the ESS [20] model predictions.

Various systematics have also been considered and assessed. The potential impact of surface roughness in ARIANNA has been discussed and seen to have a minimal effect. Variations in

reflectivity at the ice-water boundary does not change the aperture of the station significantly, and it was seen that increases in ice-shelf thickness does not translate into an equivalent rise in aperture.

This dissertation also described techniques for neutrino energy and angular reconstruction using single station measurements. Using simulated data, we find the energy resolution of ARIANNA single station, expressed as an uncertainty in the fraction of reconstructed energy to the true energy, as

$$\sigma\left(\frac{E_\nu^{meas.}}{E_\nu}\right) \approx 2.2.$$

This estimate is independent of flavor identification and vertex reconstruction.

The angular resolution is set at

$$\sigma(\theta_\nu) \approx 2.9^\circ \qquad\qquad \sigma(\phi_\nu) \approx 2.5^\circ$$

respectively.

These resolutions improve significantly with determination of the angle difference between observed signal and the Cherenkov cone. This observation angle can be deduced from time-domain pulse shape information. The development and implementation of an advanced waveform capture technology at the station and its emulation in the software in terms of time-domain will only serve to refine the simulation package.

7.2 Future outlook

The deployment of ARIANNA prototype stations and tests carried out have enabled the investigation of physics and anthropogenic backgrounds over a two-year period and have improved our knowledge of the attenuation and reflection properties of the ice shelf. The *in situ* performance of data and control systems using inherited and newly developed waveform capture technology are being evaluated.

The main focus of the next stage are the development of:

- 4 channel data acquisition system, eventually expanding to 8 channels, for the ARIANNA station system utilizing advanced low power waveform capture technology,
- an intra-array wireless communication system to send station data to the central wireless data and communication installed by NSF contractor, Raytheon Polar Services,
- a real-time, in-situ calibration system to evaluate time dependent parameters in timing and signal sensitivity, and
- a system to monitor and control the power provided by solar panels, wind generators, and more conventional oil-based electrical generators. This system must supply power reliably during austral summer, perform "safing" operations during periods of low power such as the onset of winter, and restore power after periods of hibernation.

The deployment of the first seven stations will be through the **Hexagonal Radio Array**: six at the edges of a hexagon and one in the center. Table 7.1 provides the timeline of critical milestones for the design, testing, integration, deployment and commissioning of the various components of the data acquisition system. Integration of the design and fabrication processes will be in a phased approach, starting with the existing design of the advanced

ATWD chip, and guided by the successful deployment of a single channel system. The plans for the major integrated phases are:

Phase I, for deployment in December 2011:

Work have expanded the existing single-channel system design to include 4 channels. We have modularized the channels into a card and backplane system, such that each card contains one channel, and which can be swapped easily. The modular 4-channel system will utilize the existing, proven ATWD chips. Its software payload will contain essential functions for test and evaluation as a single-station via direct USB computer connection (e.g., USB or Ethernet) to complement the wireless network functions. The main purpose will be to test a full 4-channel system including second-level triggering that combines multiple channels in a majority-logic fashion, and to test the timing accuracy between channels.

Phase II, for deployment in December 2012:

We envision a modest redesign of the advanced ATWD chip that will be completed in spring 2012. The redesign will include a few but important changes, namely the expansion of the signal memory depth to 256 samples (from the existing 128) and cutting the power consumption in half by reducing the depth of the trigger pattern search feature from 72 to 16 trigger patterns (computer simulation of detector response have concluded that 16 is sufficient). This new chip is expected to be pin-compatible with the existing chip, and to require only minimal changes to system software. In addition, any changes and improvements to the hardware of the 8-channel system will be accomplished (e.g., to accommodate the new-generation chip), and its software payload will be expanded to include full wireless networking functionality. Improved power generation and conditioning hardware is expected to be included, and a new support tower will be fabricated such that the new system can be permanently deployed on the ice and remotely operated over the winter.

date	critical milestone
Dec 2011	Deploy and test prototype 4-channel DAQ system
Jan 2012	Phase II: Begin design of DAQ, wireless comms, and calibration systems
May 2012	Complete DAQ design and fabrication, begin testing and integration
Jun 2012	Develop Firmware, and command and monitoring software
Oct 2012	Train personnel deploying to Antarctica to install, test, and operate DAQ
Dec 2012	Deployment of first ARIANNA station with new DAQ technology
Feb 2013	Phase III: Complete evaluation of performance of ARIANNA DAQ
May 2013	Complete iteration of DAQ design, begin fabrication of DAQ for 6 stations
Sep 2013	Integrate DAQ with intra-array wireless communication and calibration
Dec 2013	Deploy, test, and commission 6 stations, integrate with existing station
Aug 2014	Report on performance of hexagonal array

Table 7.1: Timeline of future ARIANNA work and phased approach. (DAQ: Data Acquisition electronics)

We also plan to develop, test, and integrate a wireless network system based on the communication products produced by AFAR Communications. This company provides the communication equipment now deployed at the ARIANNA site by Raytheon Polar Services. Finally, we will test and integrate the inter-station calibration system based on the short pulse generating technology of Pockel Cell Drivers, which have been used by the ANITA collaboration and during the previous ARIANNA field studies.

Phase III, for deployment in December 2013:

In this phase, once we have completed our evaluation of the performance of the first ARIANNA station deployed in Phase II, a total of 6 complete stations will be prepared for deployment. In addition, one station will be constructed and maintained at UCI for local system tests and debugging. Any final changes and fixes to both the ATWD chips and system boards and software will be made and verified in the laboratory. We expect to transition to a commercial fabrication house for the assembly of the full-scale system boards (e.g., 64 single-channel modules and 8 system backplane boards, plus spares). This reduces risk by greatly speeding up larger-scale fabrication as well as by providing better uniformity in construction quality. A total of 7 stations will be deployed on the Ice.

Appendices

A Antenna Theory

Determining the choice of antenna is critical for ARIANNA as it affects sensitivity and installation costs. The experiment uses a log periodic dipole array (LPDA). For simulation purposes, it is important to understand the mathematical properties of antenna parameters.

The discussion below is from Ref.[130] and we refer the reader to the textbook for a more detailed description and useful visual figures.

Antenna Basics

Although the radiation pattern characteristics of an antenna involve three-dimensional vector fields for a full representation, several simple single-valued scalar quantities can provide the information required for many engineering applications. There are:

- half-power beam-width, here referred to as *hpbw*
- beam area, Ω_A
- beam efficiency, ϵ_M
- directivity D or gain G
- effective aperture A_e

Half-Power Beam-Width(*hpbw*) The half power beamwidth is the angular separation between the half power points of the main lobe on the antenna radiation pattern, where the gain is one half the maximum value (or -3dB).

Beam area The beam area or *beam solid angle* or Ω_A, with units of steradians, of an antenna is given by the integral of the normalized power pattern over a sphere (4π sr)

$$\Omega_A = \int_{\phi=0}^{\phi=2\pi} \int_{\theta=0}^{\theta=\pi} P_n(\theta,\phi) \sin\theta d\theta d\phi = \iint_{4\pi} P_n(\theta,\phi) d\Omega$$

where $d\Omega = \sin\theta d\theta d\phi$ (sr) and P_n is a dimensionless[1] quantity for the normalized power pattern, given by the ratio of the Poynting vector (power per unit area) at (θ,ϕ) to its maximum value: $P_n(\theta,\phi) = \frac{S(\theta,\phi)}{S(\theta,\phi)_{max}}$.

The beam area Ω_A is the solid angle through which all of the power radiated by the antenna would stream if $P(\theta,\phi)$ maintained its maximum value of Ω_A and was zero elsewhere. Thus the power radiated is $P(\theta,\phi)\Omega_A$ watts.

The *beam area* of an antenna can often by described *approximately* in terms of the angles subtended by the *half-power points* of the main lobe in the two principal planes. Thus,

$$\text{Beam area} \cong \Omega_{\text{A}} \cong \theta_{\text{HP}}\phi_{\text{HP}} \text{ (sr)}$$

where θ_{HP} and ϕ_{HP} are the *half-power beamwidths*(*hpbw*) in the two principal planes, minor lobes being neglected.

Beam efficiency The (total) *beam area* Ω_A (or *beam solid angle*) consists of the main beam area (or solid angle) Ω_M plus the minor-lobe area (or solid angle) Ω_m:

$$\Omega_A = \Omega_M + \Omega_m.$$

[1]The decibel level is given by $dB = 10\log_{10} P_n(\theta,\phi)$.

The ratio of the main beam area to the (total) beam area is called the (main) *beam efficiency* ϵ_M:

$$\text{Beam efficiency} = \epsilon_{\text{M}} = \frac{\Omega_{\text{M}}}{\Omega_{\text{A}}} \text{ (dimensionless)}$$

Similarly, we have the *stray factor* ϵ_m for the minor-lobe area (Ω_m) It follows that $\epsilon_M + \epsilon_m = 1$.

Directivity D and Gain G The directivity D and the gain G are probably the most important parameters of an antenna. The *directivity* of an antenna is equal to the ratio of the maximum power density $P(\theta,\phi)_{max}$ (watts/m^2) to its average value over a sphere as observed in the far field of an antenna. Thus,

$$D = \frac{P(\theta,\phi)_{max}}{P(\theta,\phi)_{av}} \tag{A.1}$$

The directivity is a dimensionless ratio ≥ 1. The idealized isotropic antenna (Ω_A) has the lowest possible directivity $D = 1$. Now, the average power density over a sphere is given by

$$P(\theta,\phi)_{av} = \frac{1}{4\pi} \iint_{4\pi} P(\theta,\phi) d\Omega \ (W sr^{-1})$$

Therefore, the directivity from beam area Ω_A

$$D = \frac{4\pi}{\iint_{4\pi} P_n(\theta,\phi) d\Omega} = \frac{4\pi}{\Omega_A} \tag{A.2}$$

where $P_n(\theta,\phi)d\Omega = P(\theta,\phi)/P(\theta,\phi)_{max}$ = normalized power pattern.

Thus, the directivity is the ratio of the area of a sphere (4π sr) to the beam area Ω_A of the antenna.The smaller the beam area, the larger the directivity D. For an antenna that radiates over only half a sphere the beam area $\Omega_A = 2\pi$ sr and the directivity is

$D = 4\pi/2\pi = 2 = 3.01$ dBi, where dBi = decibels over isotropic. The simple short dipole has a beam area $\Omega_A = 2.67\pi$ sr and a directivity $D = 1.5$ (= 1.76 dBi).

The *gain* G of an antenna is an actual or realized quantity which is less than the directivity D due to ohmic losses in the antenna. In transmitting, these losses involve power fed to the antenna which is not radiated but heats the antenna structure. A mismatch in feeding the antenna can also reduce the gain. The ratio of the gain to the directivity is the *antenna efficiency factor*. Thus,

$$G = kD$$

where k = efficiency factor ($0 \leq k \leq 1$) and is dimensionless. In many well-designed antennas, k may be close to unity. In practice, G is always less than D, with D its maximum idealized value.

If the half-power beamwidths of an antenna are known, its directivity is

$$D = \frac{41253^{\square}}{\theta^{\circ}_{HP}\phi^{\circ}_{HP}}$$

where

$41253^{\square}$ = number of square degrees in sphere= $4\pi(180/\pi)^2$ square degrees ($^{\square}$). Neglecting minor lobes, the above value in the equation can be approximated to $40000^{\square}$.

For example, if an antenna has a main lobe with both half-power beamwidths (HPBWs)=20°, its directivity from above is *approximately*

$$D = \frac{4\pi(\text{sr})}{\Omega_a((\text{sr}))} \cong \frac{41253(\text{deg}^2)}{\theta^{\circ}_{HP}\phi^{\circ}_{HP}} = \frac{41253(\text{deg}^2)}{20^{\circ} \times 20^{\circ}} \cong 103 \cong 20 \text{ dBi}$$

which means that the antenna radiates a power in the direction of the main-lobe maximum which is about 100 times as much as would be radiated by a non-directional (isotropic)

antenna for the same power input.

Antenna apertures A_e Due to edge effects, the physical aperture A_p of an antenna usually does not have a uniform field response to extract power from an incident wave. There is an aperture efficiency ϵ_{ap} that gives an *effective aperture*A_e through

$$\epsilon_{ap} = \frac{A_e}{A_p}.$$

For horn and parabolic reflector antenna, aperture efficiencies are commonly in the range of 50 to 80%; large dipole or patch arrays with uniform field to the edges of the physical aperture may attain higher aperture efficiencies approaching 100%.

Consider an antenna with an effective aperture A_e, which radiates all of its power in a conical patter of beam area Ω_A (Figure). Assuming a uniform field E_a over the aperture, the power radiated is

$$P = \frac{E_a^2}{Z_0} A_e$$

where Z_0 is the intrinsic impedance of medium (377 Ω for air or vacuum). Assuming a uniform field E_r in the far field at a distance r, the power radiated is also given by

$$P = \frac{E_r^2}{Z_0} r^2 \Omega_A.$$

Equation the two equations above and noting that $E_r = E_a A_e / r\lambda$ yields the aperture-beam-area relation

$$\lambda^2 = A_e \Omega_A$$

where Ω_A is beam area (sr). Noting that $D = 4\pi/\Omega_A$, it follows that

$$D = 4\pi\frac{A_e}{\lambda^2}. \tag{A.3}$$

All antennas have an effective aperture which can be calculated or measured. Even the hypothetical, idealized isotropic antenna, for which $D = 1$, has an effective aperture

$$A_e = \frac{D\lambda^2}{4\pi} = \frac{\lambda^2}{4\pi} = 0.0796\lambda^2.$$

When the antenna is receiving with a load resistant R_L matched to the antenna radiation resistance R_r ($R_L = R_r$), as much power is reradiated from the antenna as is delivered to the load. This is the condition of *maximum power transfer* (antenna assumed lossless).

In the circuit case of a load matched to a generator, as much power is dissipated in the generator as is delivered to the load. Thus, for the case of the dipole antenna in Figure ? we have a load power

$$P_{\text{load}} = SA_e$$

where S is the power density at the receiving antenna in (W/m^2) and A_e is the effective aperture of antenna (m^2).

Effective Height The *effective height* h(meters) of an antenna is another parameter related to the apeture. Multiplying the effective height by the incident field E (volts per meter) pf the same polarization gives the voltage V induced. Thus,

$$V = hE$$

Accordingly, the effective height may be defined as the ratio of the induced voltage to the incident field or

$$h = \frac{V}{E}$$

Effective height can also be expressed more generally as a vector quantity. Thus (for linear polarization) we can write

$$V = \mathbf{h}_e \cdot E = h_e E \cos\theta$$

where

h_e = effective height and polarization angle of antenna, m

$\mathbf{E}$ = field intensity and polarization angle of incident wave, V m^{-1}

θ = angle between polarization angles of antenna and wave, deg.

For an antenna of radiation resistance R_r matched to its load, the power delivered to the load is equal to

$$P = \frac{1}{4}\frac{V^2}{R_r} = \frac{h^2 E^2}{4R_r}. \tag{A.4}$$

In terms of the effective aperture, the same power is given by

$$P = SA_e = \frac{E^2 A_e}{Z_0}.$$

Equating the two above equations gives

$$h_e = 2\sqrt{\frac{R_r A_e}{Z_0}} \qquad \text{and} \qquad A_e = \frac{h_e^2 Z_0}{4R_r} \tag{A.5}$$

Thus, effective height and effective aperture are related via radiation resistance and the intrinsic impedance of space.

B Effects from Non-uniform Index of Refraction

We document two Physics effects arising from a varying index of refraction. The first effect resulting from propagation through a continuously layered medium is a curvature of the signal and gives rise to a 'shadow' locus around an observation point that excludes rays beyond it from reaching it. The second is the Fresnel equation that applies for refraction through discontinuous media boundary.

B.1 Graded Index of Refraction

We here follow the treatment given in Chapter 1 of Ref [131]. We consider a continuously layered medium with refraction index $n_{eff}(z) = \frac{c(z_0)}{c(z)} = \frac{n(z)}{n(z_0)}$. Note that an effective expression $n_{eff}(z)$ is used, explicitly given as the ratio of the index equation[speed of light], $n(z)[c(z)]$, to the index[speed of light] at the source point, $n(z_0)[c(z_0)]$. Let $r = 0$, $z = z_0$ be the coordinates of the source S and $P_1(r, z)$ be the observation point. If the ray leaves the source at an angle θ_0 with respect to the vertical (Fig B.1), Snell's law $\sin\theta(z) = n_{eff}^{-1}\sin\theta_0$ holds at any arbitrary horizon z. Integrating $dr = \tan\theta(z)dz$ along the upgoing part of the ray we obtain

$$r(\theta_0, z) = \int_{z_0}^{z} \tan\theta(z)dz = \sin\theta_0 \int_{z_0}^{z} [n_{eff}^2(z) - \sin^2\theta_0]^{-1/2}dz \tag{B.6}$$

where we have used the fact that $\tan\theta = \sin\theta/\sqrt{1-\sin^2\theta}$.

The general expression for r, when the ray turns once at the horizon z_r between the source and the receiver, contains two terms:

$$r(\theta_0, z) = \sin\theta_0 \left| \int_{z_0}^{z_r} [n_{eff}^2(z) - \sin^2\theta_0]^{-\frac{1}{2}}dz \right| + \sin\theta_0 \left| \int_{z}^{z_r} [n_{eff}^2(z) - \sin^2\theta_0]^{-1\,\bar{2}}dz \right|. \tag{B.7}$$

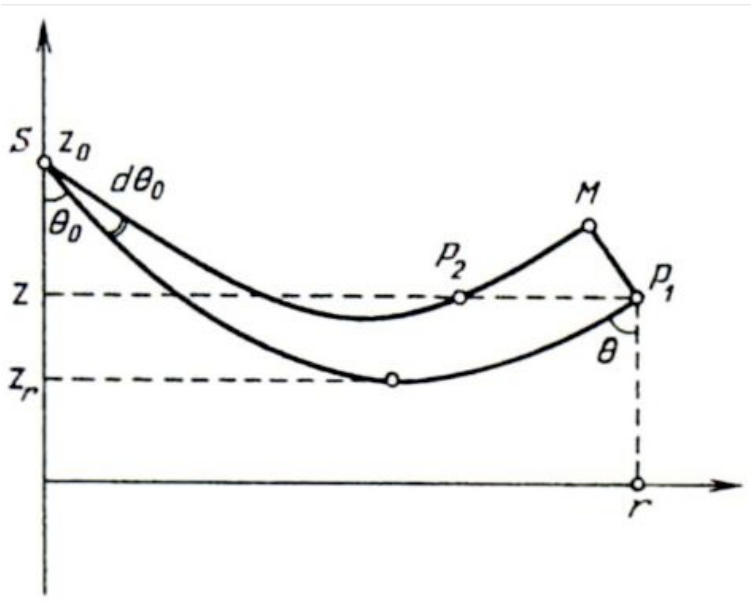

Figure B.1: Fig 1.4 from [131] showing path ray curvature through a continuously layered medium. Note that in this diagram, the index increases along the positive z axis.

Curved Path and Timing We extend the above idea to calculate the curved path distance that can be used for deriving timing information for instance. Denoting the path length by l and the time by t, we have $dl = \sec\theta(z)dz$ and $dt = c^{-1}n(z)dl$, where c is the speed of light in vacuum. Integrating for path-length and time respectively, we have

$$\begin{aligned} l(\theta_0, z) &= \int_{z_0}^{z} \sec\theta(z)dz \\ t(\theta_0, z) &= \frac{1}{c}\int_{z_0}^{z} n(z)\cdot\sec\theta(z)dz = \frac{1}{c}\int_{z_0}^{z} \frac{n_{eff}\cdot n(z)}{\sqrt{n_{eff}^2 - \sin^2\theta_0}}dz \end{aligned} \tag{B.8}$$

where we have used $\sec\theta = 1/\sqrt{1-\sin^2\theta}$ and n_{eff} defined as $\frac{n(z)}{n(z_0)}$ as before.

B.2 Fresnel Equations at a Plane Interface

The Fresnel equations that characterize the transmission and reflection properties between two dielectric media are discussed in most standard electrodynamics textbooks. We reproduce them here for completeness.

Reflectance and Transmisttance The fraction of the incident power that is reflected from the interface is called the reflectance R, and the refracted fraction is given by transmittance T. R and T are the square of the reflection (r) and transmission (t) coefficients respectively. Note that as a consequence of the conservation of energy, the transmission coefficient in each case is given by $T_s = 1 - R_s$ and $T_p = 1 - R_p$, and this is applied in Equations B.12 and B.13 below. It is also assumed that the media are linear, isotropic, homogeneous and that they are non-magnetic , i.e dielectrics satisfy $\mu_1 = \mu_2 = \mu_0$.

Since reflectance and transmittance depend on the incident polarization, we consider two sets of equations: one for the polarization vector along the plane of incidence (p-polarized) and the other for the polarization vector lying perpendicular to the plane of incidence (s-polarized). For p-polarization, the reflectance is

$$R_p = \left(\frac{n_2^2 \sqrt{n_1^2 - n_1^2 \sin^2\theta_1} - n_1^2 \sqrt{n_2^2 - n_1^2 \sin^2\theta_1}}{n_2^2 \sqrt{n_1^2 - n_1^2 \sin^2\theta_1} + n_1^2 \sqrt{n_2^2 - n_1^2 \sin^2\theta_1}} \right)^2 = \left(\frac{n_1 \cos\theta_2 - n_2 \cos\theta_1}{n_1 \cos\theta_2 + n_2 \cos\theta_1} \right)^2 \quad \text{(B.9)}$$

For s-polarized electric field, the reflectance is given by

$$R_s = \left(\frac{\sqrt{n_1^2 - n_1^2 \sin^2\theta_i} - \sqrt{n_2^2 - n_1^2 \sin^2\theta_i}}{\sqrt{n_1^2 - n_1^2 \sin^2\theta_i} + \sqrt{n_2^2 - n_1^2 \sin^2\theta_i}} \right)^2 = \left(\frac{n_1 \cos\theta_1 - n_2 \cos\theta_2}{n_1 \cos\theta_1 + n_2 \cos\theta_2} \right)^2 \quad \text{(B.10)}$$

The equations have re-expressed with the substitutions given by Snell's Law:

$$n_1 \sin\theta_1 = n_2 \sin\theta_2 \tag{B.11}$$

Arbitrary Incident Polarization In the context of our ice-firn interface simulation, the above equations will apply for the situation of uniform firn and ice. For generality, we uses number indices to refer to different medium. For an arbitrary polarization vector, we split the incident electric field ($\vec{E_1}$) into its s- and p-components and treat them with the individual Fresnel transmission equations, and recombine them to obtain the transmitted electric field ($\vec{E_2}$). This option is available in the code for case studies of a uniform firn as may needed. The calculations are implemented in the following way.

First, three planes are defined:
(a) one perpendicular to the plane of incidence

$$\vec{n}_{2\perp} = \vec{P}_2 \times \vec{n}_{normal},$$

(b) one parallel to the plane of incidence the firn medium

$$\vec{n}_{2\parallel} = \vec{n}_{2\perp} \times \vec{P}_2, \text{and}$$

(c) another parallel to the plane of incidence in the ice medium

$$\vec{n}_{1\parallel} = \vec{n}_{2\perp} \times \vec{P}_1,$$

where we note that $\vec{n}_{2\perp}$ defines the same plane as $\vec{n}_{1\perp}$. We break the components of incident electric field $\vec{E_1}$ into:

$$E_{1\perp} = \vec{E_1} \cdot \vec{n}_{2\perp}, \text{and} \qquad E_{1\parallel} = \vec{E_1} \cdot \vec{n}_{1\parallel}.$$

Using alternative and simpler forms of the Fresnel equations, we have the reflection and transmission coefficients for both p- and s-polarizations:

$$r_p = \frac{\tan(\theta_1 - \theta_2)}{\tan(\theta_1 + \theta_2)}, \qquad t_p = \sqrt{1 - r_p^2} = \sqrt{1 - R_p} \tag{B.12}$$

and

$$r_s = -\frac{\sin(\theta_1 - \theta_2)}{\sin(\theta_1 + \theta_2)} \qquad t_s = \sqrt{1 - r_s^2} = \sqrt{1 - R_s}. \tag{B.13}$$

These explicitly give us the components of transmitted polarization $\vec{E_2}$ as

$$E_{2\parallel} = t_p \cdot E_{1\parallel} \qquad E_{2\perp} = t_s \cdot E_{1\perp}.$$

Putting them together, we have the transmitted polarization vector as:

$$\vec{E_2} = E_{2\perp}(\vec{n}_{2\perp}) + E_{2\parallel}(\vec{n}_{2\parallel}). \tag{B.14}$$

C Instructions on Running ARIANNA Code

C.1 Installation of ROOT

The *shelfmc* code is a C, C++, ROOT combined program. ROOT is a C++ based large sale data analysis tool developed at CERN. LINUX system generally has a default C/C++ compiler but may not have ROOT. In order to compile and run the *icemc* code users need to install the ROOT software. Instruction of how to download and install ROOT can be found at

`http://root.cern.ch`.

C.2 How to Compile and Run *shelfmc*

The latest version of `Makefile` for *shelfmc* is reproduced in the set of pages of the end of this current subsection. The usual commands at the prompt apply:

`make`

to compile the files in the directory of *shelfmc*, and

`make clean`

to clean up the previously created files.

Upon compilation, there will be an executable file generated called `shelfmc.exe`. To run the code with the default parameters, the following is entered: `./shelfmc.exe`

For a series of tests that requires different desired parameters, like for example evaluating apertures for various specified energies, the user can enter a script named `run` at the terminal where the file will contain a sequence of terminal commands as follows:

```
./shelfmc.exe 1000000 17
./shelfmc.exe 1000000 17.5
./shelfmc.exe 1000000 18
./shelfmc.exe 1000000 18.5
# a series of simulations with NNU = 10^6 and varying EXPONENT
```

The above commands have two arguments that *shelfmc* will have been modified to accept as `NNU` and `EXPONENT`, for the number of neutrinos and energy respectively (see also the next subsection for comment about this energy runs).

C.3 Steering File Parameters

In `input.txt` and `declaration.hh`, there are sets of parameters that can be varied as needed for various studies. Most of the parameter options are fairly self explanatory and/or briefly commented within the code itself. The more obscure or frequently used parameters are discussed below. Usually, the `input.txt` will contain those arguments that would be readily changed for a given series of comparative study and do not require re-compilation of the code. On the other hand, the `declaration.hh` contains those options that will be less frequently modified, for example the 'shadowing', nu-tau regeneration and LPM effects.

Future users may find it useful to shift some options around from `declaration.hh` and relocate them into `input.txt` and move options that are no longer investigated away from that latter file.

Computational Times and Accuracy

The simulation tasks can usually be handled by a single machine. As estimate of the running times and the accompanying errors on the statistics are provided in the following Table C.2.

The errors were derived by running with at least 10 random seeds and with a choice of output value (in this case the integral weight), we calculated the standard deviation as a percentage fraction of the mean.

NNU	Flux	Array Type	Approx. Time	Error on Statistics
10000	GZK	Single	<1min	22%
100000	GZK	Single	2 min	8%
200000	specific E_ν	Single	5 min	3%
200000	specific E_ν	Hexagonal	15 min	3%
200000	specific E_ν	30×30	1 hr	3%
1000000	GZK	Hexagonal	45 min	<1%
1000000	GZK	30×30	3 hr 45 min	<1%
2000000	GZK	Single	25 min	<1%
10000000	GZK	Hexagonal	8 hr	<1%

Table C.2: Approximate computational times and statistical errors for select input parameters.

Input file with default value for selected parameters

* * * START OF FILE * * *

```
#inputs for ARIANNA simulation
1000000 #NNU
18 #EXPONENT, !should be exclusive with SPECTRUM
1000  #STGap, m
8  #N_Ant_perST, not to be confused with ST_TYPE above
3  #N_Ant_Trigger, this is the minimum number of AT to trigger
1      #FIRN
1.325#NFIRN
75   #FIRNDEPTH in meters
1      #NROWS 12 initially
1      #NCOLS 12 initially
1      #SPECTRUM, use spectrum for flux
0      #CONST_ATTENLENGTH, use constant attenuation length if ==1
450  #ATTEN_UP, this is the conjunction of the plot attenlength_up
#and attlength_down when setting REFLECT_RATE=0.5(3dB)
5      #NSIGMA, threshold of trigger
1.     #ATTEN_FACTOR, change of the attenuation length
0.5    #REFLECT_RATE,power reflection rate at the ice bottom
1      #GZK, 1 means using GZK flux, 0 means E-2 flux
0      #FANFLUX, use flux which only covers from 10^17 eV to 10^20 eV
0      #WIDESPECTRUM, use 10^16 eV to 10^21.5 eV as the energy spectrum,
#otherwise use 10^17-10^20
#-----------------------------------------------------
1  #DEPTH_DEPENDENT_N; 1 means n of firn is function of depth
```

```
1 #LPM;
1 #TAUREGENERATION,if 1=tau regeneration effect, if 0=original
1 #SIGNAL_FLUCT
1  #SHADOWING
575 #ICETHICK in meters
```

* * * END OF FILE * * *

C.4 Makefile script

* * * START OF FILE * * *

```
# make file to compile and link a test program that uses the verbmenu library
CCFILE       = shelfmc.cc  functions.cc

# Define filename suffixes
ObjSuf        = .o
SrcSuf        = .cc
IncSuf        = .hh
ExeSuf        = .exe
DllSuf        = .so
OutPutOpt     = -o

# Define the compile and link commands
CXX           = g++
CXXFLAGS      = -c -g -O2 -o $(OBJ) -Wall -fPIC -I$(ROOTSYS)/include
LD            = g++
LDFLAGS       = -O

# Define root libraries
#ROOTLIBS      = -L$(ROOTSYS)/lib
ROOTLIBS      = `${ROOTSYS}/bin/root-config --libs`

# Define all my libraries
LIBS          = $(ROOTLIBS)
```

```
# Define shortcuts for compiling and linking
COMPILE = $(CXX) $(CXXFLAGS) $(SCRATCH)
LINK =  $(LD) $(LDFLAGS) $(OBJ) $(LIBS) $(OutPutOpt) $(EXE)
#------------------------------------------------------------------------

# Define the file names
OBJ       = shelfmc.obj
SRC       = $(CCFILE)
EXE       = shelfmc.exe
SCRATCH   = tmp.cc
INC       = shelfmc.inc

all:            $(EXE)

# Update the executable if the object file has changed
$(EXE):  $(OBJ)
$(LINK)

# Update the object file if the source, or include file changed
$(OBJ):     $(SRC)
      cat $(CCFILE) > $(SCRATCH)
$(COMPILE)

clean:
@rm -f $(OBJ) $(EXE) core* shelfmc.exe shelfmc.obj shelfmc.root $(SCRATCH)

.SUFFIXES: .$(SrcSuf)
```

```
.$(SrcSuf).$(ObjSuf):
$(CXX) $(CXXFLAGS) -c $<
```

* * * END OF FILE * * *

Bibliography

[1] J. K. Becker, "High-energy neutrinos in the context of multimessenger physics," *Phys.Rept.* **458** (2008) 173–246, arXiv:0710.1557 [astro-ph].

[2] T. K. Gaisser, F. Halzen, and T. Stanev, "Particle astrophysics with high energy neutrinos," *Physics Reports* **258** no. 3, (1995) 173 – 236. http://www.sciencedirect.com/science/article/pii/037015739500003Y.

[3] K. Greisen, "End to the Cosmic-Ray Spectrum?," *Physical Review Letters* **16** (Apr., 1966) 748–750.

[4] G. T. Zatsepin and V. A. Kuz'min, "Upper Limit of the Spectrum of Cosmic Rays," *Soviet Journal of Experimental and Theoretical Physics Letters* **4** (Aug., 1966) 78–+.

[5] J. G. Learned and K. Mannheim, "High-Energy Neutrino Astrophysics," *Annual Review of Nuclear and Particle Science* **50** (2000) 679–749.

[6] **HiRes Collaboration** Collaboration, R. Abbasi *et al.*, "First observation of the Greisen-Zatsepin-Kuzmin suppression," *Phys.Rev.Lett.* **100** (2008) 101101, arXiv:astro-ph/0703099 [astro-ph].

[7] M. Takeda, N. Sakaki, K. Honda, M. Chikawa, M. Fukushima, *et al.*, "Energy determination in the Akeno Giant Air Shower Array experiment," *Astropart.Phys.* **19** (2003) 447–462, arXiv:astro-ph/0209422 [astro-ph].

[8] P. W. Gorham *et al.*, "The ExaVolt Antenna: A Large-Aperture, Balloon-embedded Antenna for Ultra-high Energy Particle Detection," *Astropart. Phys.* **35** (2011) 242–256, arXiv:1102.3883 [astro-ph.IM].

[9] R. J. Gould and G. Schréder, "Opacity of the universe to high-energy photons," *Phys. Rev. Lett.* **16** (Feb, 1966) 252–254. http://link.aps.org/doi/10.1103/PhysRevLett.16.252.

[10] J. V. Jelley, "High-energy γ-ray absorption in space by a 3.5° k microwave field," *Phys. Rev. Lett.* **16** (Mar, 1966) 479–481. http://link.aps.org/doi/10.1103/PhysRevLett.16.479.

[11] V. S. Beresinsky and G. T. Zatsepin, "Cosmic rays at ultra high energies (neutrino?)," *Physics Letters B* **28** (Jan., 1969) 423–424.

[12] F. W. Stecker, "Ultrahigh Energy Photons, Electrons, and Neutrinos, the Microwave Background, and the Universal Cosmic-Ray Hypothesis," *Astrophys.Space Sci* **20** (Jan., 1973) 47–57.

[13] R. Gandhi, C. Quigg, M. H. Reno, and I. Sarcevic, "Neutrino interactions at ultrahigh energies," *Phys. Rev. D* **58** no. 9, (Nov., 1998) 093009–+, arXiv:hep-ph/9807264.

[14] F. W. Stecker, C. Done, M. H. Salamon, and P. Sommers, "High-energy neutrinos from active galactic nuclei," *Physical Review Letters* **66** (May, 1991) 2697–2700.

[15] E. Waxman and J. Bahcall, "High Energy Neutrinos from Cosmological Gamma-Ray Burst Fireballs," *Physical Review Letters* **78** (Mar., 1997) 2292–2295, arXiv:astro-ph/9701231.

[16] S. Yoshida, H.-y. Dai, C. C. Jui, and P. Sommers, "Extremely high-energy neutrinos and their detection," *Astrophys.J.* **479** (1997) 547–559, arXiv:astro-ph/9608186 [astro-ph].

[17] O. E. Kalashev, V. A. Kuzmin, D. V. Semikoz, and G. Sigl, "Ultrahigh-energy neutrino fluxes and their constraints," *Phys. Rev. D* **66** no. 6, (Sep, 2002) 063004.

[18] L. A. Anchordoqui and T. Montaruli, "In Search of Extraterrestrial High-Energy Neutrinos," *Annual Review of Nuclear and Particle Science* **60** (Nov., 2010) 129–162, arXiv:0912.1035 [astro-ph.HE].

[19] F. Wu, *Using ANITA-I to constrain ultra high energy neutrino-nucleon cross-section.* PhD thesis, University of California, Irvine, 2009.

[20] R. Engel, D. Seckel, and T. Stanev, "Neutrinos from propagation of ultrahigh energy protons," *Phys. Rev. D* **64** no. 9, (Oct, 2001) 093010.

[21] M. Ave, N. Busca, A. Olinto, A. Watson, and T. Yamamoto, "Cosmogenic neutrinos from ultra-high energy nuclei," *Astroparticle Physics* **23** no. 1, (2005) 19 – 29. http://www.sciencedirect.com/science/article/pii/S0927650504001859.

[22] M. Ahlers, L. A. Anchordoqui, H. Goldberg, F. Halzen, A. Ringwald, and T. J. Weiler, "Neutrinos as a diagnostic of cosmic ray galactic-extragalactic transition," *Phys. Rev. D* **72** no. 2, (Jul, 2005) 023001.

[23] D. Allard, M. Ave, N. Busca, M. A. Malkan, A. V. Olinto, E. Parizot, F. W. Stecker, and T. Yamamoto, "Cosmogenic neutrinos from the propagation of ultrahigh energy nuclei," *Journal of Cosmology and Astroparticle Physics* **2006** no. 09, (2006) 005. http://stacks.iop.org/1475-7516/2006/i=09/a=005.

[24] H. Yüksel and M. D. Kistler, "Enhanced cosmological grb rates and implications for cosmogenic neutrinos," *Phys. Rev. D* **75** no. 8, (Apr, 2007) 083004.

[25] Connolly. A., "The radio cherenkov technique for ultra-high energy neutrino detection," *Nuclear Instruments and Methods in Physics Research Section A: Accelerators, Spectrometers, Detectors and Associated Equipment* **595** no. 1, (2008) 260 – 263. http://www.sciencedirect.com/science/article/pii/S0168900208009911. RICH 2007, Proceedings of the Sixth International Workshop on Ring Imaging Cherenkov Detectors.

[26] D. Hooper, A. Taylor, and S. Sarkar, "The impact of heavy nuclei on the cosmogenic neutrino flux," *Astroparticle Physics* **23** no. 1, (2005) 11 – 17. http://www.sciencedirect.com/science/article/pii/S0927650504001847.

[27] F. W. Stecker, "Photodisintegration of ultrahigh-energy cosmic rays by the universal radiation field," *Phys. Rev.* **180** no. 5, (Apr, 1969) 1264–1266.

[28] J. Abraham, P. Abreu, M. Aglietta, E. J. Ahn, D. Allard, I. Allekotte, J. Allen, J. Alvarez-Muñiz, M. Ambrosio, L. Anchordoqui, and et al., "Measurement of the Depth of Maximum of Extensive Air Showers above 10^{18}eV," *Physical Review Letters* **104** no. 9, (Mar., 2010) 091101, arXiv:1002.0699 [astro-ph.HE].

[29] **The Telescope Array Collaboration** Collaboration, D. Ikeda, "Ultra-high energy cosmic-ray spectra measured by the Telescope Array experiment from hybrid observations," in *International Cosmic Ray Conference*, 32nd International Cosmic Ray Conference. 2011.

[30] N. A. Bahcall, J. P. Ostriker, S. Perlmutter, and P. J. Steinhardt, "The Cosmic Triangle: Revealing the State of the Universe," *Science* **284** (May, 1999) 1481, arXiv:astro-ph/9906463.

[31] S. M. Carroll, "The Cosmological Constant," *Living Reviews in Relativity* **4** (Feb., 2001) 1, arXiv:astro-ph/0004075.

[32] A. J. Bunker, E. R. Stanway, R. S. Ellis, and R. G. McMahon, "The star formation rate of the Universe at z˜ 6 from the Hubble Ultra-Deep Field," *Mon.Not.Roy.Astron.Soc.* **355** (Dec., 2004) 374–384, arXiv:astro-ph/0403223.

[33] E. Waxman, "Cosmological Origin for Cosmic Rays above 10 19 eV," *Astrophys.J.* **452** (Oct., 1995) L1, arXiv:astro-ph/9508037.

[34] A. Mucke, R. Engel, J. P. Rachen, R. J. Protheroe, and T. Stanev, "Monte Carlo simulations of photohadronic processes in astrophysics," *Comput. Phys. Commun.* **124** (2000) 290–314, arXiv:astro-ph/9903478.

[35] E. Fermi, "On the origin of the cosmic radiation," *Phys. Rev.* **75** (Apr, 1949) 1169–1174. http://link.aps.org/doi/10.1103/PhysRev.75.1169.

[36] F. W. Stecker, "Note on high-energy neutrinos from active galactic nuclei cores," *Phys. Rev. D* **72** no. 10, (Nov., 2005) 107301, arXiv:astro-ph/0510537.

[37] R. J. Protheroe, "High energy neutrinos from blazars," arXiv:astro-ph/9607165.

[38] K. Mannheim, R. J. Protheroe, and J. P. Rachen, "Cosmic ray bound for models of extragalactic neutrino production," *Phys. Rev. D* **63** no. 2, (Jan., 2001) 023003, arXiv:astro-ph/9812398.

[39] E. Waxman, S. R. Kulkarni, and D. A. Frail, "Implications of the Radio Afterglow from the Gamma-Ray Burst of 1997 May 8," *Astrophys.J.* **497** (Apr., 1998) 288, arXiv:astro-ph/9709199.

[40] E. Waxman and J. N. Bahcall, "Neutrino Afterglow from Gamma-Ray Bursts: ~10^{18} EV," *Astrophys.J.* **541** (Oct., 2000) 707–711, arXiv:hep-ph/9909286.

[41] S. Razzaque, P. Mészáros, and E. Waxman, "High Energy Neutrinos from Gamma-Ray Bursts with Precursor Supernovae," *Physical Review Letters* **90** no. 24, (June, 2003) 241103, arXiv:astro-ph/0212536.

[42] **ANITA collaboration** Collaboration, P. Gorham *et al.*, "New Limits on the Ultra-high Energy Cosmic Neutrino Flux from the ANITA Experiment," *Phys.Rev.Lett.* **103** (2009) 051103, arXiv:0812.2715 [astro-ph].

[43] E. Waxman and J. N. Bahcall, "High-energy neutrinos from astrophysical sources: An Upper bound," *Phys.Rev.* **D59** (1999) 023002, arXiv:hep-ph/9807282 [hep-ph].

[44] K. Mannheim, "High-energy neutrinos from extragalactic jets," *Astroparticle Physics* **3** (May, 1995) 295–302.

[45] G. Sigl, S. Lee, P. Bhattacharjee, and S. Yoshida, "Probing grand unified theories with cosmic-ray, gamma-ray, and neutrino astrophysics," *Phys. Rev. D* **59** no. 4, (Feb., 1999) 043504, arXiv:hep-ph/9809242.

[46] R. Abbasi, Y. Abdou, T. Abu-Zayyad, J. Adams, J. A. Aguilar, M. Ahlers, K. Andeen, J. Auffenberg, X. Bai, M. Baker, and et al., "Constraints on the extremely-high energy cosmic neutrino flux with the IceCube 2008-2009 data," *Phys. Rev. D* **83** no. 9, (May, 2011) 092003, arXiv:1103.4250 [astro-ph.CO].

[47] **The AUGER Collaboration** Collaboration, Y. Guardincerri, "The Pierre Auger Observatory and ultra-high energy neutrinos: upper limits to the diffuse and point source fluxes ," in *International Cosmic Ray Conference*, 32nd International Cosmic Ray Conference. 2011.

[48] I. Kravchenko, C. Cooley, S. Hussain, D. Seckel, P. Wahrlich, *et al.*, "Rice limits on the diffuse ultrahigh energy neutrino flux," *Phys.Rev.* **D73** (2006) 082002, arXiv:astro-ph/0601148 [astro-ph].

[49] **The ANITA** Collaboration, P. W. Gorham *et al.*, "Observational Constraints on the Ultra-high Energy Cosmic Neutrino Flux from the Second Flight of the ANITA Experiment," *Phys. Rev.* **D82** (2010) 022004, arXiv:1003.2961 [astro-ph.HE].

[50] R. Abbasi, T. Abu-Zayyad, M. Allen, J. Amann, G. Archbold, *et al.*, "An upper limit on the electron-neutrino flux from the HiRes detector," arXiv:0803.0554 [astro-ph]. * Brief entry *.

[51] F. Halzen and S. R. Klein, "Astronomy and astrophysics with neutrinos," *Phys.Today* **61N5** (2008) 29–35.

[52] J. A. Aguilar, A. Albert, F. Ameli, M. Anghinolfi, G. Anton, S. Anvar, E. Aslanides, J.-J. Aubert, E. Barbarito, S. Basa, and et al., "First results of the Instrumentation Line for the deep-sea ANTARES neutrino telescope," *Astroparticle Physics* **26** (Nov., 2006) 314–324, arXiv:astro-ph/0606229.

[53] NEMO Collaboration, "The Neutrino Mediterranean Observatory Project," *Nuclear Physics B Proceedings Supplements* **143** (June, 2005) 359–362.

[54] The Nestor Collaboration, E. G. Anassontzis, A. E. Ball, G. Bourlis, W. Chinowsky, E. Fahrun, G. Grammatikakis, C. Green, P. Grieder, P. Katrivanos, P. Koske, A. Leisos, J. Ludvig, E. Markopoulos, P. Minkowsky, D. Nygren, K. Papageorgiou, G. Przybylski, L. K. Resvanis, I. Siotis, J. Sopher, T. Staveris, V. Tsagli, A. Tsirigotis, and V. A. Zhukov, "Operation and performance of the NESTOR test detector," *Nuclear Instruments and Methods in Physics Research A* **552** (Nov., 2005) 420–439.

[55] For The Km3NeT Collaboration, R. Coniglione, C. Distefano, E. Migneco, P. Sapienza, and For the KM3NeT Collaboration, "KM3NeT: Optimization studies for a cubic kilometer neutrino detector," *Nuclear Instruments and Methods in Physics Research A* **602** (Apr., 2009) 98–100.

[56] B.K and Lubsandorzhiev, "Photodetectors of lake baikal neutrino experiment and tunka air cherenkov array," *Nuclear Instruments and Methods in Physics Research Section A: Accelerators, Spectrometers, Detectors and Associated Equipment* **442** no. 1-3, (2000) 368 – 373. http://www.sciencedirect.com/science/article/pii/S0168900299012528.

[57] G. A. Askar'yan, "Coherent Radio Emission from Cosmic Showers in Air and in Dense Media," *Soviet Journal of Experimental and Theoretical Physics* **21** (Sept., 1965) 658.

[58] N. G. Lehtinen, P. W. Gorham, A. R. Jacobson, and R. A. Roussel-Dupré, "Forte satellite constraints on ultrahigh energy cosmic particle fluxes," *Phys. Rev. D* **69** (Jan, 2004) 013008. http://link.aps.org/doi/10.1103/PhysRevD.69.013008.

[59] P. Gorham, P. Allison, B. Baughman, J. Beatty, K. Belov, *et al.*, "Erratum: Observational Constraints on the Ultra-high Energy Cosmic Neutrino Flux from the Second Flight of the ANITA Experiment," arXiv:1011.5004 [astro-ph.HE]. * Temporary entry *.

[60] P. W. Gorham, C. L. Hebert, K. M. Liewer, C. J. Naudet, D. Saltzberg, and D. Williams, "Experimental limit on the cosmic diffuse ultrahigh energy neutrino flux," *Phys. Rev. Lett.* **93** (Jul, 2004) 041101. http://link.aps.org/doi/10.1103/PhysRevLett.93.041101.

[61] R. Dagkesamansky, A. Beresnyak, A. Kovalenko, and I. Zheleznykh, "The upper limit to the EHE neutrino flux from observations of the moon with Kalyazin radio telescope," *Int.J.Mod.Phys.* **A21S1** (2006) 142–146.

[62] C. James, R. M. Crocker, R. Ekers, T. Hankins, J. O'Sullivan, *et al.*, "Limit on UHE Neutrino Flux from the Parkes Lunar Radio Cherenkov Experiment," *Mon.Not.Roy.Astron.Soc.* **379** (2007) 1037–1041, arXiv:astro-ph/0702619 [astro-ph].

[63] O. Scholten, J. Bacelar, R. Braun, A. de Bruyn, H. Falcke, *et al.*, "Optimal radio window for the detection of ultra-high-energy cosmic rays and neutrinos off the moon," *J.Phys.Conf.Ser.* **81** (2007) 012004.

[64] www.skatelescope.org.

[65] C. James, R. Ekers, J. Alvarez-Muniz, J. Bray, R. McFadden, *et al.*, "LUNASKA experiments using the Australia Telescope Compact Array to search for ultra-high energy neutrinos and develop technology for the lunar Cherenkov technique," *Phys.Rev.* **D81** (2010) 042003, arXiv:0911.3009 [astro-ph.HE].

[66] P. Allison, J. Auffenberg, R. Bard, J. Beatty, D. Besson, *et al.*, "Design and Initial Performance of the Askaryan Radio Array Prototype EeV Neutrino Detector at the South Pole," arXiv:1105.2854 [astro-ph.IM]. * Brief entry *.

[67] P. Gorham, D. Saltzberg, A. Odian, D. Williams, D. Besson, G. Frichter, and S. Tantawi, "Measurements of the suitability of large rock salt formations for radio detection of high-energy neutrinos," *Nuclear Instruments and Methods in Physics Research Section A: Accelerators, Spectrometers, Detectors and Associated Equipment* **490** no. 3, (2002) 476 – 491. http://www.sciencedirect.com/science/article/pii/S016890020201077X.

[68] J. Alvarez-Muniz, E. Marques, R. Vazquez, and E. Zas, "Simulations of radio emission from electromagnetic showers in dense media," *Int.J.Mod.Phys.* **A21S1** (2006) 55–59.

[69] R. D. Stewart and R. R. Unterberger, "Seeing through rock salt with radar," *Geophysics* **41** no. 1, (1976) 123–132. http://geophysics.geoscienceworld.org/cgi/content/abstract/41/1/123.

[70] **HiRes Collaboration** Collaboration, K. Martens, "HiRes Estimates and Limits for Neutrino Fluxes at the Highest Energies," arXiv:0707.4417 [astro-ph].

[71] **Pierre Auger Collaboration** Collaboration, J. Abraham *et al.*, "Properties and performance of the prototype instrument for the Pierre Auger Observatory," *Nucl.Instrum.Meth.* **A523** (2004) 50–95.

[72] J. Abraham, P. Abreu, M. Aglietta, C. Aguirre, E. J. Ahn, D. Allard, I. Allekotte, J. Allen, P. Allison, J. Alvarez-Muñiz, and et al., "Limit on the diffuse flux of ultrahigh energy tau neutrinos with the surface detector of the Pierre Auger Observatory," *Phys. Rev. D* **79** no. 10, (May, 2009) 102001, arXiv:0903.3385 [astro-ph.HE].

[73] G. A. Gusev and I. M. Zheleznykh, "Neutrino and muon detection from the radio-emission of cascades created by them in natural dielectric media," *Soviet Journal of Experimental and Theoretical Physics Letters* **38** (Nov., 1983) 611.

[74] S. W. Barwick, "ARIANNA: A New Concept for UHE Neutrino Detection," *Journal of Physics Conference Series* **60** (Mar., 2007) 276–283, arXiv:astro-ph/0610631.

[75] T. Barrella, S. Barwick, and D. Saltzberg, "Ross Ice Shelf (Antarctica) in situ radio-frequency attenuation," *Journal of Glaciology* **57** (Mar., 2011) 61–66, arXiv:1011.0477 [astro-ph.IM].

[76] G. A. Askar'yan, "Excess Negative Charge of an Electron-Photon Shower And Its Coherent Radio Emission," *Soviet Journal of Experimental and Theoretical Physics* **14** (1962) 441–444.

[77] M. H. Reno, "Neutrino cross sections at HERA and beyond," *Nuclear Physics B Proceedings Supplements* **151** (Jan., 2006) 255–259, arXiv:hep-ph/0412412.

[78] P. W. Gorham, D. P. Saltzberg, P. Schoessow, W. Gai, J. G. Power, R. Konecny, and M. E. Conde, "Radio frequency measurements of coherent transition and Cherenkov radiation: Implications for high-energy neutrino detection," *Phys.Rev.* **E62** (2000) 8590–8605, arXiv:hep-ex/0004007 [hep-ex].

[79] D. Saltzberg, P. Gorham, D. Walz, C. Field, R. Iverson, A. Odian, G. Resch, P. Schoessow, and D. Williams, "Observation of the Askaryan Effect: Coherent Microwave Cherenkov Emission from Charge Asymmetry in High-Energy Particle Cascades," *Physical Review Letters* **86** (Mar., 2001) 2802–2805, arXiv:hep-ex/0011001.

[80] P. W. Gorham, D. Saltzberg, R. Field, E. Guillian, R. Milincic, *et al.*, "Accelerator measurements of the Askaryan effect in rock salt: A Roadmap toward teraton underground neutrino detectors," *Phys.Rev.* **D72** (2005) 023002, arXiv:astro-ph/0412128 [astro-ph].

[81] P. Miocinovic, R. Field, P. Gorham, E. Guillian, R. Milincic, *et al.*, "Time-domain measurement of broadband coherent Cherenkov radiation," *Phys.Rev.* **D74** (2006) 043002, arXiv:hep-ex/0602043 [hep-ex].

[82] P. W. Gorham, S. W. Barwick, J. J. Beatty, D. Z. Besson, W. R. Binns, C. Chen, P. Chen, J. M. Clem, A. Connolly, P. F. Dowkontt, M. A. Duvernois, R. C. Field, D. Goldstein, A. Goodhue, C. Hast, C. L. Hebert, S. Hoover, M. H. Israel, J. Kowalski, J. G. Learned, K. M. Liewer, J. T. Link, E. Lusczek, S. Matsuno, B. Mercurio, C. Miki, P. Miočinović, J. Nam, C. J. Naudet, J. Ng, R. Nichol, K. Palladino, K. Reil, A. Romero-Wolf, M. Rosen, L. Ruckman, D. Saltzberg, D. Seckel, G. S. Varner, D. Walz, and F. Wu, "Observations of the Askaryan Effect in Ice," *Physical Review Letters* **99** no. 17, (Oct., 2007) 171101, arXiv:hep-ex/0611008.

[83] S. Barwick, D. Besson, P. Gorham, and D. Saltzberg, "South Polar in situ radio-frequency ice attenuation," *Journal of Glaciology* **51** (2005) 231–238.

[84] C. S. Neal, "The dynamics of the Ross Ice Shelf revealed by radio echo-sounding," *Journal of Glaciology* **24** (1979) 295–307.

[85] L. Gerhardt, S. Klein, T. Stezelberger, S. Barwick, K. Dookayka, J. Hanson, and R. Nichol, "A prototype station for ARIANNA: A detector for cosmic neutrinos," *Nuclear Instruments and Methods in Physics Research A* **624** (Dec., 2010) 85–91, arXiv:1005.5193 [astro-ph.IM].

[86] E. Rignot, "Is antarctica melting?," *Wiley Interdisciplinary Reviews: Climate Change* **2** no. 3, (2011) 324–331. http://dx.doi.org/10.1002/wcc.110.

[87] B. Riffenburgh, *Encyclopedia of the Antarctic*. New York:Routledge, 2007.

[88] M. Oppenheimer, "Global warming and the stability of the West Antarctic Ice Sheet," *Nature* **393** (May, 1998) 325–332.

[89] **The ARIANNA Collaboration** Collaboration, J. Hanson, "Ross Ice Shelf Thickness, Radio-frequency Attenuation and Reflectivity: Implications for the ARIANNA UHE Neutrino Detector ," in *International Cosmic Ray Conference*, 32nd International Cosmic Ray Conference. 2011.

[90] K. W. Nicholls, E. P. Abrahamsen, J. J. H. Buck, P. A. Dodd, C. Goldblatt, G. Griffiths, K. J. Heywood, N. E. Hughes, A. Kaletzky, G. F. Lane-Serff, S. D. McPhail, N. W. Millard, K. I. C. Oliver, J. Perrett, M. R. Price, C. J. Pudsey, K. Saw, K. Stansfield, M. J. Stott, P. Wadhams, A. T. Webb, and J. P. Wilkinson, "Measurements beneath an Antarctic ice shelf using an autonomous underwater vehicle," *Geophysical Research Letters* **330** (Apr., 2006) 8612.

[91] J. Dowdeswell and S. Evans, "Investigations of the form and flow of ice sheets and glaciers using radio-echo sounding," *Reports on Progress in Physics* **67** no. 10, (2004) 1821–1861. http://www.ingentaconnect.com/content/iop/ropp/2004/00000067/00000010/art00r03.

[92] A. Kovacs, A. J. Gow, and R. M. Morey, "The in-situ dielectric constant of polar firn revisited," *Cold Regions Science and Technology* **23** no. 3, (1995) 245 – 256. http://www.sciencedirect.com/science/article/pii/0165232X9400016Q.

[93] MacAyeal, Douglas, Olga Sergienko Ted Scambos, and Atsu Muto, "Ross Ice Shelf firn temperature, Antarctica," Digital Media.

[94] D. Z. Besson, J. Jenkins, S. Matsuno, J. Nam, M. Smith, S. W. Barwick, J. J. Beatty, W. R. Binns, C. Chen, P. Chen, J. M. Clem, A. Connolly, P. F. Dowkontt, M. A. Duvernois, R. C. Field, D. Goldstein, P. W. Gorham, A. Goodhue, C. Hast, C. L. Hebert, S. Hoover, M. H. Israel, J. Kowalski, J. G. Learned, K. M. Liewer, J. T. Link, E. Lusczek, B. Mercurio, C. Miki, P. Miočinović, C. J. Naudet, J. Ng, R. Nichol, K. Palladino, K. Reil, A. Romero-Wolf, M. Rosen, L. Ruckman, D. Saltzberg, D. Seckel, G. S. Varner, D. Walz, and F. Wu, "In situ radioglaciological measurements near Taylor Dome, Antarctica and implications for ultra-high energy (UHE) neutrino astronomy," *Astroparticle Physics* **29** (Mar., 2008) 130–157, arXiv:astro-ph/0703413.

[95] J. W. Glen and J. W. G., "Glaciological research by the norwegian-british-swedish antarctic expedition: Review," *The Geographical Journal* **125** no. 2, (1959) pp. 239–243. http://www.jstor.org/stable/1790509.

[96] http://www.scannermaster.com/v/vspfiles/files/pdf/CLP-5130-1N-manual.pdf.

[97] G. S. Varner, L. L. Ruckman, J. W. Nam, R. J. Nichol, J. Cao, P. W. Gorham, and M. Wilcox, "The large analog bandwidth recorder and digitizer with ordered readout (LABRADOR) ASIC," *Nuclear Instruments and Methods in Physics Research A* **583** (Dec., 2007) 447–460, arXiv:physics/0509023.

[98] G. S. Varner *et al.*, "Detection of ultra high energy neutrinos via coherent radio emission,". Presented at International Symposium on Detector Development for Particle, Astroparticle and Synchrotron Radiation Experiments (SNIC 2006), Menlo Park, California, 3-6 Apr 2006.

[99] G. S. Varner, "The modern fpga as discriminator, tdc and adc," *Journal of Instrumentation* **1** no. 07, (2006) P07001. http://stacks.iop.org/1748-0221/1/i=07/a=P07001.

[100] J. Hanson, *PhD Disseration in prepartion*. PhD thesis, University of California, Irvine, 2013.

[101] W. Huang, S.-h. Chiang, and S. Kleinfelder, "Waveform digitization with programmable windowed real-time trigger capability," in *Nuclear Science Symposium Conference Record (NSS/MIC), 2009 IEEE*, pp. 422 –427. 24 2009-nov. 1, 2009.

[102] J. Alvarez-Muñiz, R. A. Vázquez, and E. Zas, "Calculation methods for radio pulses from high energy showers," *Phys.Rev.* **D62** no. 6, (Sept., 2000) 063001–+, arXiv:astro-ph/0003315.

[103] **The ARIANNA Collaboration** Collaboration, F. Wu and J. Nam, "Simulation of ARIANNA Capabilities," in *International Cosmic Ray Conference*, vol. 5 of *30th International Cosmic Ray Conference*, pp. 1527–1530. 2008.

[104] R. Gandhi, C. Quigg, M. H. Reno, and I. Sarcevic, "Ultrahigh-energy neutrino interactions," hep-ph/9512364.

[105] E. Zas, F. Halzen, and T. Stanev, "Electromagnetic pulses from high-energy showers: Implications for neutrino detection," *Phys.Rev.* **D45** (Jan., 1992) 362–376.

[106] J. Alvarez-Muñiz and E. Zas, "Cherenkov radio pulses from EeV neutrino interactions: the LPM effect," *Physics Letters B* **411** (Sept., 1997) 218–224, arXiv:astro-ph/9706064.

[107] J. Alvarez-Muñiz and E. Zas, "The LPM effect for EeV hadronic showers in ice: implications for radio detection of neutrinos," *Physics Letters B* **434** (Aug., 1998) 396–406, arXiv:astro-ph/9806098.

[108] J. W. Clough and B. L. Hansen, "The Ross Ice Shelf Project," *Science* **203** (Feb., 1979) 433–434.

[109] C. A. Balanis, *Antenna theory : analysis and design*. John Wiley & Sons, Inc., 2005.

[110] **ANITA collaboration** Collaboration, . P. Gorham *et al.*, "The Antarctic Impulsive Transient Antenna Ultra-high Energy Neutrino Detector Design, Performance, and Sensitivity for 2006-2007 Balloon Flight," *Astropart.Phys.* **32** (2009) 10–41, arXiv:0812.1920 [astro-ph]. * Brief entry *.

[111] J. Alvarez-Muniz, A. Romero-Wolf, and E. Zas, "Cherenkov radio pulses from electromagnetic showers in the time-domain," *Phys.Rev.* **D81** (2010) 123009, arXiv:1002.3873 [astro-ph.HE].

[112] J. Alvarez-Muñiz, A. Romero-Wolf, and E. Zas, "Practical and accurate calculations of Askaryan radiation," *ArXiv e-prints* (June, 2011) , arXiv:1106.6283 [astro-ph.HE].

[113] J. Hanson, "Private communication.".

[114] J. G. Learned and S. Pakvasa, "Detecting nu_tau oscillations at PeV energies," *Astroparticle Physics* **3** (May, 1995) 267–274, arXiv:hep-ph/9405296.

[115] F. Halzen and D. Saltzberg, "Tau Neutrino Appearance with a 1000 Megaparsec Baseline," *Physical Review Letters* **81** (Nov., 1998) 4305–4308, arXiv:hep-ph/9804354.

[116] L. Gerhardt and S. R. Klein, "Electron and photon interactions in the regime of strong Landau-Pomeranchuk-Migdal suppression," *Phys. Rev.D* **82** no. 7, (Oct., 2010) 074017, arXiv:1007.0039 [hep-ph].

[117] T. Barrella, A. Vieregg, and D. Saltzberg, "Monte Carlo studies for neutrino detection from Minna Bluff and other mountainsides in Antarctica," *APS April Meeting Abstracts* (Apr., 2011) 9007.

[118] G. J. Feldman and R. D. Cousins, "Unified approach to the classical statistical analysis of small signals," *Phys. Rev. D* **57** (Apr., 1998) 3873–3889, arXiv:physics/9711021.

[119] S. Barwick, "Private communication.".

[120] L. Landau and I. Pomeranchuk, "Limits of applicability of the theory of bremsstrahlung electrons and pair production at high-energies," *Doklady Akad. Nauk S.S.S.R.* **92 No. 3** (1953) 535.

[121] L. Landau and I. Pomeranchuk, "Electron-cascade processes at ultra-high energies," *Doklady Akad. Nauk S.S.S.R.* **92 No. 4** (1953) 735.

[122] A. B. Migdal, "Bremsstrahlung and Pair Production in Condensed Media at High Energies," *Physical Review* **103** (Sept., 1956) 1811–1820.

[123] M. Nieto-Vesperinas and J. A. Sánchez-Gil, "Light scattering from a random rough interface with total internal reflection," *J. Opt. Soc. Am. A* **9** no. 3, (Mar, 1992) 424–436. http://josaa.osa.org/abstract.cfm?URI=josaa-9-3-424.

[124] P. Beckmann and A. Spizzichino, *The scattering of electromagnetic waves from rough surfaces*. 1987.

[125] M. Griswold, M. Harrison, and D. Saltzberg, "Observation of light transmission through randomly rough glass surfaces beyond the critical angle," *J. Opt. Soc. Am. A* **24** no. 10, (Oct, 2007) 3207–3210. http://josaa.osa.org/abstract.cfm?URI=josaa-24-10-3207.

[126] www.breault.com.

[127] www.lumerical.com.

[128] F. Wu, "Private communication.".

[129] W. D. Arnett, J. N. Bahcall, R. P. Kirshner, and S. E. Woosley, "Supernova 1987A," *Ann.Rev.Astron.Astrophys.* **27** (1989) 629–700.

[130] J. D. Kraus and R. J. Marhefka, *Antennas for all applications*. 2002.

[131] Brekhovskikh and Godin, *Acoustics of Layered Media II*, vol. 10 of *Wave Phenomena*. Springer-Verlag, 1992.

* * *